Modelling and simulation of the production process of thin film composite membranes for gas separation

Vom Promotionsausschuss der

Technischen Universität Hamburg

Zur Erlangung des akademischen Grades

Doktor-Ingenieur (Dr.-Ing.)

genehmigte Dissertation (Monografie)

von

Florian Brennecke

aus

Celle

2026

Vorsitzender des Prüfungsausschusses:	Prof. Dr.-Ing. Mirko Skiborowski
Erster Gutachter:	Prof. Dr.-Ing. Michael Schlüter
Zweite Gutachterin:	Prof. Dr.-Ing. Irina Smirnova
Dritter Gutachter:	Dr. Torsten Brinkmann

https://doi.org/10.15480/882.17313

Tag der mündlichen Prüfung: 23.04.2026

Acknowledgments

When you submit the condensed result of many years of work in form of a thesis and you finally defend it, it feels like a huge personal accomplishment. And while your own input is of course central, it is well worth remembering how many people contributed to this work and made it even possible. Without the help and support of others, I would not be holding this thesis in my hands now, thus an honourable mention is the least I can do to express my gratitude.

First of all, I thank Prof. Schlüter for accepting to supervise this dissertation, even though it was conducted externally at Helmholtz-Zentrum Hereon. I appreciate the constructive review process and feedback that clearly improved the final result of this work.

Secondly, I thank Prof. Smirnova for being the second reviewer of this external thesis, despite her many other responsibilities at the university.

This project was conducted in the group of Dr. Torsten Brinkmann at Helmholtz-Zentrum Hereon and I thank him a lot for 3,5 wonderful years. His support and supervision helped me a lot and he always made sure that there was the technical and financial basis that I needed to finish this work successfully. Moreover, I would like to thank Prof. Abetz for giving me the opportunity to conduct my dissertation project at his institute.

Talking about the institute at Hereon, there are of course many former colleagues that come to my mind, who helped me with many things. We had fruitful discussions about work and sometimes also non-work-related topics and they made my time there very enjoyable. I specifically thank Jule for helping me with all the membrane coating experiments and constantly discussing ideas and testing new approaches. I thank Jan Pohlmann for helping me a lot with the LabView Software and Petra for being the helping hand in the rheology department. Microscopy images play a big role in the experimental validation of my work and I thank everyone in the microscopy group for their reliably good work. Moreover, I thank Fynn, Kristian, Felix, Volkan and everyone else for the fun times at the kitchen and the shared laughter, which any good work place also needs. There are many more people at Hereon that gave me advice, challenged ideas and contributed to the success of this project and I thank all of you!

I also thank my friends in Hamburg and also those from my university days in Aachen. A received a lot of motivation and moral boosts from you, and I thank you all for that.

Last but certainly not least, I thank my dear and beloved parents, who helped me throughout all these years and always had my back when times became stressful. I was never in doubt about your unconditional support and for that I will always be grateful.

Contents

Nomenclature

Latin symbols

A	Area	[m²]
A_η	Pre-factor in the Andrade equation	[N·s·m^{-2}]
$\vec{a}$	Acceleration vector	[m·s^{-2}]
a_{vW}	Attraction parameter in the van der Waals model of a real gas	[m^6]
B_η	Exponential factor in the Andrade equation	[K]
b_{vW}	Repulsion parameter in the van der Waals model of a real gas	[m³]
C	Specific heat capacity	[J· K^{-1}·kg^{-1}]
Ca	Capillary number	[-]
c	Concentration	[mol·m^{-3}]
$c_{s,\infty}$	Total number of surface binding sites per unit area	[mol·m^{-2}]
c_s	Surface concentration	[mol·m^{-2}]
D	Diffusion coefficient	[m²·s^{-1}]
E	Energy	[J]
$E_{Thermal}$	Thermal energy	[J]
E_i	Interfacial free energy	[J]
e	Specific internal energy	[J·m^{-3}]
$\bar{\bar{F}}$	Deformation gradient tensor	[-]
$\vec{F}$	Force vector	[N]
F_D	Drag force on a spherical particle in Stokes flow	[N]
F_{LJ}	Force acting on a particle in the Lennard Jones potential	[N]
$\vec{F}_{st}$	Surface tension force vector per unit area	[N·m^{-2}]
$\vec{f}$	Volumetric (body) force	[N·m^{-3}]
$\overrightarrow{f_g}$	Volume specific gravitational force vector	[N·m^{-3}]
f_i	Fugacity of component *i*	[Pa]
$\vec{f}_{tr}$	Traction	[N·m^{-2}]
G	Elastic spring modulus	[N·m^{-2}]
G'	Elastic storage modulus	[N·m^{-2}]
G''	Viscous loss modulus	[N·m^{-2}]
$\vec{g}$	Gravitational acceleration vector	[m·s^{-2}]
$\bar{\bar{I}}$	Identity matrix	[-]
j_m	Mass flux	[kg· m^{-2}·s^{-1}]
J	Determinant of the deformation gradient tensor	[-]
K_c	Molar surface coverage	[-]
K_{eq}	Equilibrium constant of the Langmuir isotherm	[m³·mol^{-1}]
K_H	Huggins constant	[-]
K_{MH}	Pre-factor in the Mark-Houwink law	[m³·g^{-1}]
k_a	Langmuir adsorption constant	[m³· mol^{-1}·s^{-1}]
k_d	Langmuir desorption constant	[s^{-1}]

k_{therm}	Thermal conductivity	[J· s^{-1}·m^{-1}·K^{-1}]
L	Length	[m]
L_m	Extensibility parameter in the FENE-P model	[-]
M_W	Molecular weight	[g·mol^{-1}]
m	Mass	[kg]
$\dot{m}$	Mass flow	[kg·s^{-1}]
N	Number of atoms or molecules	[-]
n	Number molecules in	[mol]
$\vec{n}$	Normal vector	[-]
$\vec{n}_D$	Diffusion flux	[mol·m^{-2}·s^{-1}]
n_s	Number of surface molecules	[mol]
P	Pressure	[N·m^{-2}]
$\vec{p}$	Momentum vector	[kg·m·s^{-1}]
p_A	Permeability of gas through a membrane	[m^3(STP) · m^{-1}·s^{-1}·Pa^{-1}]
Q	Heat energy	[J]
$\dot{Q}$	Heat source	[J·s^{-1}]
$\dot{q}$	Heat flux	[J· m^{-2}·s^{-1}]
Re	Reynolds number	[-]
r	Radius	[m]
r_a	Langmuir adsorption rate	[mol· m^{-2}·s^{-1}]
r_d	Langmuir desorption rate	[mol·m^{-2}·s^{-1}]
r_{LJ}	Distance between interacting atoms in the Lennard Jones model	[m]
S	Free binding sites per unit area in	[mol·m^{-2}]
S_A	Gas solubility in a polymer	[m^3(STP) ·m^{-3}·Pa^{-1}]
$s_{A/B}$	Selectivity of a membrane with respect to gasses A and B	[-]
T	Temperature	[K]
T_c	Critical temperature	[K]
$\vec{t}$	Tangential vector	[-]
V	Volume	[m^3]
v	Scalar velocity	[m·s^{-1}]
$\vec{v}$	Velocity vector	[m·s^{-1}]
$\dot{v}_{gas}$	Volumetric gas flux	[m^3·m^{-2}·s^{-1}]
$\vec{v}_s$	Surface velocity	[m·s^{-1}]
W	Thermodynamic work	[J]
x_i	Molar fraction of component *i*	[-]

Universal constants

k_B	Boltzmann constant $1.381 \cdot 10^{-23}$	$[J \cdot K^{-1}]$
N_A	Avogadro constant $6.022 \cdot 10^{23}$	$[1 \cdot mol^{-1}]$
σ_{SB}	Stefan-Boltzmann constant $5.670 \cdot 10^{-8}$	$[J \cdot m^{-2} \cdot s^{-1} \cdot K^{-4}]$
$k_{Eötvös}$	Eötvös constant $2.100 \cdot 10^{-7}$	$[J \cdot K^{-1} \cdot mol^{-2/3}]$
R	Ideal gas constant 8.314	$[J \cdot K^{-1} \cdot mol^{-1}]$

Greek symbols

α	Exponential Mark-Houwink parameter	[-]
β	Interaction parameter in the van der Waals surface energy	$[N \cdot m^3 \cdot mol^{-2}]$
Γ	Torque	[N·m]
γ	Relative shear or strain	[-]
$\dot{\gamma}$	Shear rate	$[s^{-1}]$
δ	Final polymer thickness after evaporation of solvent	[m]
ϵ	Emissivity	[-]
$\dot{\varepsilon}$	Elongation rate	$[s^{-1}]$
ε_{LJ}	Depth of the Lennard Jones potential	[J]
ζ	Drag coefficient in Stokes law	$[N \cdot s \cdot m^{-1}]$
η	Viscosity	$[N \cdot s \cdot m^{-2}]$
$\bar{\eta}$	Elongational viscosity	$[N \cdot s \cdot m^{-2}]$
η_i	Intrinsic viscosity	$[m^3 \cdot g^{-1}]$
η^*	Complex viscosity	$[N \cdot s \cdot m^{-2}]$
θ_{eq}	Static equilibrium contact angle	[°]
$\theta_{d,eq}$	Dynamic equilibrium contact angle	[°]
λ	Viscoelastic relaxation time	[s]
μ	Mobility parameter in the Einstein relation	$[m^2 \cdot s\text{-}1 \cdot J^{-1}]$
υ	Molecular volume	$[m^3]$
Π	Surface tension	$[N \cdot m^{-1}]$
ρ	Density	$[kg \cdot m^{-3}]$
$\bar{\bar{\sigma}}$	Cauchy stress tensor	$[N \cdot m^{-2}]$
σ_{LJ}	Distance for which the Lennard Jones potential is zero	[m]
τ	Stress	$[N \cdot m^{-2}]$
$\bar{\bar{\tau}}$	Deviatoric stress tensor	$[N \cdot m^{-2}]$
φ_{sus}	Volume fraction of a suspended particle	[-]
χ	Map function between Eulerian and Lagrangian frame of reference	[-]
ω	Angular velocity or oscillation frequency	$[s^{-1}]$

Abbreviations

A

ALE..... *Arbitrary Lagrange-Eulerian*
AMB..... Alternating multiblock copolymer

C

CCD..... Central composite design
CCS ..... *Carbon capture and storgae*
CCU..... *Carbon capture and utilization*
CFD ..... *Computational fluid dynamics*
CMC.....*Critical micelle concentration*

D

DOE ..... Design of experiments

F

FEM .....*Finite element method*
FFV..... *Fractional free volume*, Fractional free volume
FVM ..... *Finite volume method*

G

GSA..... Gauss-Seidel algorithm

M

MBCP..... Multiblock copolymers
MMM ..... *Mixed matrix membranes*

P

PAN ..... Polyacrylonitrile
PBT..... Polybutyleneterephtalate
PDE..... Partial differential equation
PDMS ..... Polydimethylsiloxane
PEO ..... *Polyethylenoxide*
PEOT.....*Polyethylene oxide terephthalate*
PMPS..... *Polymethylphenylsilylene*
PPO ..... Polypropylenoxide

R

RSM..... *Response surface method*

S

SDS .....Sodiumdodecylsulfate
SEM .....*Scanning electron microscope*
SMC..... *Solvent mixture component*

T

TFC ..... Thin-film composite

V

VOF .....Volume of fluid

Abstract

Despite the growing attention for membrane-based processes, especially those targeted at the reduction of greenhouse gas emissions, the transfer of a membrane production process from laboratory scale to the large scale is still a challenge. Many production steps involve manual fine-tuning and a large number of experiments to find the appropriate process parameters for the desired coating result. Adding to the complexity of the problem, increasing awareness is raised to sustainability of the fabrication process and materials utilized for membranes. The anticipated increase in restrictions on the use of toxic or environmentally harmful solvents fuels the search for greener alternatives. This implies a growing demand for a better understanding of how chemical and physical properties of the used polymers and solvents interact in the fabrication process of membranes, and how this can be modelled and predicted to save time and resources.

In this thesis, the roll-to-roll coating process in the large-scale fabrication of thin film composite membranes is modelled and simulated by means of computational fluid dynamics. The interface of the free-surface flow is captured using a moving mesh approach and the evaporation of solvent and its effect on the polymer concentration, and thus viscosity and density of the solution, is incorporated. To reduce the computational effort, the model was set up in two dimensions only.

For the model validation, several measurement techniques were employed. The final polymer thickness on the membrane is determined via electron microscopy images and also derived from mass-loss measurements of the polymer solution feed during coating experiments. Furthermore, the liquid film thickness on the applicator roll of the coating device is measured via a confocal laser displacement sensor and compared to the model predictions. As a first step, the predictive quality of the model was evaluated for the polydimethylsiloxane (PDMS) based coating of the protective top layer of the membranes and demonstrated the principal validity of the approach. The final polymer thickness could be predicted with an error of approximately 20% compared to the empirical mean value for several coating conditions.

Subsequently, the same model was used to predict coating thicknesses of PolyActive™ solution, a multiblock copolymer that is used for the selective layer of membranes that are designated for CO_2 separation tasks. The polymer is dissolved in a mixture of three solvents, which are concealed for confidential reasons and will be abbreviated as solvent mixture component 1-3 (SMC 1-3). This marks another difference to the PDMS coating which is done in one solvent (isooctane).

In contrast to the PDMS homopolymer, the coating thickness on the membrane was found to deviate strongly from model predictions, showing an approximately four-times thicker polymer layer than expected. Two main changes in the model were done that might account for this, namely the inclusion of viscoelastic effects of the polymer and the Marangoni effects caused by the inhomogeneous distribution of the polymer at the interface, which is thought to act like a surfactant that induces surface tension gradients and therefore secondary flow patterns. Shear rate and oscillatory viscosity measurements of PolyActive™ solution were performed and, together with simulation results and data from literature, suggest that viscoelasticity is not likely to be the cause of the observed thickening effect. In contrast, the implemented Marangoni effects were able to reproduce the observed thickening effect in large parts. As literature data on similar block copolymers demonstrate the amphiphilic character and surface activity of such polymers, this explanation seems more plausible, although several uncertainties concerning numerical robustness and model parameters remain to be addressed in future research. In addition, the coating of PolyActive™ was repeated with pure SMC 3 as the solvent. Here, the thickening effect was even stronger and could not be explained via simulations

so far, even though some results hint at thermal effects that might play a role due to the high volatility of SMC 3. Nevertheless, the implemented computational fluid dynamics (CFD) model delivers valuable insights into the complexities of this particular coating process and highlights the sensitivity of the system to fluid-mechanical force gradients on the micro-scale.

Zusammenfassung

Trotz der wachsenden Beachtung von Membran-basierten Prozessen, insbesondere jenen, die der Reduktion von Treibhausgasen dienen, ist der Transfer von Membranproduktionsprozessen vom Labormaßstab zum Großmaßstab weiterhin eine Herausforderung. Viele Produktionsschritte erfordern manuelle Feinjustierung und eine hohe Zahl von Experimenten, um die geeigneten Prozessparameter für das gewünschte Beschichtungsresultat zu finden. Die Komplexität des Problems wird zusätzlich erhöht, indem die Nachhaltigkeit des Fabrikationsprozesses und der eingesetzten Materialien steigende Beachtung erfährt. Die zu erwartende Verschärfung von Regularien in Bezug auf die Verwendung von toxischen oder umweltschädlichen Lösemitteln befeuert die Suche nach „grünen" Alternativen. Dies verlangt jedoch ein besseres Verständnis der Interaktionen von chemischen und physikalischen Eigenschaften der eingesetzten Polymere und Lösemittel mit dem Fabrikationsprozess von Membranen und nach akkuraten Modellen zur Vorhersage des Beschichtungsprozesses, um Zeit und Geld in der experimentellen Fabrikation zu sparen.

In dieser Arbeit wurde der Rollenbeschichtungsprozess zur großskaliegen Herstellung von Dünnschicht Komposit Membranen mit Hilfe von numerischer Strömungsmechanik (auf Englisch computational fluid dynamics (CFD)) modelliert und simuliert. Dabei wurde die Phasengrenzfläche der Strömung mit einem beweglichen Rechennetz erfasst und die Verdunstung des Lösemittels, sowie dessen Effekt auf die lokale Polymerkonzentration, Viskosität und Dichte, wurde mitberücksichtigt. Um den Rechenaufwand zu reduzieren, wurde dabei ein zweidimensionales Modell verwendet.

Für die Modellvalidierung wurden verschiedene Messmethoden eingesetzt. Die finale Polymerdicke auf der Membran wurde mittels Rasterelektronenmikroskopie vermessen und zusätzlich aus Massenverlustmessungen der Polymerlösung während des Beschichtungsvorganges hochgerechnet. Zudem wurde die Dicke des Flüssigkeitsfilms auf der Auftragsrolle der Beschichtungsanlage mittels Konfokal Laser gemessen und mit den Modellvorhersagen verglichen. In einem ersten Schritt wurde die Vorhersagegüte des Modells für die Beschichtung von Polydimethylsiloxan (PDMS), welches für die Deckschicht der Membranen eingesetzt wird, evaluiert und bewies dabei die prinzipielle Validität des gewählten Modellansatzes. Für eine Reihe von Beschichtungsbedingungen konnte dabei die finale Polymerdicke innerhalb eines Fehlerbereiches von 20% genau vorhergesagt werden.

Danach wurde das gleiche Modell genutzt, um die Beschichtungsdicke bei der Verwendung von einer PolyActive™-Lösung vorherzusagen, einem Multiblock Copolymer welches für die Selektivschicht von Membranen für die Abtrennung von CO_2 eingesetzt wird. Das Polymer ist dabei gelöst in einem drei-Komponenten Lösemittelgemisch, was ein weiterer Unterschied zur PDMS-Beschichtung darstellt, wo reines Iso-Oktan als Lösemittel fungiert. Aus Lizenz rechtlichen Gründen werden die genauen Komponenten des Lösemittelgemisches hier nicht genannt und nur durch „solvent mixture component 1-3" (SMC 1-3) abgekürzt.

Im Gegensatz zu dem PDMS Homopolymer weicht die Polymerdicke hier deutlich von den vorhergesagten Werten ab, mit einer Dicke die ca. dem vierfachen der Erwartung entspricht. Daraufhin wurden zwei Ergänzungen zum Modell getestet, welche beide die gefundenen Abweichungen erklären könnten. Dies waren zum einen eine mögliche Viskoelastizität der Polymerlösung und zum anderen ein möglicher Marangoni-Effekt verursacht durch eine inhomogene Verteilung des Polymers an der Phasengrenzfläche, welches hier als oberflächenaktives Molekül modelliert wird, das damit Unterschiede in der Oberflächenspannung mit Sekundärströmen induziert. Scherratenabhängige und oszillierende Viskositätsmessungen der PolyActive™-Lösung wurden ebenso durchgeführt und legen nahe, zusammen mit den Simulationen und Ergebnissen aus der Literatur, dass viskoelastische

Eigenschaften eher unwahrscheinlich sind, um den beobachteten Verdickungseffekt zu erklären. Im Gegensatz dazu konnte die Implementierung von Marangoni-Effekten den beobachteten Verdickungseffekt zum größten Teil erklären und reproduzieren. Da Literaturdaten zu ähnlichen Multiblock Copolymeren eine amphiphilen Charakter und Oberflächenaktivität solcher Polymere nahe legen, scheint diese Erklärung plausibler, auch wenn einige Restzweifel in Bezug auf die numerische Robustheit und Wahl der Modellparameter verbleiben und in zukünftigen Arbeiten adressiert werden sollten.

Zusätzlich wurde die Beschichtung von PolyActive™ in reinem SMC 3 als Lösemittel durchgeführt. In diesem Fall war der beobachtete Verdickungseffekt sogar noch stärker und konnte bisher nicht durch Simulationen erklärt werden, auch wenn es Hinweise gibt, dass thermische Effekte durch die höhere Verdunstungsrate von SMC 3 hier eine Rolle spielen könnten. Nichtsdestotrotz liefert das implementierte Modell wertvolle Einblicke in die Komplexitäten dieses speziellen Beschichtungsverfahrens und stellt die hohe Sensitivität des Systems in Bezug auf Fluid-mechanische Kraftgradienten heraus, welche sich auf mikroskopischen Skalen manifestieren können.

1. Introduction

The introduction of this thesis shall motivate the use of membrane processes, in particular thin-film composite membranes, and give an overview of production processes of membranes with a focus on roll coating procedures, which are also utilized in this thesis. Parts of the following text are very similar to the introduction sections of the publications by the author (Brennecke et al., 2021, 2024).

1.1 Motivation for membrane processes

Since the first industrial revolution, the economic model of the world is a linear one. Materials are extracted from the earth, converted to useful products via manifold value chains across the globe, distributed and then, after consumption, finally disposed as waste. Thermodynamically, these processes create complex structures and thereby locally decrease entropy, hence they need energy input and release waste heat to the surrounding. Until today, the prevalent energy sources are fossil fuels, but the extraction of materials and energy sources, as well as the disposal of waste, puts an unsustainable burden on our eco-systems, drives climate change and causes biodiversity loss. A new industrial revolution is needed, which limits the extraction of materials and replaces it with a circular economy that is fuelled by non-fossil energy sources. This vision of a circulating flow of materials implies a great demand in efficient separation technologies of all sorts. For instance, we need separation technologies for water desalination, for downstream processing of biotechnological processes that seek to replace the current petrochemical industry, or we need processes for gas separation to close the loop between exhaust gasses and power-to-gas or power-to-liquid technologies (Jarvis & Samsatli, 2018).

This can be seen in recent publications elucidating the way towards a net-zero CO_2 energy system fuelling the economy. It seems inevitable, that many elements of a new post-carbon industry require gas separation and purification technologies at different points (Davis et al., 2018). Carbon capture and storage (CCS) or utilization (CCU) might be the most prominent applications for CO_2 separation technologies, for which several methods are possible. These include chemical processes based on special liquids or solids for ab- or adsorption, respectively, mineralization or physical processes like cryogenic cooling and membrane separation.

The decision upon a favourable technology strongly depends on the CO_2 concentration and general composition of the CO_2 source gas, the related costs and ease of use (Abetz et al., 2006). A big aspect of the attractiveness of CO_2 capture is the energy that is needed for the process. If a very high purity of the separated CO_2 is desired (i.e. in excess of 99 mol.-%), membrane processes alone still fall short to adsorption-based methods(Brinkmann et al., 2017). However, as the currently prevalent amine scrubbing method is relatively energy intensive, membranes offer an attractive alternative (Brinkmann et al., 2015). For the lack of toxic chemicals in the process, the lower energy input and less waste, membrane processes seem the most environmentally friendly option overall (Liang et al., 2019). It should be kept in mind that CCU methods (like power-to-gas/liquid/chemicals) also hold the promise of valuable products to be made from sequestered CO_2, and the revenue of these products might help reduce the net separation cost, and thus significantly increase incentives to widely install such technologies. Moreover, if the separation task could be coupled with additional value creation, for example by including catalysts within the membrane, such processes have the potential to deliver very cost-effective utilization processes (Bell et al., 2020).

Since the attention on membrane processes for gas separation is on the rise for years, the range of applications for membrane-based CO_2 removal is very noticeable. Besides natural gas and biogas, a growing number of flue gasses from power-plants, steel industry and cement industry are considered for CO_2 removal (Kárászová et al., 2020).

For now, polymeric membranes have the advantages of much easier large-scale production, flexibility of geometry with respect to installation in membrane modules, price and operational ruggedness compared to ceramic membranes which in turn have advantages in terms of temperature and pressure stability (Wang et al., 2017). In terms of constancy of permeation performance, polymeric membranes can sometimes be competitive to ceramic ones, provided the right pre-treatment is given. Moreover, further scale up of existing membrane systems is relatively straightforward due to the modularity.

Nevertheless, as big the promises of polymeric membranes might be, to be suitable for industrial production, it is also necessary that the fabrication procedure is very easily scalable and the adoption to different separation tasks can be done efficiently.

1.2 Thin-film composite membranes for CO_2 separation

1.2.1 Membrane structure taxonomy

Commonly, membranes are classified according to their physical structure. One category are dense and homogeneous membranes made from one polymer, usually prepared by solvent evaporation or extrusion of the melted polymer. In order to be stable, these membranes have to attain a certain thickness which usually restricts their permeance (Ladewig & Al-Shaeli, 2017).

The second category are porous membranes. These can be further sub-divided into symmetric (isotropic) or asymmetric (anisotropic) membranes. Furthermore, the pore size is another typical classification characteristic. Asymmetric membranes can be structured in different ways. If the pore size changes gradually, ending with very small pores (or even a dense film) on the surface, they are called integrally skinned. One other type of asymmetric membrane, which is often found in the industry, are thin-film composite (TFC). Here, the membrane consists of at least two different materials, a porous substrate layer and a dense polymer layer on top, which is responsible for the selective properties but also very thin, thus enabling high permeance. The dimensions of the layers may vary from case to case, but usual thicknesses for the thin layer are 0.1 -5μm and 100-300μm for the porous substrate (Ladewig & Al-Shaeli, 2017). For TFC membranes, the most prevalent geometries are hollow fibres and flat sheets.

1.2.2 Separation principle of TFC membranes

The separation principle of all non-porous polymeric membranes, and therefore also of the top layers of TFC membranes, lies in the different solubility and diffusion speed of gas molecules in and through the polymeric material, respectively (Sanders et al., 2013). The ability of a specific gas to permeate through a polymeric material is expressed as its permeability coefficient

$$p_A = \frac{\dot{v}_{gas} L}{\Delta P} \tag{1}$$

where L is the thickness of the membrane, $\dot{v}_{gas}$ is the volumetric gas flux and ΔP is the pressure difference across the membrane. In the case of gas mixtures, ΔP refers to the partial pressure

difference (If the gas cannot be assumed to behave ideally, the difference in fugacity Δf_i has to be used). Thus, the volumetric gas flux through a membrane is proportional to the pressure difference and permeability and inversely proportional to the thickness of the membrane.

In the solution-diffusion model, p_A can be thought of as a material property, depending only on the gas and the utilized polymer, and is given by the product of the effective gas diffusion coefficient in the membrane (D_A) and the gas solubility coefficient (S_A)

$$p_A = D_A S_A \tag{2}$$

The diffusion coefficient depends on the molecular size of the permeating gas but also on the flexibility of polymer chains and the free volume in between polymer segments. The free volume between polymers is usually expressed as the fractional free volume (FFV), defined as

$$FFV = \frac{V - V_0}{V} \tag{3}$$

where V is the experimentally found specific volume of the polymer, i.e. its inverse density, and V_0 is the theoretical specific volume that is occupied by the polymer chains. The difference between the two arises due to non-ideal packing of polymers or motions of polymer chains that open space for gas molecules to diffuse through the material.

The solubility, in contrast, depends strongly on the interaction between gas molecules and the condensability of the gas, being closely linked to gas properties like boiling point or enthalpy of vaporization. But also, the interaction between polymer and gas as well as the morphology of the polymer can play a role (Sanders et al., 2013).

As one typical application of polymeric membranes is the separation of a gas from a mixture of two or more gasses, another important characterization parameter of a membrane is the selectivity, which is the ratio of the corresponding permeabilities of the gas combination looked at

$$s_{A/B} = \frac{p_A}{p_B} \tag{4}$$

In addition to the selective properties, the choice of polymers also influences the thermal and mechanical stability of the membrane and its durability, which is limited by the aging effect, a term used to describe the shrinkage of free volume in membranes made of glassy polymers due to slow rearrangement of the polymer chains over time (Sanders et al., 2013).

1.2.3 Membranes specifically made for CO_2 removal

For the specific task of separating CO_2 from gas streams, a variety of membrane materials is industrially used or researched, for instance cellulose acetate(Houde et al., 1996), polyimide membranes (Jankowski et al., 2021) or POLARIS™ (Lin et al., 2014) membranes developed by the company MTR. As it has been investigated for quite a while (Metz et al., 2004), polymeric materials of multi-block copolymers (MBCP) that contain polyethylene oxide (PEO), such as Pebax which contains polytetramethylene oxide (PTMO) and PEO, show high selectivity for CO_2, making such polymers excellent candidates for CO_2 removal tasks. Having been developed at Helmholtz-Zentrum Hereon (formerly known as Helmholtz-Zentrum Geesthacht), PolyActive™ membranes are another prominent example. Here the polymer consists of repeating units of polyethylene oxide chains linked to a

terephthalate group (PEOT) and polybutylene terephthalate (PBT). This type of membranes has a long history of research at Helmholtz-Zentrum Hereon (Brinkmann et al., 2015; Car et al., 2008; Yave et al., 2010) and has recently been used in pilot scale setups to remove CO_2 from industrial sources (Pohlmann et al., 2016). In PolyActive™, the two blocks of the polymer fulfil different functions. The PBT forms a rigid block material that is responsible for the mechanical stability, while PEO segments yield 'rubbery' blocks that primarily cause the high selectivity for CO_2 (Brinkmann et al., 2017). Consequently, the permeability can be tuned by adjusting the block length of the PEO chain in the polymer (Yave et al., 2010). Typically, PolyActive™ membranes produced at Hereon use PEO blocks with a molecular weight of 1500 g/mol (often referred to as PolyActive™ 1500). The content of PEO in the polymer is given as 77 wt% (weight percent) of the total polymer.

Because of the close connection between diffusive transport of gasses through and the free volume of polymers, there is an empirically observed correlation between selectivity and permeability of polymeric membranes which is famous as the upper-bound trade-off (Ding, 2020), stating that both selectivity and permeability cannot be maximised at the same time. To overcome this hurdle, recent research has been directed at the incorporation of inorganic materials with very specific pore sizes into the polymer layer. The so-created hybrid materials should then act as a molecular sieve and are called mixed matrix membranes (MMMs), even though the term also applies to other hybrid material membranes that serve different purposes like enhancement of stability. Some examples of these added compounds include zeolites, graphene and metal-organic frameworks (Galizia et al., 2017). Yet another promising branch of membrane research is the use of facilitated transport membranes. Here, diffusion of the gas of interest is mediated by a carrier molecule, which can itself be mobile and diffuse through the membrane or fixed as an integral part of the polymer structure. In the case of CO_2 transport, the latter can for instance be achieved with aminated polymers (Rafiq et al., 2016).

As the variety of aforementioned approaches already indicates, there exist a myriad of material combinations to be tested for their suitability as membrane materials. However, as the use of membranes is primarily hailed for their environmental friendliness, a growing focus lies in finding sustainable materials and efficient production processes, which are needed if membranes are supposed to challenge conventional separation processes. Many thoughts are put into the development of elaborated high-performance materials for membranes, but often the scale-up from laboratory dimensions poses great challenges as well (X. Dong et al., 2021).

1.3 Membrane fabrication methods

When it comes to the fabrication methods of polymeric membranes, a good overview and classifications can be found in the literature (Lalia et al., 2013; Nunes et al., 2020). Lalia *et al.* provided an excellent summary, which is briefly recapitulated here. Among the many fabrication methods, one important category can be summarized as phase inversion methods, in which the polymer is initially dissolved in a solvent and transformed to a solid by some form of demixing process. Depending on the utilized demixing mechanism, the following sub-classes of phase inversion methods can be distinguished:

1) Immersion precipitation: Immersion of the polymer solution in a bath of non-solvent (that is with respect to the polymer) leads to an exchange of solvent and non-solvent in the polymer solution. When a critical concentration of non-solvent is reached, the polymer starts to precipitate.

2) Thermally induced phase separation: Many solvents show a decrease in mixing quality for lower temperatures, thus cooling of a polymer solution can also cause precipitation and leads to solid polymer films when the remaining solvent is removed.
3) Evaporation induced phase separation: In some context, this is also called solution casting. The solvent of the polymer solution evaporates and the polymer concentration in the remaining liquid rises until precipitation. If the volatility is not high enough, the evaporation can be enhanced by heating.
4) Vapour induced phase separation: Exposition of the polymer solution to an atmosphere that contains vapour of a non-solvent leads to absorption of the non-solvent in the solution, which eventually also leads to precipitation.

All of the above methods usually start with a substrate on which the polymer solution is casted, and the separation mechanism is then initiated - either immediately or shortly afterwards - by exposing the casted solution to the respective environment capable to induce the desired separation mechanism. In immersion precipitation, for instance, a viscous polymer solution is often casted onto a substrate using a doctor blade to ensure the desired and homogeneous film thickness. The casted film then goes into the coagulation bath containing the non-solvent. Solvent exchange leads to precipitation of the polymer onto the substrate. For an illustration of such a casting process, see Figure 1.

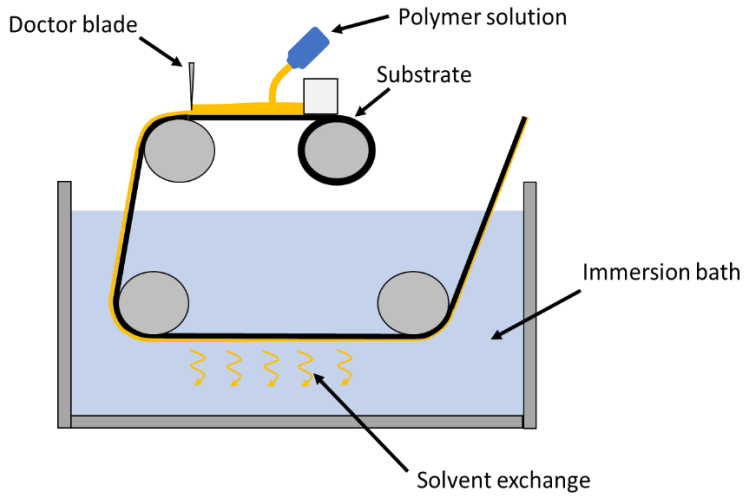

Figure 1 Schematic depiction of a membrane casting process using immersion precipitation. The solution containing the casting polymer is poured onto a substrate and a homogeneous thickness is ensured with a doctor blade. The solution -covered substrate then goes into the immersion bath where solvent exchange leads to precipitation of the polymer, leading to a thin, porous polymer film on the substrate.

If evaporation induced phase separation is the desired method, a similar operational procedure may be applied but the casted film is simply exposed to a suitable atmosphere. Alternatively, homogeneous films of polymer solution can be obtained by using some form of coating method, e.g. dip coating. Here, the substrate could be a fibre or plate that is immersed in the polymer solution and then pulled out (see Figure 2a). If the solution interacts strongly enough with the substrate surface, i.e. it is wetting, some of the liquid will stick on the substrate as it leaves the bath, forming a thin film where the thickness is primarily determined by the withdrawal speed, viscous forces and surface tension forces in the liquid. When the solvent evaporates into surrounding atmosphere, the evaporation induced phase separation goes hand in hand with the casting method. One way to conduct this coating process in a continuous manner is to use a roller coating setup, where the substrate is spanned on a rotating roll and at the same time in contact with the polymer solution (see Figure 2b).

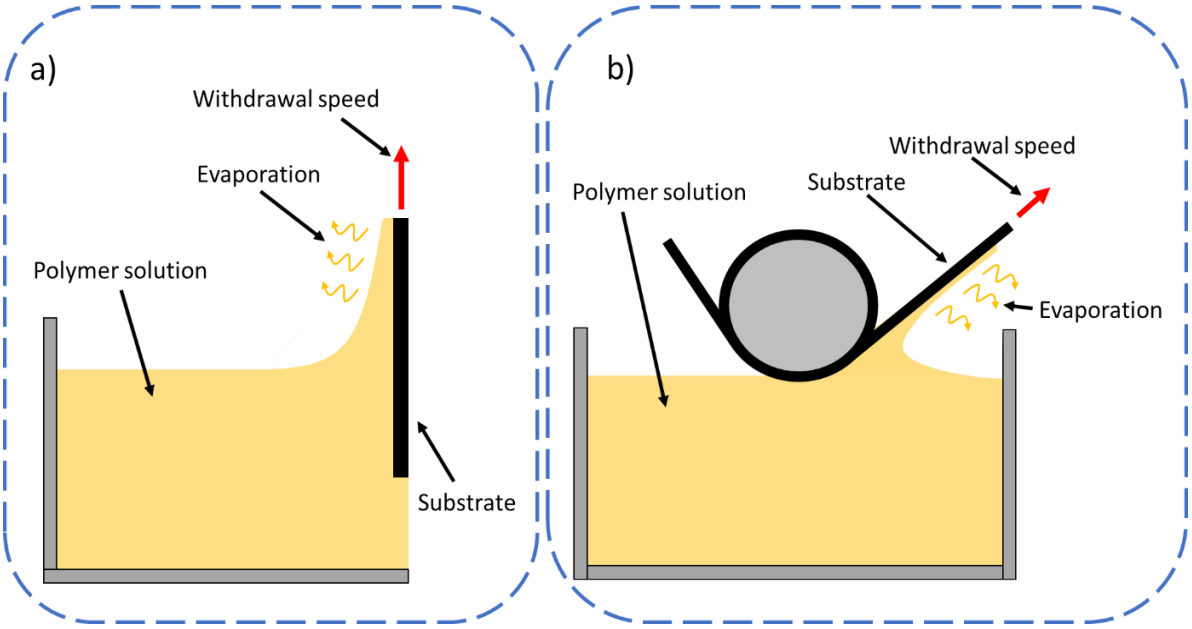

Figure 2 Illustration of membrane coating methods based on evaporation induced phase separation. The left side (a) shows the classical dip coating procedure, where a substrate is immersed in a polymer solution and then withdrawn. The solvent will evaporate, and a thin layer of precipitated polymer is left. The right side (b) shows the same principle applied in a continuous manner, where the substrate is put on a roll in direct contact with the coating solution.

Somewhat more intricate methods involve one or more applicator rolls in between the polymer solution and the substrate, as it is done at the process engineering group at Helmholtz-Zentrum Hereon and further explained in the next section (1.4). Here, the applicator roll picks up some of the solution and delivers it as a thin film to the substrate. In that case, the coating of the substrate happens in the small gap region between both rolls, where the distance between the rolls is small enough so that the liquid gets in contact with the substrate. For a schematic picture of this so-called roll-to-roll coating process, see Figure 3. As the liquid between the rolls forms a meniscus on both sides of the gap, this method is sometimes also called meniscus coating. Basically, the use of rolls allows an effective way to continuously operate the coating process that usually involves a lot of manual work. Roll-coating is well known in other coating industries (Park et al., 2016) and many variations, like slot-die coating, exist, making this basic approach very promising for the up-scaling of membrane fabrication (X. Dong et al., 2021). In one interesting version of the roller coating process, the film thickness can be limited on one of the rolls by means of a doctor blade, as it is done by other research groups that also fabricate TFC membranes via roll-coating (S. Dong et al., 2020).

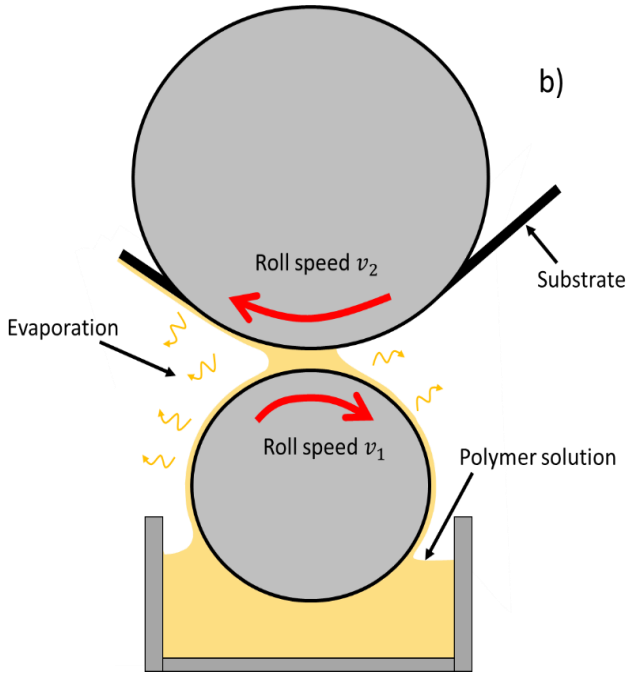

Figure 3 Schematic picture of the roll-to-roll coating process applied to produce TFC membranes. Usually, the substrate is a non-woven fabric with a porous support layer on top. Very thin and dense polymer films are then coated on the substrate by means of evaporation precipitation.

Albeit not important for this work, some other methods should briefly be mentioned. One commercially important class of fabrication methods is interfacial polymerization. As the name suggests, the process does not start with the finished polymer but uses one or more solutions of monomers that are soaked into the substrate that is to be coated. The dense polymer layer is then obtained by cross-linking of the applied monomers. This method is often utilized to produce nanofiltration and reverse osmosis membranes. For the fabrication of microporous membranes stretching is a popular method developed in the 1970s. The method does not use any solvent as it heats the polymer until melting and extrudes the melt into thin sheets which are stretched afterwards to produce small fractures that form the pores. Other ways to obtain a porous structure include the bombardment with heavy ions tearing holes in the irradiated dense polymer film, a method that is called track-etching. Finally, a more recent method is electrospinning. Here, a polymer solution is exposed to a high-voltage electrostatic potential and for a high enough potential, a charged liquid jet forms towards a collector.

1.4 Existing models of roll-to-roll coating

To produce large areas of flat sheet membrane with very thin selective polymer films, the process engineering group at the Institute of Membrane Research at Helmholtz-Zentrum Hereon employs a roll-to-roll coating process where three dense polymer layers are applied on top of a porous support substrate. These in-house produced TFC membranes consist of a highly permeable and easy to apply gutter, a selective and a protective layer (Yave et al., 2010). With this production setup, it is possible to tailor the membrane for a specific separation task by choosing the right polymer and thickness.

However, this freedom does not come without a challenge, as a change in polymer and solvent system also changes the physical properties of the polymer solution, especially viscosity and surface tension. This, in turn, changes the coating behaviour from case to case. Currently, the fine-tuning of process

parameters relies primarily on empirical knowledge and personal experience. To be ready for an efficient and agile production on industrial scale, a more structured approach guided by a model is desirable.

Some of the first mathematical analysis of roll-to-roll coating processes go back to the 70s and were done by Greener and Middleman (J. Greener & Middleman, 1981; Y. Greener & Middleman, 1975). Among other aspects, the authors were interested in the understanding of ribbing behaviour leading to wave-like surface irregularities during roller coating. For the lack of computational power, they used a lubrication approximation that ignored inertial terms in the Navier-Stokes equations. However, the lubrication approximation is only useful, when the flow field is quasi-unidirectional, i.e. the horizontal velocity components parallel to the walls in the gap are much larger than the vertical ones. For the roller coating device this limits the approximation to the 'flooded' regime, where the applicator roll delivers more liquid to the gap than what could go through. When the arriving film thickness is much smaller than the gap size, the regime is called 'starved' and the flow structure in the gap, which contains a primary transfer jet and two circulating flows, becomes important, besides the pressure gradients caused by the surface tension. The amount of liquid transferred to the membrane essentially depends on the position of the stagnation point at the exit of the gap. For a schematic image of the starved flow structure, see Figure 47 in section 4.2.5. For experimental images of the flows in reverse roll coating the reader is referred to the publications of Colye, Gaskell and Savage, among others, who made further numerical and experimental contributions to this research field in the 90s (Coyle et al., 1990; Decré et al., 1995; Gaskell et al., 1995; Gaskell, Innes, et al., 1998). With the rise of information technology and faster computational resources, the problem was also tackled with computational fluid dynamics (CFD), often solved with the finite element method (FEM) (Hao & Haber, 1999; Klostermann et al., 1994; Klostermann & Mewes, 1996). A large part of the work was motivated by problems that arise when applying this coating technique for coatings of paint, organic photovoltaic or semi-conductor materials.

Today, despite the highly increased computational power, the problem still is a difficult one to solve. The main challenges arise from the free surface flow, meaning the boundaries of the flow are not known *a priori* and must be solved simultaneously with the flow field. In former studies, the computation of the free surface was done with a volume of fluid (VOF) method (Chien & Jang, 2007), an 'interface capturing method' that tracks the surface with a scalar fraction function. For a variety of reasons, this thesis will choose a different approach based on a moving mesh, which will be explained in a later section (2.7).

1.5 Aim and outline of this thesis

The aim of this thesis is to implement a numerical model of the roll-to-roll coating process that is used to coat the thin top layers of TFC membranes using the in-house coating device in the process engineering group at Helmholtz-Zentrum Hereon. The model should compute the final polymer thickness for a given set of process parameters and material properties of the polymer and solvent used, at least predict final coating thicknesses reasonably well to be useable as a guide for the experimentalist. As most TFC membranes use Polydimethylsiloxane (PDMS) based silicone as gutter and protective layer, this often-encountered standard polymer serves as starting point and benchmark for the model. Furthermore, the application of the CO_2 selective PolyActive™ is an important part of the Institutes research and such membranes are produced on a regular basis, hence the established model should then be tested or possibly adjusted for the coating of this polymer. The gained insights should help to understand the coating process and emphasize relevant physical effects, which should

deliver guidance to the planning of coating experiments. Moreover, the model should help to determine the most sensitive fabrication parameters.

The modelling approach chosen here is a mechanistic one, which is based on the description of the multi-phase fluid flow in the roll-to-roll coating device by means of CFD. Firstly, section 2 of this thesis will briefly explain and recapitulate the fundamentals of fluid mechanics that are needed to model free surface flows and polymer solutions, as well as the numerical procedure of finite elements which is used to solve the model equations. It will also cover the essential background to understand the experimental methods used in the 'Materials and methods' section, especially those used to investigate flow behaviour and surface pressure. This third section then also covers the practical implementation, geometry and boundary conditions of the model and the experimental methods employed to validate it. In sections 4 and 5, the results and corresponding discussion are then divided into three subsections. First, the focus is on the simpler system of the PDMS homopolymer in isooctane. Then the model was extended to explain deviating effects found for the more complex polymer PolyActive™, where the findings for the three-component solvent mixture and pure SMC 3 as solvent are discussed separately.

2. Theoretical background

The theoretical background given in this section explains the fundamental laws and scientific theories needed to understand the numerical and experimental methods used in this thesis. As discussed in section 1, the final goal is a CFD model capturing the hydrodynamics of the coating process of TFC membranes. Therefore, section 2.1 covers the basics of fluid mechanics. Drawing from statistical physics and thermodynamics, a microscopic picture of fluids is established and the physical properties important for fluid mechanics are derived. Using the conservation principle for mass, momentum, and energy, one obtains the Navier-Stokes equations, a set of partial differential equations (PDEs) that model fluid flow. In the following, section 2.2 and 2.3 will deal with the additional complexities that arise when the fluid gets heterogeneous. Liquid mixtures, especially polymer solutions, complicate the interaction between fluid particles, thereby changing the rate of momentum transfer which is called viscosity (section 2.2). Adding a second phase to the system introduces a phase interface that comes with a variety of surface effects, especially surface tension, that are elaborated in 2.3. An important form of energy for fluid mechanics is thermal energy, thus section 2.4. gives some brief overview on the different modes of thermal energy transport. Having established the physical laws that govern fluid mechanics, section 2.5 deals with the numerical method of finite elements that will be used to solve these equations, while section 2.6 outlines the moving-mesh method used for multi-phase flow problems. Finally, section 2.7 briefly explains the design of experiments (DOE) method, a statistical methodology that can be used to analyse any complex system effectively. Section 2.8 is then concluding this chapter by providing some background on confocal laser measurements that will be used in the experimental section.

2.1 Modelling the flow of fluids

2.1.1 The microscopic picture of fluids

The term fluid comes from the Latin word *fluidus* meaning 'flowing'. In physics, the term fluids categorizes the class of substances that can deform continuously when subjected to a force: under normal condition these are gasses and liquids. Consequently, fluid mechanics refers to the laws describing the dynamics of flow.

To do this, several fluid properties like density ρ, pressure P, temperature T or velocity $\vec{v}$, must be defined. These can be derived from the microscopic physical laws briefly described in the following. Starting with a useful simplification, an ideal gas describes a monoatomic gas with no interactions and negligible size of the atoms (Keszei, 2012).

For an ideal gas, the kinetic theory delivers a microscopic picture of heat energy $E_{thermal}$: the kinetic energy of the random motion of atoms or molecules

$$E_{thermal} = \frac{1}{2}\sum_{i}^{N} m_i {v_i}^2 \tag{5}$$

where m_i is the mass of the individual atom or molecule, N is the number of atoms (or molecules) looked at and v_i is the velocity. As the thermal motion is random, one can ignore the individual

direction and use the magnitude of the velocity vector instead ($v_i = |\vec{v}|$). For an ideal gas, the energy can be easily related to the temperature. The equipartition theorem states that for every degree of freedom the particle has a kinetic energy of $\frac{1}{2}k_BT$, where T is the temperature in Kelvin and k_B is the Boltzmann constant (Demtröder, 2017). When the only degrees of freedom are the translational movement in the three dimensions of space, the thermal energy is

$$E_{thermal} = \frac{1}{2}\sum_{i}^{N} m_i {v_i}^2 = N\frac{3}{2}k_BT \tag{6}$$

From (6), one can directly derive the ideal gas law. Considering that the motion is random, the average kinetic energy in one spatial dimension, for example the *x*-direction, is one third of $E_{thermal}$

$$E_{thermal,x} = \frac{1}{2}\sum_{i}^{N_x} m_i {v_{i,x}}^2 = N_x\frac{1}{2}k_BT \tag{7}$$

where $v_{i,x}$ is the velocity of particle i in the direction x and N_x is the number of atoms that move in the x-direction. If all atoms are equal, this can be written as

$$m\,{v_x}^2 = k_BT \tag{8}$$

As the atoms hit the wall normal to the x-direction, the wall experiences a pressure P, which is force per unit area. That pressure is proportional to the number of atoms per unit volume $\frac{1}{2}\frac{N_x}{V}$ (in random motion only half of the atoms move in the positive x-direction, hence the factor ½), proportional to the momentum transfer $(2 \cdot m \cdot v_x)$ of the atoms and proportional to the velocity (higher random velocity means more atoms colliding with the wall in a given time window) (Demtröder, 2017). Mathematically, this translates to

$$P_x = \frac{\frac{1}{2}N_x \cdot 2 \cdot m \cdot v_x \cdot v_x}{V} = \frac{N_x}{V}k_BT \tag{9}$$

Because the motion is random, the same applies for all directions and the pressure is isotropic, thus giving the ideal gas law

$$P = \frac{N}{V}k_BT \tag{10}$$

The more common form of the equation uses the ideal gas constant R, which is the product of the Avogadro constant N_A (giving the number of molecules per mol) and k_B

$$P = \frac{N}{VN_A}RT = cRT \tag{11}$$

In non-ideal gases and liquids, these general thoughts still apply but become more complicated, as attractive interactions between atoms or molecules have to be taken into account. On the atomic scale, the interaction of atoms that are not charged or covalently bound is given by the famous Lennard Jones interaction potential E_{LJ}, which is qualitatively depicted in Figure 4 and often approximated as (Bird et al., 2007)

$$E_{LJ}(r_{LJ}) = 4\varepsilon_{LJ}\left[\left(\frac{\sigma_{LJ}}{r_{LJ}}\right)^{12} - \left(\frac{\sigma_{LJ}}{r_{LJ}}\right)^{6}\right] \tag{12}$$

where r_{LJ} is the distance between two interacting particles, $\sigma_{LJ}$is that particle distance, for which the potential is zero, and ε_{LJ} is the depth of the potential minimum, which is at distance $r_m = \sqrt[6]{2}\sigma_{LJ}$.

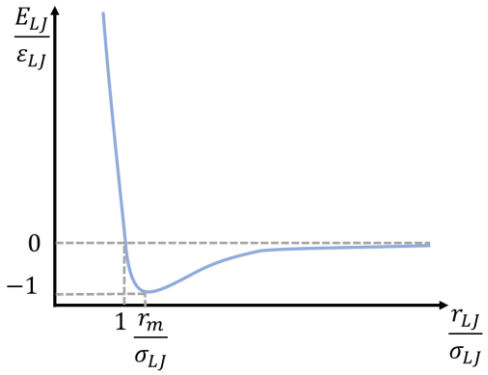

Figure 4 Schematic picture of the Lennard-Jones potential describing the interaction between uncharged, not covalently bound atoms.

The potential is composed of the attraction term $\left(\frac{\sigma_{LJ}}{r_{LJ}}\right)^6$, representing cohesive forces between molecules that are dipole-dipole interactions (also called van der Waals forces after Johannes Diderik van der Waals), and the repulsive forces $\left(\frac{\sigma_{LJ}}{r_{LJ}}\right)^{12}$ that occur when atoms or molecules are brought together so closely, that there electrons are forced into energetically higher orbitals (following the Pauli exclusion principle) (Marchand et al., 2011). The negative gradient of E_{LJ} with respect to the distance yields the force F_{LJ} acting on the particle

$$\frac{\partial E_{LJ}(r_{LJ})}{\partial r_{LJ}} = -F(r_{LJ}) \tag{13}$$

Including the attractive forces, the pressure is now corrected with a virial term

$$P = \frac{\sum_i^N m_i {v_i}^2}{V} + \frac{1}{2}\sum_i^k F(r_i) r_i \tag{14}$$

where k is the number of particle pairs within a certain cut-off radius.

When repulsive and attractive forces can be incorporated into the gas-law, one model often used is the van der Waals equation of state, where v is the molecular volume, b_{vW} represents the repulsion and a_{vW} represents the attraction parameter

$$P = \frac{k_B T}{v - b_{vW}} - \frac{a_{vW}}{v^2} \tag{15}$$

This equation is also useful to picture the transition from the gas phase to the liquid phase. In equilibrium, both phases must have the same pressure at their interface, even though the density of atoms in the gas phase is much lower than the density in the liquid. This is possible, because the strong repulsive forces in the liquid, caused by the dense packing, are counterbalanced by much stronger

attractive forces (Manikantan & Squires, 2020). At the typical mean distance between atoms or molecules in the liquid phase, the derivative of the potential is very steep, which means that very large forces are required to move the atom out of its equilibrium position. It is for that reason that liquids can be assumed to be incompressible. Even very large pressures will not lead to significant changes of the molecular distance and hence barely change the volume occupied by the liquid.

In contrast to random molecular motion, the velocity of a fluid particle may then just be defined as the non-isotropic part of the molecular motion, or, in other words, the superposition of the random movement with a motion that is not random but directed.

Finally, as every substance consists of atoms or molecules that have a molecular weight M_W, the density is just the total mass of all atoms or molecules N per unit volume V

$$\rho = \frac{N \cdot M_W}{V} \tag{16}$$

Now that the basic terms and properties of a fluid are defined and a microscopic perspective is established, one can set up laws that describe how these properties are connected and interact to yield macroscopic phenomena like flow.

But first, a disclaimer must be made. To be accessible by the tools of differential calculus, all fluid mechanical equations explained in the following sections need one fundamental assumption that is known as the continuum concept, which assumes, that all the material properties are continuously distributed in the body of particles and thus can be defined for ever smaller - even infinitesimally small - sub-divisions of the body. This theoretical concept is in reality of course not the case. Any real material consists of atoms and molecules (in this thesis sometimes collectively called particles) and macroscopically defined properties, like density and flow velocity, will stop to make sense, when we go down to or below the atomic dimension. Nevertheless, the continuum approximation turned out to be very useful still, as most fluid systems that are of interest contain such a vast number of particles, that it is possible to find a collection of fluid particles that still contain millions of elements, so that statistical properties like density, flow velocity or pressure can be calculated in a meaningful way for this ensemble. Yet, as the particles are so tiny, this collection occupies a total volume that is so small, that it can be virtually regarded as one point in space, at least for human standards.

2.1.2 The Eulerian and Lagrangian frame of reference

As already mentioned, the aim of fluid mechanics is to describe the dynamical behaviour of a fluid system. Looking at dynamics implies relative changes, for example of velocity, in the system. Therefore, one must define a frame of reference to relate these changes to. In fluid mechanics, there are two frames of reference, the Eulerian and Lagrangian frame. The explanation of both is not only practical for the subsequent discussion of balance equations but also very useful to understand the moving-mesh algorithm for free-surface flows (see section 2.7). The following explanation is inspired by the introduction to complex fluids in the literature (Alexander Morozov & Saverio E. Spagnolie, 2015), which should be consulted for further details.

When we set up a frame of reference inside the material body, every element in that material (e.g. a small blob of fluid particles) can be identified with a label $\boldsymbol{\alpha}$ that gives the coordinates of that particular element in the material frame. The description of pressure P, for instance, is thus a function of that

material position $\boldsymbol{a} = (a_1, \ldots, a_n)$ (where n is the number of dimensions) and also of time t: $P = P(\boldsymbol{a}, t)$. This perspective is called the material frame of reference or Lagrangian perspective.

A second perspective is the Eulerian description or spatial frame of reference. Here, the fluid properties are given with respect to the spatial position $\boldsymbol{x} = (x_1, .., x_n)$, thus for pressure $P = P(\boldsymbol{x}, t)$. Both perspectives are of course connected, as the property at material point $\boldsymbol{a}$ has to be the same as the property at the spatial point $\boldsymbol{x}$ that corresponds to this material point $P(\boldsymbol{a}, t) = P(\boldsymbol{x}(\boldsymbol{a}, \boldsymbol{t}), t)$. The mathematic function returning the spatial position $\boldsymbol{x}$ for a given time t and material point $\boldsymbol{a}$ is called a map χ. For an illustration of both perspectives, see Figure 5.

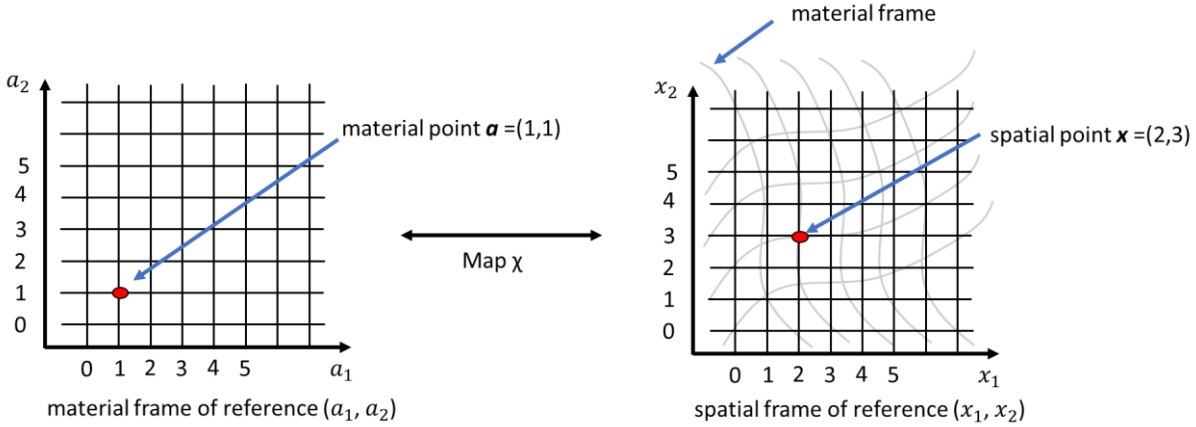

Figure 5 The material frame of reference (left side) assigns a material coordinate point to every element of a body. The spatial frame of reference (right side) assigns a spatial coordinate to each point in space. A known mathematical description of the deformation of the material with respect to the spatial frame means one can map any material point to a corresponding spatial point for any given point in time.

For simplicity, one can imagine that at time $t = 0$ both the material and spatial frame coincide. When the material experiences a force, it will start to deform accordingly and thus the material frame will also be deformed with respect to the spatial frame. If $\vec{v}(\boldsymbol{x}, t)$ is the velocity vector that describes the change of spatial position for all fluid particles (or particle blobs) at point in space $\boldsymbol{x}$ and time t, the velocity of a particle in terms of the material coordinate $\boldsymbol{a}$ is the time derivative of the map

$$\vec{v}(\boldsymbol{x}(\boldsymbol{a}, t), t) = \sum_{i=1,..,n} \frac{\partial x_i}{\partial t} = \left.\frac{d\boldsymbol{x}}{dt}\right|_{\boldsymbol{a}} = \frac{d}{dt}\chi(\boldsymbol{a}, t) \tag{17}$$

Analogously, any scalar variable f attached to a material point (e.g. a fluid property like pressure) changes over time in terms of the material frame as given by the time derivative $\left.\frac{d}{dt} f(\boldsymbol{a}, t)\right|_a$. In the spatial frame, f is a function of $\boldsymbol{x}$ and t. But since $\boldsymbol{x}$ itself is also a function of $\boldsymbol{a}$ and t, the chain rule has to be applied

$$\left.\frac{d}{dt} f(\boldsymbol{x}(\boldsymbol{a}, t), t)\right|_x = \frac{\partial f}{\partial t} + \sum_{i=1,..,n} \frac{\partial f}{\partial x_i} \cdot \frac{\partial x_i}{\partial t} = \left(\frac{\partial}{\partial t} + \vec{v} \cdot \nabla\right) f \tag{18}$$

The operator $\left(\frac{\partial}{\partial t} + \vec{v} \cdot \nabla\right)$ occurs so often in fluid mechanics that it got its own name and is called the material derivative

$$\frac{D}{Dt} \equiv \left(\frac{\partial}{\partial t} + \vec{v} \cdot \nabla\right) \tag{19}$$

To paraphrase it, if the rate of change of a material property is known for all points in the material frame, the material derivative gives the corresponding rate of change in the spatial frame. If the fluid particles do not move in space, both frames of reference coincide. If the fluid flows as described by the velocity field $\vec{v}$, the spatial derivative of the property is the superposition of any location-independent time derivative and the local flow velocity times its local spatial gradient.

A special, yet important, application of the material derivative is to be considered for a conservative property, meaning: if one follows a material point (i.e. blob of fluid particles) through the flow, its property doesn't change, hence

$$\frac{d}{dt} f(\boldsymbol{a}, t)\Big|_a = 0 \tag{20}$$

As already established above, there is a connection between the material and spatial frame, which also means that the rate of change of a property *f* at a material point ***a*** must have the same value as the rate of change of the same property at that spatial point ***x*** which corresponds to ***a***, thus

$$\frac{d}{dt} f(\boldsymbol{x}(\boldsymbol{a}, t), t)\Big|_x = \frac{d}{dt} f(\boldsymbol{a}, t)\Big|_a = 0 \tag{21}$$

Therefore, one obtains

$$\frac{Df}{Dt} = \left(\frac{\partial}{\partial t} + \vec{v} \cdot \nabla\right) f = 0 \tag{22}$$

which intuitively makes sense, as it means that the local rate of change of a conservative property can only be caused by a spatial gradient of that property which is convected by the flow.

One more useful metric in this context is the Jacobian matrix of the map $\boldsymbol{x} = \chi(\boldsymbol{a}, t)$, which is also called deformation gradient tensor $\bar{\bar{F}}(\boldsymbol{x}, t) = \frac{\partial \boldsymbol{x}}{\partial \boldsymbol{a}}$ (where $F_{ij} = \frac{\partial x_i}{\partial a_j}$), as it measures the rate of fluid deformation. If both frames coincide initially, this translates to $\bar{\bar{F}}(\boldsymbol{x}, O) = \bar{\bar{I}}$, where $\bar{\bar{I}}$ is the identity matrix. For clarification: using the deformation gradient tensor one can obtain the length of a line segment $d\boldsymbol{x}$ between two spatial points from the line segment length $d\boldsymbol{a}$ from the corresponding material points as

$$d\boldsymbol{x} = \bar{\bar{F}} \cdot d\boldsymbol{a} \tag{23}$$

For later considerations, the time derivative of the determinant $J = det\ \bar{\bar{F}}$ will be needed, which reads

$$\frac{dJ}{dt} = (\nabla \cdot \vec{v})\, J \tag{24}$$

In case the fluid is incompressible, i.e. an arbitrary control volume going through the flow can deform but the volume stays the same, the determinant $J = 1$ and thus

$$\nabla \cdot \vec{v} = 0 \tag{25}$$

2.1.3 The Navier-Stokes equations

The mass balance

One important conservative scalar property that is transported in a flow field is the total mass M of the fluid particle. When set in relation to the volume of the fluid blob, the density ρ is the property convected by the flow and can be computed by the integral of a control volume Ω as follows

$$M = \int_{\Omega} \rho(\boldsymbol{x}, t) dV_{\boldsymbol{x}} \tag{26}$$

In the context of fluid mechanics, mass is a conservative property, hence one can write

$$\frac{dM}{dt} = \frac{d}{dt} \int_{\Omega} \rho(\boldsymbol{x}, t) dV_{\boldsymbol{x}} = 0 \tag{27}$$

By considering the deformation of a control volume in the material frame with respect to the spatial frame, one finds

$$\frac{d}{dt} \int_{\Omega} \rho(\boldsymbol{x}, t) dV_{\boldsymbol{x}} = \frac{d}{dt} \int_{\Omega} \rho(\boldsymbol{x}(\boldsymbol{a}, t), t) J dV_{\boldsymbol{a}} = 0 \tag{28}$$

Pulling the time derivative inside the integral yields

$$\int_{\Omega} \left(\frac{D\rho(\boldsymbol{x}(\boldsymbol{a}, t), t)}{Dt} + \rho(\boldsymbol{x}(\boldsymbol{a}, t), t)(\nabla \cdot \vec{v}) \right) J dV_{\boldsymbol{a}} = 0 \tag{29}$$

which can be transformed back to the spatial frame

$$\int_{\Omega} \left(\frac{D\rho(\boldsymbol{x}, t)}{Dt} + \rho(\boldsymbol{x}, t)(\nabla \cdot \vec{v}) \right) J dV_{\boldsymbol{x}} = 0 \tag{30}$$

As the control volume is arbitrary and the above must hold everywhere, one can drop the integral sign

$$\frac{D\rho(\boldsymbol{x}, t)}{Dt} + \rho(\boldsymbol{x}, t)(\nabla \cdot \vec{v}) = \left(\frac{\partial}{\partial t} + \vec{v} \cdot \nabla \right) \rho + \rho(\boldsymbol{x}, t)(\nabla \cdot \vec{v}) = 0 \tag{31}$$

If the fluid in question is a liquid (or a gas at low enough pressure), the fluid can be assumed to be incompressible, as in these cases fluctuations in pressure cause no relevant variations in density (see introduction of section 2.1). Thus, ρ is a constant and (31) simplifies to the volume continuity equation (Rieutord, 2015)

$$\nabla \cdot \vec{v} = 0 \tag{32}$$

The momentum balance

The momentum balance can be thought of as a derivation of Newton`s second axiom, that says that a body experiencing a force will be accelerated in the direction of that force, with the acceleration being proportional to the force and the mass of the body. In mathematical terms this becomes the famous formula

$$\vec{F} = m \cdot \vec{a} \tag{33}$$

Since momentum $\vec{p}$ is defined as

$$\vec{p} = m \cdot \vec{v} \tag{34}$$

the term $m \cdot \vec{a}$ is nothing else than the time derivative of the momentum.

Again, one can apply the material derivative to the momentum as the transported fluid property

$$\frac{D\,(m \cdot \vec{v})}{Dt} = m \cdot \frac{D\,\vec{v}}{Dt} = \left(\frac{\partial (m \cdot \vec{v})}{\partial t} + \vec{v} \cdot \nabla (m \cdot \vec{v})\right) \tag{35}$$

Dividing by the volume to get volume specific terms, one obtains

$$\left(\frac{\partial (\frac{m}{V} \vec{v})}{\partial t} + \vec{v} \cdot \nabla (\frac{m}{V} \cdot \vec{v})\right) = \left(\frac{\partial (\rho \cdot \vec{v})}{\partial t} + \vec{v} \cdot \nabla (\rho \cdot \vec{v})\right) \tag{36}$$

Which, in the case of a non-compressible liquid, further simplifies to

$$\left(\frac{\partial (\rho \cdot \vec{v})}{\partial t} + \vec{v} \cdot \nabla (\rho \cdot \vec{v})\right) = \rho \cdot \left(\frac{\partial \vec{v}}{\partial t} + \vec{v} \cdot \nabla \vec{v}\right) \tag{37}$$

We can now utilize equation (37) when formulating Newton`s second axiom for an infinitesimal control volume Ω inside the body of fluid. Integrating over the control volume, one can state that the change of momentum must come from forces acting on that control volume. Those forces can conceptually be divided into external body forces $\vec{f}$ acting on the volume and surface forces per unit area, that is the traction $\vec{f}_t$, acting on the surface $\partial\Omega$ of the control volume, thus

$$\int_{\Omega} \rho \cdot \left(\frac{\partial \vec{v}}{\partial t} + \vec{v} \cdot \nabla \vec{v}\right) dV = \int_{\Omega} \vec{f}\, dV + \int_{\partial\Omega} \vec{f}_t\, dS \tag{38}$$

If $\vec{n}$ denotes the local outward pointing normal vector of the control volume, the traction $\vec{f}_t$, which is the resulting stress vector on the surface of the control volume, is the dot product of the normal vector $\vec{n}$ and the Cauchy stress tensor $\bar{\bar{\sigma}}$

$$\vec{f}_t = \vec{n} \cdot \bar{\bar{\sigma}} \tag{39}$$

The Cauchy stress tensor is a matrix that defines the state of stress at any point in space of a given material.

$$\bar{\bar{\sigma}} = \begin{pmatrix} \sigma_{xx} & \sigma_{xy} & \sigma_{xz} \\ \sigma_{yx} & \sigma_{yy} & \sigma_{yz} \\ \sigma_{zx} & \sigma_{zy} & \sigma_{zz} \end{pmatrix} \tag{40}$$

In three dimensions, the Cauchy stress tensor can be represented as depicted in Figure 6.

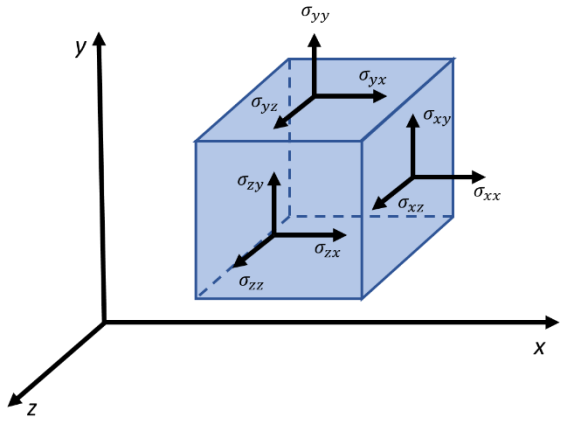

Figure 6 Schematic representation of a control volume (blue box) and all Cauchy stresses at its faces. The first index of the stress component denotes the face on which the stress acts, while the second index denotes the direction of the stress. In three dimensions, this yields the 3x3=9 stress components that constitute the Cauchy stress tensor.

Using equation (38) we can apply the divergence theorem (Bird et al., 2007) on (40) and transform the surface integral to a volume integral, yielding

$$\int_{\Omega} \rho \cdot \left(\frac{\partial \vec{v}}{\partial t} + \vec{v} \cdot \nabla \vec{v} \right) dV = \int_{\Omega} \vec{f}\, dV + \int_{\Omega} \nabla \cdot \bar{\bar{\sigma}}\, dV \tag{41}$$

Equation (41) must hold for any arbitrary control volume, thus one can derive the differential form of the momentum balance

$$\rho \cdot \left(\frac{\partial \vec{v}}{\partial t} + \vec{v} \cdot \nabla \vec{v} \right) = \vec{f} + \nabla \cdot \bar{\bar{\sigma}} \tag{42}$$

When the pressure *P* of a fluid is defined to be the isotropic part of the Cauchy stress tensor, $\bar{\bar{\sigma}}$ can be reformulated as $\bar{\bar{\sigma}} = -P\bar{\bar{I}} + \bar{\bar{\tau}}$, where $\bar{\bar{I}}$ is the identity matrix and $\bar{\bar{\tau}}$ is the remaining so called deviatoric stress tensor. In that definition, the pressure is that part of the normal stress, that does not change when changing the frame of reference.

Using this definition of $\bar{\bar{\sigma}}$ and assuming the gravitational body force $\overrightarrow{f_g}$ equals $\rho \cdot \vec{g}$ (with $\vec{g}$ being the gravitational acceleration vector with a magnitude of 9.81 $\frac{m}{s^2}$) and is the only relevant body force to be accounted for, one obtains the following common form of the momentum balance for an incompressible fluid (Rieutord, 2015)

$$\rho \cdot \left(\frac{\partial \vec{v}}{\partial t} + \vec{v} \cdot \nabla \vec{v} \right) = -\nabla P + \nabla \cdot \bar{\bar{\tau}} + \rho \cdot \vec{g} \tag{43}$$

It should be noted that in this case the transported property is a vector quantity and the common nation from vector calculus, as given above, is a convenient way to collapse all the dimensional

information into one equation. The momentum balance can also be written down in terms of each spatial dimension, i.e. a scalar, and then yields a system of equations, one for each spatial dimension:

$$\rho \cdot \left(\frac{\partial u}{\partial t} + u \cdot \frac{\partial \mathrm{u}}{\partial x} + v \cdot \frac{\partial \mathrm{u}}{\partial y} + w \cdot \frac{\partial u}{\partial z}\right) = -\frac{\partial P}{\partial x} + \frac{\partial \tau_{xx}}{\partial x} + \frac{\partial \tau_{xy}}{\partial y} + \frac{\partial \tau_{xz}}{\partial z} + \rho \cdot g_x \tag{44}$$

$$\rho \cdot \left(\frac{\partial v}{\partial t} + u \cdot \frac{\partial \mathrm{v}}{\partial x} + v \cdot \frac{\partial \mathrm{v}}{\partial y} + w \cdot \frac{\partial v}{\partial z}\right) = -\frac{\partial P}{\partial y} + \frac{\partial \tau_{xy}}{\partial x} + \frac{\partial \tau_{yy}}{\partial y} + \frac{\partial \tau_{zy}}{\partial z} + \rho \cdot g_y \tag{45}$$

$$\rho \cdot \left(\frac{\partial w}{\partial t} + u \cdot \frac{\partial \mathrm{w}}{\partial x} + v \cdot \frac{\partial \mathrm{w}}{\partial y} + w \cdot \frac{\partial w}{\partial z}\right) = -\frac{\partial P}{\partial z} + \frac{\partial \tau_{xz}}{\partial x} + \frac{\partial \tau_{yz}}{\partial y} + \frac{\partial \tau_{zz}}{\partial z} + \rho \cdot g_z \tag{46}$$

The equations can be interpreted as a balance of forces: in the absence of other body forces (like electromagnetic forces), the inertial force of a fluid particle equals the pressure, viscous and gravitational forces acting on it. In this context, one important dimensionless number in fluid mechanics is the Reynolds number *Re*, which is the ratio of inertial forces to viscous forces

$$Re = \frac{v \cdot d \cdot \rho}{\eta} \tag{47}$$

where d is a characteristic length of the flow scenario, η is the viscosity and v is the characteristic velocity magnitude.

The energy balance

Lastly, another important balance that is to be considered, is the energy balance. As stated by the first law of thermodynamics, energy cannot be created nor destroyed, i.e. the energy in a closed system is constant. In an open system, the energy E of the system can change when external work or heat is provided (Demtröder, 2017). By convention, Q denotes the heat added to the system while W denotes work done by the system, thus

$$E = Q - W \tag{48}$$

Of course, for a control volume Ω of fluid, the first law must also hold. The energy E can be separated into a volume specific kinetic energy term $\left(\frac{1}{2}\rho|\vec{v}|^2\right)$ and internal energy (ρe), where e is the specific internal energy.

The work done by the system can be separated into work by viscous forces acting on the surface of the control volume $(\tau \cdot \vec{v})$ and work done by volume forces $(\vec{f} \cdot \vec{v})$. The change in thermal energy can be separated into the balance of in- and outgoing heat fluxes $\vec{q}$ over the surface of the control volume and the internal creation $\dot{Q}$ from any kind of heat source. Integration over the control volume yields

$$\frac{d}{dt}\int_{\Omega} \rho(\frac{1}{2}|\vec{v}|^2 + e)\, dV = \int_{\Omega} \vec{f} \cdot \vec{v}\, dV + \int_{\partial\Omega} \bar{\bar{\sigma}} \cdot \vec{v}\, dS + \int_{\Omega} \dot{Q}\ dV - \int_{\partial\Omega} \vec{q}\, dS \tag{49}$$

Using the divergence theorem, the surface integrals can be converted to volume integrals

$$\frac{d}{dt}\int_{\Omega} \rho(\frac{1}{2}|\vec{v}|^2 + e)\, dV = \int_{\Omega} \vec{f}\cdot\vec{v} dV + \int_{\Omega} (\nabla\cdot(\bar{\bar{\sigma}}\cdot\vec{v}) + \bar{\bar{\sigma}}\colon\nabla\vec{v})\, dV + \int_{\Omega} \dot{Q}\, dV - \int_{\Omega} \nabla\cdot\vec{q}\, dV \tag{50}$$

If the fluid is incompressible, the density is constant and can also be written in front of the integral. Moreover, as the control volume is arbitrary, the integral can be dropped, and one gets the differential formulation. Realizing that above considerations apply to the Lagrangian perspective of a fluid particle moving through a flow field, one can replace the time derivative with the material derivative to obtain the Eulerian perspective (Rieutord, 2015)

$$\rho\frac{D\left(\frac{1}{2}|\vec{v}|^2 + e\right)}{Dt} = \vec{f}\cdot\vec{v} + \nabla\cdot(\bar{\bar{\sigma}}\cdot\vec{v}) + \bar{\bar{\sigma}}\colon\nabla\vec{v} + \dot{Q} - \nabla\cdot\vec{q} \tag{51}$$

The energy term on the left side combines kinetic energy and internal energy. However, one can split the equation in two, as the kinetic energy is only determined by the force terms (since changes in heat energy represent changes in the random motion of molecules rather than their directed motion). Looking at the kinetic terms only, one realizes a resemblance to the momentum balance form section 2.1.5

$$\rho\frac{D\left(\frac{1}{2}|\vec{v}|^2\right)}{Dt} = \vec{f}\cdot\vec{v} + \vec{v}\cdot(\nabla\cdot\bar{\bar{\sigma}}) \tag{52}$$

Indeed, the kinetic energy balance follows directly from the momentum balance (43), which is revealed if the scalar product with $\vec{v}$ is taken on both sides of the equation

$$\rho\cdot\frac{D\vec{v}}{Dt}\cdot\vec{v} = \vec{f}\cdot\vec{v} + \vec{v}\cdot(\nabla\cdot\bar{\bar{\sigma}}) \tag{53}$$

Now, one can use the product rule to find the equivalency of (52) and (53)

$$\rho\cdot\frac{D\vec{v}}{Dt}\cdot\vec{v} = \rho\cdot\left(\frac{\partial\vec{v}}{\partial t} + \vec{v}\cdot\nabla\vec{v}\right)\cdot\vec{v} = \rho\cdot\left(\frac{\partial\vec{v}}{\partial t}\cdot\vec{v} + \vec{v}\cdot\nabla(\vec{v})\cdot\vec{v}\right) = \rho\cdot\left(\frac{\partial\frac{1}{2}|\vec{v}|^2}{\partial t} + \vec{v}\cdot\nabla\left(\frac{1}{2}|\vec{v}|^2\right)\right) = \rho\frac{D\left(\frac{1}{2}|\vec{v}|^2\right)}{Dt} \tag{54}$$

In other words, the momentum balance can be seen as a derivation that follows from the conservation of kinetic energy. Incorporating kinetic energy in the energy balance provides no additional

information and is thus redundant. Hence, one can focus on inner, i.e. thermal, energy only. The material derivative of inner energy must equal the remaining terms:

$$\rho \cdot \left(\frac{\partial e}{\partial t} + \vec{v} \cdot \nabla \mathrm{e}\right) = -\nabla \cdot \dot{q} + \dot{Q} + \bar{\bar{\sigma}} : \nabla \vec{v} \tag{55}$$

where $\bar{\bar{\sigma}} : \nabla \vec{v}$ is the work of stresses providing thermal energy via dissipation.

Realizing that the inner energy *e* is thermal energy only, one can replace it with a specific heat capacity (C) term

$$\rho \cdot \left(\frac{\partial (C \cdot T)}{\partial t} + \vec{v} \cdot \nabla (C \cdot T)\right) = -\nabla \cdot q + \dot{Q} + \bar{\bar{\sigma}} : \nabla \vec{v} \tag{56}$$

The heat capacity gives the energy needed to increase the temperature of the corresponding material by one Kelvin and it is assumed to be constant for the relevant temperature range. This simplifies equation (56) to

$$C \cdot \rho \cdot \left(\frac{\partial T}{\partial t} + \vec{v} \cdot \nabla T\right) = -\nabla \cdot \dot{q} + \dot{Q} + \bar{\bar{\sigma}} : \nabla \vec{v} \tag{57}$$

The heat flux $-\nabla \cdot \dot{q}$ can be specified further by Fourier's law (see section 2.5), which is very analogous to Fick's law for a diffusion problem (section 2.2.1), thus giving the following equation

$$C \cdot \rho \cdot \left(\frac{\partial T}{\partial t} + \vec{v} \cdot \nabla T\right) = k_{therm} \nabla^2 T + \dot{Q} + \bar{\bar{\sigma}} : \nabla \vec{v} \tag{58}$$

The generic source term $\dot{Q}$ can describe the heat generated from a variety of causes, for instance chemical reactions or radioactive decay. However, especially interesting in the context of this thesis is the energy loss due to the heat of evaporation. As for solids and gasses, the energy of molecules in the liquid follows a Maxwell-Boltzmann distribution. Those molecules falling in the part of the distribution with a high enough kinetic energy can leave the liquid phase and change to the gas phase. Since this process steadily removes those molecules with the highest kinetic energy, and therefore temperature, evaporation effectively removes heat energy from the system (Demtröder, 2017).

2.2 Modelling dissolved species via material balances

2.2.1 General material balance in the bulk

Like the mass balance in the previous section, another property of fluid moving through a flow field is the concentration of a dissolved species c in a reference volume. Again, if there is no mechanism that creates or destroys molecules of the species, the concentration in the control volume is constant

$$\frac{Dc}{Dt} = 0 \Leftrightarrow \frac{\partial c}{\partial t} + \nabla \cdot (\vec{v}c) = 0 \Leftrightarrow \frac{\partial c}{\partial t} + (\nabla \cdot \vec{v}) \cdot c \; + \; (\nabla \mathrm{c}) \cdot \vec{v} = 0 \tag{59}$$

For an incompressible fluid, one can use (32) to simplify (59) and find

$$\frac{\partial c}{\partial t} + \; (\nabla \mathrm{c}) \cdot \vec{v} = 0 \tag{60}$$

Equation (59) is the convection equation and valid if convection, that is the flow of the solvent, is the only mode of transport for the dissolved species. However, as described by Fick's first law, the random Brownian motion of molecules will equilibrate any concentration differences in space over time. The diffusion flux $\vec{n}_D$ (where flux denotes a number of molecules per area and time) of a species is proportional to the negative gradient of the concentration and the diffusion coefficient D. By convention, a positive value means net outflux, thus

$$\vec{n}_D = \; -D \nabla c \tag{61}$$

Ignoring convection for a moment, the concentration *c* inside an infinitesimal control volume of liquid will change, if the outgoing fluxes do not equal the incoming fluxes, i.e. one has to integrate all the fluxes over the surface $\partial\Omega$ of an arbitrary control volume Ω

$$\int_{\Omega} \frac{\partial c}{\partial t} dV = - \int_{\partial\Omega} \vec{n}_D \, dS \tag{62}$$

Applying the divergence theorem, one can transform the surface integral in (62) to a volume integral

$$\int_{\Omega} \frac{\partial c}{\partial t} dV = \; - \int_{\Omega} \nabla \cdot \vec{n}_D \, dV \tag{63}$$

As this equation must hold for any arbitrary control volume, one can drop the integral sign and get a differential formulation that is Fick's second law. If the diffusion coefficient D is constant, the further simplified equation describing the change of concentration c over time reads as

$$\frac{\partial c}{\partial t} = \; -\nabla \cdot \vec{n}_D = -\nabla \cdot (-D \nabla c) = \; D \nabla^2 c \tag{64}$$

Incorporating this phenomenon into the convection equation (60) yields the so-called convection-diffusion equation

$$\frac{\partial c}{\partial t} + \; (\nabla \mathrm{c}) \cdot \vec{v} = D \nabla^2 c \tag{65}$$

The diffusion coefficient *D* measures how fast the random Brownian motion of molecules will equilibrate a given concentration gradient. It is thus proportional to the thermal energy causing the random motion, as described in the Einstein relation

$$D = \mu k_B T \tag{66}$$

where μ is a mobility parameter. In the limit of low Reynolds numbers (see section 2.1.3), the mobility of a spherical particle is the inverse of the drag coefficient ζ, as given by Stokes' law (Bird et al., 2007) that describes the drag force F_D exerted by a rigid sphere in a laminar flow at terminal velocity v_∞

$$F_D = \zeta v_\infty = 6\pi\eta r v_\infty \tag{67}$$

where r is the particle radius. The combination of both equations (66) and (67) yields the Stokes-Einstein relation to compute the diffusion coefficient

$$D = \frac{k_B T}{6\pi\eta r} \tag{68}$$

2.2.1 Special material balance at a surface

The balance equation describing the distribution of a surface-active agent (surfactant) on the interface between a liquid and gas phase (or equivalently a liquid-liquid interface) can be thought of as a special case of the general material balance. As for the material balance, the surfactant distribution on the interface will depend on the velocity of the solvent molecules, in which the surfactant is embedded, and the gradients of surface concentration. But since we are looking at an interface, i.e. a two-dimensional curved surface, all vectors (like velocity or gradient operator) in the equation have to be converted to the local tangential projection of that vector. By the rules of elementary vector calculus any vector $\vec{v}$ at the interface can be decomposed into the sum of the part normal to the interface and the part tangential to the interface (see Figure 7 for further illustration). Here, the tangential projection is denoted by the subscript *s* and the normal projection by the subscript n.

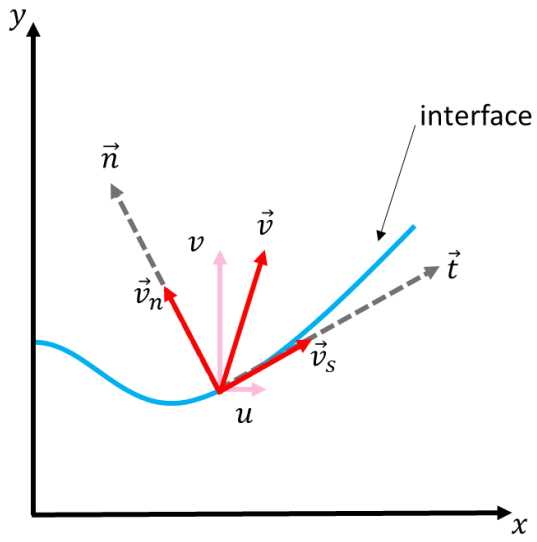

Figure 7 A velocity vector $\vec{v}$ can be decomposed into the x- and y-component (u and v, respectively). At the interface between different fluids, it can also be decomposed into the projection normal to the interface ($\vec{v}_n$) plus the projection tangential to the interface ($\vec{v}_s$). To compute these components, one needs the normal vector $\vec{n}$ and the tangential vector $\vec{t}$.

To obtain the normal part of the vector $\vec{v}$, one must take the dot product of $\vec{n}$ and $\vec{v}$ (giving the magnitude of $\vec{v}_n$) and multiply the resulting scalar with vector $\vec{n}$ (which has unit length by definition)

$$\vec{v}_n = (\vec{n} \cdot \vec{v})\vec{n} \tag{69}$$

and analogously for the tangential part

$$\vec{v}_s = (\vec{t} \cdot \vec{v})\vec{t} \tag{70}$$

Moreover, since the both the normal vector and the tangential vector must have unit length and must be orthogonal to each other, it can easily be shown, that if $\vec{n} = \binom{n_x}{n_y}$ it follows that $\vec{t} = \binom{n_y}{-n_x}$, and thus

$$\vec{v}_s = \left(\binom{n_y}{-n_x} \cdot \binom{u}{v}\right)\binom{n_y}{-n_x} = \begin{pmatrix} {n_y}^2\, u \; - \; n_x n_y\, v \\ -n_x n_y\, u \; + \; {n_x}^2\, v \end{pmatrix} \tag{71}$$

The same procedure can be applied to the gradient operator to yield the surface gradient operator

$$\nabla_s = (\vec{t} \cdot \nabla)\vec{t} = \left(n_y \frac{\partial}{\partial x} - n_x \frac{\partial}{\partial y}\right) \cdot \binom{n_y}{-n_x} = \begin{pmatrix} {n_y}^2 \frac{\partial}{\partial x} \; - \; n_x n_y \frac{\partial}{\partial y} \\ -n_x n_y \frac{\partial}{\partial x} \; + \; {n_x}^2 \frac{\partial}{\partial y} \end{pmatrix} \tag{72}$$

Now, one can reformulate the material balance (59) from section 2.1.3 in terms of a two-dimensional interface.

Firstly, consider the case of a surfactant that is insoluble in the bulk liquid, so there is no connection between the bulk concentration and the surface concentration. Here, c_s denotes the number of surfactant molecules n_s per surface area A: $c_s = \frac{n_s}{A}$. Thus, the surface mass balance reads

$$\frac{\partial c_s}{\partial t} + (\nabla_s \cdot \vec{v}_s)c_s \; + \; (\nabla_s c_s) \cdot \vec{v}_s = 0 \tag{73}$$

In a non-steady state problem, generally both the number of molecules and the surface area in the term $\frac{n_s}{A}$ can be time dependent, hence the quotient rule must be applied for the time derivative term in (73)

$$\frac{\partial c_s}{\partial t} = \frac{\partial(\frac{n_s(t)}{A(t)})}{\partial t} = \frac{\frac{\partial(n_s(t))}{\partial t} \cdot A(t) - n(t) \cdot \frac{\partial A(t)}{\partial t}}{A(t)^2} \tag{74}$$

Intuitively this makes sense, as the surface concentration increases when the number of molecules on a given control surface element increases or if the area of the control surface element decreases, or vice versa for a decrease of concentration. If the surface is at steady state, i.e. the area does not change over time, the calculation simplifies to

$$\frac{\partial c_s}{\partial t} = \frac{\partial(\frac{n_s(t)}{A})}{\partial t} = \frac{1}{A}\frac{\partial(n_s(t))}{\partial t} \tag{75}$$

In the following, we will only look at surfaces at steady-state and ignore the time derivative of surface area. As argued for the material balance, surfactant molecules at the surface also undergo random

Brownian motion (but only along the two-dimensional surface) according to the surface concentration gradient

$$\frac{\partial c_s}{\partial t} = -\nabla_s \cdot (-D_s \nabla_s c_s) = D_s {\nabla_s}^2 c_s \tag{76}$$

And thus, the combined equation for surface convection and diffusion is (Pohjoranta & Tenno, 2011; Stone, 1990)

$$\frac{\partial c_s}{\partial t} + (\nabla_s \cdot \vec{v}_s) c_s + (\nabla_s c_s) \cdot \vec{v}_s = D_s {\nabla_s}^2 c_s \tag{77}$$

At this point it is useful to interpret the terms in equation (77). In contrast to the material balance in the bulk, the surfactant equation contains a term with the surface velocity gradient. This term disappears in the material balance, since for an incompressible fluid the divergence of velocity is zero in the bulk (continuity equation, see section 2.1.3). Here, this is not the case: a positive surface velocity gradient just means there is an increase in surface velocity which must be compensated by a net-positive rate of liquid molecules coming from within the bulk and being transferred to the interface. Analogously, a negative gradient means surface velocity decreases and the resulting accumulation of molecules pushes the surplus surface molecules back into the bulk. If the surfactants are insoluble in the bulk, this compensating flux can only be provided by solvent molecules. Thus, the surfactant concentration changes locally. A positive gradient can be regarded as a stretching that dilutes the surfactant concentration, while a negative gradient has a compression effect that concentrates the surfactants.

Secondly, the case of a soluble surfactant has to be considered. In this case, the same species of molecule that is adsorbed to the surface can also be found in the bulk liquid. Depending on the chemical nature of the molecule, the adsorption at the interface decreases the surface energy and is thus energetically favourable. However, the higher the discrepancy between surface and bulk concentration, the less likely it becomes in terms of entropy to find this configuration. In equilibrium, the Gibb's energy will be minimized, and the surface concentration found for the energetically optimal configuration is the equilibrium concentration. Whenever the surface concentration is driven out of equilibrium, for instance due to surface velocity gradients that follow from the flow pattern in the bulk liquid, there will be a tendency to readjust, which can be described by a corresponding adsorption kinetic.

One often employed mathematical model to describe adsorption processes of molecules on a surface is the Langmuir adsorption isotherm. The model assumes several simplifications: the surface can be thought of as a homogenous collection of energetically equivalent binding sites for the adsorbing species. There is only one molecule per binding site allowed (mono-layer coverage) and there is no (or only irrelevant) interaction between adsorbed molecules.

A kinetic derivation of the model starts by defining adsorption and desorption rates r_a and r_d, which have dimension of molecular flux (molecules per surface area and time). The rate of adsorption is assumed to be proportional to the bulk concentration *c* of the adsorbing species and also proportional to the surface concentration of free binding sites *S*, where k_a is the proportionality constant

$$r_a = k_a c S \tag{78}$$

When the total number of possible binding molecules is $c_{s,\infty}$, *S* can be replaced by $c_{s,\infty} - c_s$

$$r_a = k_a c\left(c_{s,\infty} - c_s\right) \tag{79}$$

The desorption is only proportional to the surface concentration c_s, as the bulk is assumed to be far away from a saturated concentration *c.* Again, k_d denotes the proportionality constant for desorption

$$r_d = k_d c_s \tag{80}$$

In equilibrium, we have $r_a = r_d$, thus

$$k_a c\left(c_{s,\infty} - c_s\right) = k_d c_s \tag{81}$$

Rearranging for c_s yields

$$\frac{c_{s,\infty}}{c_s} - 1 = \frac{k_d}{c\ k_a} \Leftrightarrow \frac{c_{s,\infty}}{c_s} = \frac{k_d + c\ k_a}{c\ k_a} \Leftrightarrow \frac{c\ k_a\ c_{s,\infty}}{k_d + c\ k_a} = c_s \tag{82}$$

The ratio of k_a and k_d is called equilibrium constant K_{eq}, thus at equilibrium one finds the surface concentration to be

$$c_s = \frac{c\ K_{eq}\ c_{s,\infty}}{1 + c\ K_{eq}} \tag{83}$$

Using the Langmuir isotherm for the surface mass balance, one can just add the adsorption and desorption rates as an additional source and sink term on the right-hand side of (77) (Pohjoranta & Tenno, 2011; Rio & Boulogne, 2017)

$$\frac{\partial c_s}{\partial t} + (\nabla_s \cdot \vec{v}_s)c_s + (\nabla_s c_s) \cdot \vec{v}_s = D_s {\nabla_s}^2 c_s + k_a c\left(c_{s,\infty} - c_s\right) - k_d c_s \tag{84}$$

The interpretation of the terms in equation (84) is the same as in the insoluble case, only that the adsorption and desorption enforces equilibrium and weakens the effect of velocity gradients.

2.3 Viscosity and viscoelasticity

2.3.1 Newtonian viscosity

Viscosity can be interpreted as the rate by which fluid particles exchange their momentum. Generally, this will depend on the interaction strength between particles but especially for bigger and more complex molecules sterical effects may also play a role.

A simple experiment, which is usually given at the beginning of any textbook on viscosity (Christen, 2010), is the movement of plate on top of a liquid which is in contact with a non-moving ground (see Figure 8).

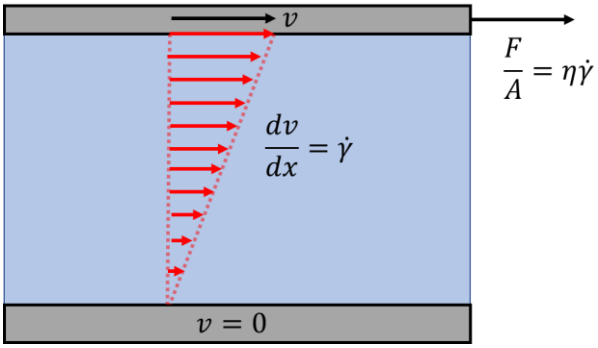

Figure 8 Scheme of the moving plate experiment. A liquid sample (blue) is between two solid plates (grey). The upper plate is moving with velocity v while the lower plate is stationary. Directly at the wall, the liquid will assume the velocity of the solid (also known no-slip condition). Consequently, there will be a velocity gradient from the moving wall to the bottom. In a Newtonian liquid, the velocity gradient will be linear. The force required to move the upper plate per unit area is then given by the product of the liquid's viscosity η and the velocity gradient, which is also called shear rate $\dot{\gamma}$.

For this thought experiment, it is assumed that the plates extend infinitely into the planar directions, so that boundary effects at the edges can be ignored. It is also assumed, that the liquid is incompressible. Since the liquid molecules directly in contact with the plate are thought to be in thermodynamic equilibrium with the solid, they assume the solid wall velocity. Thus, the molecules directly at the bottom are still, while the molecules at the upper plate are moving with the plate`s velocity *v*. In the simplest case, the fluid behaves as a Newtonian fluid (Christen, 2010). That means that the velocity profile in between is linear and the derivative $\frac{\partial v}{\partial y}$, which is called shear rate $\dot{\gamma}$, is constant. When dividing the liquid into infinitesimally thin layers, the stress τ at the surface of each layer, i.e. the force per area, is proportional to the shear rate, with the proportionality factor η being the viscosity

$$\tau = \eta \cdot \dot{\gamma} \tag{85}$$

As the shear stress has a unit of force per area [Pa] and the shear rate has a unit of inverse time [1/s], the unit of viscosity is [Pa·s].

In the macroscopic view, for the upper plate to be moving, it needs a force *F* per area. That force will need to be higher, if the velocity of the plate should be increased (thus increasing the velocity gradient or shear rate), but it also needs to be higher, if the molecules of the liquid interact strongly and exchange their momentum quickly, in other words, if the liquid has a high viscosity.

Generalizing the above considerations for the three-dimensional case and arbitrary flow fields, the stress tensor follows from the gradient of the velocity vector plus its transposed

$$\tau = \eta \cdot (\nabla\vec{v} + \nabla\vec{v}^{T}) \tag{86}$$

By addition of the transposed, it is ensured that the stress tensor is symmetrical, which is needed to prevent a torque on a control volume in a pure shearing flow.

For a Newtonian incompressible fluid, i.e. when the viscosity and density is constant, the viscous stress terms in (43) can be simplified and the momentum balance then reads (Moukalled et al., 2016)

$$\rho \cdot \left(\frac{\partial \vec{v}}{\partial t} + \vec{v} \cdot \nabla \vec{v}\right) = \vec{f} - \nabla P + \nabla \cdot \left(\eta \cdot (\nabla \vec{v} + \nabla \vec{v}^T)\right) = \vec{f} - \nabla P + \eta \nabla^2 \vec{v} \tag{87}$$

For a pure liquid at standard conditions, the empirically found values of viscosity are often tabulated in the literature. However, it must be considered that the viscosity of a liquid depends on several parameters. For liquids, the viscosity decreases with increasing temperature, while for gases the opposite is true. The physical explanation for this comes from a molecular picture. For gases, the viscosity is the interaction of molecules due to collisions. An increase in thermal energy increases the thermal motion and thus the chance of collision. In liquids, on the other hand, interaction via attractive forces between molecules in different flow layers cause the transfer of momentum. Here, increasing the thermal energy means that attractive forces are overcome more easily.

One simple model for liquid that describes the viscosity decrease of many liquids is the exponential Andrade equation (White, 2011)

$$\eta(T) = A_\eta e^{\frac{B_\eta}{T}} \tag{88}$$

Where $A_\eta$and $B_\eta$are two empirical model parameters.

Moreover, the viscosity becomes a function of the composition when looking at liquid mixtures. For a mixture of solvents (that are chemically relatively similar), approximations for the mixed viscosity take the respective molar fractions and densities into account. Two recent models found in the literature are given below (Dey et al., 2016)

$$\eta_{mix} = \sum_{i=1,..,n} \frac{x_i \cdot \eta_i}{\rho_i} \cdot \sum_{i=1,..,n} x_i \cdot \rho_i \tag{89}$$

$$\eta_{mix} = \sum_{i=1,..,n} e^{x_i \cdot \ln\left(\frac{\eta_i}{\rho_i}\right)} \cdot \sum_{i=1,..,n} x_i \cdot \rho_i \tag{90}$$

where *n* is the number of components, x_i is the molar fraction of the *i*th component, η_i is the pure components' viscosity and ρ_i the respective density. While the somewhat simpler model (89) works very well for mixtures of alkanes, the logarithmic model (90) has better overall performance, especially for multi-component mixtures. Of course, many other models also exist, and the presented models should only indicate that the molecular transfer of momentum in a mixture is a complicated problem not easily computed by the individual viscosities and molar fractions.

When a polymer is dissolved in a liquid, the viscosity can increase strongly, even for dilute polymer concentrations c_p. For dilute to semi-dilute concentrations, a quadratic dependency can often be observed, which is described by the Huggins equation

$$\eta_0(c_p) = \eta_s \cdot \left(1 + \eta_i \cdot c_p + K_H \cdot (\eta_i \cdot c_p)^2\right) \tag{91}$$

Where c_p is the polymer concentration (given in $\left[\frac{g}{cm^3}\right]$), η_s is the viscosity of the pure solvent, η_i is the so-called intrinsic viscosity (that has units of $\left[\frac{cm^3}{g}\right]$) and K_H is the dimensionless Huggins constant. Since the viscosity of polymer solutions is often dependent on the shear and strain rates experienced in the flow field (as explained in further detail in section 2.3.2), the Huggins equation refers to the zero-shear

viscosity η_0, i.e. the viscosity at the limit of negligible shear or strain. The intrinsic viscosity can be interpreted as the effective volume of the polymer coil in the solvent when interactions between different polymer molecules are negligible. A relatively high volume of the polymer in solution means stronger interaction between neighbouring layers of liquid in the flow, and thus higher momentum transfer i.e. higher viscosity. The intrinsic viscosity therefore depends on the molecular weight of the polymer and the solvent quality. In a colloquially called "good" (i.e. energetically favourable) solvent, interactions between solvent molecules and polymer chains are strong, the polymer swells and the radius of gyration is bigger (Kol et al., 2021). In a colloquially called "bad" solvent, the interactions are weak and the polymer contracts, minimizing the contact area. This complex interplay is empirically captured in the Mark-Houwink equation with model parameters K_{MH} and α

$$\eta_i = K_{MH} {M_w}^{\alpha} \tag{92}$$

For very dilute system the quadratic term in equation (91) can be neglected, and the function becomes linear, often given in terms of the polymer volume fraction φ_p

$$\eta_{mix}(\varphi_p) = \eta_0 \cdot (1 + U_\eta \cdot \varphi_p) \tag{93}$$

The constant U_η is described in the literature as universal for all polymer system, depending only on the solvent quality (Sunthar, 2010).

2.3.2 Non-Newtonian viscosity

Shear rate dependent viscosity

The Newtonian approximation works well in many cases, especially for small molecules like water, as in such cases the underlying flow field does not alter the interaction and energy dissipation of the individual molecules. For larger and more complex molecules, or particles dispersed in the liquid, this approximation often no longer holds, and the flow will affect the interaction (Alexander Morozov & Saverio E. Spagnolie, 2015).

When the viscosity depends on the local shear rate, the constitutive law for the Cauchy stress tensor becomes

$$\sigma = -PI + \eta(\dot{\gamma})\dot{\gamma} \tag{94}$$

In this context, two important categorizations are shear-thickening, also called dilatant, ($\frac{\partial \eta}{\partial \dot{\gamma}} > 0$) and shear-thinning ($\frac{\partial \eta}{\partial \dot{\gamma}} < 0$) liquids, also called pseudoplastics. In the case of dilatant liquids, the increase in shear rate changes the flow structure in such a way, that the interaction of particles increases. The mechanistic explanation given for this is that, when subjected to a flow field, a stable colloidal suspension transitions to an unstable state where flocculation occurs that increases interaction. This is thought to happen, when the hydrodynamic forces due to the flow are stronger than the repulsive

forces between particles and thus particles start to “cram”. A typical example of a shear thickening liquid is corn-starch in water.

For shear-thinning liquids, the opposite effect happens. Typical examples are solutions and melts of polymers, but the thinning effect is usually more pronounced for concentrated solutions. In the case of polymer solutions, the shear experienced by polymers in the flow field is thought to change the conformation from a random coil to a more linear conformation aligned with the flow, thereby decreasing the interaction between fluid layers mediated by the polymers. However, for bad solvents the shear can also to lead micro-phase separation and increase the viscosity at some point.

Mathematically, shear thinning is often described by a power law (95) or Carreau-Yasuda model (96)

$$\eta(\dot{\gamma}) = K_p\,\dot{\gamma}^{n-1} \tag{95}$$

$$\eta(\dot{\gamma}) = \eta_\infty + (\eta_0 - \eta_\infty)[1 + (K_{CY}\dot{\gamma})^a]^{\frac{n-1}{a}} \tag{96}$$

where η_∞ is the asymptotic viscosity at infinite shear rate, while n, K_p, K_{CY} and a are model parameters.

Experimentally, the shear rate dependence of viscosity is often analysed in a Couette-cell(Wakeham et al., 2007), which consists of a solid cylinder inside of a larger, hollow cylinder. The gap between the two cylinders is then filled with the liquid sample and the inner cylinder rotates (see Figure 9).

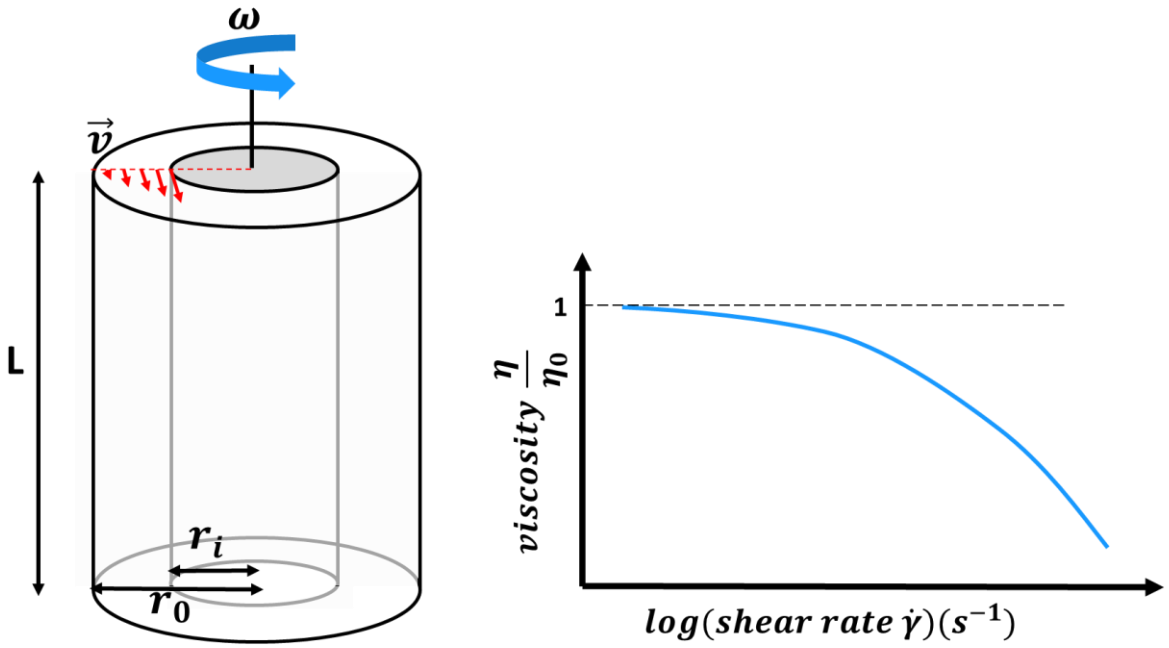

Figure 9 The shear rate dependent viscosity can be measured in a Couette-cell, which consists of a rotating solid cylinder inside a bigger, hollow cylinder (left part of the illustration). When the inner cylinder rotates, there is a shear stress in the liquid sample in between the cylinders due to its viscosity. By measuring the torque needed to rotate the inner cylinder, one can defer the viscosity of the liquid under shear. The right part of the illustration shows the typical curve for a shear thinning polymer solution.

By measuring the torque of the inner cylinder, one can then defer the resistance against the rotation that is caused by the viscosity of the liquid. Let Γ denote the torque, ω is the angular velocity, r_i the inner radius, r_O the outer radius, $\tau_{r\theta}$ is the shear stress between the rotating infinitesimal liquid layers and L the length of the cell.

$$\Gamma = \underbrace{-\tau_{r\theta} 2\pi r_i L}_{Force} \underbrace{r_i}_{\substack{lever \\ arm}} \tag{97}$$

Using a cylindrical coordinate system, where θ is the angle and the other dimensions are radius and length, one obtains for the shear stress (for constant angular velocity ω)

$$\tau_{r\theta} = \eta \dot{\gamma}_{r\theta} = \eta \left[r \frac{\partial}{\partial r} \left(\frac{v_\theta}{r} \right) + \frac{1}{r} \frac{\partial v_r}{\partial \theta} \right] \tag{98}$$

If we assume perfect laminar flow, all streamlines are concentric and there is no radial flow, hence

$$\tau_{r\theta} = \eta \dot{\gamma}_{r\theta} = \eta \left[r \frac{\partial}{\partial r} \left(\frac{r\omega}{r} \right) \right] = \eta r \frac{\partial \omega}{\partial r} \tag{99}$$

Integrating (99) and using the no-slip condition, i.e. at the outer wall $\omega_O = 0$, one finds

$$\frac{\Gamma}{2\pi\eta L} \int_{r_i}^{r_O} \frac{dr}{r^3} = -\int_{\omega_i}^{0} d\omega \Leftrightarrow \frac{\Gamma}{4\pi\eta L} \left(\frac{1}{{r_i}^2} - \frac{1}{{r_O}^2} \right) = -\omega_i \tag{100}$$

Thus, if the geometry of the Couette-cell and the angular velocity is known, one can measure the torque of the inner cylinder and determine the viscosity over a range of shear rates. However, the assumption made in (99) is crucial: the flow needs to be laminar and on concentric streamlines only. For very high angular velocities (i.e. shear rates), the viscous forces between liquid particles may not be sufficient anymore to provide the centripetal forces needed to balance the centrifugal forces arising from the rotation. In this case, the streamlines may detach and cause complex three-dimensional flow patterns, so called Taylor vortices, that increase the interaction between fluid particles and thus increase the measured viscosity (see Figure 10) (Laun et al., 2014).

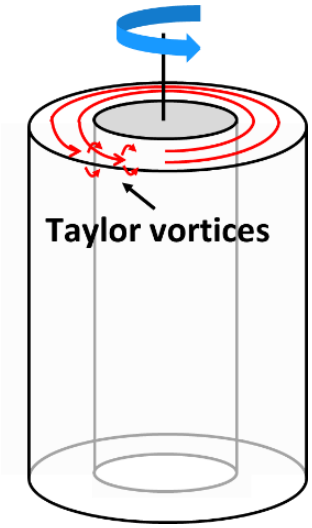

Figure 10 Schematic picture of Taylor vortices forming in the liquid inside a Couette-cell. When the centrifugal forces coming from the rotation of the inner cylinder are bigger than the centripetal viscous forces, the streamlines detach and cause secondary flow-patterns in the form of Taylor vortices.

Extensional flow

Since the last part of this section will introduce the concept of viscoelasticity, it is useful to explain the difference between shear flow and extensional flow first. The shear rate describes the derivative of the velocity perpendicular to its flow direction, for instance $\frac{\partial u}{\partial y}$ or $\frac{\partial u}{\partial z}$. In contrast, the strain rate is the derivative of the velocity in the same direction as the flow, e.g. $\frac{\partial u}{\partial x}$ or $\frac{\partial v}{\partial y}$. Consequently, the Cauchy stress can be divided into the shear stresses and normal (or strain) stresses. Looking at a control volume of fluid, we can see the consequence of normal stress applied to one of the faces (see Figure 11).

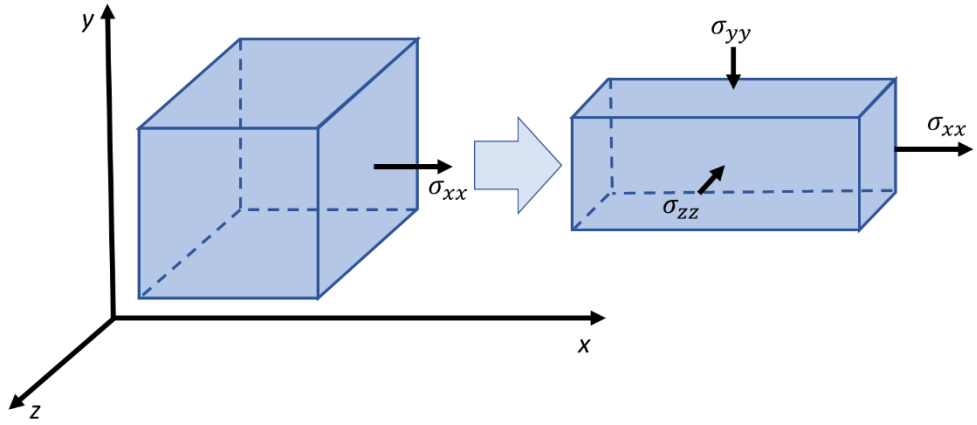

Figure 11 Elongation of a control volume of liquid. Subjected to a normal stress σ_{xx}, the control volume gets stretched.

If the stress is only applied normally to one face, the volume will undergo elongation. One can define an elongation (or strain) rate $\dot{\varepsilon} = \frac{\partial u}{\partial x}$. In analogy to the shear viscosity, one can then also define an elongational viscosity $\bar{\eta}$, that the proportionality between elongation rate and the difference in (normal) stress. In three dimensions, there are two differences in normal stress and thus two elongational viscosities two be considered.

$$\bar{\eta}_1 = -\frac{\sigma_{xx} - \sigma_{zz}}{\dot{\varepsilon}} \tag{101}$$

$$\bar{\eta}_2 = -\frac{\sigma_{yy} - \sigma_{zz}}{\dot{\varepsilon}} \tag{102}$$

From the conservation of mass, it must hold that

$$\frac{\partial v}{\partial y} + \frac{\partial w}{\partial z} = -\frac{\partial u}{\partial x} \tag{103}$$

That means, that the acceleration of fluid in the x-direction must be compensated by an acceleration normal to that. If no other forces are at play, the compensation will be equal in both directions *y* and *z*, i.e.

$$\frac{\partial w}{\partial z} = \frac{\partial v}{\partial y} \tag{104}$$

This case is called uniaxial elongation and also means, that $\sigma_{yy} = \sigma_{zz}$, i.e. $\bar{\eta}_2 = 0$.

Substitution of (104) into (103) yields

$$2\frac{\partial v}{\partial y} = -\frac{\partial u}{\partial x} = -\dot{\varepsilon} \Leftrightarrow \frac{\partial v}{\partial y} = -\frac{\dot{\varepsilon}}{2} \tag{105}$$

Since there is no shear stress in this theoretical example, the Cauchy stress tensor is given as

$$\sigma = \begin{pmatrix} -P+\tau_{xx} & \tau_{xy} & \tau_{xz} \\ \tau_{yx} & -P+\tau_{yy} & \tau_{yz} \\ \tau_{zx} & \tau_{zy} & -P+\tau_{zz} \end{pmatrix} = \begin{pmatrix} -P+\tau_{xx} & 0 & 0 \\ 0 & -P+\tau_{yy} & 0 \\ 0 & 0 & -P+\tau_{zz} \end{pmatrix} \tag{106}$$

Where the pressure *P* is that part of the normal stress, that is independent of the choice of coordinate system. With (101) and (105) it follows

$$\sigma = \begin{pmatrix} -P+\eta 2\frac{\partial u}{\partial x} & 0 & 0 \\ 0 & -P+\eta 2\frac{\partial v}{\partial y} & 0 \\ 0 & 0 & -P+\eta 2\frac{\partial w}{\partial z} \end{pmatrix} \tag{107}$$

and thus

$$\sigma = \begin{pmatrix} -P-2\eta\dot{\varepsilon} & 0 & 0 \\ 0 & -P-\eta\dot{\varepsilon} & 0 \\ 0 & 0 & -P-\eta\dot{\varepsilon} \end{pmatrix} \tag{108}$$

Hence, for the elongational viscosity $\bar{\eta}_1$ one finds

$$\bar{\eta}_1 = -\frac{\sigma_{11}-\sigma_{33}}{\dot{\varepsilon}} = -\frac{-P-2\eta\dot{\varepsilon}-(-P-\eta\dot{\varepsilon})}{\dot{\varepsilon}} = 3\eta \tag{109}$$

For an incompressible Newtonian fluid, the elongational viscosity is three times the shear viscosity. The ratio of these viscosities is known as the Trouton ratio (Sunthar, 2010) and, intuitively, the finding makes sense: in a purely elongational flow, the acceleration in one direction will be compensated by a perpendicular acceleration in both normal directions to the flow to fulfil the conservation of mass. Thus, the amount of relative fluid particle motion with respect to each other is tripled, giving three times the interaction, i.e. viscosity.

However, complex liquids like polymer solutions often do not act in a Newtonian way, especially when subjected to extensional flow fields. As already discussed for shear, polymers experiencing high strain rates might react by leaving their equilibrium conformation and become stretched. When the stress due to the strain rate stops, they start to contract again, effectively acting like an elastic material. The detailed description of this behaviour follows in the next section.

Shear rate dependent viscosity, as described earlier, is one example of a non-Newtonian behaviour, where the stress changes with the velocity gradient. Nevertheless, liquids like this are still called generalized Newtonian, as they share one important aspect with the simple Newtonian liquids: the structure of the stress tensor remains the same, in other words the velocity field changes instantaneously when there is a change in stress (Alexander Morozov & Saverio E. Spagnolie, 2015). This is not true for viscoelastic fluids. Here, the stress depends on the flow history of the molecules or fluid particles, as some part of the mechanical energy is stored elastically and then given off to the surrounding molecules thereafter. Thus, viscoelastic fluids partially exhibit properties of a solid. In a solid, the stress is related to the deformation, that is shear or strain γ, with the proportionality constant being the elastic modulus G

$$\tau = G \cdot \gamma \tag{110}$$

Notice the difference to a (purely) viscous fluid, where the stress is proportional to the shear rate (shear viscosity) or strain (elongational viscosity) rate ($\tau = \eta \cdot \dot{\gamma}$). Viscoelastic models try to incorporate both effects, the stress of a viscoelastic particle is the combination of both the elastic stress (proportional to strain) and viscous stress (proportional to strain rate). To picture both mechanisms, it is common to use mechanical analogies from the macroscopic world. The elastic component is visualized by a spring, the viscous component by a dashpot. Those two components can be connected serially or in parallel, giving the Maxwell and Kelvin-Voigt viscoelastic model, respectively (see Figure 12).

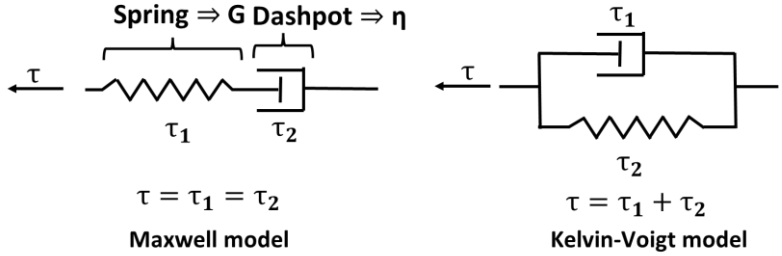

Figure 12 Schematic representation of a viscoelastic material in the Maxwell and Kelvin-Voigt model. When a stress τ acts on the viscoelastic material, some part of the mechanical energy is stored elastically, as symbolized by the spring component. The rest is dissipated via viscous interaction, as symbolized by the dashpot. As both components experience the same stress in serial connection, the Maxwell model represents a viscoelastic fluid. In contrast, a parallel connection of both elements represents a viscoelastic solid.

The Maxwell model represents a viscoelastic fluid, while the Kelvin-Voigt model represents a viscoelastic solid (Alexander Morozov & Saverio E. Spagnolie, 2015) and is thus ignored in the further explanations. Using the above analogy, one can imagine the reaction, when the Maxwell element is subjected to a stress. Initially, both the dashpot and spring are stretched. Over a certain time period, which will depend on the spring modulus and damping strength of the dashpot, the spring will relax and go back to its initial length, as it is giving off its elastically stored energy to the dashpot, where the energy then finally dissipates. This behaviour is typically found for polymer solutions, where the stress experienced by a polymer drives it out of its equilibrium conformation towards a stretched conformation, that might be held as long as the stress on the polymer continues. When the exterior stress vanishes, the polymer relaxes back to the thermodynamically favourable equilibrium conformation, while interacting with the surrounding solvent molecules and thereby dissipating the stored energy (Willenbacher & Georgieva, 2013).

To express the dynamics of the system, the Maxwell model can be used to derive a constitutive equation. Connected serially, the sum of strain from both the dashpot (γ_1) and spring (γ_2) must give the total strain γ, while the experienced stress τ is the same for all components

$$\gamma = \gamma_1 + \gamma_2 \rightarrow \dot{\gamma} = \dot{\gamma}_1 + \dot{\gamma}_2 \tag{111}$$

$$\tau = \eta \cdot \dot{\gamma}_2 = G \cdot \gamma_1 \tag{112}$$

Substituting (112) into (111) yields

$$\frac{d\gamma}{dt} = \frac{1}{G}\frac{\partial \tau}{\partial t} + \frac{\tau}{\eta} \Rightarrow G\frac{d\gamma}{dt} = \frac{\partial \tau}{\partial t} + \frac{\tau}{\lambda} \tag{113}$$

where $\lambda = \frac{\eta}{G}$ is the ratio of viscous forces to the elastic modulus. It has the dimension of time and is therefore called relaxation time (Alexander Morozov & Saverio E. Spagnolie, 2015). The differential equation (113) can be solved analytically to yield the following integral expression for the (time dependent) stress τ, where t' is the integration variable representing the timespan until now and t is the point in time currently looked at

$$\tau(t) = \frac{1}{\lambda}\int_{-\infty}^{t} e^{-\frac{t-t'}{\lambda}} \eta\, \dot{\gamma}(t')dt' \tag{114}$$

To experimentally analyse the viscous and elastic behaviour of a liquid, a convenient way is to apply a periodic stress to the sample with defined frequency ω. If the deformation γ of the sample follows a sine function, the deformation rate is the corresponding time derivative

$$\gamma(t) = \gamma_0 \sin \omega t \tag{115}$$

$$\dot{\gamma}(t) = \gamma_0 \omega \cos \omega t \tag{116}$$

and substituting (116) into (114) yields the corresponding evolution of stress over time (Alexander Morozov & Saverio E. Spagnolie, 2015)

$$\tau(t) = \gamma_0\, \eta\omega \frac{\cos \omega t + \lambda\omega \sin \omega t}{1 + (\lambda\omega)^2} \tag{117}$$

As can be seen, the stress response is also periodic and can be decomposed into a viscous part that peaks, when the deformation rate is at its maximum, and an elastic part that peaks, when the absolute deformation is at its maximum.

$$\tau(t) = \frac{\eta}{1 + (\lambda\omega)^2}\dot{\gamma}(t) + G\frac{(\lambda\omega)^2}{1 + (\lambda\omega)^2}\gamma(t) \tag{118}$$

Conveniently defining a viscous modulus G'' and an elastic modulus G', the stress response can be reformulated

$$\tau(t) = G'\gamma_0 \sin\omega t + G''\gamma_0 \cos\omega t \tag{119}$$

It is common to avoid the notation of sin and cos terms by invoking Euler's identity ($e^{i\varphi} = \cos\varphi + i\sin\varphi$), where *i* is the imaginary number and the operator $\Im(\cdot)$ gives the imaginary part of its complex argument

$$\tau(t) = \Im\left[(G' + iG'')\gamma_0 e^{i\omega t}\right] \tag{120}$$

Equation (120) can be substituted into (113) to yield

$$G\frac{d\gamma(t)}{dt} = \frac{\partial\tau(t)}{\partial t} + \frac{\tau(t)}{\lambda} \Rightarrow G\left[\Im\left(\gamma_0 i\omega e^{i\omega t}\right)\right] = \frac{d}{dt}\left[\Im\left((G' + iG'')\gamma_0 e^{i\omega t}\right)\right] + \frac{\Im\left((G'+iG'')\gamma_0 e^{i\omega t}\right)}{\lambda} \tag{121}$$

$$\Rightarrow\ G[\Im(i\omega)] = \Im(i\omega(G' + iG'')) + \frac{\Im(G' + iG'')}{\lambda} \tag{122}$$

The $\Im(\cdot)$ operator is present in all terms of equation and can therefore be omitted. Then, one can compare the real and imaginary parts of the equation

imaginary parts:

$$\omega G = \omega G' + \frac{G''}{\lambda} \tag{123}$$

real parts:

$$0 = -\omega G'' + \frac{G'}{\lambda} \tag{124}$$

And so, for the viscous and elastic modulus one finds

$$G' = \frac{G\omega^2\lambda^2}{1 + \omega^2\lambda^2} \tag{125}$$

$$G'' = \frac{G\omega\lambda}{1 + \omega^2\lambda^2} \tag{126}$$

The viscous modulus represents viscous dissipation and is therefore also called loss modulus, while the elastic modulus describes the elastically stored energy and is thus also called store modulus. Both loss and store modulus are automatically provided by modern commercial rheometers, that analyse the periodic stress response. In analogy to the shear and strain viscosity, a complex viscosity η^* is defined, that is the proportionality constant connecting frequency ω and the moduli G' and G''

$$\eta^*\omega = \sqrt{G'^2 + G''^2} \tag{127}$$

The above derivation is of course only applicable if the material behaves like the idealized Maxwell model. That is often not the case due to other dissipation mechanisms (Alexander Morozov & Saverio E. Spagnolie, 2015).

One can experimentally analyse the behaviour of G', G'' and η^* over a range of frequencies ω by utilizing the same Couette-cell setup as described for shear-rate dependent viscosity measurements. However, in this case the inner cylinder of the device is oscillating with a frequency ω with a corresponding maximum amplitude of strain (Chhabra, 2010). For an illustration, see Figure 13.

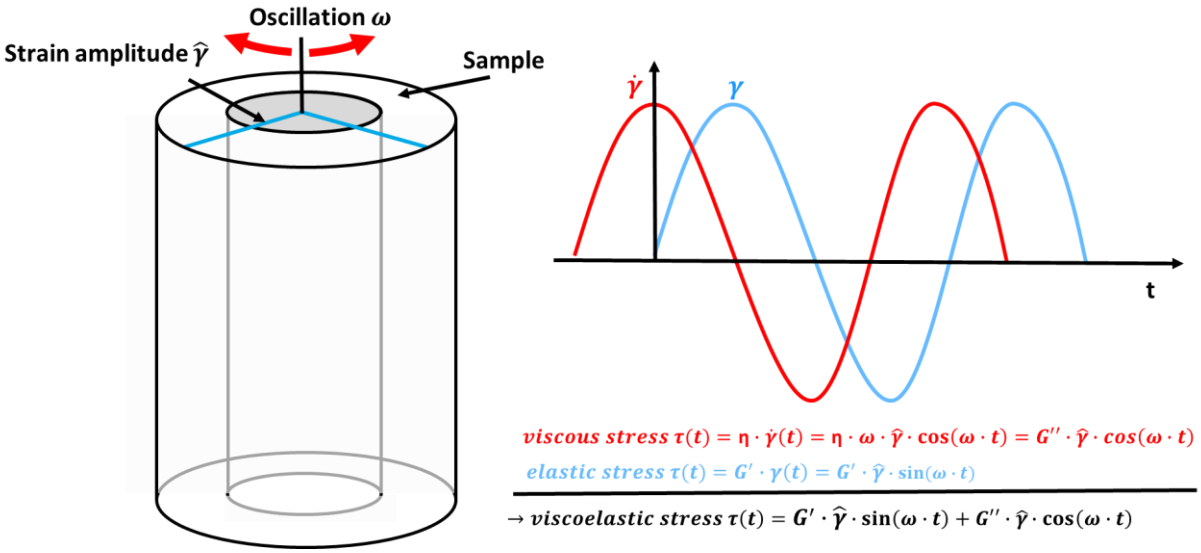

Figure 13 Oscillatory mode of a rheometer that uses the Couette-cell geometry. The inner cylinder oscillates with a maximum amplitude of strain and by measuring the torque over time, one can decompose the viscous and elastic components of the stress.

Thus far, all considerations were made from the Lagrangian standpoint of the viscoelastic particle that experiences stress. The Maxwell model delivers a simplified description of the viscous and elastic response of such particle and allows to define characteristic viscoelastic properties like G' and G'', that describe the periodic stress response to a periodic deformation of the material.

However, as pointed out in Section 2.1.2, in fluid mechanics one is generally not interested in the Lagrangian viewpoint, but rather the Eulerian viewpoint that describes the stresses at fixed point in space, not for a fixed particle that is moving through space. Again, we change perspectives by regarding the state of stress of a fluid particle as a property that is transported by the flow and substitute the time derivative *d/dt* in (113) with another operator that acts like the material derivative *D/Dt*. One cannot simply use the material derivative itself for reasons that are elaborated only briefly. An in-depth discussion can be found in the literature (Alexander Morozov & Saverio E. Spagnolie, 2015). Essentially, a problem arises because the elements of the stress tensor contain all possible velocity gradients with respect to space. But since the stress is experienced by the material particle, the strain and shear that is perceived by the particle must be considered, that means the velocity gradients must be taken with respect to the material frame, not the spatial frame. To translate between the frames, each gradient has to be converted such that it accounts for the deformation of the material frame with respect to the spatial frame. One can define base vectors for the spatial frame and material frame and use the deformation gradient tensor to analyse how the material base vectors change as the material is deformed. As the result of that procedure, one obtains two essentially equivalent expressions for the stress tensor with respect to the spatial coordinates, wherein the stress is treated as a fluid property that is embedded in a flow field

$$\overset{\nabla}{\tau} \equiv \frac{\partial \tau}{\partial t} + \vec{v} \cdot \nabla \tau - (\nabla \vec{v})^T \cdot \tau - \tau \cdot \nabla \vec{v} \tag{128}$$

$$\overset{\Delta}{\tau} \equiv \frac{\partial \tau}{\partial t} + \vec{v} \cdot \nabla \tau + \tau \cdot (\nabla \vec{v})^T + \nabla \vec{v} \cdot \tau \tag{129}$$

The expressions (128) and (129) are called the lower and upper convected derivative of a second rank tensor, respectively. All CFD computations in this thesis are done with COMSOL Multiphysics™, which uses the lower convected derivative to model the behaviour of a viscoelastic fluid (*Microfluidics Module User's Guide, COMSOL Version 5.5 (Accessed 25.06.2025)*, n.d.). Recalling the Maxwell model that describes the stress response of a viscoelastic material $\eta \frac{d\gamma}{dt} = \lambda \frac{\partial \tau}{\partial t} + \tau$ and formulating the deformation rate $\frac{d\gamma}{dt}$ more generally as $(\nabla \vec{v} + (\nabla \vec{v})^T)$ yields

$$\eta(\nabla \vec{v} + (\nabla \vec{v})^T) = \lambda \frac{\partial \tau}{\partial t} + \tau \tag{130}$$

Now, one can replace the Lagrangian time derivative with the lower convected derivative to get the lower convected Maxwell model of a viscoelastic fluid in the Eulerian frame

$$\tau_e + \lambda \cdot \overset{\nabla}{\tau_e} = \eta_p(\nabla \vec{v} + (\nabla \vec{v})^T) \tag{131}$$

This equation can be interpreted as follows: due to the elasticity of the polymers, the stress of the dissolved polymer is now a function of time (see (114)), it depends on the stress-history experienced so far along the polymer's trajectory in the flow field. It can be regarded as a property that is convected by the flow of the solvent, hence the first part of the convected derivative that looks like a material derivative. As the polymer follows the streamline, it experiences further stress due to shear or strain in the flow field ($\eta_p(\nabla \vec{v} + (\nabla \vec{v})^T)$). Effectively, these act like a 'source term' that increases the elastically stored mechanical energy. However, as an ongoing stress will change the conformation of the polymer (e.g. stretch it), thereby changing the effect that a shear or extensional flow field of the surrounding fluid will have on it, a polymer in coil conformation reacts differently to a high strain rate in the flow field as a polymer that is already strained. To account for the conformational change (i.e. deformation of the elastic material), the term $\tau \cdot (\nabla \vec{v})^T + \nabla \vec{v} \cdot \tau$ in the convected derivative corrects for the change of the material frame, essentially converting the shear or strain rates in the solvent flow field to the 'perceived' shear or strain rate by the polymer.

However, to yield more realistic results, two modifications are often made. Firstly, the polymer solution consists of some polymers that show viscoelasticity, but which are embedded in a purely viscous solvent. The stress tensor is thus thought to be the sum of a purely viscous (τ_s) and viscoelastic (τ_e) part

$$\sigma = -PI + \tau_s + \tau_e \tag{132}$$

where, as discussed in 2.3.1, the purely viscous stresses are

$$\tau_s = \eta_s(\nabla\vec{v} + (\nabla\vec{v})^T) \tag{133}$$

and η_s denotes the (Newtonian) viscosity of the pure solvent. As derived above, the elastic stress component is

$$\tau_e = \eta_p(\nabla\vec{v} + (\nabla\vec{v})^T) - \lambda \cdot \overset{\nabla}{\tau_e} \tag{134}$$

where η_p is the viscous interaction of the polymer with the solvent. The combination of a viscous background solvent plus a viscoelastic polymer is known as the Oldroyd-B model and named after its creator James G. Oldroyd.

Secondly, real polymers cannot be stretched infinitely, but the Oldroyd-B model can produce infinite stretches for ideal extensional flow scenarios. To adjust for this, a model called FENE-P is implemented, where FENE stands for finitely extensible nonlinear elastic and P for the physicist Anton Peterlin, who was involved in the development of this model. The expression for the elastic stress tensor in the FENE-P model reads

$$\left(1 + \frac{\frac{3}{1-\frac{3}{{L_m}^2}} + \frac{\lambda}{\eta_p}\, tr(\tau_e)}{{L_m}^2}\right)\tau_e = \frac{1}{1-\frac{3}{{L_m}^2}}\eta_p(\nabla\vec{v} + (\nabla\vec{v})^T) - \lambda \cdot \overset{\nabla}{\tau_e} \tag{135}$$

where *tr(·)* is the trace of its tensor argument and L_m is a dimensionless extensibility parameter.

The above elaborations on viscoelasticity are all made from a fluid-mechanical (i.e continuum) perspective. Alternatively, the behaviour of polymers in solution is also considered from the microscopic view, where polymers are modelled as connections of beads and springs. The stretching and contraction of polymers in solvent can then also be described using this mechanical analogue, as done in pioneering work by Rouse and Zimm (Kol et al., 2021).

Viscoelastic behaviour of polymer solutions (but especially polymer melts) can cause numerous unexpected effects in process engineering applications. One of the typical effects is the swelling of an extrusion strand when a viscoelastic polymer solution is pressed through a nozzle. The constriction of the nozzle accelerates the flow, which imposes a strain on the polymer chains causing them to stretch elastically. When the solution left the nozzle, the polymers can start to relax again. The contraction back to their equilibrium conformation causes a drag on surrounding solvent molecules via viscous interaction, thereby thickening the strand radially (Christen, 2010). A schematic picture of this process is shown in Figure 14. Another famous phenomenon in the same context is the Weissenberg effect that describes the formation of an upwards creeping meniscus at the shaft of a rotating stirrer during the mixing of a polymer solution.

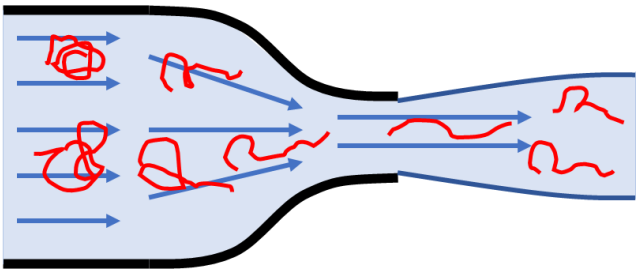

Figure 14 Extrusion of a viscoelastic polymer solution causes a swelling effect on the exiting strand. Approaching the nozzle, the flow is accelerated, and the polymers experience a strain, effectively stretching them. When the solution left the nozzle the polymers can relax again, thereby thickening the strand.

2.4 Surface tension and the Marangoni effect

2.4.1 The origin of surface tension

So far, the focus was on the bulk properties of fluids - particularly liquids. In other words, the system of fluid particles was assumed to span infinitely in all directions. In a fluid system where two distinct phases are present, these are separated by an interface that causes a range of physical effects. In the following, the focus will be on liquid/gas interfaces, but the elaborations could be transferred to other systems like immiscible liquids.

The interface between gas and liquid is a small region in space in which the bulk properties of the fluid particles, like density and pressure, change abruptly. As discussed in the beginning of section 2, the inter-particle distance between liquid molecules is much smaller than between gas molecules. In the gas phase, the thermal energy contained in the random motion of the molecules is so big, that it overcomes attractive forces. Consequently, a gas will fill up any volume almost instantly.

In a liquid, the thermal energy is not as big, attractive forces still are relevant in addition to the repulsive forces. Nevertheless, the thermal energy is still large enough to move the molecules out of the Lennard-Jones equilibrium position, the liquid still flows when subjected to a force.

When the thermal energy is even lower and below attractive forces, the material becomes a solid, in which the molecules essentially stay in place. The random motion due to thermal energy manifests as vibration around the equilibrium distance only.

Following the above explanation, the interface between gas and liquid marks an asymmetry in terms of mutually attracting forces (see Figure 15). A liquid molecule in the bulk experiences attractive forces equally from all sides. Due to the abrupt decrease in density at the liquid-vapour interface, the molecules at the interface experience an imbalance of attractive forces normal to the interface.

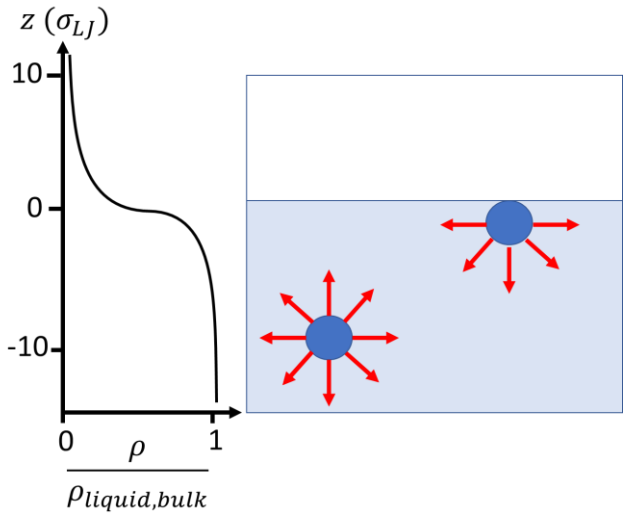

Figure 15 At the interface between a gas and liquid phase, there is a sharp drop in density when moving orthogonally across the interface (schematically depicted on the left side). This causes an asymmetry of mutually attracting forces (red arrows) between liquid molecules (blue dot) at the interface, as depicted on the right.

Effectively, that means there is a net force pulling the interfacial molecules inward. In order to be at the interface, those molecules must be at a higher energetical level, as putting them there required working against a force (Wakeham et al., 2007). The energy needed to create a unit surface of interfacial molecules is the surface energy Π that has units of $\left[\frac{J}{m^2}\right]$ or equivalently $\left[\frac{N}{m}\right]$.

Alternatively, the surface energy can also be interpreted in terms of the force *F* required to stretch a surface by a factor *dx*

$$Fdx = \Pi dA \tag{136}$$

where the interface has the width L and the length is stretched by dx, thus $L \cdot dx = \mathrm{d}A$. Therefore, the surface energy between fluids is also called surface tension.

These two interpretations, though both valid, come from two different points of view, the thermodynamical and fluid mechanical one. Looking at both pictures, there seems to be a contradiction. The thermodynamical point of view (resulting in the interpretation of surface energy) asserts, that there is an asymmetry of forces normal to the interface, while the fluid mechanical view speaks about surface tension, i.e. the force required to stretch a surface by unit length, which is parallel to the interface. The question arises how these two viewpoints can be reconciled. This was already addressed in the scientific literature (Manikantan & Squires, 2020) and is quickly reviewed here. Essentially, the picture depicted in Figure 15 is incomplete. Firstly, one has to consider inter-molecular repulsive forces as well as the attractive ones (see Figure 16). Secondly, one has to take into account that the repulsive forces, due to their very short range, can approximately taken to be isotropic contact forces between molecules, that depend on the number of molecules in direct contact (and therefore on the density) and are independent of molecular structure (black arrows in Figure 16). In contrast, the attractive forces act over a longer range and depend on the local molecular structure. At the interface, the attractive forces normal to the interface show an asymmetry due to the lack of attractive forces from the gas phase and hence have to balance with the repulsive ones, in order for the interface to be in equilibrium. The attractive forces parallel to the interface do not face the same asymmetry and do not need to equal the repulsive forces. As can be seen, the fact that molecules directly at the interface readjust their structure influences the distribution of attractive forces, such that an

equilibrium exists, which in effect produces a net increase of attractive forces parallel to (and in close vicinity of) the interface.

Using a cut-off distance of ten times the molecular distance σ_{LJ}, one can define the surface tension as the integrated difference between normal and tangential pressure $(P_N - P_T)$ along the orthogonal of the interface

$$\Pi = \int_{-10\sigma_{LJ}}^{10\sigma_{LJ}} (P_N - P_T)dz = \int_{-10\sigma_{LJ}}^{10\sigma_{LJ}} \left[P(z)_{zz} - \frac{1}{2}\left(P(z)_{xx} + P(z)_{yy}\right)\right] dz \tag{137}$$

Following that definition, it also becomes clear why yet another way to interpret surface tension is as a surface pressure (Manikantan & Squires, 2020).

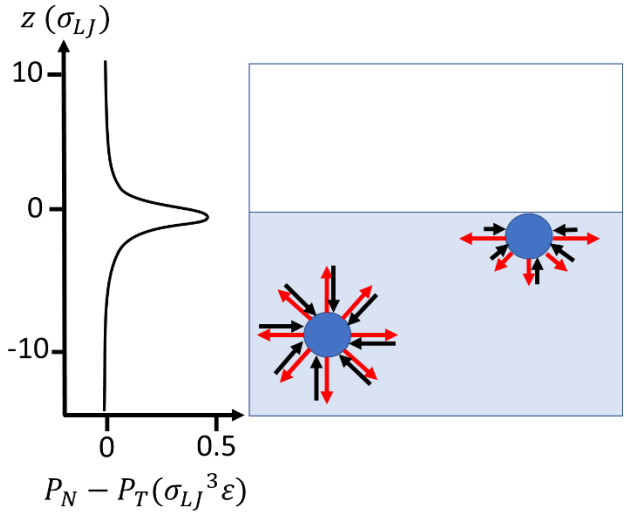

Figure 16 The right side depicts attractive and repulsive forces between liquid molecules (blue dot) in the bulk and at the interface. The repulsive forces are approximately isotropic and depend only on density. Directly at the interface, the attractive forces orthogonal to the interface must be balanced by the repulsive forces (equilibrium condition), as there are no attractive forces from the gas phase. The attractive forces in the tangential plane balance each other and thus do not have to equal the repulsive ones. In effect, the difference between normal stress P_N and tangential stress P_T peaks directly at the interface (as depicted on the left), causing a surface pressure, also called surface tension.

In fluid mechanics, the surface tension has several important ramifications, many of which concern multi-phase flows such as coatings, bubble column reactors or spraying applications. Looking at a small bubble of liquid floating in air, the surface tension will cause an over-pressure in the droplet known as Laplace pressure. The derivation of the Laplace pressure follows from mechanical equilibrium of both phases. If one considers a bubble of liquid with radius R and pressure P_1 in a domain of air with pressure P_{atm}, increasing the radius of the bubble by dR will increase the volume by dV and means a pressure-volume work is done by the liquid system. Vice versa, the air will be compressed by this work. Moreover, increasing the radius will also increase the surface area, thus the work needed to increase the surface area by dA has to be provided as well. In equilibrium, we obtain

$$P_{atm}dV + \Pi dA = P_1 dV \tag{138}$$

Using elementary geometry, one gets

$$P_{atm} 4\pi r^2 dr + \Pi 8\pi r dr = P_1 4\pi r^2 dr \tag{139}$$

and thus

$$P_{atm} - P_1 = -2\frac{\Pi}{r} \tag{140}$$

which is the well-known Young-Laplace equation for a spherical bubble, with $2\frac{\Pi}{r}$ being the Laplace pressure. For an ellipsoid with radius r_1 and r_2, the equation reads

$$P_{atm} - P_1 = -\Pi(\frac{1}{r_1} + \frac{1}{r_2}) \tag{141}$$

For arbitrary surface shapes, on can also use the mean curvature $\nabla \cdot \vec{n}$ from vector calculus (Manikantan & Squires, 2020)

$$P_{atm} - P_1 = -\Pi(\nabla \cdot \vec{n}) \tag{142}$$

Another special case to be considered is when all three phases, i.e. liquid, gas and solid, are present in one system and in contact with each other, as it is for instance found in sessile droplets. As for the interface between liquid and gas, one can define surface energy Π_{LS} for the liquid /solid and Π_{GS} for the gas/solid interface, representing the difference in binding energy per unit area at the respective heterogeneous boundaries. If the droplet is small, it can be approximated as a spherical cap with radius r_c and contact angle θ, as depicted in Figure 17. The interfacial free energy E_i is the sum of the three distinct surface energies times the respective interfacial area (van der Heijden et al., 2018)

$$E_i(r_c, \theta) = \pi {r_c}^2 \left(\Pi_{LS} - \Pi_{GS} + \frac{2\Pi}{1 + cos\theta}\right) \tag{143}$$

For a given volume of the cap, r_c and θ are connected and E_i can be expressed as a function of θ only. Minimizing $E_i(\theta)$ to find the equilibrium configuration, one obtains the famous Young's equation (Wakeham et al., 2007) for the equilibrium contact angle θ_{eq}

$$\Pi_{LS} - \Pi_{GS} - \Pi\, cos\theta_{eq} = 0 \tag{144}$$

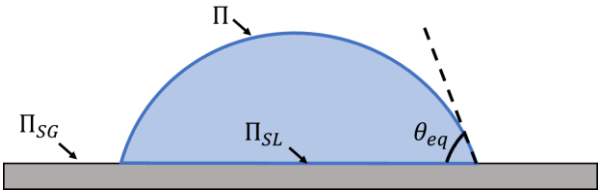

Figure 17 Equilibrium contact angle θ_{eq} for a liquid droplet on a solid surface surrounded by a gas phase. In equilibrium, the contact angle depends on the three surface energies of solid and gas (Π_{GS}), liquid and solid (Π_{LS}) and liquid and gas (Π), as described by Young's equation.

As stated, Young's equation only holds at equilibrium. A more complicated situation arises when the contact line of the droplet is not static, which could be the case for an evaporating liquid or if the droplet moves relative to the solid plate, for instance because it is tilted so that gravity pulls the drop downwards. Generally, the equilibrium angle for a receding contact line is smaller than the static equilibrium angle, while an advancing contact angle is bigger, a phenomenon that is called contact angle hysteresis. The literature provides different theoretical approaches to explain this phenomenon, either from a hydrodynamic or microscopic/molecular kinetic standpoint (Wakeham et al., 2007). Both approaches point to an increased viscous dissipation energy directly at the moving contact line, which violates the assumptions in Young's model that is fundamentally derived form a surface energy balance. Consequently, the local change of interface shape is determined by the ratio of viscous forces to surface tension forces, which is called the capillary number

$$Ca = \frac{v\eta}{\Pi} \tag{145}$$

where v is a characteristic velocity of the system.

In the range of 10^{-4}<Ca<10^{-1}, the difference between dynamic contact angle $\theta_{d,eq}$ and the static one can be expressed in the Cox-Voinov-Tanner scaling law, at least for Newtonian liquids (Kim & Rothstein, 2015)

$$\theta_{d,eq}{}^3 - \theta_{eq}{}^3 \propto Ca \tag{146}$$

The dynamic contact line occurring in the meniscus of a roll-to-roll coating device poses an intricate modelling problem. The implementation of a conventional no-slip condition would cause a stress singularity, as two contradicting boundary conditions arise at the dynamic contact point. The conventional no-slip condition of fluid mechanics would assign the velocity of the moving wall directly adjacent to the fluid element while reaching a steady state position of the meniscus at the contact point requires the local velocity to be zero. The implementation in COMSOL™ takes the approach of Gerbeau *et al.* (Gerbeau & Lelièvre, 2009) by applying a force to the fluid which is tangential to the wall surface and moves the fluid towards the pre-defined dynamic equilibrium contact angle $\theta_{d,eq}$ (per default assumed to be 90°).

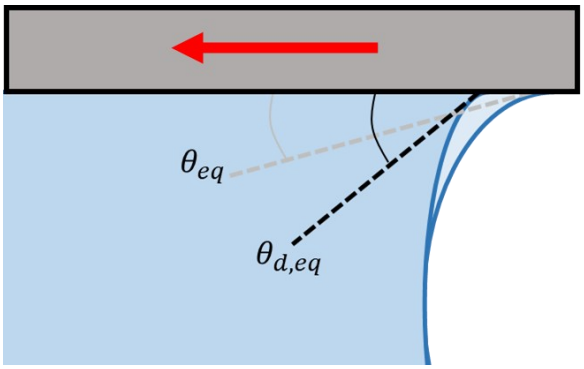

Figure 18 Schematic illustration of the contact angle at a dynamic contact point. When the solid wall is moving with respect to the liquid meniscus, this changes the contact angle from the static equilibrium (θ_{eq}) to the dynamic equilibrium ($\theta_{d,eq}$). Due to the relative motion of the wall, the equilibrium dynamic contact angle $\theta_{d,eq}$ is an advancing contact angle in this case.

2.4.2 Surfactants and the Marangoni effect

The word surfactant stands for surface active agent and describes the property of some substances to adsorb to an interface between different fluids like air and water. In many cases, the higher affinity to adsorb to an interface is result of an amphiphilic character of the molecules, meaning the molecule contains both hydrophobic and hydrophilic parts. By adsorbing to the surface, these molecules can minimize energetically unfavourable interactions, as the hydrophilic parts point inwards to the water, while hydrophobic parts point outwards. This molecular configuration of course comes with a smaller number of microstates compared to the free position in the bulk, so the energy win will be balanced by an entropic 'penalty'. Nevertheless, in some extreme cases the surfactant can also be completely insoluble in the solvent. When the whole surface is covered, adding more surfactant to the solution will cause the surfactants to reorganize in small vesicles that are called micelles. The concentration of surfactant causing the formation of micelles is therefore called critical micelle concentration (CMC).

Even though the typical surfactant is a low molecular weight amphiphilic compound like Sodiumdodecylsulfate (SDS) or Triton X-100, the same behaviour can be observed for a wide range of molecule classes and sizes. Examples of high molecular weight molecules that do not follow the simple binary hydrophilic/hydrophobic structure include proteins and synthetic polymers. Very well-known examples of surfactant polymers are the di- and triblock copolymers consisting of PEO and polypropyleneoxide (PPO), which are commercially available under the name Pluronics®. Those polymers will decrease the surface tension in aqueous solutions significantly and can, when a threshold concentration is reached, form micelles like their low-molecular counterparts (Raffa et al., 2015). For even bigger polymers consisting of several repeating units, i.e. multiblock copolymers (MBCP), surface activity data is more scarce. However, there are literature results showing similar surface activity for MBCP's with 6 and 10 repeating diblock units of PEO and PPO, having a molecular weight of 130000 and 69000 Da, respectively (Rikiyama et al., 2018). Both polymers exhibited surface tension reduction in water and a CMC value could also be determined. Interestingly, even though the authors estimated the radius of gyration to be 6-8 nm, the occupied surface area of the polymers at the air/water interface was estimated to be around 1 nm², thus indicating structural reorientation of the polymer chain at the interface. Moreover, in a study of MBCPs of polymethylphenylsilylene (PMPS) and PEO, a strong effect on surface tension in water was shown, that is similar to PEO homopolymers, therefore surface activity was primarily attributed to the PEO segment by the authors (Milling et al., 2000).

Giving a general review on the surface activity of alternating multiblock copolymers (AMB) at the interface, a structural classification of polymeric surfactants and summary of the surface activity data

of polymers can be found in the literature (Raffa et al., 2015). The proposed polymeric surface structure is schematically reproduced in Figure 19. The hydrophobic part is usually assumed to have a two-dimensional 'pancake' structure, while the hydrophilic part reaches inside the liquid. When the polymers get compressed, the inside parts may become elongated to form a brush-like structure (Monteux, 2014).

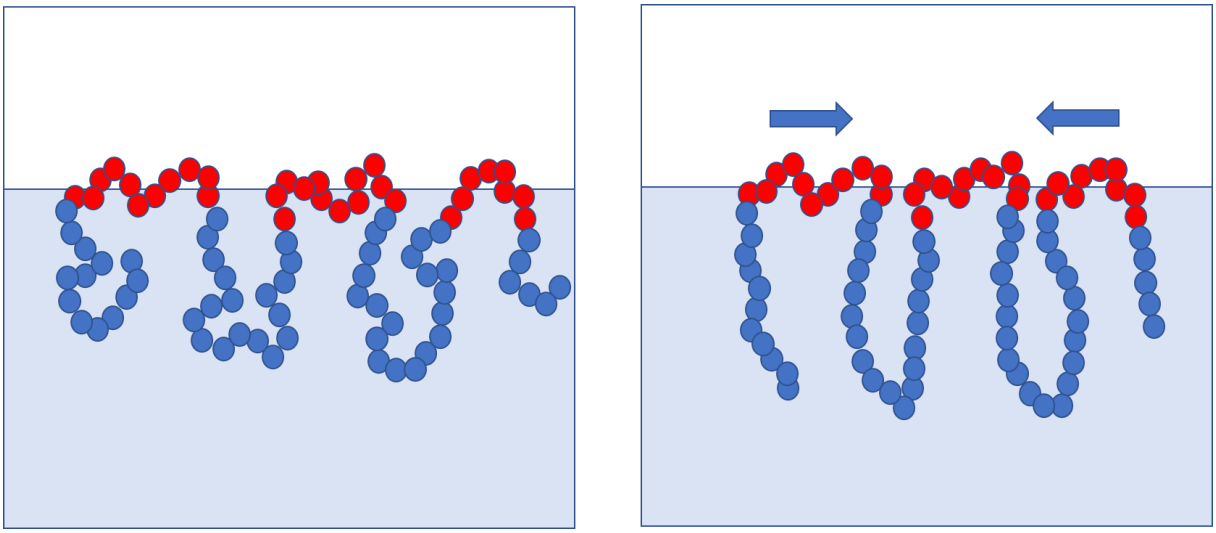

Figure 19 Schematic illustration of the suspected conformation of a multiblock copolymer at the phase interface between gas and liquid (left side). The dots represent the monomer units and the colours the alternating block segments. In an amphiphilic copolymer, the hydrophobic segments (red) align at the interface, while the hydrophilic parts (blue) face inwards. When the surface gets compressed (right side), the polymers go from a coiled to a more stretched conformation, forming a brush-like structure.

As surfactants adsorb to the interface, they reduce the surface tension by replacing the solvent molecules and their asymmetric interactions (see section 2.4.1). Using the assumptions of the Langmuir isotherm (section 2.2.1) one can compute the change in surface tension due to a given surfactant concentration (Manikantan & Squires, 2020) as

$$\Delta\Pi_{Langmuir} = RTc_{s,\infty}\ln\left(\frac{1}{1-\frac{c_s}{c_{s,\infty}}}\right) \tag{147}$$

Like in the Langmuir adsorption isotherm, it is assumed that the interface can be regarded as a lattice with points representing the available binding sites and with each surfactant molecule only occupying one point on the lattice.

If, on the other hand, the surface is not treated as a lattice and the surfactants simply have a finite size A_s which reduces the total area available by binding to the interface, one obtains the Volmer isotherm for surface tension reduction

$$\Delta\Pi_{Volmer} = RTc_s\left(\frac{1}{1-\frac{c_s}{c_{s,\infty}}}\right) \tag{148}$$

Both expressions can be extended further to include interactions between molecules, resembling the interaction term in the van der Waals equation (Section 2.1.1), for instance in the following form, where β is a model parameter representing the interaction between two surfactant molecules

$$\Delta\Pi_{van\ der\ Waals} = RTc_s\left(\frac{1}{1-\frac{c_s}{c_{s,\infty}}}\right) - \beta\frac{{c_s}^2}{2} \tag{149}$$

As described in section 2.3.1, the surface tension comes from a peak in the tangential stress that can also be interpreted as a surface pressure. At higher surface tension, the attractive interaction between surface molecules is higher than at lower surface tension. Consequently, a gradient of surface tension along an interface is essentially a gradient of attractive forces which provokes a flow of surface molecules going from low to high surface tension. This is called the Marangoni effect. The movement of liquid molecules at the interface along the surface tension gradient will cause a transfer of momentum to the next layers of liquid just beneath the surface via viscous interactions, in other words a viscous shear stress is exerted

$$\nabla_s\Pi = \eta\vec{n}\cdot\nabla\vec{v}_s \tag{150}$$

where $\vec{n}\cdot\nabla\vec{v}_s$ is the velocity gradient normal to the interface.

So far, the discussion focused on the gradients of surface tension caused by inhomogeneous surfactant concentration at the interface. Another important mechanism for the Marangoni effect is the temperature dependence of surface tension (also called thermocapillary effect). The surface tension for a pure liquid decreases with rising temperature. A relatively good approximation is the Eötvös rule, that states, that the decrease is linear and surface tension vanishes when the critical temperature T_c of the liquid is reached

$$\Pi(T) = \frac{k_{Eötvös}(T_c - T)}{\left(\frac{M_w}{\rho}\right)^{\frac{2}{3}}} \tag{151}$$

where the Eötvös constant $k_{Eötvös}$ has a universal value of $2.1\cdot10^{-7}\ \frac{J}{K\cdot mol^{\frac{2}{3}}}$.

Thus, Marangoni effects can also be caused by temperature gradients along the interface, for example due to inhomogeneous evaporation. Often, both the chemical composition and temperature effect can happen at the same time and interact with each other, which is important to consider especially for microfluidic systems (Karbalaei et al., 2016).

2.5 Modes of heat transport

The transport of heat – or thermal energy - can be divided into three main mechanisms: convection, conduction and radiation.

2.5.1 Convection

In the case of convection, the thermal energy is a physical property of a fluid particle that moves in space and thereby transports the energy. If the movement of particles is caused only by the buoyancy forces arising from density difference of hot and cold parts of the liquid, this is called natural convection. If other reasons, like pressure gradients, are the cause of the fluid motion, this is called forced convection (Bird et al., 2007). The mathematical description of convection is already treated in the energy balance (see section 2.1.3) and therefore not repeated here.

2.5.2 Conduction

Conduction refers to the transfer of thermal energy in a material following from direct contact of the molecules, thus mass transport and energy transport are not coupled here (Demtröder, 2017). The heat flux $\dot{q}$ is proportional to the negative temperature gradient and a material property called thermal conductivity, as described by Fourier's law

$$\dot{q} = -k_{thermal} \nabla T \tag{152}$$

Ignoring convection, the thermal energy at a given point in a material changes, if there is a gradient of heat flux

$$C\rho \frac{\partial T}{\partial t} = -\nabla \dot{q} \tag{153}$$

Thus, one gets

$$\frac{\partial T}{\partial t} = \frac{k_{thermal}}{C\rho} \nabla^2 T \tag{154}$$

where the ratio $\frac{k_{thermal}}{C\rho}$ is called thermal diffusivity, hinting at the resemblance to Fick's diffusion laws. Fourier's law is also valid for solids, where the thermal energy manifests as vibration and the vibrational energy is transported as adjacent atoms or molecules are coupled. In metals, the freely moving electrons also transport heat via collisions and are responsible for the relatively high thermal conductivity of metallic solids (Demtröder, 2017). In consequence, this also means, that thermal conductivity and electrical conductivity are proportional, as expressed in the Wiedmann-Franz law.

In liquids, the molecules are not strongly coupled and therefore the conduction of thermal energy is much lower. The contribution of electrons to thermal conductivity is missing in liquids with no electrical conductivity. However, here the molecules themselves can move freely and exchange thermal energy via collisions. The same goes for gases, but as the density is much lower compared to liquids, so is the number of collisions and therefore the thermal conductivity of gases is usually very low (Demtröder, 2017).

It should be noted that the thermal conductivity of a material is generally not a constant but depends on the temperature itself, making conduction a non-linear and thus more complicated problem.

2.5.3 Radiation

The third mode of thermal energy transport is radiation, that is emission and absorption of electromagnetic waves. Radiation transports thermal energy through matter and vacuum as well (Demtröder, 2017). The intensity and frequency of the emitted waves depends strongly on the temperature of the material that is emitting and is therefore also called thermal radiation. The amount of radiated energy per time and unit area $\dot{q}_{rad}$ is given by the Stefan-Boltzman law

$$\dot{q}_{rad} = \epsilon \cdot \sigma_{SB} \cdot T^4 \tag{155}$$

Where σ_{SB} is the Stefan-Boltzmann constant and ϵ is the dimensionless emissivity, that can assume values between 0 and 1. A perfect black body, that is an idealized body absorbing all incident light, has an emissivity of 1, real materials are always <1.

2.6 Fundamentals of the finite element method

All presented physical laws are supposed to model some physical process in the real world by means of a differential equation. To do this, they define a set of dependent variables that are thought to be relevant for the process in question, such as fluid velocity, pressure or temperature, and describe how the derivative of this variable depends on some mathematical function that may in turn also use all dependent variables as input. This derivative might be with respect to any independent variable, which usually is time or any of the spatial dimensions. Ultimately, the goal is to describe the spatial distribution and time development of all the dependent variables for the system of interest, hence these PDEs must be solved to yield functions for every dependent variable as a result, which only need the independent variables as input. For instance a function describing the temperature field depending on a given position and time: $T = T(x, y, z, t)$.

The problem is that there is no recipe or generalized formula of how to solve any given PDE. While there are methods to derive analytical solutions for certain special cases, generally there is no such method, and the solution function can only be approximated by numerical methods. This is especially true for fluid mechanics, where complex software is needed to compute the approximate solution to a given physical problem. Adding to the challenge to formulate the correct physical laws describing the problem mathematically, a useful problem statement also needs initial and boundary conditions that ensure the uniqueness of the solution.

When the appropriate model of the process is chosen and the boundary conditions of the problem are set up, it may be solved numerically. Modern CFD software mainly uses two numerical methods to solve the PDE: the finite volume method (FVM) or the already mentioned FEM (see section 1.4). Even though quite different in their mathematical procedure, there are some commonalities. Essentially, for both methods the independent variables (time and space) are discretized, and the solution of all dependent variables is therefore only computed on discrete points in time and space. The goal of both methods is then the same: the (complicated) set of differential equations describing the continuum shall be replaced with an easier (but much larger) set of algebraic equations describing the discretized space. Hence, the result of the numerical procedure is a tensor for each dependent variable, that

contains the computed approximate value of the respective dependent variable for each discretization point. The difference between the two numerical methods lies in the approach of how the algebraic equation is obtained.

For the discretization, the FVM divides the spatial dimension into very small sub-volumes or cells. The differential equation must hold everywhere, so one can integrate both sides of the equation over the volume of each cell. Hence, for each cell one gets a volume integral equation that can be reformulated according to the Gauss Theorem, whereby a gradient of a dependent variable in the integrand disappears, as the volume integral is replaced by a surface integral going over the complete surface of the cell. Consequently, second order derivatives become first order and, if the cells are small enough, can be approximated by a Taylor expansion. Finally, it is then possible to replace the differential equation with an algebraic one (Andersson et al., 2011).

Since all numerical simulations in this thesis were done with COMSOL Multiphysics™, which uses the FEM, this method will now be explained in greater detail.

To illustrate the procedure, it is worthwhile to go through the process for a concrete example of a certain PDE. The method can then be used analogously for any other form of PDE. One relatively simple PDE is the Poisson equation in two dimensions defined on a subspace $\Omega \in \mathbb{R}^2$

$$\nabla^2 u = \frac{\partial^2 u}{\partial x^2} + \frac{\partial^2 u}{\partial y^2} = f(x, y) \tag{156}$$

where u is the dependent variable and f is any function of x and y. For simplicity, the following boundary condition is chosen

$$u(\partial\Omega) = 0 \tag{157}$$

That means, on the boundary of the domain the dependent variable assumes the value zero. The formulation of the boundary condition in terms of the dependent variable directly is called Dirichlet boundary condition, while a formulation with respect to a derivative of the dependent variable is called Neumann boundary condition.

By comparison, one can immediately see the resemblance to the heat transport (section 2.5). If, for instance, $f = 0$, the equation may simply describe steady state heat conduction in the absence of convection and other source terms. Including arbitrary source terms, we may also write it as

$$\nabla^2 T = f \tag{158}$$

This PDE is now transferred to what is called the “weak formulation”. For this, the equation is multiplied by an unspecified function w (called weight function) and both sides of the equation are integrated over the domain Ω

$$\int_\Omega w \nabla^2 T dA = \int_\Omega w f dA \tag{159}$$

The weight function w is somewhat arbitrary, but not completely. Mathematically speaking, w is element of a function space H that contains all functions that are bounded, that is quadratic integrable

$$H(\Omega) = \left\{ w: \Omega \to \mathbb{R}: \int_{\Omega} w^2 dA \,, \int_{\Omega} \frac{\partial w^2}{\partial x}\, dA \,, \int_{\Omega} \frac{\partial w^2}{\partial y}\, dA < \infty \right\} \tag{160}$$

which is needed to ensure a meaningful result of the integration. Furthermore, one can make use of the boundary condition by defining a subspace X

$$X = \{ w \in \mathrm{H}(\Omega): w|_{\partial\Omega} = 0 \} \tag{161}$$

Since for a realistic physical problem one can expect the real solution function T to behave as demanded in the function space H, the stated boundary condition means the real solution to T must be in the subspace X of H. One can therefore also restrict the weight function w to be in the subspace X, i.e. $w, T \in X$

To reformulate the left-hand side term of (159), the product rule can be applied to rewrite it as

$$\int_{\Omega} w\nabla^2 T \, dA + \int_{\Omega} \nabla w \cdot \nabla T \, dA = \int_{\Omega} \nabla(w\nabla T) dA \tag{162}$$

Invoking Gauss theorem on the right side, one obtains

$$\int_{\Omega} \nabla(w\nabla T) \, dA = \int_{\partial\Omega} w\nabla T \cdot \vec{n} \, dS = 0 \tag{163}$$

which is zero, since $w|_{\partial\Omega} = 0$.

Going back to (159), one can now replace the left-hand side

$$-\int_{\Omega} \nabla w \cdot \nabla T dA = \int_{\Omega} w f dA \tag{164}$$

This formulation is what is called the weak formulation. In the next step, both the function T and w are replaced by approximation functions $\widehat{T}$ and $\widehat{w}$, leading to a further simplification that is needed for the algebraic formulation of the problem.

To understand how the function T is approximated, see Figure 20 showing a simplified scheme of an arbitrary one-dimensional function T over space x that is approximated by a set of linear functions. The spatial dimension is discretized into n elements with $n + 1$ nodes separating the elements. The combination of linear segments is the approximation function $\widehat{T}$.

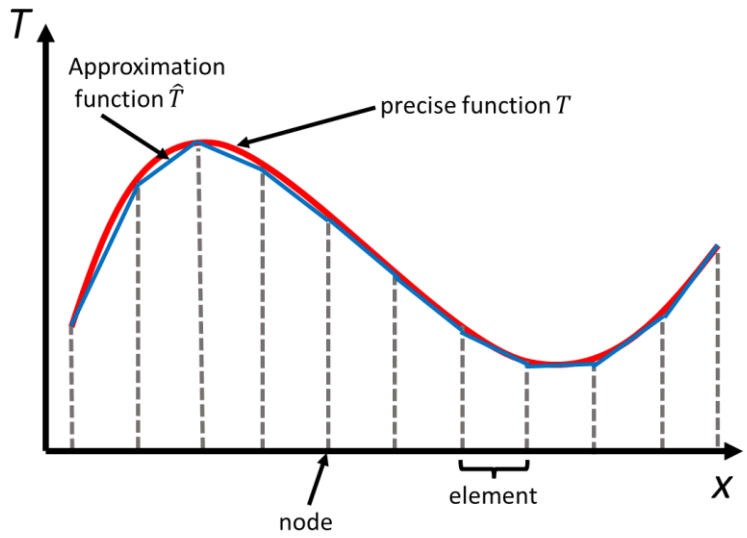

Figure 20 A polynomial function T(x) is approximated by a set of linear functions between nodal points that discretize the space x.

To obtain this approximation curve $\hat{T}$, one can use a construction involving so called basis functions b. The basis function b_i assumes the value 1 at node i and zero at all other nodes. It is non-zero only on elements i and $i+1$, that is the elements neighbouring node i. If the value T at node i is known, the approximation function from Figure 20 can be obtained by summing up all basis functions weighted by the respective nodal value of $T = \hat{T}_i$

$$\hat{T} = \sum_{i=1}^{n} b_i \hat{T}_i \tag{165}$$

See Figure 21 for the representation of basis functions and their addition to yield $\hat{T}$.

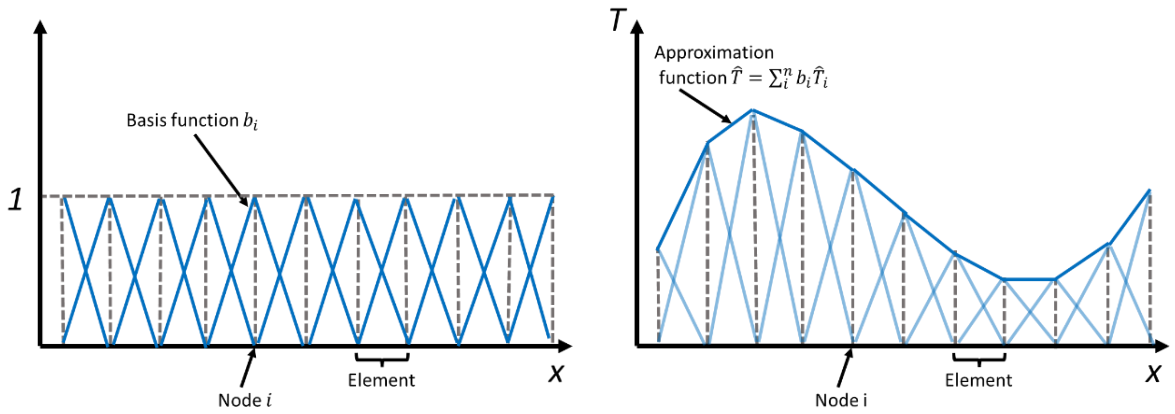

Figure 21 The left side shows the simplest form of a basis function b_i, which has a triangular shape and assumes value 1 at the respective nodal point I and 0 at the neighbouring points i-1 and i+1. When the basis functions are summed up and multiplied by an individual weight factor $\hat{T}_i$, one obtains the approximation function $\hat{T}$ (right side).

It should be noted here that the basis functions do not have to be linear functions, they could also be (and in fact often are) second or higher order polynomials.

Going back to the weak formulation of the PDE, one can assume that both the actual temperature field that is the solution to the problem and the weight function w can be approximated by basis functions in the very same way, and the approximation will be increasingly accurate for ever smaller element sizes. When the same basis functions are used for the dependent variable and the weight function, this is called the Galerkin method (Madenci & Guven, 2015). Substitution of the approximation functions into the governing PDE (164) yields

$$-\int_{\Omega} \nabla \sum_{j=1}^{n} b_j \widehat{w}_j \cdot \nabla (\sum_{i=1}^{n} b_i \widehat{T}_i) dA = \int_{\Omega} \sum_{j=1}^{n} b_j \widehat{w}_j \, f dA \tag{166}$$

As equation (166) looks quite confusing now, one can conveniently define operators $a(\cdot)$ and $l(\cdot)$ as follows

$$a(w, T) \equiv \int_{\Omega} \nabla w \cdot \nabla T dA \tag{167}$$

$$l(w) \equiv \int_{\Omega} w \cdot f \, dA \tag{168}$$

and use these operators to write instead

$$a(\sum_{j=1}^{n} b_j \widehat{w}_j \, , \sum_{i=1}^{n} b_i \widehat{T}_i) = l(\sum_{j=1}^{n} b_j \widehat{w}_j) \tag{169}$$

Realizing that integrating over the sum of independent functions must yield the same as summing up the integrals of each function, one obtains

$$\sum_{j=1}^{n} \sum_{i=1}^{n} a(b_j \widehat{w}_j, b_i \widehat{T}_i) = \sum_{i=1}^{n} l(b_j \widehat{w}_j) \tag{170}$$

Furthermore, the coefficients $\widehat{T}_i$ and $\widehat{w}_j$ are only constant numbers and can thus be pulled out of the respective operator

$$\sum_{j=1}^{n} \widehat{w}_j \sum_{i=1}^{n} a(b_j, b_i) \widehat{T}_i = \sum_{i=1}^{n} \widehat{w}_j l(b_j) \tag{171}$$

Which can be written more compactly in matrix notation

$$\vec{w}^T \bar{A} \vec{T} = \vec{w}^T \vec{F} \Leftrightarrow \bar{A} \vec{T} = \vec{F} \tag{172}$$

where $\vec{w} = [\widehat{w}_1, \widehat{w}_2, \dots, \widehat{w}_n]^T$, $\vec{T} = \left[\widehat{T}_1, \widehat{T}_2, \dots, \widehat{T}_n\right]^T$, $\vec{F} = [l(b_1),\ l(b_2), \dots, l(b_n)]^T$ and

$$\bar{A} = \begin{pmatrix} a(b_1, b_1) & \cdots & a(b_1, b_n) \\ \vdots & \ddots & \vdots \\ a(b_n, b_1) & \cdots & a(b_n, b_n) \end{pmatrix} \tag{173}$$

Finally, one obtains the desired result, which is a system of algebraic equations that can be solved by a computer.

To shortly rephrase the process verbally: first, the original governing PDE was transformed into a weak formulation by the multiplication of a (suitable) weight function and subsequent integration. This allowed to shift one derivative from the dependent variable to the weight function, thus reducing the order of the PDE by one (thereby also explaining the naming convention of a 'weak formulation'). Secondly, the continuous functions for the dependent variable and weight function were replaced by approximation functions, which are constructed as the sum of simple basis functions. Here, one exploited the fact that the distribution of real physical metrics cannot follow any arbitrary form of mathematical construct (which might be discontinuous or not differentiable) but should be describable by some sort of polynomial. Rearrangement then led to a result in which the differentiation and integration operations only need to be computed for the basis functions, which can be done analytically, since the basis functions are known and relatively simple. Finally, the only thing left to determine is the weighting coefficients of the basis functions for each node of the discretized space, such that the system of algebraic equations – and therefore the approximation of the PDE- is fulfilled.

To solve the algebraic system, one could theoretically employ the Gauss elimination procedure. However, in practice this is not feasible, as real-life problems often consist of hundred thousand or millions of cells, yielding a correspondingly large matrix to be solved, for which the Gauss elimination would take a very long time. Instead, modern CFD software uses iterative methods that are often based on some form of Gauss-Seidel algorithm (GSA). Conceptually, the GSA solves the equations for each cell individually. To do this, it needs some initial guess for all dependent variables, since the value of a dependent variable in one cell depends on the value of the dependent variables in all neighbouring cells. When the value of this variable is computed, the matrix containing the values of all cells is updated at the corresponding position and the next cell is computed based on the updated matrix. The process is repeated for all cells. Nevertheless, in the end most equations are likely violated, since the computation of a cell depended on the neighbouring cells, which subsequently changed during the rest of the procedure. Therefore, the whole process is computed in an iterative manner, until a user-defined quality criteria of convergence is met, for instance when the overall residual of the equations is below a certain value (Andersson et al., 2011).

2.7 Modelling multi-phase flow with a moving mesh

In former studies of free-surface coating flows, the computation of the surface movement was done with a VOF method (Chien & Jang, 2007), which is an interface capturing method that tracks the phase interface with a scalar fraction function describing the position of the interface in space. Contrasted to this are interface tracking methods, which track the interface position directly, as it coincides with the boundaries of a moving mesh. To solve the problem of free surface flows, COMSOL™ provides several algorithms from both classes of methods. The Phase-field and Level-set method belong to the class of interface capturing methods, where the phases are modelled by an auxiliary function. The value of the function can assume values between -1 and 1, where 1 represents phase 1 and -1 represents phase 2. The interface is represented by a narrow transition region of the phase variable. The evolution of the

interface region is then modelled by a Cahn-Hillard equation, which originates from thermodynamics of phase separation (*Microfluidics Module User's Guide, COMSOL Version 5.5 (Accessed 25.06.2025)*, n.d.).

In contrast, the interface tracking method provided in COMSOL™ is based on a moving mesh, that uses the Arbitrary Lagrange-Eulerian (ALE) method. While the first two methods have the advantage, that topological changes of the interface geometry can be simulated, their main disadvantage is that mass transfer across the interface is very difficult to implement realistically. The ALE method based on a moving mesh cannot handle strong deformations of the surface or topological changes, but the mass transfer at the interface is easily implemented, and thus the method of choice in this thesis. Moreover, the explicit modelling of the interface also allows for the easy formulation of additional two-dimensional PDE's on that boundary, as is needed for a surfactant mass balance (see section 2.2.1) and was therefore also used by other authors working on free surface flows in the presence of surfactants (Pohjoranta & Tenno, 2011).

2.7.1 The ALE method

Recalling the introduction of section 2, the governing equations in fluid dynamics are formulated in a Eulerian - or spatial- reference frame, that is with respect to a fixed point in space. In solid mechanics, on the other hand, it is more useful to formulate the PDE's with respect to the material frame, i.e. the Lagrangian reference frame. The latter method is not feasible for the vast number of fluid particles usually looked at but has the advantage of being able to compute the movement of boundaries. The ALE method represents a mixture of both approaches, that utilizes a third reference frame, the mesh frame (Donea et al., 2004). Instead of material points, the mesh frame describes the spatial position of all mesh nodes. Initially, the mesh frame and material frame may coincide, but as the material deforms over time, they diverge. The three reference frames are denoted by Xs for the spatial, Xm for the material and Xg for the grid (i.e. mesh).

In free surface flows, the boundary of the material domain always coincides with the interface and can move according to the velocity field in the material, which follows from the mass and momentum balance (see section 2.1.3). If the forces at the interface are not in equilibrium, the fluid velocity normal to the interface is not zero and thus the interface boundary of the domain deforms, given the velocity and a small time-step dt. The mesh nodes directly at the interface also follow the same movement, but the mesh nodes inside the domain do not necessarily follow the material movement. Instead, the mesh deforms such that the nodes are still distributed in a way that resembles the original mesh configuration to some extent (see Figure 22 for a conceptual Illustration). This is done to avoid numerical problems arising from strongly deformed mesh elements. Thus, the movement of the individual mesh elements is somewhat arbitrary, hence the name Arbitrary Lagrange-Eulerian method.

Technically, the mesh nodes move with a velocity $\vec{v}_{mesh}$ that is different from the material velocity and is the solution of a smoothing equation.

As already discussed, the evolution of a variable F in the material frame is mapped to the Eulerian frame via the material derivative

$$\left.\frac{\partial F}{\partial t}\right|_{Xm} = \frac{DF}{Dt} = \left.\frac{\partial F}{\partial t}\right|_{Xs} + \vec{v} \cdot \nabla F \tag{174}$$

Analogously, the derivative with respect to the material is also coupled to the mesh frame

$$\left.\frac{\partial F}{\partial t}\right|_{Xm} = \left.\frac{\partial F}{\partial t}\right|_{Xg} + (\vec{v} - \vec{v}_{mesh}) \cdot \nabla F \tag{175}$$

Thus, the variable describing a physical property at a given material point follows from the derivative at a fixed grid point plus a convective correction accounting for the difference between material and mesh velocity.

COMSOL™ provides four different algorithms to govern the mesh deformation across the grid, namely Laplace, Winslow, hyperelastic smoothing and Yeoh smoothing. The COMSOL™ manual describes the Yeoh smoothing method as the most numerically robust, hence only this method was used in this thesis. Both in the hyperelastic and Yeoh smoothing model the mesh is regarded as a hyperelastic material, for which a deformation energy is computed that is based on some artificial modulus and elastic material properties. In the Yeoh method, one such parameter is the stiffening factor, that controls the nonlinear stiffening of the artificial "mesh-material"(Comsol Multiphysics Reference Manual, Version 5.5).

Nevertheless, even though the stated algorithms can distribute the mesh deformation more smoothly, in many cases the mesh will still deform too much over the time of the simulation, which would cause numerical instabilities. To circumvent this, COMSOL™ allows automatic re-meshing, which stops the solver when deformations become too large, for instance if the quality any mesh element (ratio of shortest to longest edge) goes beneath a certain threshold (default value here is 0.2). The geometry is then re-meshed and the solution from the last time-step is interpolated on the new mesh.

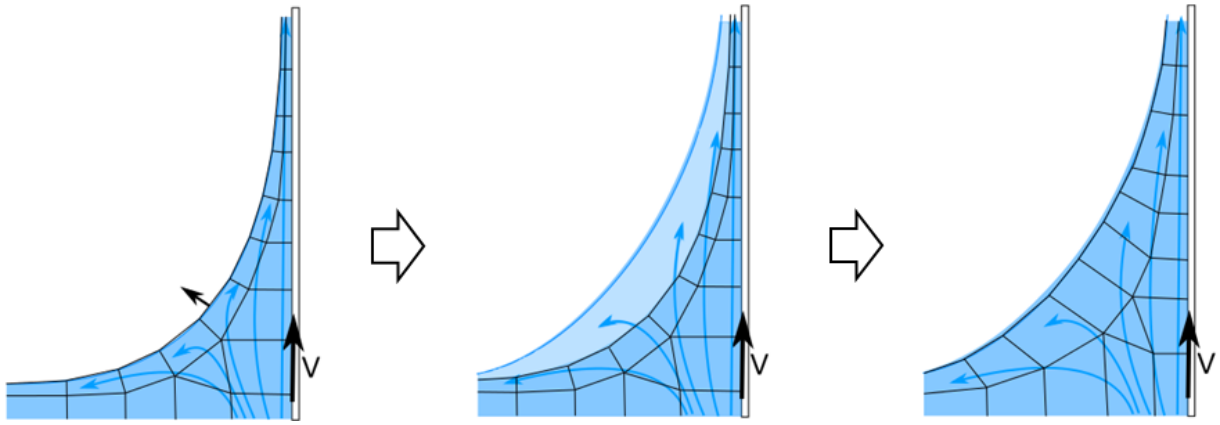

Figure 22 Schematic representation of a moving mesh algorithm used in free-surface flow problems. For simplification, the dip coating scenario is shown, where a plate is dragged out of a liquid with constant velocity v. The fluid mechanical equations are solved on a spatial frame of reference in the liquid domain (coloured in blue). If the solution of the equations implies an imbalance of forces on the free surface (as indicated by the black arrow in the left picture), the surface of the liquid domain moves towards equilibrium (based on a small timestep). Then, the mesh is readjusted such that the edges are again coinciding with the surface and the elements inside the domain are distributed similar to the original configuration.

2.7.2 Boundary conditions at the interface

At the interface between the gas and liquid phase, the mass and momentum balance must be modified to account for the effects of evaporation and surface tension, respectively. If subscript 1 denotes the liquid phase and subscript 2 denotes the gas phase, the boundary condition for the mass balance reads

$$\vec{v}_1 - \frac{j_{m,evap}}{\rho_1} \cdot \vec{n} = \vec{v}_2 - \frac{j_{m,evap}}{\rho_2} \cdot \vec{n} \tag{176}$$

where $j_{m,evap}$ is the evaporative mass flux and $\vec{n}$ is the normal vector to the interface. The equation ensures, that the tangential velocity components of both phases are equal (no stress condition, i.e. gas molecules at the interface assume the liquid velocity due to the comparably negligible gas viscosity), while the normal components are corrected for the "shrinking" of the liquid phase – with parallel expansion of the gas phase - due to the evaporation.

The mesh follows the interface, thus for the mesh velocity one obtains

$$\vec{v}_{mesh} = \left(\vec{v}_1 \cdot \vec{n} - \frac{j_{m,evap}}{\rho_1}\right) \cdot \vec{n} \tag{177}$$

At equilibrium, the stresses at the interface have to balance, hence

$$\vec{n} \cdot \bar{\bar{\sigma}}_1 + \vec{F}_{st} = \vec{n} \cdot \bar{\bar{\sigma}}_2 \tag{178}$$

where F_{st} is the force vector per unit area due to the surface tension.

The gas viscosity is much smaller than the liquid viscosity, thus (178) can be simplified to

$$\vec{n} \cdot \bar{\bar{\sigma}}_1 + \vec{F}_{st} = -\vec{n} \cdot P_{ext} \tag{179}$$

assuming the gas phase has constant external pressure P_{ext}.

Using the insights on surface tension from section 2.4, the surface tension force F_{st} can be decomposed into the normal part (Laplace pressure) plus the tangential part (Marangoni stresses). Taken together, one gets

$$\vec{F}_{st} = -\Pi(\nabla_s \cdot \vec{n})\vec{n} + \nabla_s \Pi \tag{180}$$

and therefore

$$\vec{n} \cdot \bar{\bar{\sigma}}_1 = -\vec{n} \cdot P_{ext} + \Pi(\nabla_s \cdot \vec{n})\vec{n} - \nabla_s \Pi \tag{181}$$

In words: the normal stress of the liquid at the interface equals the sum of the external pressure plus Laplace pressure, while the tangential stress equals the gradient of the surface tension (Microfluidics Module User's Guide, COMSOL Version 5.5).

2.8 Analysing process parameters using design of experiments

DOE is a statistical tool to investigate the relationship between a set of input factors and a resulting output or response for any real or virtual system. The term DOE refers to a broad range of methods that can be used to identify the important factors influencing a process and quantify their contributions

or interactions. In this study, the response surface method (RSM) (Lenth, 2009) was used to analyse the variation of coated polymer thickness depending on the fluctuation of several process parameters.

Usually, the RSM is used, when the important input factors of a process are already known from previous experiments and the next goal is the detailed quantitative description of the system (Lawson & Zidek, 2015). The RSM procedure can be divided into three steps:

1. Setting up a design plan of experiments that is conducted in order to generate the necessary data effectively
2. Fitting a regression model to the obtained data
3. Analysing the regression model to understand the systems behaviour. Often, this means finding a minimum or maximum of the output metric of interest. Moreover, fitting quality and statistical robustness must be checked and the predictions of fitted model should be validated by further experiments, which may lead to a re-iteration of the procedure to further improve the model

The design plan defines a set of input factor combinations for which data points must be generated. There are many possible design plans, but in this thesis only the famous central composite design (CCD) is used. A schematic depiction of a two-dimensional CCD plan can be seen in Figure 23. The general idea is to cover the complete input parameter space of the model with the least number of experiments. Every input factor needs to be assigned a respective minimum and maximum value that determines the edges of the design space. Effectively, the normalization by the maximum and minimum value ensures comparability of the different parameters, which might have completely different units and dimensions.

Firstly, the design plan starts with a centre point, where all input factors are at their normalized mean value. In the case of a real experiment, this parameter combination is tested multiple times to estimate the standard deviation of the resulting data. When k denotes the number of input parameters, the design plan consists of $2k$ axial points, that is those points where one input parameter assumes its minimum or maximum, while all others are at their centre value. Finally, one adds 2^k factorial points, that are characterized by the fact that all input factors are not at their centre value but have the same normalized distance to the centre of the parameter space as the axial points. Thereby, the non-linear interaction of parameters will appear in the data.

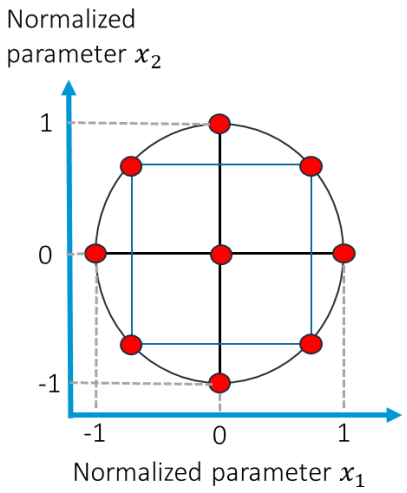

Figure 23 Central composite design for two input factors x_1 and x_2, which are normalized to their respective minimum and maximum values.

In the next step, one can then use any polynomial or other meta-functions (like neural networks) to fit the generated data. Nevertheless, the default fitting function is often the simplest form of a non-linear interaction, a general quadratic equation. If input parameters are denoted as x_i, b stands for the model parameters, ϵ_{res} the residual error and y denotes the output parameter of interest, the quadratic equation reads

$$y = b_0 + \sum_{i=1}^{k} b_i x_i + \sum_{i=1}^{k} b_{ii} {x_i}^2 + \sum_{\substack{i=1 \\ i<j}}^{k} \sum_{j=1}^{k} b_{ij} x_i x_j + \epsilon_{res} \tag{182}$$

For the fitting process, the root mean squared values of the residual error is minimized by some optimization algorithm. In this thesis, the open-source statistics software called “R” with the response surface package “rsm” is used for the DOE study and all fitting calculations.

Finally, the fitted model can be analysed, for instance by graphical methods that show the contour plot of the fitted function over the parameter space. Thereby, one can identify extrema of the fitting function, which predicts a corresponding maximum or minimum value of the real systems’ response at (or around) this configuration of input factors.

As already stated, the method can be applied in any context and usually the data needed for the RSM calculation is provided by actual experiments and measurements. However, the same method can also be applied to a digital process or mathematical model too complicated to predict intuitively. In this thesis, the DOE method is applied to the CFD model of the roll-to-roll coating process of TFC membranes. In this case, the input factors are the process parameters, which are not known precisely, or which may fluctuate during the process. Thus, in this context the term ‘experiment’ refers to a simulation run with the given set of parameters, while the output parameter of interest is the coated membrane thickness.

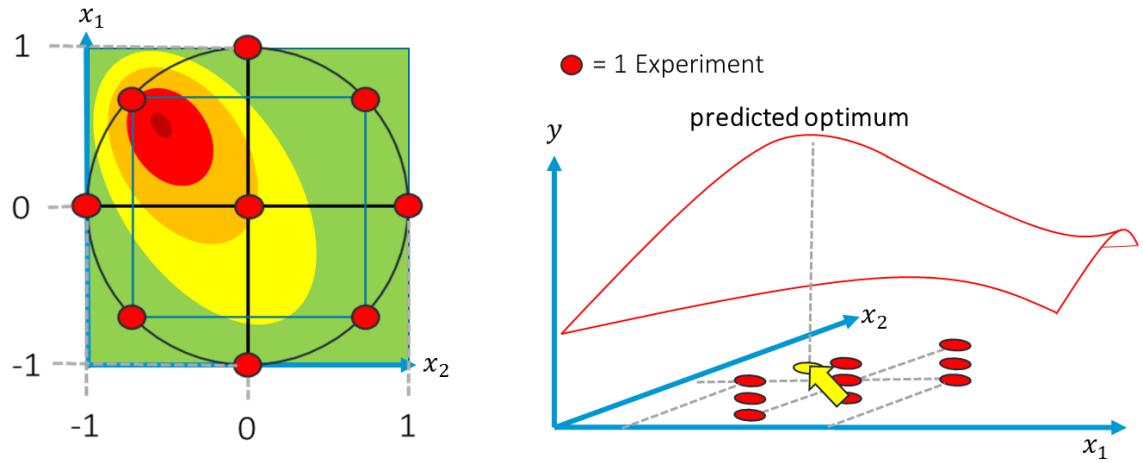

Figure 24 Having measured the resulting output parameter y for all design points in the CCD, a quadratic model is fitted to obtain an approximate functional relationship between the input parameters x_i and output parameter y. The fitted functional relationship can be visualized as a contour plot (left side) or three dimensional graph (right side). Analysing the fitted function yields a prediced maximum output (often the desired optimum) for a specific input configuration.

2.9 Basics of confocal laser measurements

To measure the thickness of a transparent material or liquid film, one can employ a confocal laser displacement sensor (as referred to in section 3.6). The principle of this measurement method is shortly outlined in this section.

The confocal laser device mainly consists of two components: the optical unit and the sensor unit. Starting with a white light source going through a pinhole, thereby creating a point source, the light is then focused by a refracting lens. The utilized lens shows chromatic aberration, meaning the refractive index changes with the wavelength. This leads to a range of individual focal points, one for each wavelength. If a reflecting surface happens to be exactly on the focal point of a specific wavelength, the reflection of the light with this wavelength is maximal. Going back through the lens, the light is then sent to a spectrometer via a beam splitter. If the position of the focal points is known exactly for each wavelength, one can then analyse the intensity of the reflected light over the wavelength and find the reflection peak for a certain wavelength. The distance of the reflecting surface is then equal to the focal point of this wavelength.

If the sensor can detect the small difference between two peaks of reflected light, it is then also possible to defer the thickness of a transparent layer on top of the reflecting surface. Of course, this assumes, that the transparent layer transmits and reflects some of the incident light at the same time. If all the relevant wavelengths are completely transmitted or reflected by the otherwise transparent layer, this would jeopardize the technique. However, in practical scenarios this is unlikely to be the case. Moreover, the light going through the transparent layer is refracted according to the refractive index of the transparent medium, which must be taken into account when calculating the layer thickness. This is done automatically by the control software, but the refractive index must be provided by the user.

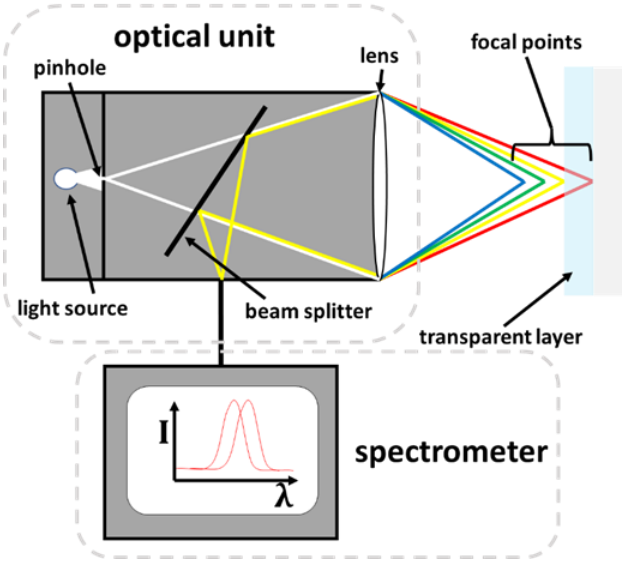

Figure 25 Conceptual architecture of a confocal displacement sensor. Coming from a light source, a pinhole essentially creates a point source of light beams going through the optical unit. Going through the lens, the light beams have different focus points depending on their wavelength. Coming into contact with a reflecting surface, the reflected light goes back through the lens and a beam splitter sends the light to a spectrometer, where the Intensity I is measured over the range of wavelengths λ. When the focus point of a particular wavelength exactly coincides with the reflecting surface, the reflected light intenisty is at maximum for that wavelength. If the focus points are known, the intensity peak of reflected light can be used to determine the distance of one or more reflecting surfaces.

3 Materials and methods

The following chapter describes the materials and methods used experimentally to produce TFC membranes and the specifications used to implement the corresponding CFD model of the coating process. As a disclaimer, it must be noted that not all steps of the experimental procedures were conducted by the author alone. The implementation of the LabVIEW software was done by a colleague in the Process Engineering group, while the preparation and analysis of electron microscopy samples were done by experts from the Microscopy group of the Institute. The fabrication of TFC membranes was always done in close collaboration with a long-experienced colleague working mainly on the complete membrane fabrication process. Zero-shear viscosities of polymer solution samples and density measurements were also often analysed by others, e.g. as part of routine analyses conducted by the Material Characterization group, since those measurements were usually run in parallel using material samples taken directly during a membrane coating experiment. Moreover, instrumentation and handling of the shear-rate dependent or oscillatory viscosity measurements were also done in this group. The primary contributions of the author were the theoretical modelling and literature review to plan experiments, preparing material samples, choosing, helping, and sometimes overseeing with useful viscosity and microscopy measurements, setting up and running the confocal laser and infrared device during membrane coating, conducting the contact angle measurements, and analysing both the experimental and numerical results to further govern the next steps of the study. Parts of this section are similar to the methods section in the publications by the author (Brennecke et al., 2021, 2024).

3.1 Membrane fabrication procedure

The TFC membranes analysed in this thesis were all produced in-house at Helmholtz-Zentrum Hereon, as also described in former publications by the group and the author (Brennecke et al., 2021, 2024; Yave et al., 2010). The fabrication of TFC membranes is a multi-step process starting with a commercially obtained non-woven fabric made of polyester. On top of that, a support layer of polyacrylonitrile (PAN) is casted by means of phase inversion. A more detailed description of this process step can be found in the literature (Scharnagl & Buschatz, 2001). The resulting PAN support layer has a thickness of around 50 µm, while the total membrane thickness (support and non-woven) is usually around 200 µm. Because of fabrication tolerances of the non-woven base material, a deviation of a few micrometres is possible.

The subsequent thin films consist of a PDMS based gutter- and protective layer, as well as the selective layer in between. The PDMS is purchased form the company Wacker (München, Germany) as part of their Dehesive® 944 silicone coating packages. The PDMS silicone is then dissolved in isooctane.

For the selective layer, the polymer is chosen according to the desired separation task. Membranes made for the separation of CO_2 from exhaust gases are mostly based on a MBCP with repeating units of PEOT and PBT, which is commercially available as PolyActive™ and is purchased from the company PolyVation (Groningen, Netherlands). The standard in-house production of TFC membranes with PolyActive™ uses a solvent mixture of three components (SMC 1-3) in a weight ratio of 2:1:1. All components have a similar molecular weight of approximately 100 g/mol and also similar surface tension of 25-29 mN/m. However, one component (SMC 3) is more volatile with an approximately 10x equilibrium vapor pressure.

Both coating processes (PDMS and PolyActive™) were done with the same roller-coating device, as depicted schematically in Figure 26 and further described in the literature (Brinkmann et al., 2017; Yave et al., 2010). To recapitulate the process briefly, the polymer solution for the respective coating step is fed from a feed reservoir into a basin where it is transferred to the membrane via a rotating applicator roll. A meniscus is formed in the gap between applicator roll and membrane roll and the fluid mechanical forces in this meniscus region primarily determine the resulting transferred film thickness on the membrane. As in the gap region the rotation of the rolls is in the opposite directions, this is also called reverse roll-coating. The volumetric inflow rate of the feed is manually adjusted, such that the overflow at both axial ends of the basin is relatively small. In the case of PDMS coatings, the overflow is usually discarded, while the overflow in PolyActive™ coatings is fed back into the reservoir, as this polymer is more expensive and should not be wasted.

During the roller coating process, the solvent will start to evaporate already but for the most part the remaining solvent is removed by drying the wetted membrane in an oven that immediately follows the coating step. As the solvent evaporates, the remaining polymer forms a dense film on the membrane. In the case of PDMS the polymer chains are also bound covalently by a catalysed crosslinking reaction. Typically, the flat-sheet membrane rolls that are produced with this setup have a width of 0.3 m and a length of 200 m. For larger membranes the roll width can be doubled to 0.6 m.

3.2 Deferring the coating thickness form mass loss measurements

During membrane coating, the mass loss of the polymer feed solution is measured online as a function of time. A data acquisition and control software written in LabVIEW is employed for this task. Since the overflow of the basin is fed back to a reservoir on the same balance as the feed, the measured mass loss represents the sum of solvent evaporation in the coating apparatus and the transferred fluid.

To determine the evaporative mass loss $\dot{m}_e$, a series of measurements was conducted with only the applicator roll spinning in the solution basin, while no membrane roll was present. This mass loss then accounts for the evaporation only and the calculated average evaporative mass loss from those measurements was subtracted from the total mass loss measurements during membrane coating to obtain the transferred mass flow. A scheme of the experimental setup is depicted in Figure 26. The result of the mass loss measurement is a series of data points that were fitted with a linear regression model in Microsoft Excel™ to yield a time-averaged mass loss rate in terms of gram per second. The thickness can then be estimated from the mass of polymer left on the membrane per surface area after evaporation of the solvent, which is then divided by the polymer density.

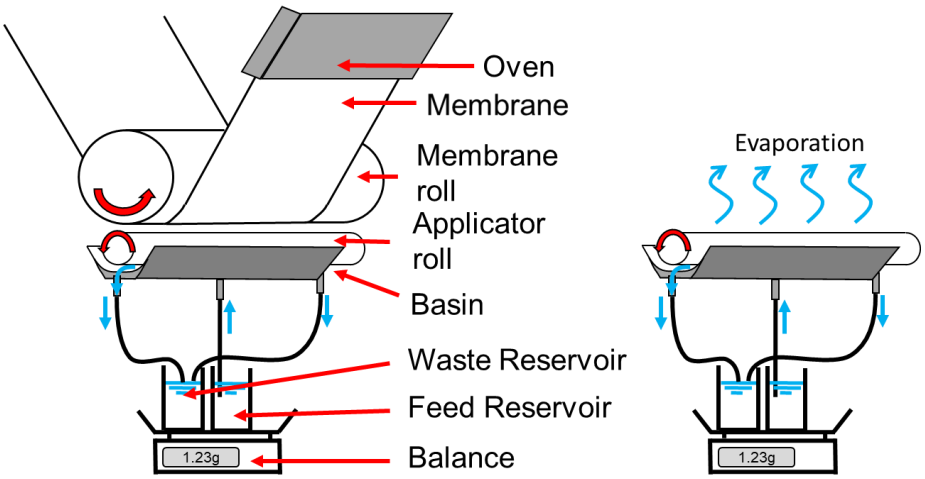

Figure 26 Scheme of the roll-to-roll coating device used for the last step in TFC membrane production with integrated mass loss measurement of the feed solution (left side). For evaporative mass loss measurements (right side), the membrane s not present and the loss of mass on the balance is only due to evaporation. For coating mass loss, the mass loss during the coating procedure is measured and the evaporative mass loss subtracted.

3.3 Measuring the coating thickness in cross-sectional SEM images

Additionally, samples of the coated membrane were taken and the thickness of the selective or protective layer was determined with a scanning electron microscope (SEM) (Merlin, Carl Zeiss Microscopy GmbH, Oberkochen, Germany). For the sample preparation, the membrane surface was coated with a thin layer of platinum (approximately 2 nm). This step was followed by fixing a self-adhesive copper tape on top to protect the surface. The cross sections of the membranes were prepared by argon ion milling in a PECS II (AMETEK GmbH, München, Germany). Finally, to eliminate charging effects during SEM investigations, the cross sections were coated with a 4 nm thick carbon layer. The section of the membrane sample was randomly chosen. For each sample, the top layer thickness was determined ten times in subsequent 100 µm long frames.

3.4 Measuring viscosity and viscoelasticity of polymer solutions

3.4.1 *Zero-shear viscosity*

For measuring the zero-shear viscosity, a Lovis 2000M/ME (Anton Paar GmbH, Graz, Austria) falling ball viscometer was used. In this device, a capillary is filled with the liquid sample and a small steel ball with (diameter of 1.59 mm and density 7.66 g/cm³) is released from the top, sinking down through the liquid due to the force of gravity. As it sinks through the liquid, the ball experiences a drag force that is expressed by Stokes law (see equation (67) in Section 2.1.3) and at equilibrium and the ball assumes its terminal velocity. By measuring the terminal velocity one can thus defer the viscosity. As the density difference between ball and liquid is needed, the density of the liquid sample is also measured in a coupled densitometer (DMA4100M, Anton Paar GmbH, Graz, Austria).

This measurement was done for all PDMS and PolyActive™ solutions at different polymer concentrations. For PDMS in isooctane, concentrations of 0.5, 1, 2 and 3 wt% were measured. For

PolyActive™, concentrations above 1.5 wt% are not feasible as a higher polymer content will precipitate in the solvent over time. Hence, only concentrations of 0.5, 0.75, 1 and 1.5 wt% were measured. The pure solvent was also measured in both cases. All measurements were done at room temperature (20°C).

Based on comparisons between the Lovis 2000M/ME and zero-shear measurements from the rotational rheometer MCR 502 (see section 3.4.2), a measurement error of 10% was estimated for all zero-shear measurements. For the density measurement, the manufacturer gives an accuracy of 0.0001 g/cm³ under ideal conditions. However, based on the observed variation in repeated measurements and the fact, that the assumed polymer concentration in the solution might deviate from the theoretical value due to loss of solvent over time (due to evaporation), we assume the error to be at least 0.0005 g/cm³. These errors are the basis for the error bars in the corresponding figures in the Appendix (see section 8.1).

3.4.2 Shear rate dependent and viscoelastic measurements

To test for non-Newtonian effects, samples of PolyActive™ solution at concentrations of 0.5, 1 and 1.5 wt%, as well as the pure solvent mixture without polymer, were tested in a rotational rheometer MCR 502 (Anton Paar GmbH, Graz, Austria). All measurements were performed at room temperature (20°C) and standard pressure. For shear-rate dependence, the torque was measured for a range of constant shear rates. To ensure that evaporation of the solvent during the measurement had no effect on the measured viscosity, the experiment was repeated with the measurement program starting at low shear rates in one case and with high shear rates in the other. For viscoelastic measurements, the same device can be utilized. Here the rotating cylinder operates in an oscillatory mode with a maximal strain amplitude of 10% and a frequency sweep was carried out for the 1.5 wt% PolyActive™.

3.5 Surface activity of polymer solution via contact angle measurements

For contact angle measurements, a DSA 100 (Krüss GmbH, Hamburg, Germany) was used together with the corresponding image analysis software Drop Shape Analyzer. Sample drops of 3 µl were put on a membrane substrate (non-woven fabric + PAN support + PDMS based gutter layer) which was fixed on a glass slide and the software method ‘Tangent-1’ was used for contact angle computation, using manual baseline adjustment. The procedure was carried out for the pure solvent mixture (SMC 1-3) and solvent plus PolyActive™ with a concentration of 1 wt% and repeated three times each. Via manual adjustment of the platform position, it was ensured that the drop was placed at a previously unused spot to avoid contamination between measurements. For comparison, the same procedure was repeated using a hydrophobic Teflon strip as surface.

3.6 Measuring the film thickness on the roll via confocal laser measurements

To gain further information on the film thicknesses on the applicator roll during the coating process, a confocal laser sensor was employed. The used device is the CL-PT010 displacement sensor produced and sold by the company KEYENCE (Keyence Deutschland GmbH, Neu-Isenburg, Deutschland). The

sensor was placed manually in front or behind the roller coating setup to measure film thickness H_1 or H_3, respectively (see Figure 27 for clarification).

For a reliable measurement of the film thickness, the altitude and azimuth of the sensor's optical unit with respect to the applicator roll must be 90 degrees. Otherwise, the perceived film thickness as it is measured by the sensor will be increased. While the altitude of the sensor can be adjusted by means of a spirit level, the correct azimuth can only be approximated by measuring the distance of the sensor mounting on the basin at both sides via a spacer.

As discussed in the theoretical background, the signal from the spectrometer is send to a software provided by the producer, which processes the raw data and allows for refractive index correction. As the solvents used for both PDMS and PolyActive™ solutions all had a similar refractive index of approximately 1.4, this value was set for all confocal laser measurements in this thesis.

3.7 Temperature profiles during coating via infrared images

To measure the temperature distribution in the liquid films of roll-to-roll device during the coating process, an infrared camera (FLIR i60, InfrarotTec Systems, Ranstadt, Germany) was utilized. The infrared camera uses the fact that all bodies emit light, and the emission power is directly linked to the body's surface temperature (see section 2.5.3). To defer the temperature, one must know the emissivity of the surface. For liquids, the emissivity is usually relatively high around 0.9-0.95, and a value of 0.95 was set for all temperature measurements. For other surfaces, especially metallic ones, the emissivity is typically much lower, as these materials reflect a lot of the incident light. Thus, measurements on metallic surfaces cannot be trusted, as they must be expected to be overestimate the actual temperature.

3.8 Numerical model of the coating process

3.8.1 *Two-dimensional geometry of the roll-to-roll coating device*

In order to be computationally feasible, the CFD model of the coating process needed to be simplified to a two-dimensional model, thereby ignoring any gradients along the applicator roll axis. This is not completely realistic, as in reality the basin containing the polymer solution has a central feed inlet and a free overflow at the sides. However, since there was no big change in measured viscosity and density when comparing the stock solution and the liquid leaving the basin at the overflow, no substantial concentration gradient along the axis of the applicator roll is expected. Figure 27 schematically depicts the two-dimensional model of the coating device.

The applicator roll speed is v_1 while the membrane roll speed is v_2. Thick lines in the geometry represent walls of the rolls and basin, while the thin lines are the open boundaries of the system. The dashed blue line represents the liquid-gas interface.

The incoming feed flow is $\dot{m}_{in}$, the evaporation mass flow is $\dot{m}_e$, the mass transferred to the membrane roll is $\dot{m}_m$ and the flow of the remaining mass on the applicator roll is $\dot{m}_a$. Subtracting the evaporation, transferred and remaining mass flows from the feed flow yields the outflow $\dot{m}_{out}$, which was estimated to be 0.1 $\frac{\mathrm{g}}{\mathrm{s}}$. It should be noted that a precise estimation of the overflow rate is unfeasible

in the current setup, as it depends on the volumetric flow of the feed pump, which is adjusted manually and will also fluctuate slightly between experiments and during the coating process. However, preliminary simulations yielded no substantial difference in the results when the estimated overflow rate was five time higher or lower, thus an overflow of 0.1 $\frac{\mathrm{g}}{\mathrm{s}}$ was chosen for all further studies.

For clarification, the initial film height H_1 in Figure 27 refers to the thickness of the film when it leaves the dynamic meniscus region. The denoted angle α of 15.8° is used for the estimation of the liquid surface area. The wetted surface is approximated by the following formula, where we use the applicator roll radius r_a (0.0271 m) and the roll width r_w (0.3 m).

$$A_{Surface} = \frac{180\,^\circ + 2 \cdot \alpha}{360\,^\circ} \cdot \pi \cdot 2 \cdot r_a \cdot r_w = 0.03\ m^2 \tag{183}$$

The value for α is known as it follows from the geometry of the roll and basin, which were constructed in-house. Further parameters are the gap height H_0 which as approximated to be 165 μm in the standard case but varied in some simulations (see section 3.9.2). This value was determined by measuring the exact radius of the applicator roll by means of a caliper gauge on several points of the applicator roll, thereby deferring a total gap size of approximately 365 µm (with a standard deviation of 25 µm). Then, the average thickness of the membrane support layer (approximately 200 µm with a standard deviation of approximately 5 µm) was subtracted. The membrane roll has a radius of 29 cm and a standard velocity v_2 of 0.011 m/s (again, changes of v_2 were examined in a parameter study in section 3.9.2), while the applicator roll has a velocity varying between 0.027 m/s and 0.056 m/s. For additional intuition, the scaling of the model is represented by the arrow in the lower left corner of the two-dimensional model in Figure 27.

For comparison, the same two-dimensional model was also set up without the overflow, as depicted in Figure 28. In this setup, the filling height of the liquid in the basin is approximately 1 cm lower (and more accurate in resembling the situation in the real coating basin) and consequently, there is no outflow $\dot{m}_{out}$. All other definitions are exactly analogous.

Note that the two-dimensional schematic geometry and the three-dimensional schematic overview show the same process, but from a different viewpoint. The overview is looking at it from the left, while the two-dimensional blow-up is looking at it from the right, hence the different directions of the velocity-arrows of the rolls.

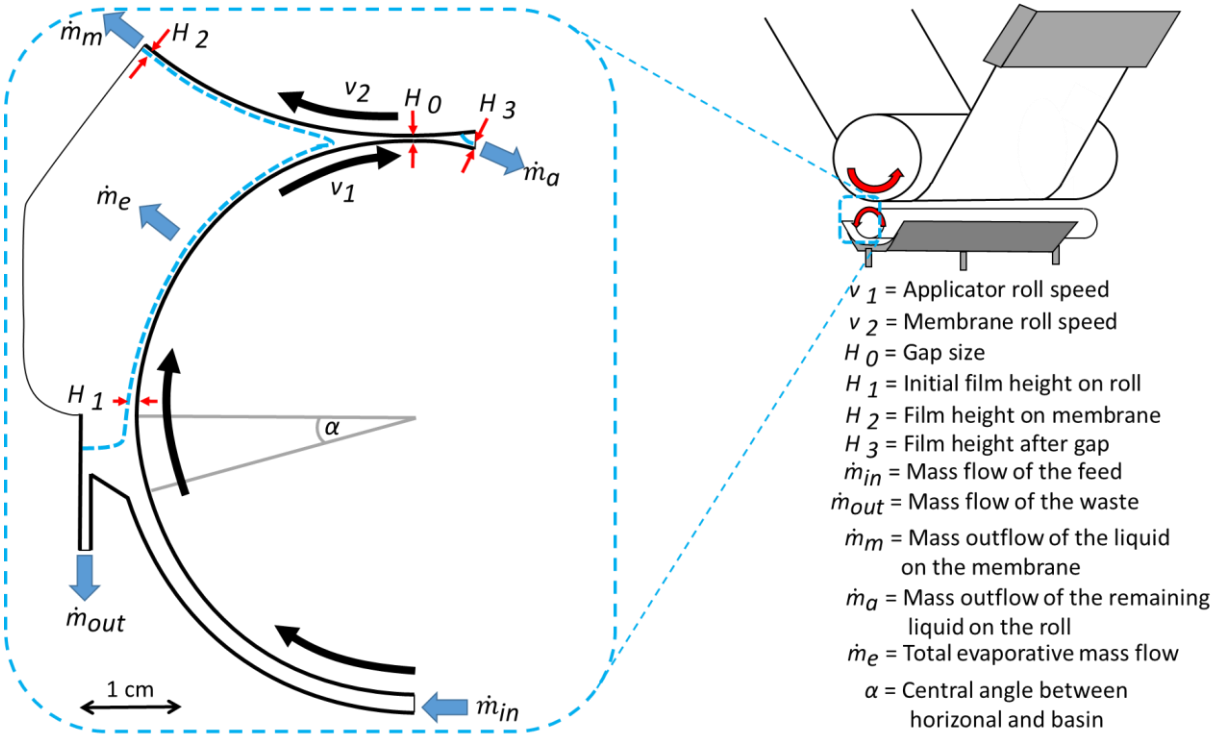

Figure 27 Geometry of the two-dimensional CFD model (left side) which is used to simulate the membrane coating procedure in the roll-to-roll device (schematically depicted on the top right). Only that part of the liquid and air domain is simulated which is needed to compute the coated film thickness on the membrane roll. The model includes an overflow on the left side of the basin. In reality, thie overflow is on both axial ends of the applicator roll and the liquid filling height is at least 1 cm lower.

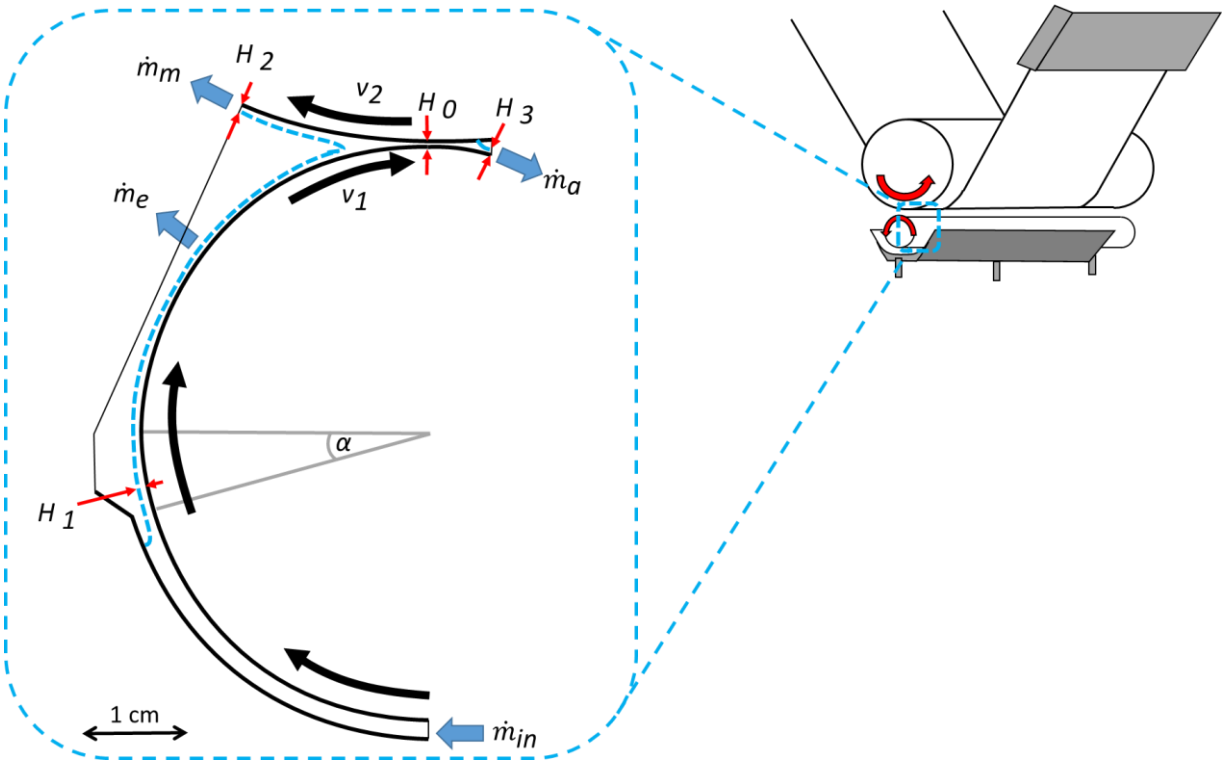

Figure 28 Alternative geometry of the two-dimensional CFD model (left side) which is used to simulate the membrane coating procedure in the roll-to-roll device (schematically depicted on the top right). This model unrealistically excludes an overflow of the polymer solution in the basin but the liquid filling height is approximately 1 cm lower, which is more accurate in terms of the lower meniscus position when compared to the real coating setup.

3.8.2 Basic CFD model of the roll-to-roll coating process

As can be seen in Figure 27, the computational domain consists of a liquid and a gas phase. Since there are no relevant pressure differences or flow velocities in the air domain, both the liquid and gas phase were computed based on the incompressible Navier-Stokes equations, which - for the isothermal basic model - consist of the continuity equation and the momentum balance (see section 2.1.3). Both the density and viscosity values were measured (see shear zero viscosity measurement in section 3.4.1) for each polymer in the respective concentration range of interest. The surface tension was estimated to be that of the solvent, as found in the literature or given by the supplier. In case of PDMS in Isooctane, this was 18.77 mN/m(Isooctane Data Sheet Carl ROTH).

The surface tension was assumed to be that of pure Isooctane for PDMS coating and for the solvent mixture in the case of PolyActive™, a mean surface tension value based on the molar fraction of each component was used as a rough approximation (see equation (184)), which yielded around 28 mN/m.

$$\Pi_{mix} = \sum_{i=1}^{3} \Pi_i x_i \tag{184}$$

Additionally, the distribution of the coating polymer in the solvent is modelled with a convection-diffusion equation (see (65) in section 2.2.1). The diffusion coefficient of the polymer was approximated based on its respective solution viscosity using the Einstein formula with an estimated polymer radius of 17 nm for PDMS (based on intrinsic viscosity estimations from PDMS viscosity measurements) at the respective molecular weight of 70000 Da, as estimated from data given by the PDMS supplier) and 9-10 nm for PolyActive™ (based on the radius of gyration as derived from intrinsic viscosity estimations and on former publications of the research group at Hereon (Yave et al., 2011)). In all isothermal calculations, the liquid is assumed to be at room temperature (293.15 K).

At the interface between gas and liquid, evaporation of the solvent causes an increase of the polymer concentration, thus the material balance has a local source term

$$S = \frac{c}{V_m} \cdot \frac{A_m \cdot \frac{\dot{m}_e}{A_{Surface}}}{\rho_{Solvent}} \tag{185}$$

where $\dot{m}_e$ is the evaporation mass flow based on mass loss measurements (see section 3.2), c is the local polymer concentration, V_m is the local mesh volume and A_m is the local interface area of the mesh element.

The dependence of the viscosity on the polymer concentration is modelled via a quadratic equation, as described for the Huggins equation (see section 2.2.1) that is fitted to experimental values. The density dependence with respect to the polymer concentration was also based on experimental measurements but approximated by a linear equation (see Appendix section 8.1 for the overview of the actual measurement values). The local polymer concentration then determines the local viscosity and density as given in these empirical relations (again, see Appendix section 8.1 for viscosity measurements and fitted equations), thereby coupling the material balance to the Navier-Stokes equation.

For the gas phase, a density and viscosity of air at standard pressure (1 bar) was utilized from the COMSOL™ materials library.

Concerning the boundary conditions, the inflow mass flow was not set to a fixed value but calculated during the simulation. It is a variable that, at each time step, equals the sum of the fixed overflow $\dot{m}_{out}$, the evaporation $\dot{m}_e$, and mass flow of liquid leaving the domain on the applicator roll ($\dot{m}_a$) and on the membrane ($\dot{m}_m$). Effectively, this means that the inflow is constantly adjusted during the computation to ensure that the total amount of liquid in the domain stays constant.

At the outlets where the liquid films H_2 and H_3 are leaving the domain, the boundary condition reads

$$\vec{n} \cdot \tau = 0 \tag{186}$$

As it is common practice in CFD computations to compute pressure P as the difference to a reference pressure (standard atmospheric pressure of 1 bar in this case), this boundary condition effectively states that there is standard pressure and no shear stress at the outlet. The same boundary condition is used for the open boundary of the air domain.

Directly adjacent to the roller wall, the liquid assumes the roll-velocity of v_1 or v_2, respectively (no-slip condition).

Finally, the effective polymer thickness δ on the membrane (after drying in the oven, which is not modelled in this thesis) was estimated by the total amount of polymer dissolved in the liquid film H_2 at the outlet.

$$\delta = \int_0^{H_2} \frac{c \cdot M_{w,polymer}}{\rho_{polymer}} \, dH \tag{187}$$

Combining the mass, momentum and material balance, one obtains the fluid mechanical forces controlling the coating process. The balance of these forces is then used to determine the movement of the gas-liquid interface by using a moving mesh method (see ALE method in section 2.7). In COMSOL Multiphysics™, moving mesh calculations are always transient problems, that start with some initial guess for all dependent variables and that are then computed for a user-specified physical time. Over time, the solution will then converge to a point, where the output parameters (like for instance δ or H_2) of the simulation do not change anymore, thus reaching the sought steady state. Typical physical simulation times needed to reach steady-state were between 10 s and 30 s, depending on the quality of the initial guess.

For further understanding of the coating dynamics, a residence time distribution was computed in some cases. This was done by defining a second convection-diffusion equation with a concentration-like dummy variable c_{RT} representing the residence time. The initial value was set to 0 mol/m³, a source term of 1 mol/(s·m³) was set across the complete liquid domain and the self-diffusivity was approximated to be 10^{-9} m²/s. This implementation creates a concentration distribution of the dummy variable c_{RT} that corresponds directly to the local residence time. The physical effects captured in standard model are schematically depicted in Figure 29.

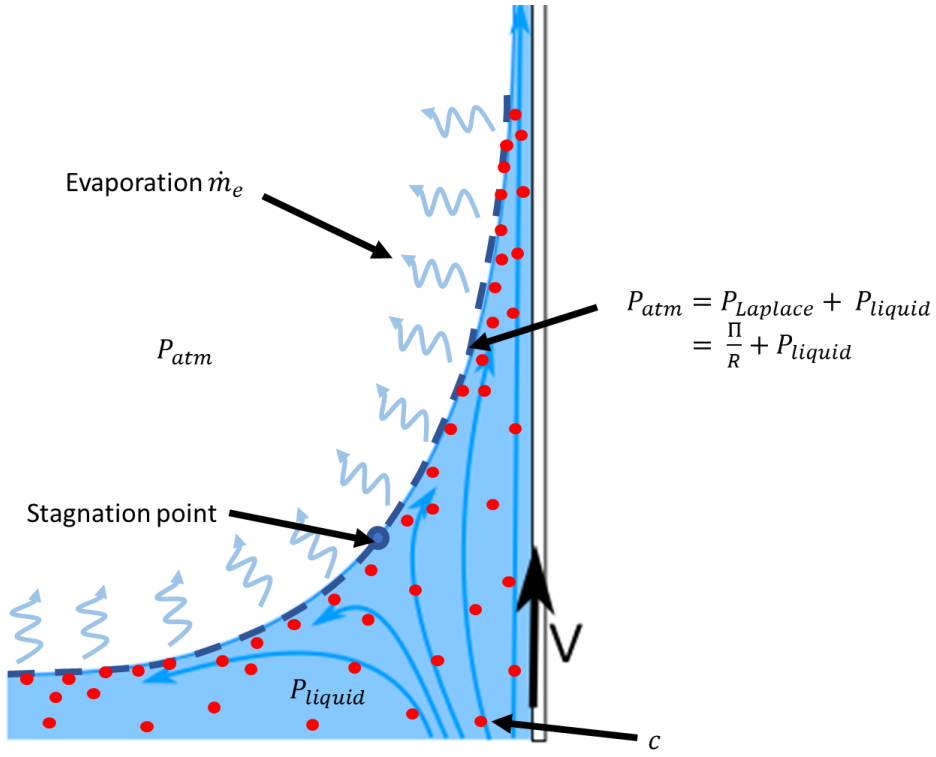

Figure 29 Graphical representation of the effects modelled in the standard CFD model. The coating problem is a free surface flow, where the position of the free surface is not known a-priori and is computed during the simulation via a moving-mesh algorithm. In steady state, a mechanical equilibrium is reached between the inertial forces of the liquid, which is dragged by the moving wall, and the ambient air pressure plus Laplace pressure, arising from the surface tension ∏ of the liquid. This produces a meniscus with a curvature characterized by a radius R. At the interface, evaporation of the solvent leads to the enrichment of polymer concentration c (indicated by the red dots), which influences the local density and viscosity, as determined by empirical equations that were fitted to experimental data.

3.8.3 Extensions of the basic CFD model to capture additional complexities

Extending the CFD model with the Marangoni effect

The standard model assumes a constant surface tension based on the value found for the respective solvent or solvent-mixture. As explained in section 2.3.2, this simplified assumption may not be valid. Since PolyActive™ is an amphiphilic MBCP, it might behave as a surfactant, thus altering the surface tension depending on the local surface concentration of the polymer. To test this hypothesis, the mass balance of a soluble surfactant (see equation (84) in section 2.1.4) was added to the model. Literature data of PMPS/PEO copolymers showed a strong effect of about 5-6 mN/m difference in surface tension at a surface concentration of around $3.6 \cdot 10^{-7}$ mol/m² (Milling et al., 2000), which is better captured by the Volmer isotherm (compare Figure A 23 and Figure A 24 in the Appendix). The relationship between surface concentration and surface tension in the CFD model was hence computed using this model (see equation (148) in section 2.3.2).

Based on the experimental findings for similar sized block copolymers (Rikiyama et al., 2018), the interfacial area of the polymer was assumed to be 2 nm² and the theoretical maximum surface concentration $c_{s,\infty}$ is thus

$$c_{s,\infty} = \left(\frac{1}{2\ nm}\right)^2 \cdot {N_A}^{-1} \approx 4.2 \cdot 10^{-7} \frac{mol}{m^2} \tag{188}$$

The kinetic parameters k_a and k_d are not known and therefore varied in a parameter study. While the kinetic parameter k_a was changed explicitly, the parameter k_d was changed implicitly (for reasons of better interpretability) by defining a relative surface coverage at equilibrium

$$K_c = \frac{c_s}{c_{s,\infty}} \tag{189}$$

For the surface diffusivity, an estimated value of 10^{-10} m²/s (Li et al., 2020) was chosen as a constant, since the surface diffusivity of a macromolecule is expected to be small and relatively negligible for this problem.

As the adsorption of polymeric surfactant depends on the local volumetric concentration of the dissolved polymer, the surfactant mass balance is coupled to the material balance of the polymer in the bulk by adding a boundary condition to the corresponding convection-diffusion equation at the interface

$$\frac{\partial c}{\partial t} + \ (\nabla \cdot \mathrm{c}) \cdot \vec{v} = D\nabla^2 c - \left(k_a c\left(c_{s,\infty} - c_s\right) - k_d c_s \right) \tag{190}$$

However, this surface-to-bulk coupling was omitted in most cases to simplify the problem, as will be discussed later. Furthermore, the additional concentration effect due to solvent evaporation at the interface was also ignored in the Marangoni model.

As a surfactant mass balance is not readily implemented in the physics modules in COMSOL Multiphysics™, the corresponding PDE had to be added manually via the 'general Mathematics module' [1]as a PDE on the air/liquid boundary. The features of the Marangoni model are schematically depicted in Figure 61 in the discussion of the results (section 5.2.1).

Extending the CFD model with a FENE-P viscoelastic model

To simulate the effect that a viscoelastic polymer solution would have on the coating process, a FENE-P model (see section 2.2.4) was implemented for the liquid phase. For the solvent viscosity η_s the measured viscosity of the pure solvent mixture was used (0.001 Pa·s). In a range of simulations, the viscous interaction parameter η_p of the polymer was set to be 0.002 Pa·s and 0.003 Pa·s. This estimation was based on the fact, that the polymer plus solvent had a maximum combined viscosity of 2.4 mPa·s (see Appendix section 8.1.2), thus the chosen parameter range should be the upper bound for reasonable viscous interaction between the polymer and the solvent. This was thought of as a

[1] COMSOL™ Multiphysics uses so called Physics modules for the modelling of physical phenomena. For instance, the available CFD module has the Navier-stokes equations for fluid flow already built-in and the user only needs to choose the geometric domain, where the equations should hold, the boundary conditions and the material properties like density and viscosity to simulate the flow. If the user wants to model other phenomena, he can add a general mathematics module, where the governing equations must be provided in the internal COMSOL™/FEM syntax. This capability was already used in the literature to model surfactant dynamics (Pohjoranta & Tenno, 2011).

conservative estimate, i.e. if this viscous interaction yields no substantial effect, there likely is none present. The relaxation time λ was set to be 0.25 ms, 0.5 ms and 1 ms. As with the viscous interaction, the relaxation time in this polymer-solvent system is not known, but literature values of PEO polymers in solution with similar viscosities are on that order of magnitude(Zilz et al., 2014). The extensibility parameter was estimated to be 3 in these simulations. To test the effect of extensibility, this parameter was increased to 10 for that combination of viscosity and relaxation time parameters which yielded the biggest effect on coating thickness. Again, a graphical illustration of the proposed viscoelastic effect is provided in Figure 65 in the discussion of the results (section 5.2.1).

Extending the CFD model with a thermal energy balance

To test the influence of temperature gradients that might arise for the highly volatile SMC 3, the coating of PolyActive™ in in pure SMC 3 was simulated non-isothermally as well. Therefore, the energy balance (see section 2.1.3) was added to the model, but viscous dissipation was ignored. For the heat conductivity, a value of 0.15 W/(m·K) was estimated for the solvent (based on values found in the Dortmund database(Dortmund Data Bank)). The used heat capacity of the solvent was close to 125 J/(mol·K).

For the energy balance one needs to define further boundary conditions: At the inlet, the temperature T_{feed} of the incoming feed solution was either set to be at room temperature or 10K cooler than room temperature (assumed cooling of the feed solution), thereby testing if a cooled feed had any effect on the process.

The temperature at the wall of the applicator roll ($T_{roll\,1}$) was set to be constant and again, both room temperature and 10 K cooling were tested.

At the membrane roll, the non-woven fabric plus PAN layer forms a barrier between the roll and the liquid. Here, the heat exchange with the metallic roll was assumed to be in steady state, such that a linear temperature profile over the coated support membrane determines the temperature T directly at the boundary to the liquid domain. The boundary condition was thus set to be a heat source with the heat flux being calculated as follows

$$\dot{q} = \frac{T_{roll\,2} - T}{\frac{L_1}{k_{heat,1}} + \frac{L_2}{k_{heat,2}}} \tag{191}$$

Here, the temperature $T_{roll\,2}$ of the membrane roll was set to be at room temperature. The parameter L_1 refers to the thickness of the non-woven fabric layer (set to be 160 μm), while L_2 is the thickness of the PAN layer (set to be 30 μm). The respective heat conductivities $k_{heat,1}$ and $k_{heat,2}$ are not known exactly and can only be estimated. For a non-woven fabric, heat conductivity is a complex function of the polymeric material of the fibres, their geometry and volume fraction. Literature values for the effective thermal conductivity polypropylene fabrics are around 0.027 to 0.03 W/(mK) (Siddiqui et al., 2018), whereas values for polyethylene fabrics were reported to be between 0.03 and 0.04 W/(m·K) (Woo et al., 1994), but generally the thermal conductivity is also dependent on the alignment of fibres relative to the heat transport. For a porous PAN support, no literature values could be found but thermal conductivities for PAN base nanofibers are in a similar range of 0.02 to 0.05 W/(m·K) as found for the non-woven fabrics (Bard et al., 2019; Hamadneh et al., 2019). As no useable data was available here, the model was tested across the range of heat conductivities presented above.

The heat loss at the phase interface due to evaporation was based on the molecular enthalpy of vaporization of pure SMC 3 as follows

$$\dot{q} = -1 \cdot \frac{\dot{m}_{evap}}{M_{w,THF}} \cdot h_{evap,THF} \tag{192}$$

where $h_{evap,THF}$ is the enthalpy of vaporization and assumed to be close to 30 kJ/mol.

Using the Eötvös-equation (151) with a critical temperature close to 550K for SMC 3, the local temperature was then coupled to the surface tension. A concise overview of the thermal boundary conditions in the CFD model can be found in Figure 30.

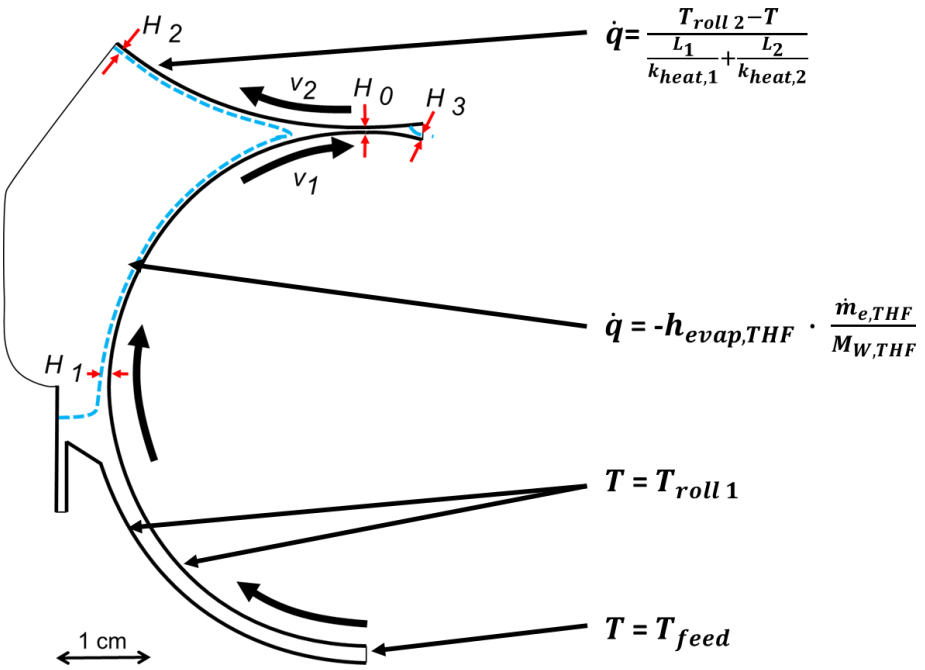

Figure 30 Two-dimensional CFD model of the roll-to-roll coating device with the corresponding thermal boundary conditions used for non-isothermal simulations. At the phase interface, evaporation of the solvent (SMC 3) causes heat loss. The metallic applicator roll has a high heat conductivity and is assumed to have a constant temperature at the wall ($T_{roll\,1}$). At the membrane roll, the non-woven fabric and porous support layer form an additional resistance to the compensating heat flux from the membrane roll.

3.9 Parameter study and model validation

3.9.1 *Mesh independence of the basic CFD model for PDMS*

As a first step, the numerical validity was checked in a mesh-independence study. Here, the resolution parameters in the liquid domain were increased in several steps, yielding a series of meshes with a total of approximately 74000, 124000, 173000,366000 and 710000 triangular elements. For the mesh study, the smallest gap size was analysed in our work, as this should yield highest velocity gradients, thus requiring the smallest element size. Hence, an applicator roll speed of 0.045 m/s was chosen and a gap size of 65 µm. The polymer concentration was set to 1 w%. For a visual representation of the low and high resolution meshes, see Figure 31 in section 4.1.6, where the mesh study is described in detail.

It was also ensured that this resolution is sufficient for a simulation with polymer concentration of 0.5 w%. Additionally, a simulation with 3 w% for a gap size of 100 µm was done, using the same mesh resolution parameters (the smallest gap size is not feasible here, as it causes complete flooding in this case).

Moreover, it was confirmed that two different solver types available in COMSOL™ (called MUMPS and PARDISO) as well as decreasing the tolerance of residual error did not change the results substantially for the stated concentrations and gap size.

To illustrate the utilized meshes in the mesh refinement study, Figure 31 highlights the resulting mesh images in Comsol™ for the upper part of the coating in the meniscus region.

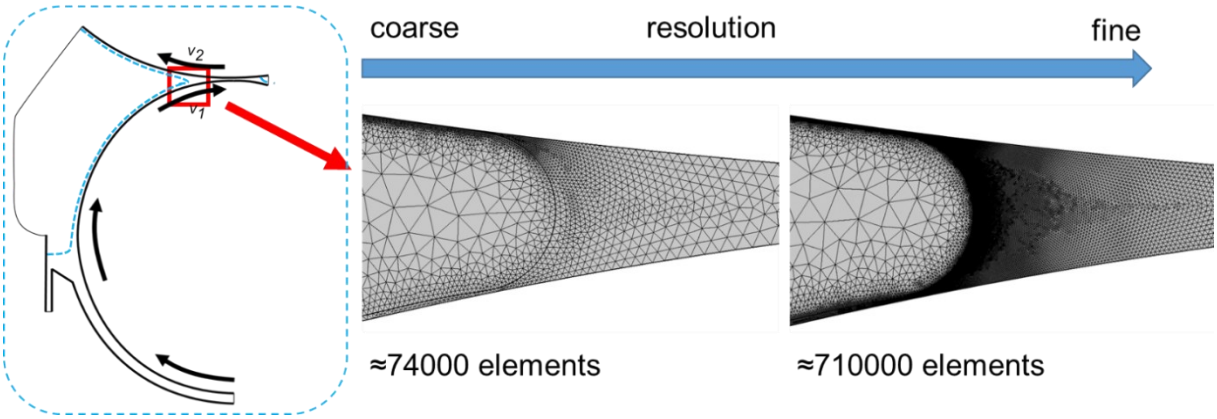

Figure 31 Images of the coarsest and finest mesh used in the PDMS mesh study, showing the excerpt of the gap region.

In contrast to the highest resolution used in the mesh refinement study, Figure 32 and Figure 33 show the mesh resolutions that were necessary to implement the viscoelastic and Marangoni extensions of the CFD model and obtain convergence in their simulations.

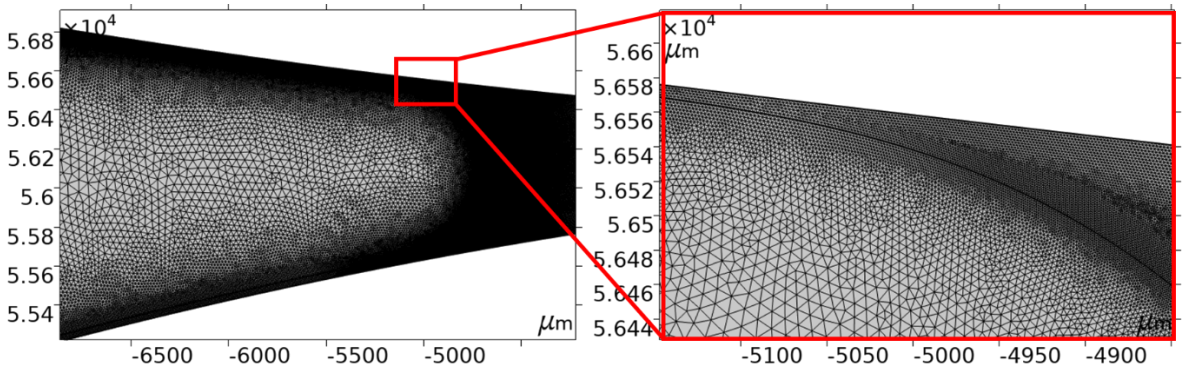

Figure 32 Typical mesh resolution in the gap region for the Marangoni extension of the CFD model. In contrast to the standard CFD model without surface gradients, the resolution along the meniscus curvature is greatly increased, leading to a total of around 1.1 -1.5 million mesh elements.

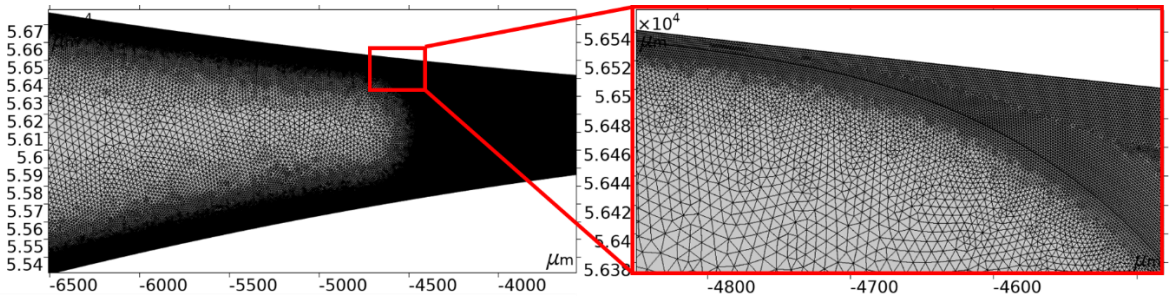

Figure 33 Typical mesh resolution in the gap region for the viscoelastic extension of the CFD model. In contrast to the standard CFD model without surface gradients, the resolution along the meniscus curvature is greatly increased and the growth rate of the elements is very small, leading to a total of around 2-2.2 million mesh elements.

3.9.2 *Validation and process parameter study of the PDMS benchmark*

To check the predictive quality of the model, simulations and coating experiments were done for a combination of polymer concentrations and applicator roll velocities. For concentrations of 0.5, 1, 2 and 3 wt%, the coating was carried out with applicator roll velocities of 0.027, 0.036 and 0.045 m/s, respectively. For a conclusive overview of the conducted experiments, see Table A 1 in the Appendix.

Moreover, a statistical analysis using DOE (see section 2.8 or the R documentation online [25]) was done to deduce a typical variation of polymer thickness given a certain fluctuation or uncertainty of three process parameters, namely: gap size, evaporation rate and membrane roll speed.

For all statistical analysis, the open-source software "R" was used (Lenth, 2009). A CCD plan with three parameters was employed and the results for predicted thicknesses were fitted to a full quadratic response surface model. The design plan was set up with intervals ranging from 135 to 195 µm for the gap size, which was based on the expected standard deviation of 30 µm for the gap size, the membrane roll speed varied between 0.0083 and 0.0133 m/s, based on the typical fluctuations of membrane roll speed measured during the coating procedure. For the evaporation, the flux can only be estimated but based on the experiments presented in section 4.1.1, it will be somewhere between 0.5 and 1 g/(m^2·s), which thus became the interval for the evaporation parameter. Table A 2 in the Appendix shows the full CCD plan. For this study, the polymer concentration was set to be 1 wt% and the applicator roll speed was v_1 =0.045 m/s. The complete study was repeated for a polymer concentration of 2 wt% to see if there is an increase in the relative deviations of polymer thickness.

Additionally, Gaskell et al. also reported the occurrence of a secondary transfer jet in the meniscus region as an effect of very small gap sizes (Gaskell, Innes, et al., 1998). Therefore, the effect of very small gaps going down to a minimum of 65 µm was analysed additionally.

3.9.3 *Parameter study for PolyActive™ coating*

Experimentally, the coating of PolyActive™ was investigated in a variety of combinations. Using the solvent mixture of SMC 1-3, the concentration of PolyActive™ was varied using concentrations of 0.5, 0.75 and 1 wt%. For each concentration, the applicator roll speed was set to 0.045 m/s and 0.032 m/s, respectively to obtain an insight to the general coating thickness in this parameter range. Mass loss measurements (see section 3.2) and cross-sectional SEM images (see section 3.3) were conducted for each parameter combination. Additionally, a possible gradient of coating thickness along the roller axis

was investigated by measuring the thickness at five points along the width of a wider (0.6m) membrane batch.

As explained in section 2.4.1, the boundary conditions at the dynamic contact line in the meniscus of the gap region poses a numerical problem and the choice of contact angle might influence the meniscus shape and force balance in some way. To investigate this possibility, the advancing contact angle value was decreased from 90° down to 75° and 60° in two subsequent simulations that were based on 1 wt% PolyActive™ solution. Since the liquid film thickness and meniscus shape is assumed to be more realistic in the model without overflow, this geometry was used in both cases.

Moreover, the coating thickness of PolyActive™ in pure SMC 3 was investigated by the same means for concentrations of 1 and 3 wt% and applicator roll speeds of 0.056 and 0.034 m/s each.

4 Results

This section will present experimental and numerical results for membrane coatings of PDMS in Isooctane and PolyActive™ in the solvent mixture or pure SMC 3. First, some preliminary analyses are presented, that should help to better understand the physics, justify made assumptions and inform modelling choices on parameters important for the coating procedure. On the experimental site, this includes the rheology of the used polymer-solvent systems, temperature profiles of the liquid in the coating device and contact angle measurements of the PolyActive™ system on different surfaces. On the numerical site, a mesh study for the utilized CFD model is presented to ensure validity of the chosen mesh resolution for the problem at hand. The subsequent results shall demonstrate the achieved coating thicknesses for PDMS and PolyActive™ under different coating conditions and compare them with numerical results from the CFD model. Experimentally, coating thicknesses are determined locally by cross-sectional electron microscopy and in an integrative manner by mass-loss measurements of the coating solution during coating. These can then be compared to CFD simulations of the same system. As will be seen, for the PolyActive™ system large discrepancies between model and experiment are found and three different physical phenomena (namely temperature gradients, viscoelasticity, and surface-tension gradients) are then incorporated into the standard CFD model to elucidate the more likely mechanism responsible for the discrepancy. To gain further insights, confocal Laser measurements of the liquid film thickness on the applicator roll are presented. Parts of the preliminary analyses and the results section on PDMS and PolyActive™ in three component solvent are similar to the corresponding sections in the publications by the author (Brennecke et al., 2021, 2024).

4.1 Preliminary Analyses

In addition to the preliminary analyses presented here, zero-shear viscosity measurements were performed for all utilized polymer-solvent systems and can be found in the Appendix section 8.1 Viscosity and density measurements for the standard model.

4.1.1 Rheological characterization of PolyActive™ in the solvent mixture

Zero-shear measurements

The zero-shear viscosities were analysed using the Huggins equation (91). Based on the estimation of overlap concentration *c* (approximately given by $\frac{M_W}{N_A \cdot V_{gyration}} \approx \frac{41000\frac{g}{mol}}{N_A \frac{4}{3}\pi(10\ nm)^3} \approx 0.015\ \frac{g}{cm^3}$), the 1.5 wt % solution was assumed to be very close to or already in the semi-dilute regime and therefore omitted for fitting of the Huggins equation. However, the zero-shear viscosity at 1.5 wt % was measured and showed a substantial increase of viscosity to 2.4 mPa·s (see Appendix section 8.1.2). Fitting a quadratic regression model to the remaining zero-shear values yields coefficients that allow the calculation of the Huggins parameters of 43 cm³/g for intrinsic viscosity and a Huggins coefficient of 0.83, as shown in Figure 34.

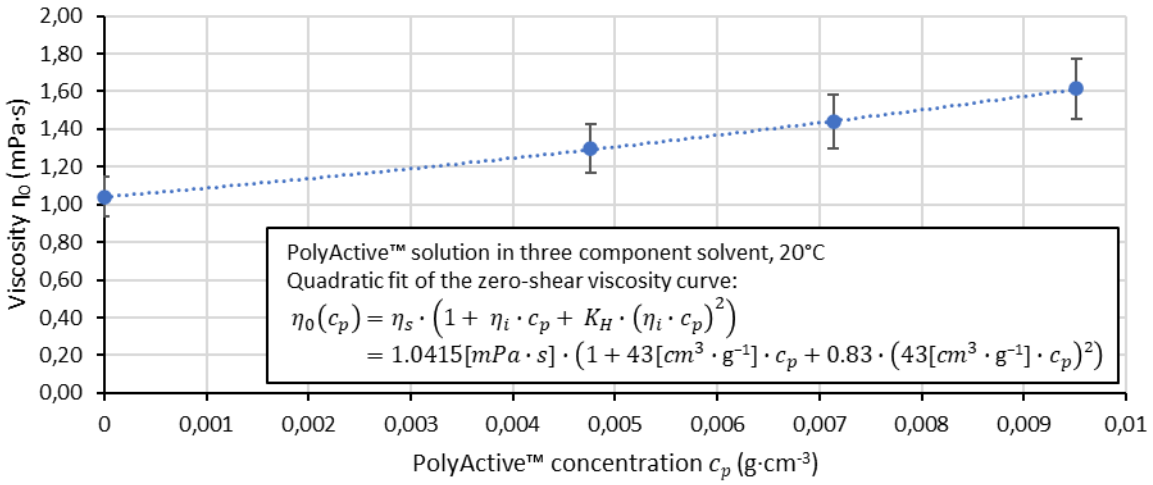

Figure 34 Zero-shear viscosity measurements (at 20°C) of differently concentrated PolyActive™ solutions and the corresponding fitted quadratic polynomial (formula shown in the graph). Based on the fitted parameters, the intrinsic viscosity is 43 (cm³/g) and the Huggins coefficient is 0.83.

Shear rate dependence

As polymer solutions might show non-Newtonian viscosity or viscoelastic behaviour, two series of dynamic viscosity measurements were conducted. Firstly, the shear rate dependence of the viscosity was analysed in a Couette-cell system as described in Section 3.4 for PolyActive™ concentrations between 0.5 and 1.5 wt%. In the shear rate regime between 10 and 100 1/s the measured viscosity stays approximately constant with a very slight increase of viscosity towards higher shear rates for polymer concentrations below 1.5 wt%. At elevated shear rates above 100 1/s, the measured viscosity rises in all cases, but the sudden increase in viscosity happens first for the pure solvent system. The increase is delayed when the polymer concentration increases. For the highest concentration, the viscosity increase is not visible before 200 1/s. Below shear rates of 10 1/s, the measured viscosity decreased abruptly in all samples (data not shown). For a graphical representation of the data, see Figure 35.

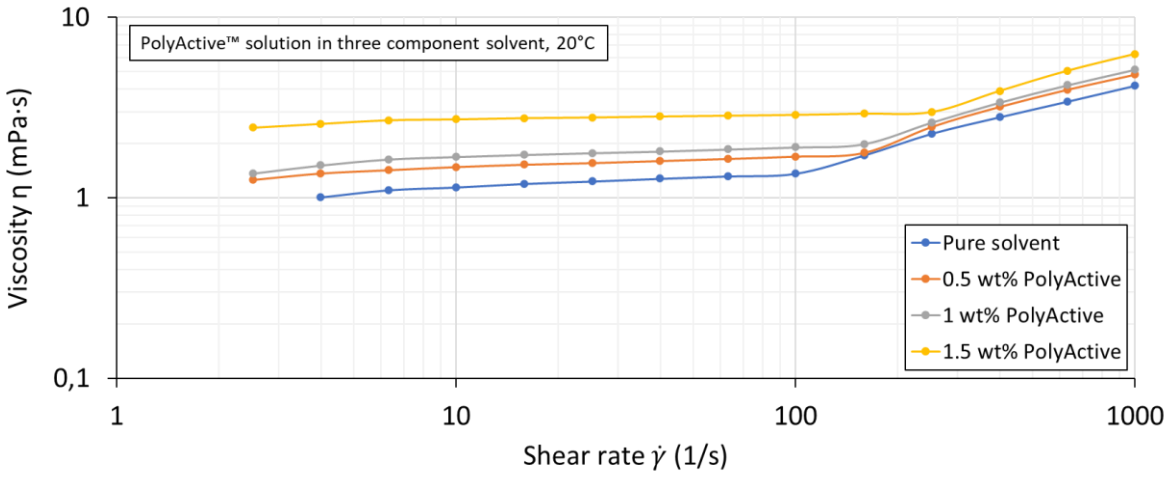

Figure 35 Shear rate dependent viscosity measurement of PolyActive™ solution at concentrations between 0 and 1.5 wt% in the standard solvent mixture of SMC 1-3. Measurements were done at room temperature (20°C).

Viscoelasticity measurement

As described in section 3.4.3, a frequency sweep was conducted for a polymer concentration of 1.5 wt %, thereby measuring the viscous loss modulus $G''$and elastic storage modulus G'. The resulting plot of each modulus over the tested frequency range can be seen in Figure 36. As can be seen, for frequencies above 1 1/s, both moduli show approximate linear increase with frequency and the elastic modulus is about four orders of magnitude smaller than the viscous modulus. Below 1 1/s, both moduli fluctuate above 10^{-4} Pa.

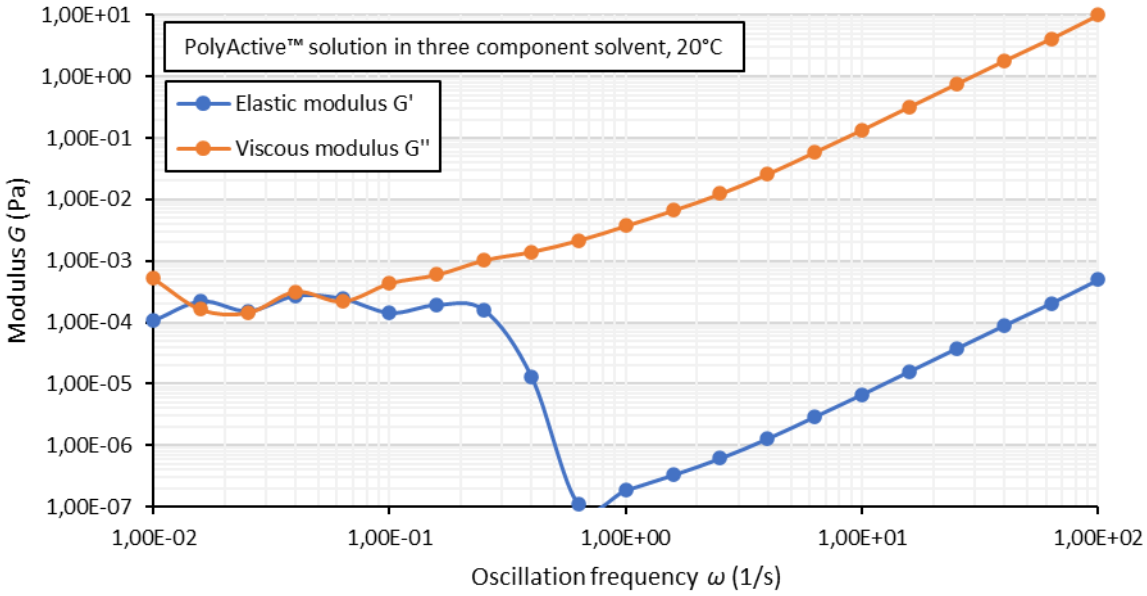

Figure 36 Measurement results for the elastic storage modulus G' and viscous loss modulus G'' over a range of rotation frequencies. The measurement was conducted at room temperature (20 °C) and with 1.5 wt% solution of PolyActive™ in solvent mixture.

4.1.2 Temperature profiles during PDMS coating

To assess the validity of the assumption of isothermal evaporation, temperature profile measurements were carried out for three different applicator roll speeds. The measurements were done during the coating process and, as can be seen in Figure 37, the temperature on the applicator roll is approximately at room temperature and does not go down substantially before the coated membrane is leaving the roll gap. This finding was the same for all roll speeds.

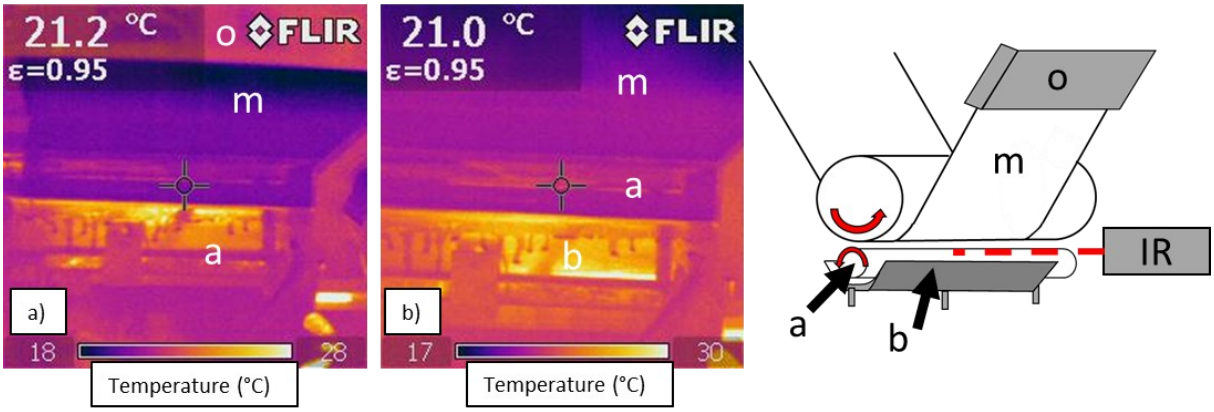

Figure 37 The two images to the left show temperature profiles during coating of PDMS with applicator roll speeds of 0.024 (a) and 0.032 m/s (b). The polymer concentration was 1 wt% in all cases. The part labelled by ´b´ shows the basin, 'a' shows the applicator roll, 'm' shows the membrane after leaving the gap and 'o' is the housing of the oven, as depicted in the scheme to the right. The temperature value on the top left in each picture shows the temperature measurement at the cross lines (for the assumed emissivity ε=0.95), while the colourbar at the bottom shows the temperature range.

4.1.3 Temperature profiles during coating of PolyActive™ in solvent mixture

As for PDMS, the temperature profiles during PolyActive™ coating were measured via infrared camera and showed no substantial cooling of the liquid as long as it is on the applicator roll. When the liquid is transferred to the membrane, the wetted area of the membrane starts to cool down to a minimum of 16°C in the chosen image frame. Figure 38 shows temperature profiles for the coating of 1 wt% PolyActive™ solution and an applicator roll speed of 0.045 m/s.

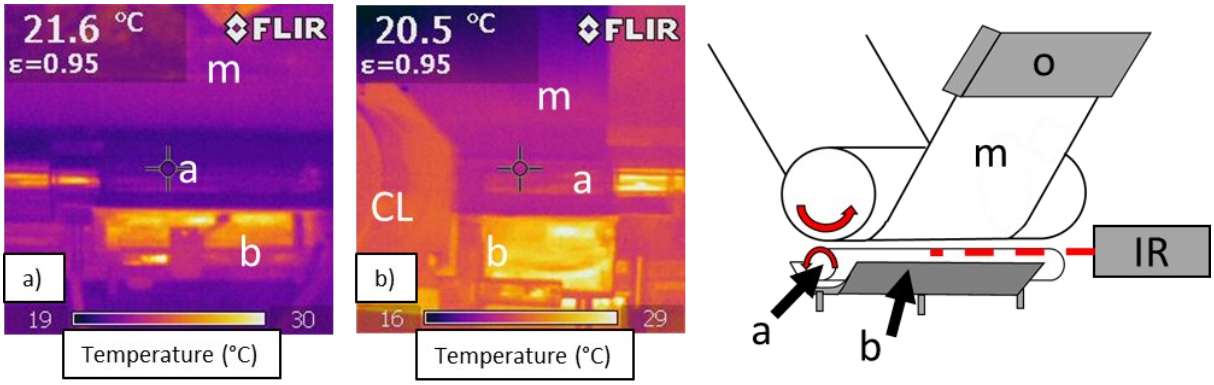

Figure 38 Temperature profile on the applicator roll during the coating of PolyActive™ solution (1 wt%, applicator roll speed 0.045 m/s) as measured via infrared. The two pictures shows the infrared profile of the front side (a) and back (b) of the coating device. The letter a denotes the applicator roll, b the basin, m the (wetted) membrane, CL the confocal laser, IR the infrared camera and o the oven. The temperature value on the top left in each picture shows the temperature measurement at the cross lines (for the assumed emissivity ε=0.95), while the colourbar at the bottom shows the temperature range. The right picture shows a scheme of the coating device and the location of the infrared camera for the back view.

4.1.4 Temperature profiles during coating of PolyActive™ in pure solvent

Temperature profiles were measured during the coating of PolyActive™ in pure SMC 3 via infrared and the resulting images are very similar for both polymer concentration and roll speeds tested. As an example, Figure 39 shows the temperature profile for the 3 wt% solution and a roll speed of 0.056 m/s. In contrast to the profiles presented before, the temperature on the applicator roll is significantly reduced with a value of 14-15 °C being at least 5 degrees colder than room temperature. Similar to aforementioned results, the temperature of the polymer solution goes down to 6°C as soon as the wetted membrane leaves the gap region between the coating rolls.

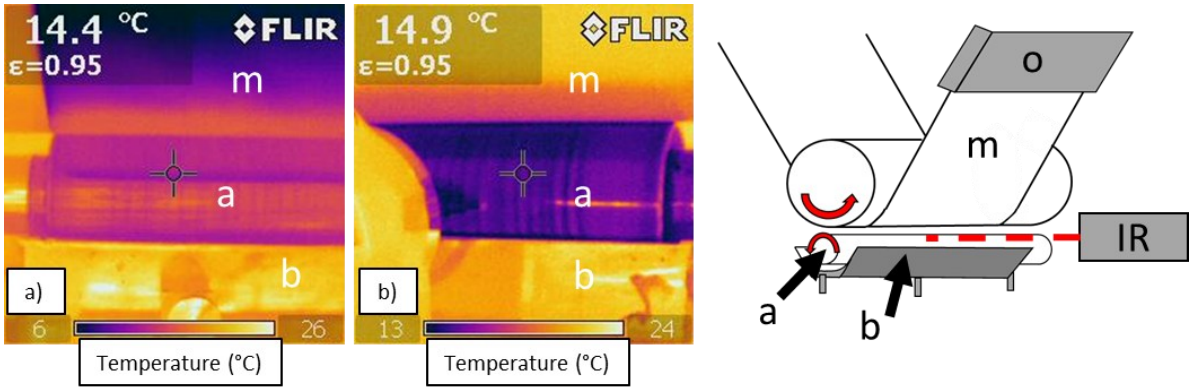

Figure 39 Temperature profile on the applicator roll during the coating of PolyActive™ solution in pure SMC3 (3 wt%, applicator roll speed 0.056 m/s) as measured via infrared. The two pictures on the left show the front side (a) and the back side (b), where the coated membrane enters the gap between the rolls. The letter a denotes the applicator roll, b the basin, m the (wetted) membrane, IR the infrared camera and o the oven. The temperature value on the top left in each picture shows the temperature measurement at the cross lines (for the assumed emissivity ε=0.95), while the colourbar at the bottom shows the temperature range . The right picture shows a scheme of the coating device and the location of the infrared camera for the back view.

4.1.5 Contact angle measurements of PolyActive™ in the solvent mixture

The contact angle measurements of 1.5 wt% PolyActive™ solution in the solvent mixture were performed on the gutter layer surface (which was on top of the non-woven plus PAN support), which exactly corresponds to the coating process of PolyActive™ TFC membranes. The resulting contact angle evolution over time is depicted in Figure 40, where pure solvent mixture and polymer solution is compared. In the mixture, the contact angle starts around 45° and decreases over 60 s towards approximately 30°, while in the pure solvent case it starts closer to 40° and then also goes down to 30°.

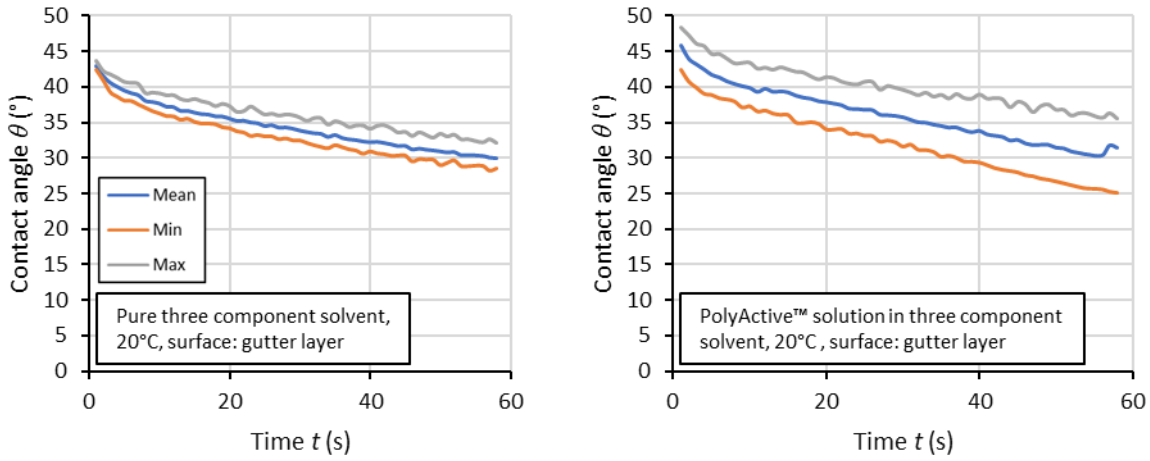

Figure 40 Contact angle measurements of pure solvent and 1.5 wt% PolyActive™ solution on a membrane substrate (non-woven, PAN support and PDMS based gutter layer on top). The graphs show the mean, maximum and minimum contact angle measured in three experiments each.

In contrast to this, Figure 41 shows the contact angle development on a Teflon surface, again for both pure solvent and polymer mixture. Here, a clear difference between both systems can be seen. Again, the beginning contact angle is relatively similar in both cases (around 45° for pure solvent and 50° for polymer solution) but while the contact angle of pure solvent stayed approximately constant, the contact angle for polymer mixture decreased to 20°. Moreover, the solvent droplet shrank very fast, and measurements were stopped after 30 s, while the droplet of polymer solution took much longer to disappear and was still visible after 60 s.

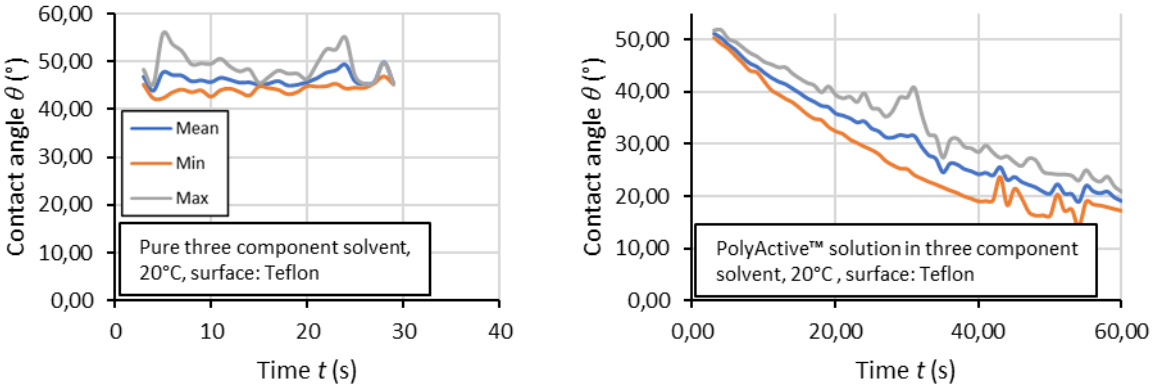

Figure 41 Contact angle measurements of pure solvent and 1.5 wt% PolyActive™ solution on a Teflon surface. The graphs show the mean, maximum and minimum contact angle measured in three experiments each.

In all cases, the contact angle measurements were stopped after 60 s or when the contact angle estimation could not be performed anymore because the droplet became too small. Also, the first 6 seconds of the measurement were omitted because here detection of the drop shape by the software was not reliable. The graphs show the mean, minimum and maximum measured angle at every corresponding time step after initiation across three repeated measurements on different spots of the substrate.

For the first results on the gutter layer surface, results between pure solvent and polymer differ only marginally, the lowest measured contact angle is somewhat smaller and the difference between starting contact angle and final contact angle bigger for the polymer solution. For the more hydrophobic Teflon surface, the results differ widely. The pure solvent shrinks quickly and shows no pinning of the contact line (i.e. constant contact angle), while the polymer solution droplet shows

pinning of the contact line and takes longer to disappear. In the literature, this pinning behaviour of the contact line of an evaporating droplet is often attributed to the presence of surfactants on the droplets surface(Wu et al., 2019). Thus, the results may suggest that the PolyActive™ polymer excerpts surface activity and influences the surface tension (and thus contact angle) of the droplet, which further motivates the implementation of the Marangoni model, where the polymer is treated as a surfactant.

4.1.6 Mesh independence study for the standard CFD model

Firstly, a mesh refinement study demonstrated that the simulation results will not change substantially once the mesh reaches a certain resolution. The results can be seen in Figure 42. While the global output parameters total volume of liquid V_{liquid} in the domain and total evaporation rate $\dot{m}_e$ do not vary with the mesh resolution, the local output parameters like polymer thickness δ (that is after evaporation of the solvent) and fluid film thicknesses H_2 and H_3 deviate strongly at low resolution meshes. When approaching a mesh size of 360000 triangular elements none of the parameters yielded a substantially different result from the highest resolution. Therefore, all simulations presented here for the standard CFD model were done with meshing parameters that correspond to the mesh with approximately 360000 triangular elements, corresponding to a cell-size that varies between 100 and 1 µm, depending on the region of the geometry. The smallest cells are on the coated liquid film on the membrane, where the film height is on the order of 5-10 µm and is thus filled by at least four to five cells.

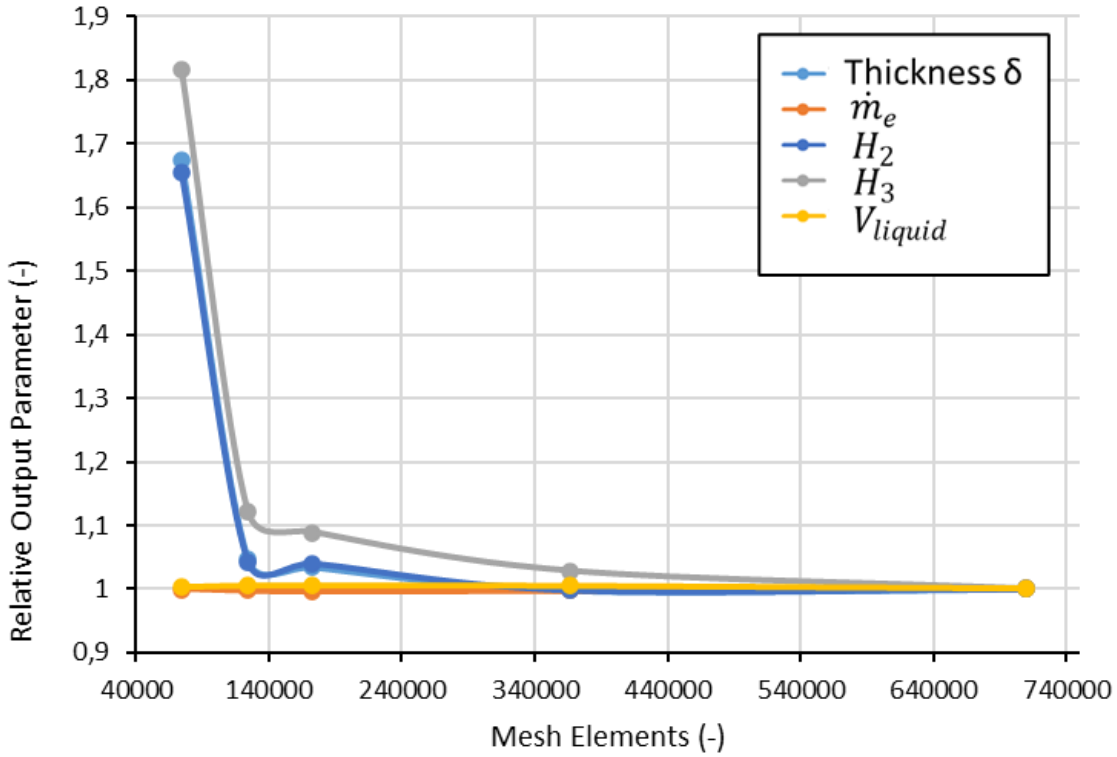

Figure 42 Mesh refinement study of the CFD model for a 1 wt% PDMS solution. The number of elements corresponds to the highly resolved liquid part of the domain, not the air domain. The air domain is also part of the model, but here no high resolution is required and the contribution of the air-domain mesh cells to the overall count is thus omitted. Output parameters H_2 and H_3 refer to the liquid film thickness on the membrane and applicator roll after the gap, respectively. The parameter $\dot{m}_e$ denotes the integrated evaporation rate, V_{liquid} the total volume of liquid in the domain and the parameter δ means the thickness of the polymer on the membrane after evaporation of solvent. All parameters are given as a relative value with respect to the value at the highest resolution.

4.2 Coating of PDMS

4.2.1 Mass loss measurements vs. simulation results

By measuring the mass loss of polymer solution on a rotating applicator roll with no membrane roll present in the coating machine, the average evaporation rate is estimated plus its deviation (see section 3.2). The evaporation rate is determined for three different applicator roll speeds (0.027, 0.036 and 0.045 m/s) and two different concentrations (1 wt% and 3 wt%), but since there is no apparent correlation of evaporative mass loss and roll speed, the mean value of mass loss for all roll speeds is considered and amounts to 0.025 and 0.023 g/s for PDMS concentrations of 1 wt% and 3 wt%, respectively. A bar chart with corresponding standard deviation can be found in Figure 43.

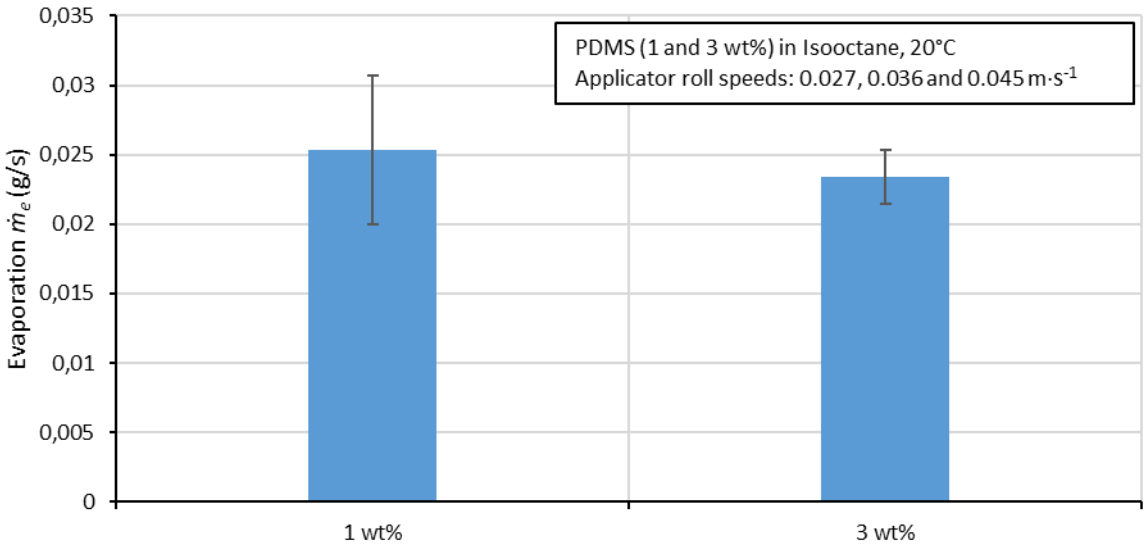

Figure 43 Mass loss of polymer solution (PDMS in Isooctane) on the applicator roll due to evaporation. The mass loss is measured over time and the respective loss rate is determined by means of linear regression. Three roll speeds and two polymer concentrations were analysed, but for the different applicator roll speeds (0.027, 0.036 and 0.045 m/s) only the mean value is given. The experiment was done under room temperature conditions of 20°C.

Since no general trend for the dependence of evaporation rate on concentration or roll speed could be concluded, further simulations were carried out with the overall mean evaporation rate of 0.0244 g/s. With an estimated surface area for the evaporating film of 0.03 m² this yields average evaporation rates of approximately 0.81 g/(m²·s). The standard deviation based on this sample is 0.0037 g/(m²·s).

For the verification of the numerical model, the mass loss was measured during several coating experiments as presented in section 3.9.2. By subtracting the mean evaporation rate of 0.0244 g/s the mass transferred to the membrane roll was deferred. By using the initial weight fraction of polymer in the solution, the mass of polymer per unit area on the membrane was determined. Division by the PDMS density yields the estimated average polymer thickness that is compared to the respective simulation result in Figure 44. The error bars are based on the standard deviation of the evaporation rate creating an uncertainty in the evaporative correction to be subtracted from the total mass loss rate. The comparison shows a reasonably good agreement of the simulation results with the experimentally estimated values for all parameters except for the highest PDMS concentration, where the experimental values are consistently around 20 percent lower than the simulation predictions.

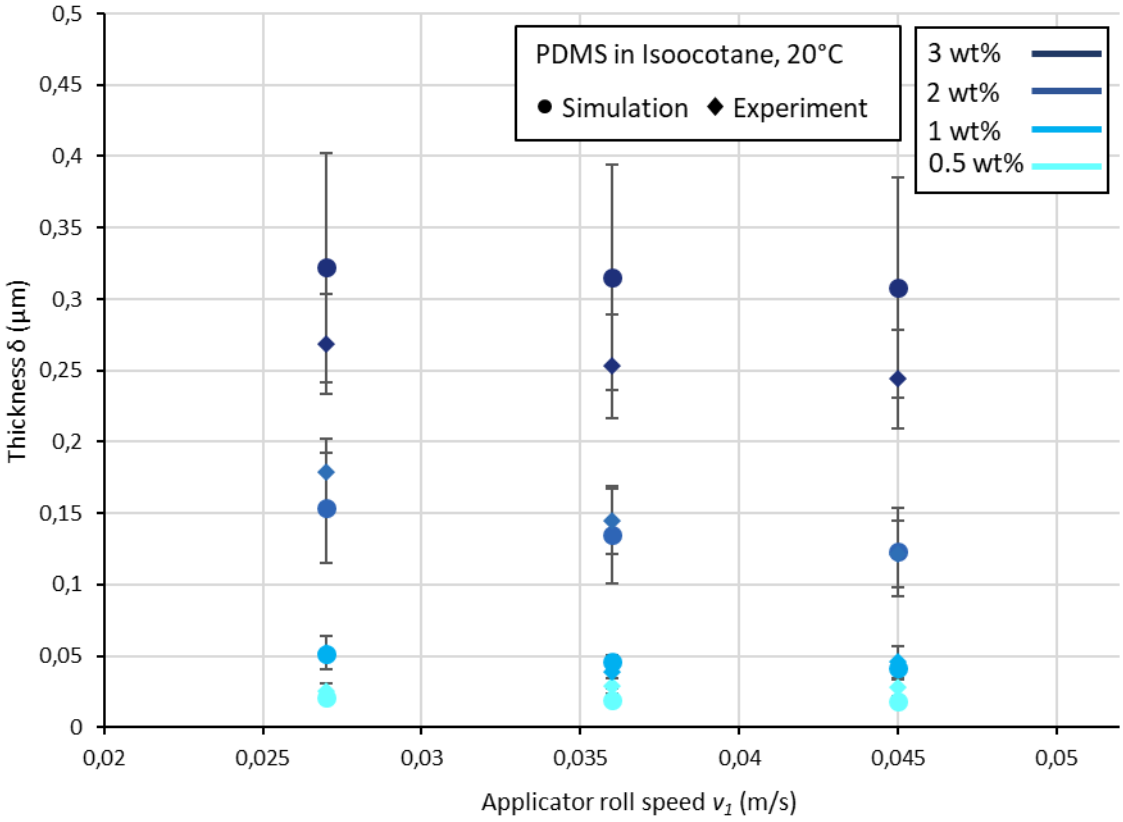

Figure 44 Comparison of the simulation results of the final PDMS layer thickness for different applicator roll speeds and polymer concentrations (circles) versus experimentally estimated thicknesses based on mass loss measurements during coating (diamonds). Errors bars on measurements represent maximum and minimum due to uncertainties in the evaporation rate. Simulation results vary by the estimated standard deviation of 25% (see section 4.1.5). The colours indicate the different concentrations, as denoted in the legend.

4.2.2 Cross sectional images vs. simulation results

Adding to the integral measurement via mass loss, the local thickness for selected samples was determined from cross sectional SEM images. Figure 45 depicts median values as well as standard deviation for the top layer thickness in the cross-sectional images. Representative cross-sectional images are given in the Appendix (Figure A 9). The thickness of the high concentration solution (3 wt %) shows the biggest variation across different samples, while the spectrum of thicknesses for the 1 wt% solution is most narrow. As can be seen, the mean values for both samples with 1 and 2 wt % PDMS are a bit smaller than the simulation results. The median values in the SEM measurements for 1 wt % are around 25-28 nm and around 80-90 nm for 2 wt %, while the simulations predict 40-50 nm, and 120 to 150 nm, respectively. For the higher concentration of 3 wt %, the median of 330 nm is close to the simulation results. One interesting observation is that the measured variation is not symmetric around the median but shows higher deviations above it, with maximum values being more than twice of the median in some cases. The simulation results have error bars of +/- 25%, which is the expected deviation based on the results in section 4.2.4.

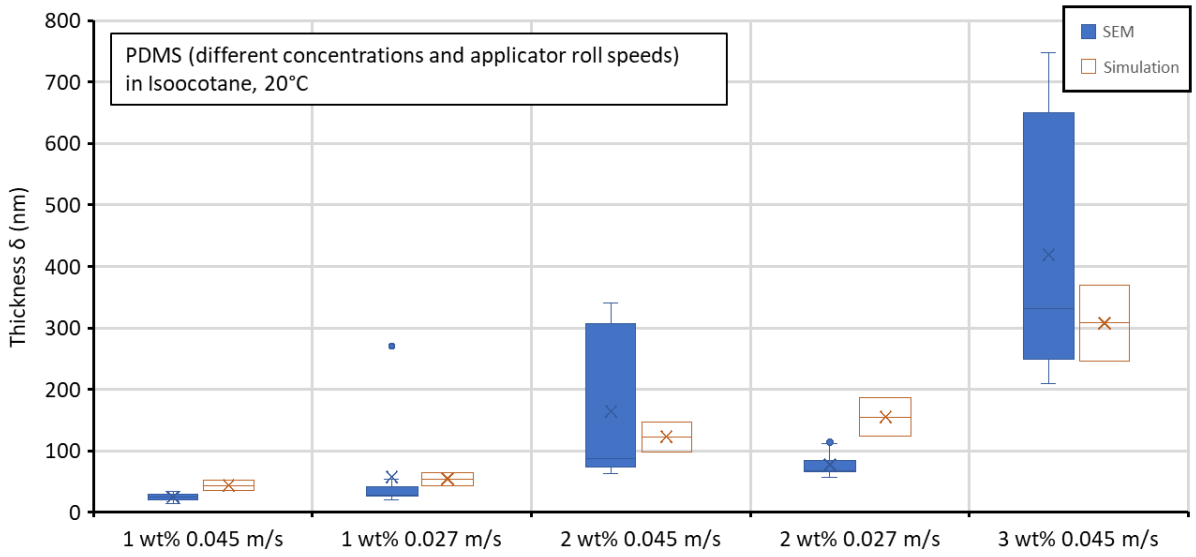

Figure 45 Comparison of simulation results (orange boxes) of the final PDMS layer thickness for different applicator roll speeds and polymer concentrations versus experimentally estimated thicknesses based on cross-sectional SEM images (blue boxplots). Small blue dots show data points that are outliers, meaning they deviate from the median by more than the 1.5-fold of the interquartile range. The width of the orange boxes denotes the estimated standard deviation of 25% respectively.

4.2.3 Confocal laser measurements

A further validation of the model was done by means of confocal laser measurements. For the 1 and 2 wt% solution of PDMS, the film thickness H_3 (see Figure 27) on the applicator roll after leaving the gap region was measured and Table 1 shows the results in comparison with the corresponding film thickness from the CFD model. It must be noted that the confocal laser measurements were always fluctuating, thus the respective amplitude of the measurement is given. For 1 wt% the measurement aligns relatively well with the prediction from the model, as the predicted thickness lies within the measured range. For 2 wt% the mean value of the fluctuating measurement is approximately 20% below the expected result.

Table 1 Comparison of simulation results and confocal laser displacement measurements of film thickness H_1 during the coating of PDMS solution at two different concentrations. The applicator roll speed was 0.045 m/s.

PDMS concentration (wt%)	Film thickness H_3 in simulation (μm)	Film thickness H_3 in confocal laser measurement (μm)
1	34	33-40
2	53	40-47

4.2.4 Variability in membrane thickness

For the parameters fluctuating or not exactly known, the variability in PDMS thickness was estimated using a DOE study combined with a response surface method. The study was done for 1 and 2 wt% polymer concentration and in both cases the evaporation rate had the lowest effect on the resulting thickness with a higher evaporation rate yielding a slightly increased thickness by few nanometres (corresponding to not more than 1-2% of the total thickness). The strongest impact comes from the

variation of membrane roll velocity, with an increase in thickness that is almost directly proportional to the increase in velocity. Thus, an increase of membrane roll speed by 20% will also increase the coated thickness by roughly 20%. When the gap size is in the range of 135 to 195 µm, it changes the thickness by 5 to 10 nm and hence is also not very substantial. Taken together, the DOE study suggests a deviation of approximately +/- 25% in the chosen parameter range. Another result of the DOE study is the lack of any strong interaction effect between parameters. In the chosen parameter range, to give an example, the impact of membrane roll speed does not depend on the evaporation and gap size and vice versa. This is also expressed by the statistical information on the response surface results, which show a non-significant parameter fit for all interaction terms. This can also be seen by the almost straight contour lines of the response surface plots (see section 8.6 in the Appendix).

However, the characteristics of the system change rapidly when a certain minimum gap size is reached, as can be seen in Figure 46. In that case, the coated thickness may suddenly increase by a factor of two or more. The threshold for this minimum gap size depends on the polymer concentration, for a concentration of 0.5 wt% the effect cannot be seen (data not shown).

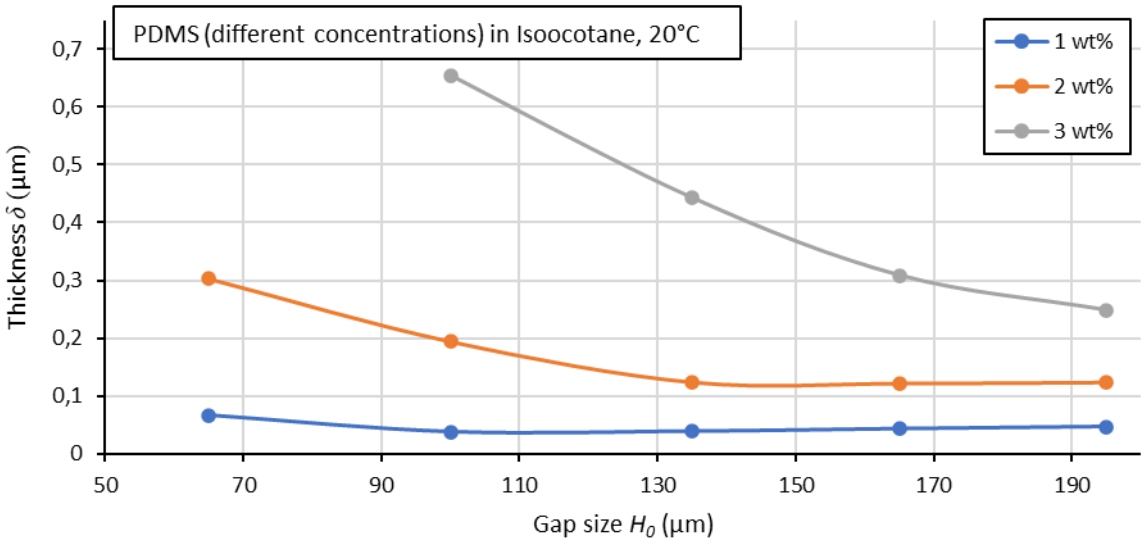

Figure 46 Effect of gap size between applicator roll and membrane and PDMS concentration on the coated top layer thickness of the PDMS membrane. The effect strength varies with polymer concentration, as indicated by the legend.

As will be discussed later, the observed thickening effect is caused by the qualitative change in flow structure in the meniscus region. The change of flow structure is characterized by a flooding of the gap region, causing a direct transfer of liquid from the applicator roll to the membrane. A scheme of the two flow structures is illustrated in Figure 47.

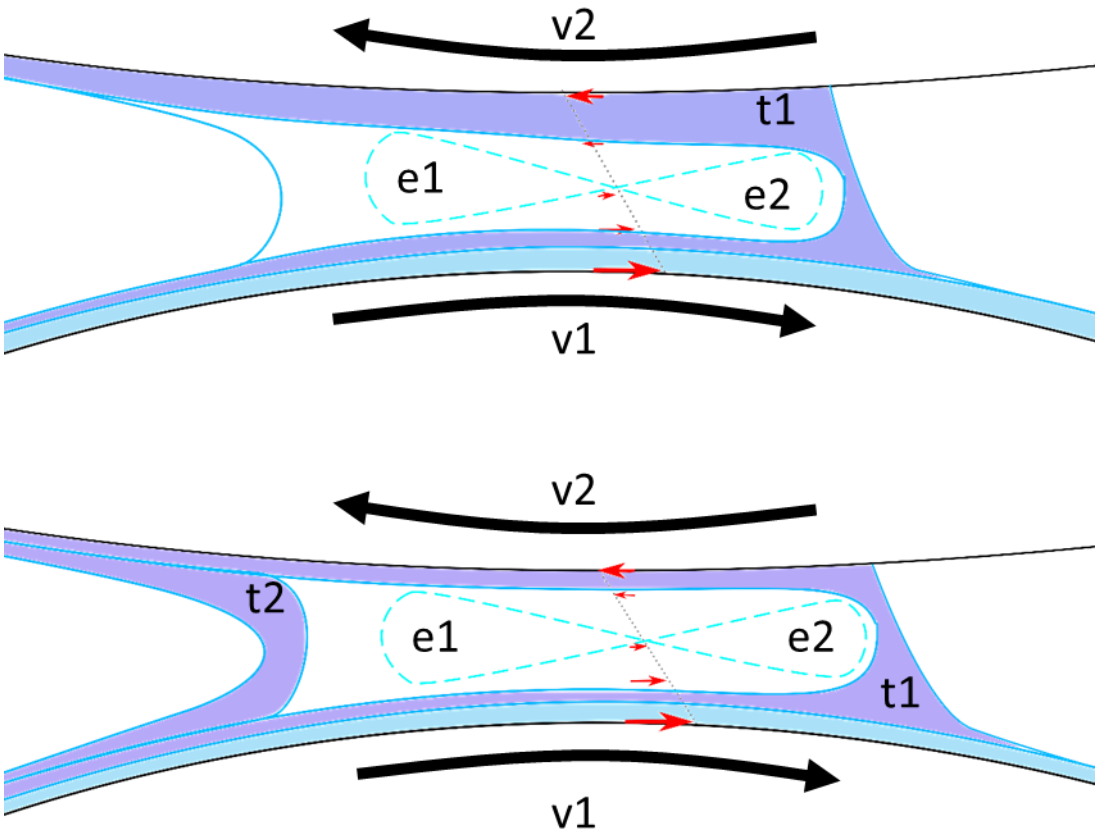

Figure 47 Scheme of the flow structure in the gap region between applicator roll with speed v1 and membrane roll with speed v2. In both cases the flow consists of two circulating flow structures (e1 and e2) and a primary transfer jet (t1) that transfers liquid to the membrane. When the gap becomes small enough, the amount of incoming liquid is too much to go through the gap and a second transfer jet (t2) occurs that thickens the film on the membrane.

4.3 Results for the coating of PolyActive™ in a solvent mixture

4.3.1 Mass loss measurements vs simulation results

For PolyActive™ solution at concentrations of 0.5, 0.75 and 1 wt% plus applicator roll speeds of 0.045 and 0.032 m/s each, the mass loss measurement of evaporation only yielded very similar results with a mean evaporation rate of 0.017 g/s with a standard deviation less than 1%.

Again, the average coating thickness is then deduced from the evaporation corrected mass loss of the feed solution during the coating procedure (a s described in Section 3.2). The empirical and simulation results can be found inFigure 48. In contrast to the PDMS coating, the simulation results underestimate the measured coating thickness significantly. Throughout the concentration range the coating thickness derived from mass loss measurements is a factor of 3 to 4 bigger than the corresponding predicted values. Moreover, simulations consistently suggest a small increase of thickness for lower applicator roll speeds. Experimental findings do not support this, rather pointing to the opposite. However, because of the relatively high uncertainty in the measurements, this trend can probably not be regarded as statistically significant.

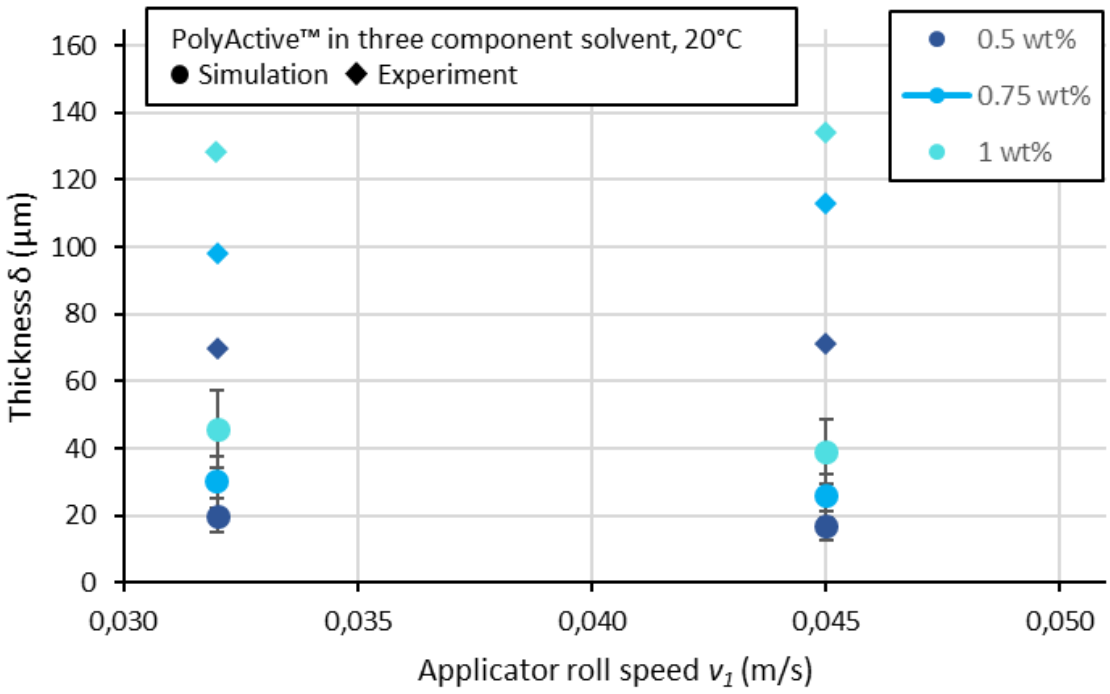

Figure 48 Comparison of the simulation results of PolyActive™ layer thickness for different applicator roll speeds and polymer concentrations (solid lines) versus experimentally estimated thicknesses based on mass loss measurements during coating (symbols). Errors bars on measurements are not given, as the variation in evaporation rate was so marginal that errors based on uncertainties of evaporation rate (as done in section 4.2.1) would not be visible. Simulation results vary again by the estimated standard deviation of 25% (see section 4.2.4). The colours indicate the different concentrations, as denoted in the legend.

4.3.2 Cross sectional images vs simulation results

The resulting mean thickness in cross-sectional SEM images was also compared to the corresponding simulation results. Like the mass loss measurements (see section 4.3.1), the simulation results differ substantially from the measured film thicknesses, again showing a thickening factor of 4-5 in direct comparison. Looking at an applicator roll speed of 0.045 m/s and PolyActive™ concentrations between 0.5 and 1 wt%, Figure 49 sums up the mean and standard deviation of polymer thickness as measured in SEM images compared to the respective simulation results. Corresponding SEM images can be found in the Appendix (see section 8.2.2).

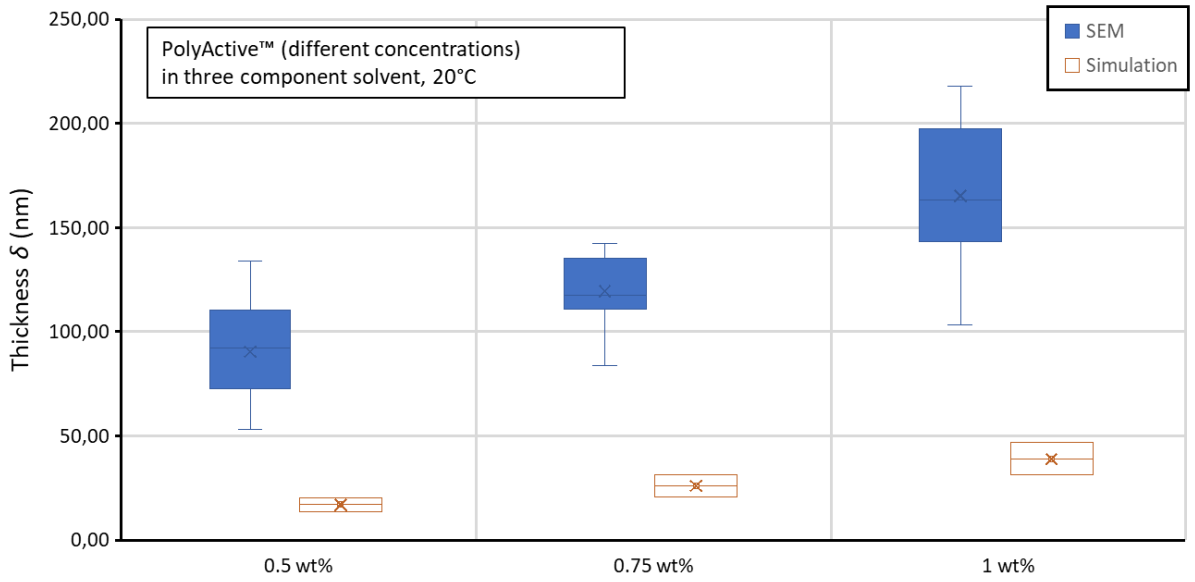

Figure 49 Comparison of simulation results (orange boxes) of the final PolyActive™ layer thickness for an applicator roll speed of 0.45 m/s and three different polymer concentrations (0.5, 0.75 and 1 wt%) versus experimentally estimated thicknesses based on cross-sectional SEM images (blue boxplots). The width of the orange boxes denotes the estimated standard deviation of 25% respectively.

Additionally, the 0.5 wt% solution was used for a coating on a long applicator roll with same radius but twice the axial length (0.6 m instead of the standard of 0.3 m). Here, the variation of polymer thickness along the roll axis was investigated by taking samples at five designated points along the roll, as can be found in Figure 50. There appears to be a general trend of a thickening of the film from the centre of the roll towards the edges. At the edges, the average film thickness is approximately 33% higher than the average thickness at the centre. However, as this effect is relatively small, since it must be noted that the standard deviation of thickness in the SEM measurements was also on the order of 30%.

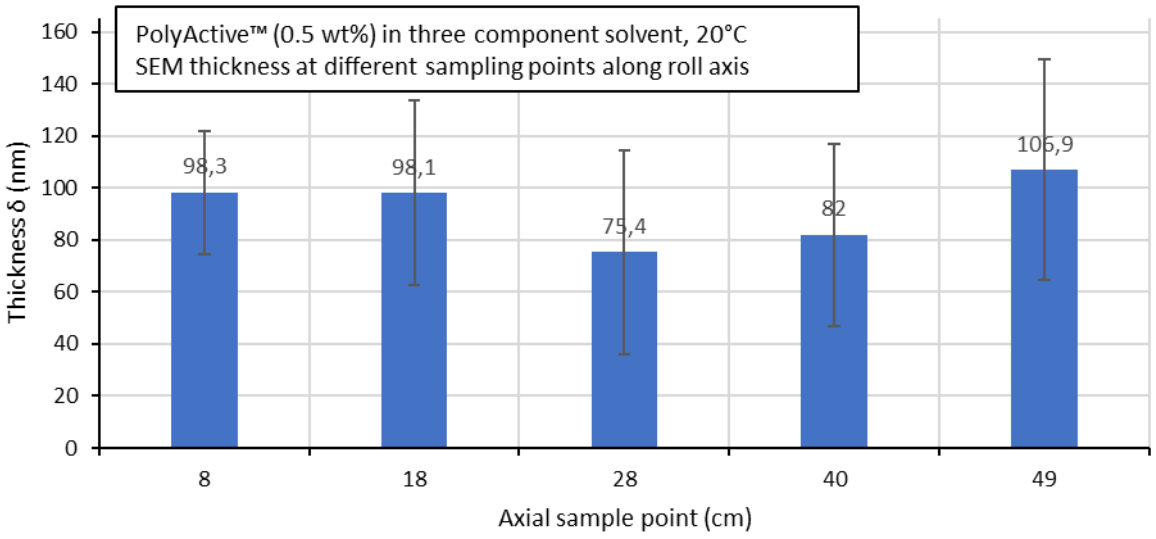

Figure 50 PolyActive™ thickness δ at different sample points along the membrane roll-axis given as the ditance from the left end of the roll. The boxes show the mean thickness while error bars designate the standard deviation based on 10 measurements for each sample.

4.3.3 Confocal laser measurements

As a further test of the model predictions, the film thickness H_1 and H_3 (see Figure 27) on the applicator roll were measured with the confocal displacement sensor. As for PDMS coating, the measured signal from the sensor is fluctuating over time. Measurements from the front side (H_1) tended to be more stable than those from the backside (H_3) and more stable for thicker films than for thinner films. Therefore, the range of polymer concentration was increased in some cases to yield thicker films and increase the confidence in the measurement results. The approximated mean, maximum and minimum values of the liquid films are contrasted with the simulation results in Table 2 for the designated polymer concentration and measurement position on the roll.

Table 2 Comparison of simulation results and confocal laser displacement measurements of film thickness H_1 during the coating of 1 wt% PolyActive™ solution at two different applicator roll speeds (first column).

Applicator roll speed v_1 (m/s)	Film thickness H_1 in simulation (μm)	Film thickness H_1 in confocal laser measurement (μm)
0.045	30	39-44
0.056	36	40-48

Table 3 Comparison of simulation results and confocal laser displacement measurements of film thickness H_3 during the coating of three different PolyActive™ solutions (concentrations in first column) at 0.045 m/s applicator roll speed.

PolyActive™ concentration c (wt%)	Film thickness H_3 in simulation (μm)	Film thickness H_3 in confocal laser measurement (μm)
1	30	33-47
1.5	43	43-57
2	54	40-45

4.3.4 Extension of the CFD model to explain the experimental findings

As described in the previous sections 4.3.1 and 4.3.2, there is a substantial difference between the simulation results for PolyActive™ coating based on the standard Newtonian CFD model and the experimental results. At first, two possible sources of error in the chosen modelling approach, the influence of the used overflow geometry and dynamic contact angle, were tested on their effect on the overall coating predictions and then dismissed as the culprit behind the observed discrepancies. In trying to find a likely explanation for the observed deviation, two extensions (namely viscoelastic behaviour and Marangoni effects) were added to the CFD model and simulations were performed to assess the possible effect of each of these phenomena on the coating behaviour.

Comparison of model geometries with and without overflow

Two model geometries were presented in section 3.8.1 and simulations point towards one major difference between both models, which is the film thickness H_1 on the applicator roll. As the liquid filling height is reduced in the second geometry with no overflow, H_1 gets thinner and decreases with the filling height. For a lowering of the filling height by approximately 1 cm (compare Figure 27 and Figure 28 in section 3.8.1), a thinning of 10% can be seen (35 µm to 27 µm). Moreover, the film thickness on the membrane is reduced accordingly and the total volume of liquid in the gap, as apparent by the meniscus position, is reduced as well (see Figure 51). Note that for this comparison, the amount of liquid in the basin was very much reduced to show the maximal effect on the film thickness. As will be discussed later, the shear and strain rates in the bulk along with the surface velocity gradient at the lower and upper meniscus are important for the viscoelastic and Marangoni extensions of the model, respectively. Here, no substantial differences between the models could be seen (not shown).

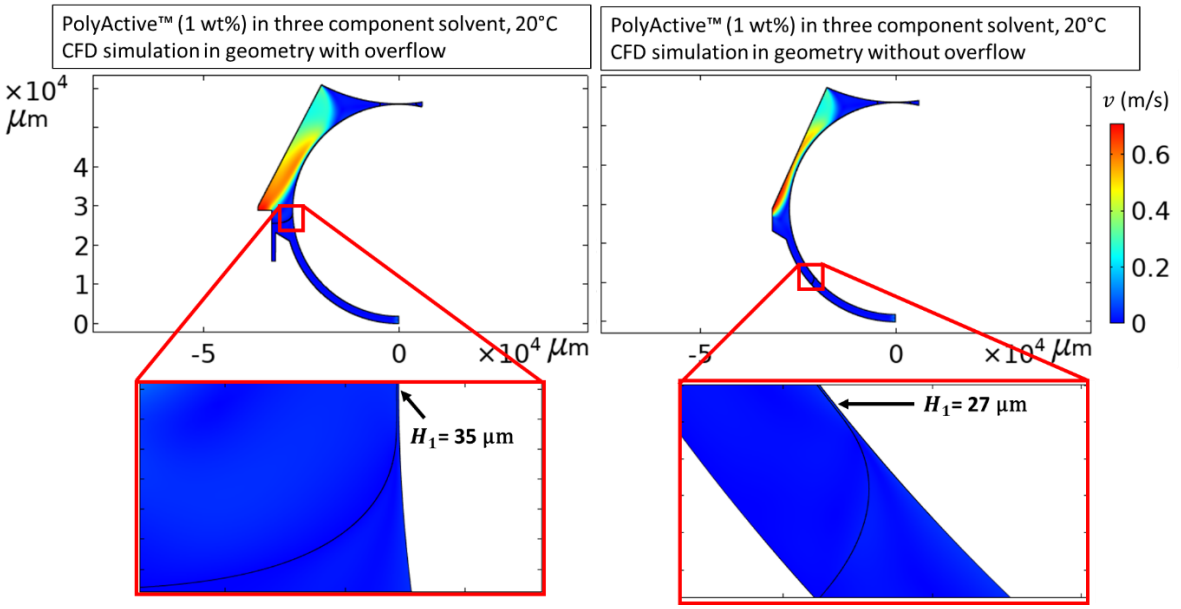

Figure 51 Comparison between the two geometries used for the CFD model. Left side shows the standard model with overflow and a higher meniscus position, while the right side shows a model without overflow and an extremely deprived amount of liquid in the basin. In this extreme opposition, the thickness H_1 on the applicator roll reduced by approximately 8 µm.

Comparison of different dynamic contact angles

To test the model behaviour for sensitivity upon dynamic contact angle at the dynamic wetting line, simulations with the standard model were done for dynamic contact angles of 90°, 75° and 60° and 1 wt% PolyActive™ solution and no substantial effect on the final film thickness on the applicator roll and membrane can be seen (see Figure A 18 in Appendix section 8.4).

Marangoni effects

In the basic CFD model, the surface tension was set constant, but as described in section 2.4.2 several mechanisms can cause gradients of surface tension which can induce secondary flow patterns (Marangoni convection). Assuming PolyActive™ shows some degree of surface activity, a surfactant

mass balance was implemented (see section 3.8.3.1) and coupled to the surface tension via the Volmer isotherm. Figure 52 shows the resulting effect on the coated polymer thickness for a variety of model parameters k_a and K_c (see equation (189) and (190)). For better comparison, the thickening factor f_2 of film thickness H_2 (that is the relative thickening in comparison to the standard model) is plotted. Overall, adding the Marangoni effect to the model caused a thickening of the coated film. The thickening factor generally increases towards lower adsorption rates until a maximum is reached, and then it decreases again. The magnitude of thickening also depends on the equilibrium ratio, as higher K_c values correspond to higher maximum thickening factors f_2 in all simulations. In the tested parameter range a maximum thickening on the membrane of factor 2.7 could be obtained. The concentration gradients were strongest in the upper meniscus region, as depicted in Figure 54. To see the corresponding gradient of surface tension along the lower and upper meniscus for this parameter combination, see Figure A 21 and in the Appendix section 8.7.

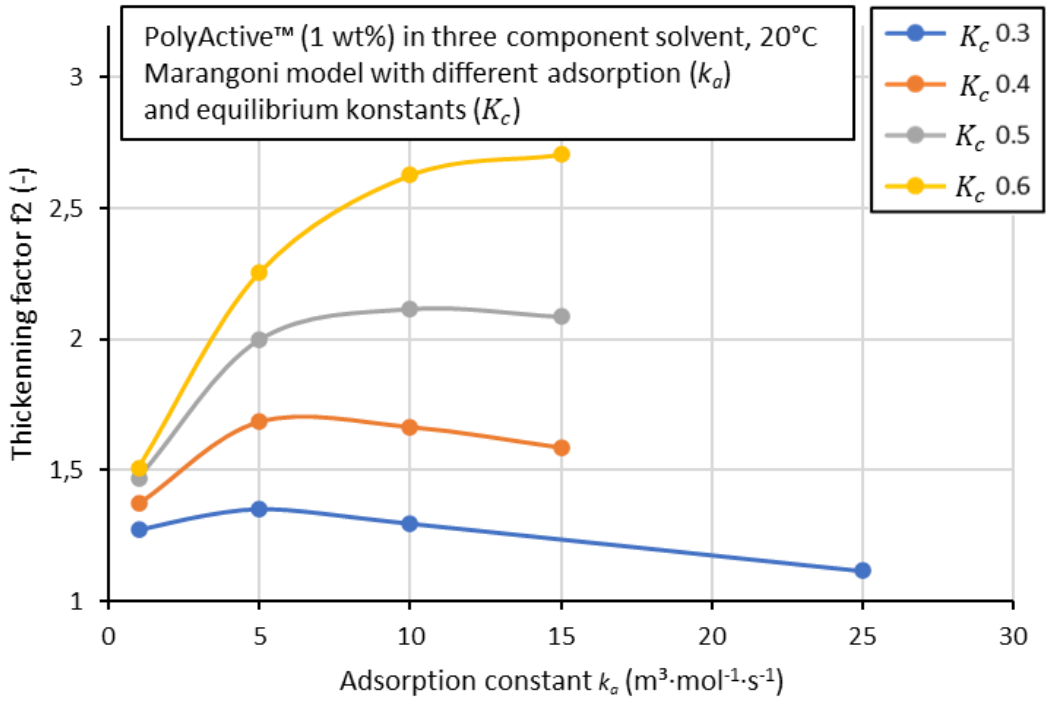

Figure 52 Comparison of the thickening factor f_2 (ratio of film thickness H_2 with respect to the standard model) when a Marangoni effect is added to the CFD model. The adsorption and desorption kinetics are determined by k_a and K_c and the thickening factor depends on both parameters.

Adding to the observations made on film thickness H_2, the Marangoni flow also had a small thickening effect on the film H_3 on the applicator roll, but this was much less pronounced compared to H_2. Again, the maximum thickening factor f_3 (ratio of H_3 with respect to the standard model) was found for the highest value of K_c and had a value of 1.25.

The observed thickening goes hand in hand with a change in flow pattern in the upper meniscus region between the applicator roll and the membrane roll, as can be seen in Figure 55. The increase in surfactant concentration on the left meniscus interface (see higher concentration indicated by the red colour in Figure 54) leads to a decrease in surface tension and this causes a Marangoni flow in the opposite direction of the surrounding flow field, transferring liquid from the applicator roll directly to the membrane. For a comparison to the standard flow field without Marangoni effect, see Figure A 22 in the Appendix section 8.6.2.

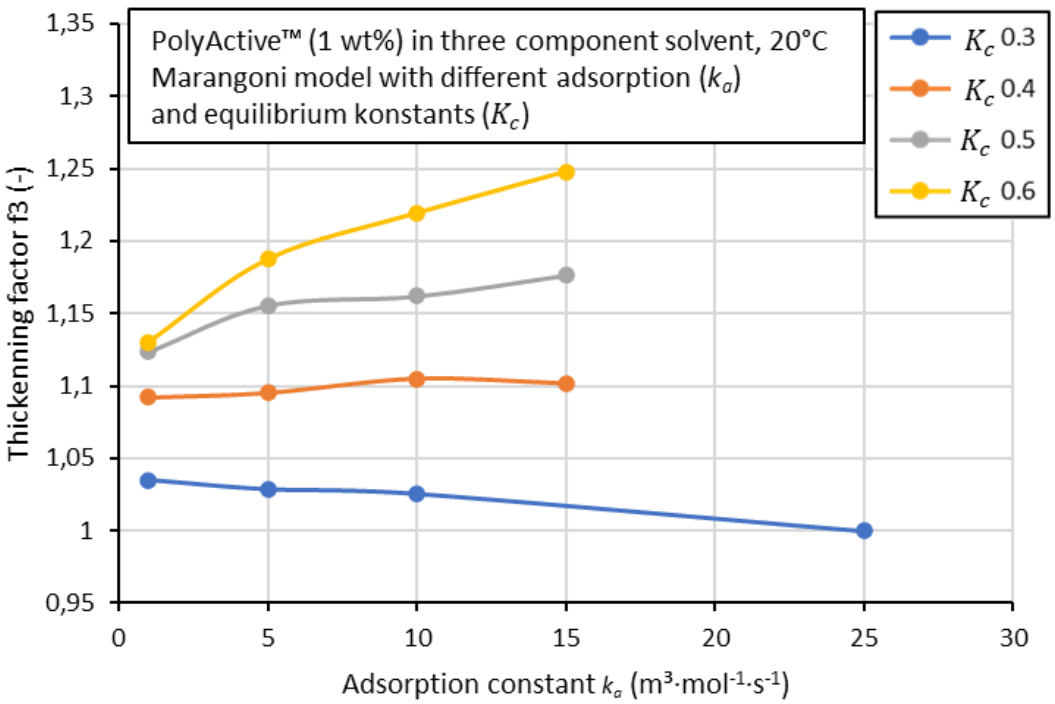

Figure 53 Comparison of the thickening factor f_3 (ratio of film thickness H_3 with respect to the standard model) when a Marangoni effect is added to the CFD model. The adsorption and desorption kinetics are determined by k_a and K_c and the thickening factor depends on both parameters.

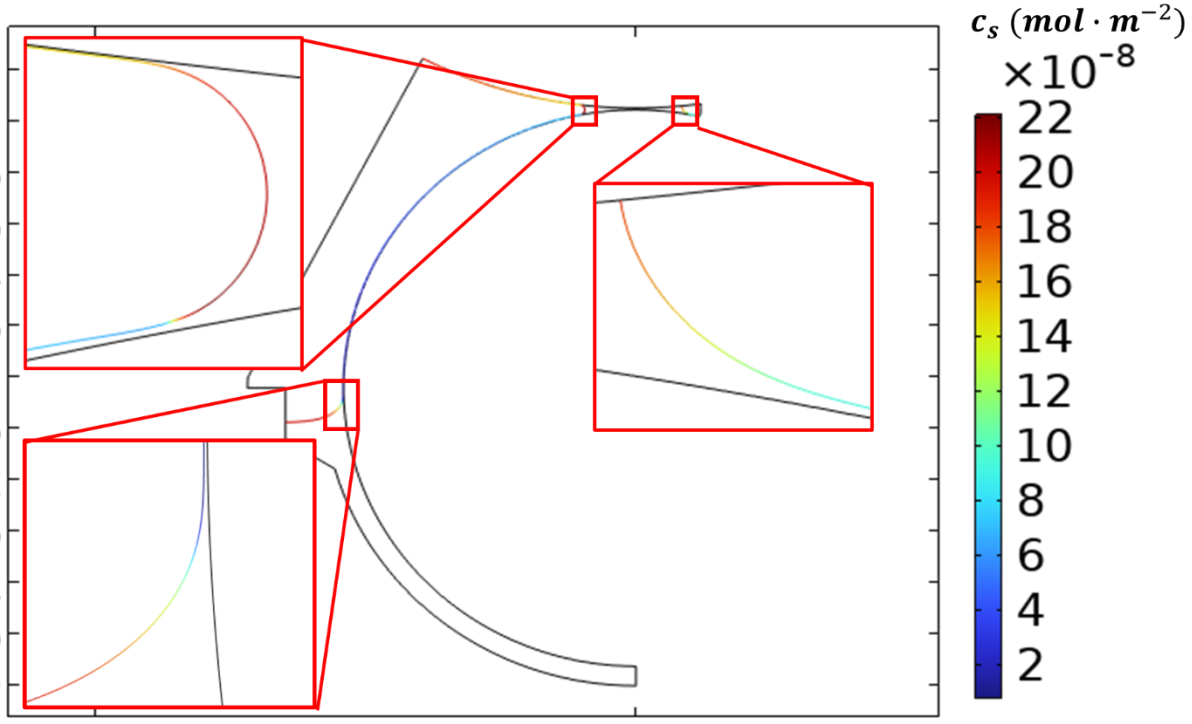

Figure 54 Surface concentration profile along the lower and upper meniscus of the roll-to-roll coating device when the polymer is assumed to behave as a surfactant. The colour of the surface line indicates the computed surfactant concentration, as given by the legend on the right. Areas where surface velocity converges show an accumulation of surfactant (red colour), diverging surface velocity causes depletion (blue colour). The blown-up images zoom in on the surface profiles in the meniscus regions at the indicated positions of the roll coating device.

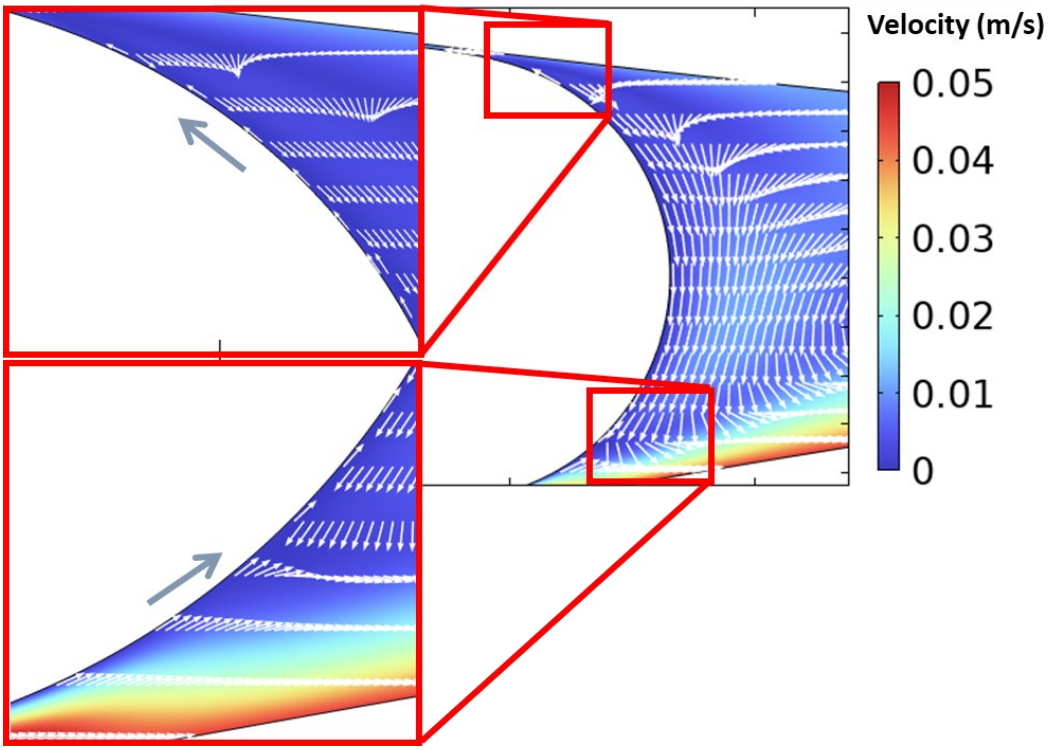

Figure 55 Flow field near the left meniscus of the gap region in the roll-to-roll coating device as computed by CFD simulations. The arrows indicate velocity vectors, while the underlying contour plot shows the local magnitude of the velocity. Including a surfactant mass balance in the model causes surface tension gradients that cause Marangoni flows (in the direction of the grey arrows) that go in the opposite direction as the bulk flow.

Viscoelastic effects

Additionally, the CFD model was extended with a FENE-P viscoelastic interaction model as described in Section 2.3.2. The model needs three parameters as input: extensibility, relaxation time and viscous interaction of the polymer with the solvent. The extensibility is not known and therefore had to be guessed. For the following computations it was set to a value of three. This can be supported by the following estimations based on the molecular properties of PolyActive™, as given in the literature(Yave et al., 2011). Based on the molecular weight of the PolyActive™ polymer of 41000 g/mol and the fact that the PEO segment, which constitutes 77 wt% of the polymer, has a molecular weight of 1500 g/mol, it can be estimated that the PolyActive™ MBCP consists of 21 segments. The overall radius of gyration of the polymer is approximately 10nm, thus the radius of gyration of one segment is roughly 3,5nm and its diameter is 7nm. Assuming a spherical geometry, the diameter of one polymer molecule is thus build of 2-3 polymer blocks. If one further assumes that the polymer could be stretched to the extent where it essentially becomes one elongated chain, this would then correspond to a relative elongation of approximately factor seven. However, this is probably unlikely under the given conditions and it was estimated that the realistic extensibility is at maximum half of that. The value of three was thus chosen as the default. Nevertheless, a factor of 10 was also tested just to make sure that this uncertainty has no big impact on the overall conclusion. Viscoelastic measurements in section 4.2.6 yielded approximative values for the two main parameters (namely viscous interaction of the polymer and relaxation time) and a series of simulations was run with parameters approaching the approximate values from the experimental data. Again, the relative thickening factor with respect to the standard model is plotted against relaxation time for a viscous interaction parameter η_p of 2 and 3 mPa·s each (see Figure 56).

In a subsequent test, the extensibility factor was varied for the parameter combination that showed the highest thickening effect but an increase of extensibility from factor 3 to factor 10 decreased the thickening effect only marginally by less than 5% (data not shown).

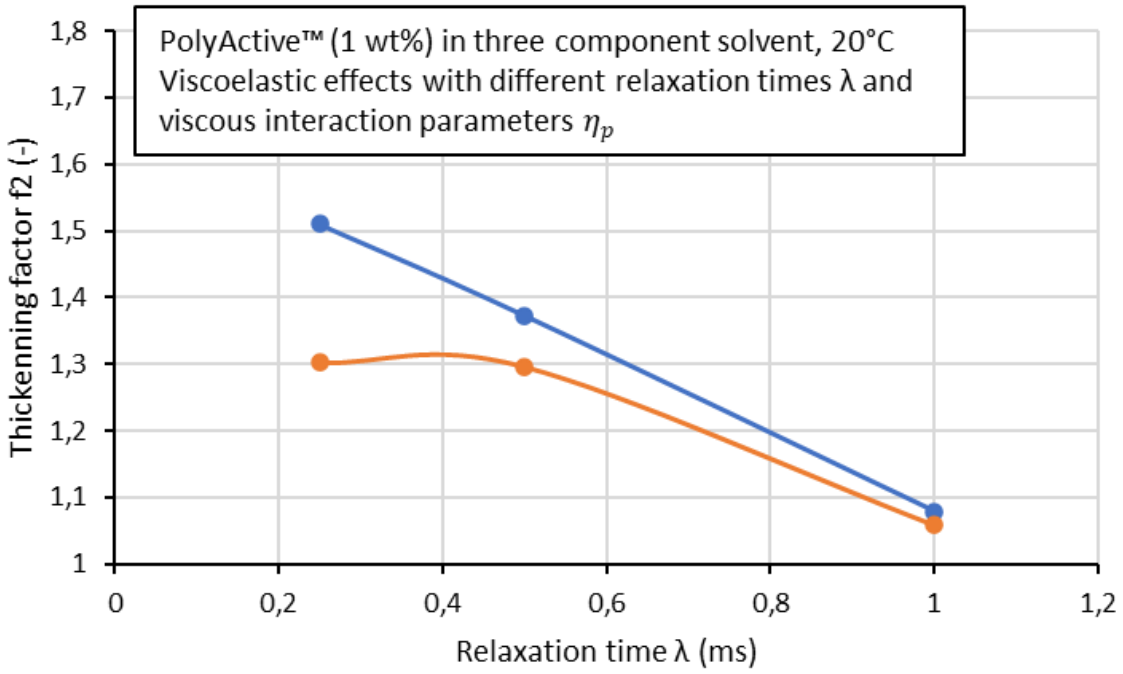

Figure 56 Comparison of the thickening factor f_2 (ratio of film thickness H_2 with respect to the standard model) when a viscoelastic effect based on a FENE-P equation is added to the CFD model. The graph shows the result for viscous interaction parameter of 2 and 3 mPa·s and relaxation times between 1 and 0.25 ms. The extensibility factor was 3 in all simulations.

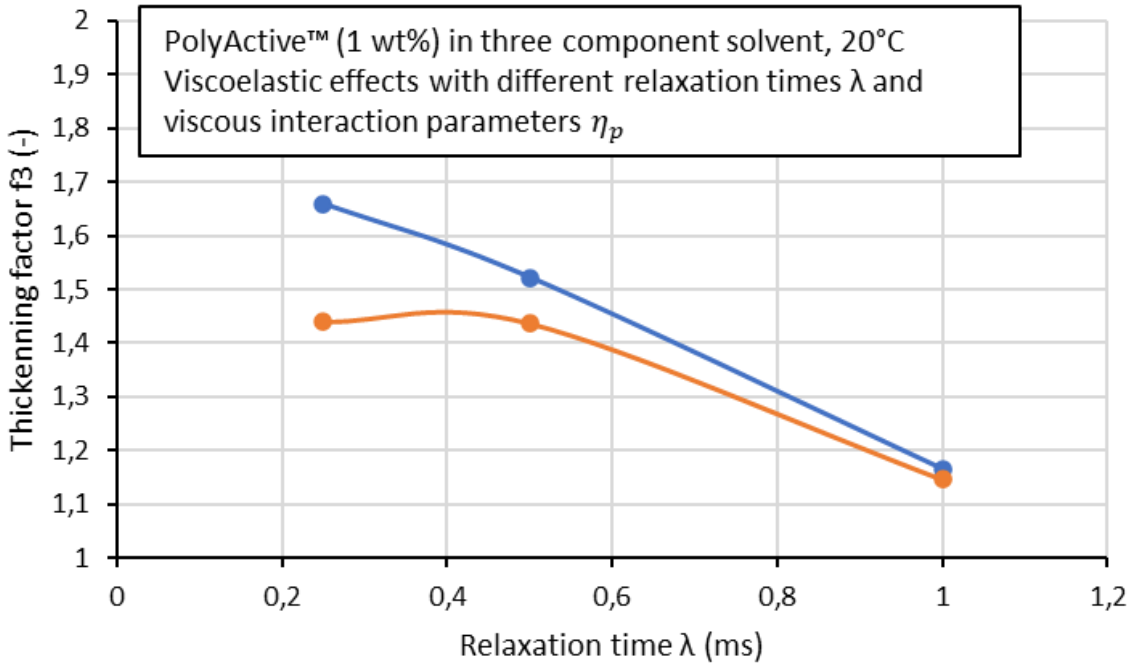

Figure 57 Comparison of the thickening factor f_3 (ratio of film thickness H_3 with respect to the standard model) when a viscoelastic effect based on a FENE-P equation is added to the CFD model. The graph shows the result for viscous interaction parameter of 2 and 3 mPa·s and relaxation times between 1 and 0.25 ms. The extensibility factor was 3 in all simulations.

As a general trend, the thickening factor increases for both viscous interaction values with lower relaxation times, reaching a maximum thickening of 1.51 for a parameter combination of 3 mPa·s and 0.25 ms. It must be noted that the viscoelastic simulations are extremely resource intensive and time consuming, thus only these six simulations were conducted. Additionally, the simulations required an increasingly fine resolution of the mesh for lower relaxation times to reach convergence. For this reason, 0.25 ms was the lowest relaxation time that could be investigated.

A very similar effect can be seen on the film H_3 on the applicator roll. The overall trends for the corresponding thickening factor f_3 are analogous to f_2, but here the highest factor had a slightly higher value of 1.66 (see Figure 57).

4.4 Coating of PolyActive™ in pure SMC 3

In addition to PolyActive™ coating in a three-component solvent mixture, the coating in pure SMC 3 was also briefly investigated, which is presented in the following section.

4.4.1 Mass loss measurements

As a first step, mass loss measurements of the evaporation were conducted for PolyActive™ concentrations of 1 and 3 wt% and applicator roll speeds of 0.056 and 0.034 m/s each. The measured evaporation rate was very similar for all measurements and was on average 0.056 g/s. In contrast to other evaporation measurements, there seems to be a slight increase for higher applicator roll speeds, as summed up in Table 4. However, given the uncertainty of the measurement method this difference is not big enough to be considered significant.

Table 4 Evaporation loss measurements of two PolyActive™ concentrations (first column) dissolved in pure SMC 3, given for high and low applicator roll speed (second column) each.

PolyActive™ concentration c (wt%)	Applicator roll speed v_1 (m/s)	Evaporation mass loss $\dot{m}_e$(g/s)
1	0.056	0.057
1	0.034	0.054
3	0.056	0.059
3	0.034	0.054

Using the respective evaporation rates, the overall mass loss during membrane coating was corrected to yield the following estimated average polymer thickness on the membrane for the same process parameters as given before (see Table 5). Simulation results of the corresponding standard CFD model are included and show an even higher deviation from the measured results than previously shown for PolyAcive™ in solvent mixture (compare section 4.3.1). For 1 wt% in pure SMC 3, the measured thickening with respect to the CFD model was approximately factor 5-6, for 3 wt% solution in pure SMC 3 it was approximately factor 6-7.

Table 5 Comparison of simulation results of the final PolyActive™ thickness for different applicator roll speeds and polymer concentrations versus experimentally estimated thicknesses based on mass loss measurements during coating. The solvent was pure SMC 3.

PolyActive™ concentration c (wt%)	Applicator roll speed v_1 (m/s)	Thickness δ in simulation (nm)	Thickness δ from mass loss measurements (nm)
1	0.056	40	258
1	0.034	49	219
3	0.056	128	788
3	0.034	159	696

4.4.2 Cross sectional images

Membrane samples from the same coating experiment described in the forementioned section were again also analysed via cross-sectional SEM. The findings are summarized in Table 6. Like the mass loss measurements (section 4.3.1), SEM measurements indicate an even stronger thickening of polymer films on the membrane compared to the solvent mixture. However, compared to mass loss measurements the SEM images show even bigger thickening. The 1 wt% solution yielded a polymer thickness of approximately 410 and 540 nm for high and low applicator roll speeds, respectively. This corresponds to a relative thickening factor of 10-13, so approximately a doubled factor when compared to mass loss measurements. Similarly drastic is the finding for a 3 wt% solution at lower roll speed. Here, the measured thickness was around 2450nm, thus also showing a thickening factor of approximately 20. This is even more striking, as the same polymer solution yielded 880 nm for the higher roll speed, which corresponds to a thickening factor of 7-8 and is much closer to the deduced factor for the corresponding mass loss measurement.

Table 6 Comparison of simulation results of the final PolyActive™ thickness for different applicator polymer concentrations (first column) and roll speeds (second column) versus experimentally estimated thicknesses based on cross-sectional SEM images. The solvent was pure SMC 3.

PolyActive™ concentration c (wt%)	Applicator roll speed v_1 (m/s)	Thickness δ in simulation (nm)	Thickness δ in SEM (+/- std.) (nm)
1	0.056	40	411 (+/-50)
1	0.034	49	539 (+/- 125)
3	0.056	128	881 (+/- 124)
3	0.034	159	2446 (+/- 168)

4.4.3 Confocal laser measurements

Confocal laser measurements of the film thickness H_3 on the applicator roll were done for 1 and 3 wt% at 0.056 and 0.034 m/s roll speed each. However, reliable measurements could only be obtained for the 3 w% solution at high roll speed. Here, the measured film thickness was around 27 µm with a typical fluctuation of 20%.

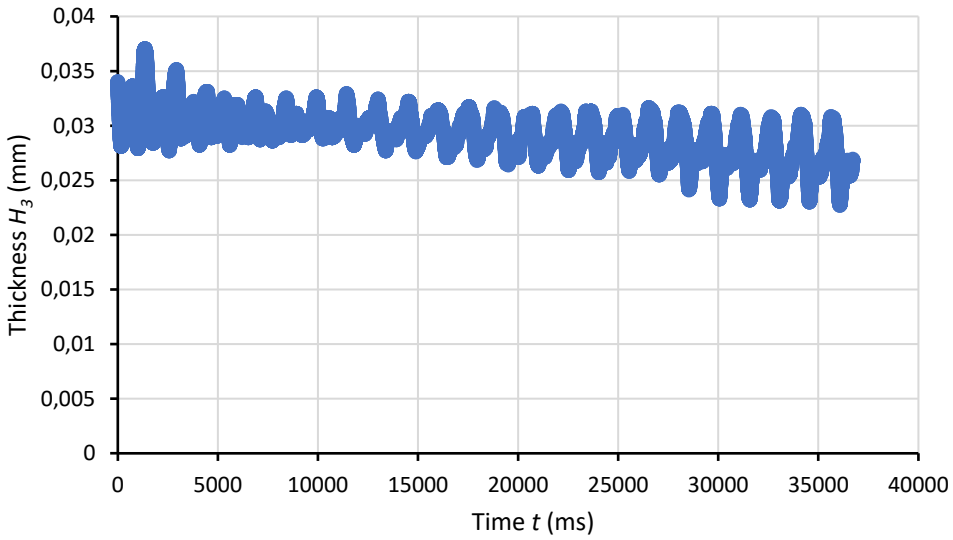

Figure 58 Confocal laser measurement of film thickness H_3 on the applicator roll for 3 wt% PolyActive™ solution in pure SMC 3 and an applicator roll speed of 0.056 m/s.

4.4.4 Non-isothermal simulation results

Since some of the boundary conditions of the temperature dependent model were uncertain, a variety of simulations was computed based on a 3 wt% PolyActive™ solution in pure SMC 3. Firstly, the feed temperature and wall temperature were varied to see, what conditions would yield a decrease of temperature on the applicator roll film of about 5 K. The concluding result was that the inlet temperature is almost irrelevant, as the liquid soon assumes the temperature of the applicator roll. To obtain a temperature decrease of 5 K, the only effective parameter was the wall temperature of the applicator roll, i.e. there was no substantial temperature gradient in the liquid film between solid wall and gas/liquid interface (see Figure A 29 and Figure A 30 in the Appendix).

Secondly, the next major unknown was the heat conductivity of the membrane, which is located between the membrane roll and coated liquid. Only for very low heat conductivities on the order of 10^{-2} W/(m·K), a temperature decrease of two or three degrees in the liquid near the membrane roll could be seen, starting right after the point where the film leaves the meniscus. Using the Eötvös equation, the temperature field was coupled to the surface tension, which caused a corresponding surface tension gradient. Using heat conductivities of 0.025 W/(m·K) for the non-woven and 0.01 W/(m·K) for the PAN layer, the temperature profile and corresponding surface tension gradient can be seen in Figure 59. In this simulation, the resulting film thickness on the membrane was slightly increased by 13.6%.

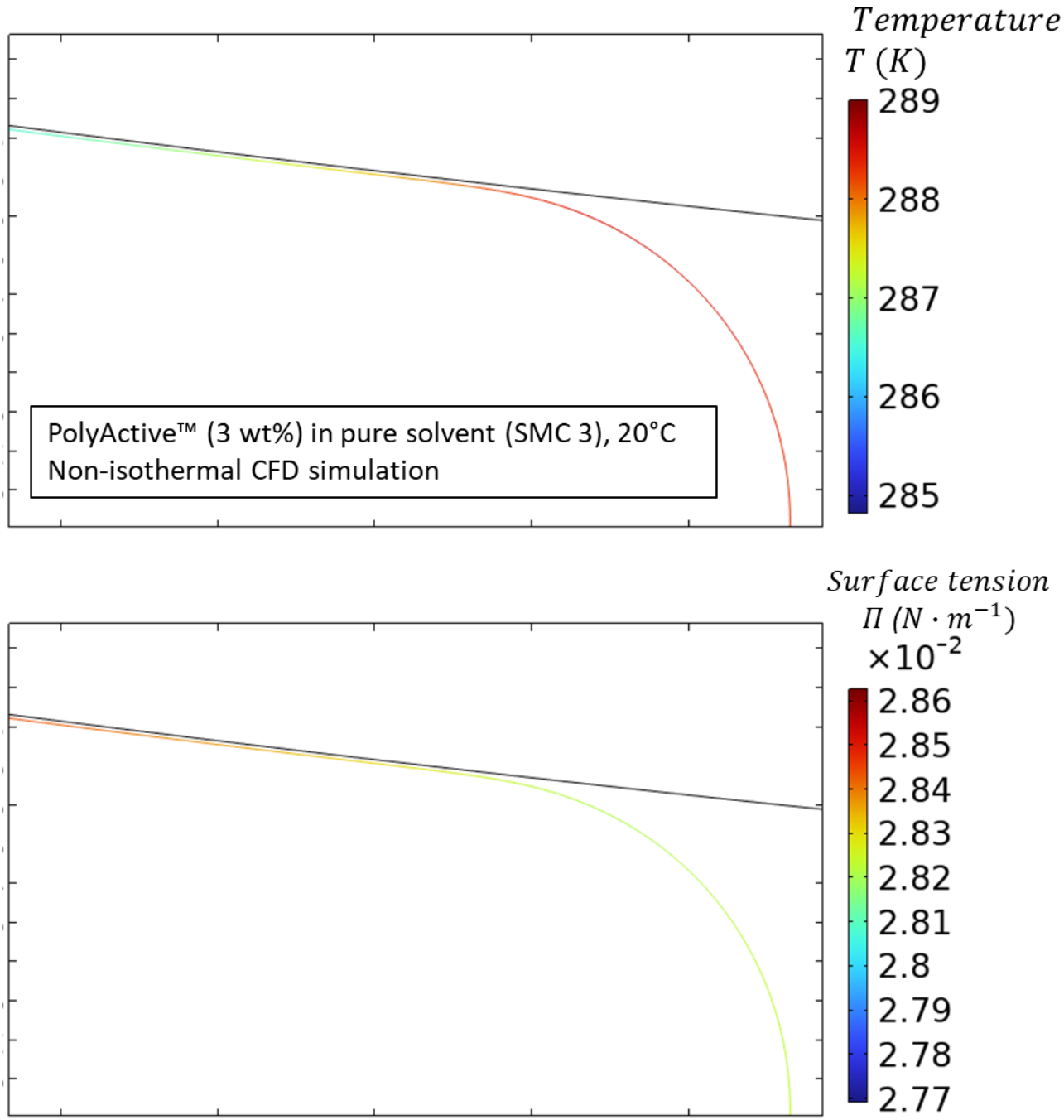

Figure 59 Temperature gradient (left) and corresponding surface tension gradient based on the Eötvös law (right) along the upper meniscus near the membrane roll. The simulation was based on the CFD model containing an energy balance and was done for 3 wt% PolyActive™ in pure SMC 3 and an applicator roll speed of 0.045 m/s.

5 Discussion

5.1 Validation of the CFD model for PDMS coating

The first goal of this thesis was to set up a starting point for a conclusive mathematical model that can predict the coating thickness of the standard polymer PDMS in the roll-to-roll fabrication of TFC membranes. Ignoring non-Newtonian viscosity and surface tension effects, a basic CFD model was set up and subsequently validated and verified. Here, 'validation' refers to the test of the numerical procedure, that is to say: showing that the implemented equations are solved reasonably well. By 'verification' we mean the comparison with experiments, i.e. checking if the implemented equations are sufficient to yield a good approximation of the physical system.

For the validation part, several mesh resolutions were compared, and it could be shown that the polymer thickness, i.e. the main parameter of interest, as well as other characteristic parameters, do not change significantly, when a certain resolution of the mesh is reached. Very coarse mesh resolutions cause strong deviations in the film thickness at the outlets of the domain. This seems to stem from problems of the solver to fulfil the boundary conditions for the free surfaces at the outlet, which are more pronounced when the resolution is too small. Further numerical validation also included robustness tests of other parameters in the solver configuration, e.g. the residual error threshold. A minimum mesh resolution was identified and showed reliable convergence for all solver configurations tested, thus ensuring a reasonable numerical robustness of this basic model.

To verify the model, the coating thickness was estimated by means of cross-sectional SEM images and mass loss measurements during the coating procedure. The SEM measurements are on the same order of magnitude and indicate that the simplified basic model is already a relatively good approximation of the real system. The variation of thickness appearing on the SEM images goes up to 100% and more, which can only be explained in parts by the statistical DOE analysis. However, if the effect of a more reduced gap size is considered, the strong upwards deviations might well be explained. When the gap becomes so small that the incoming liquid film cannot go through the gap completely, the remaining liquid is essentially directly transferred to the membrane, thus increasing the coated thickness drastically (see Figure 47 for a schematic explanation of the phenomenon). Such small gap sizes are not implausible, since 30 µm variation of the radius of the applicator roll is only the standard deviation, bigger deviations are possible. Moreover, both the membrane and applicator roll speed will fluctuate as well, which will also influence the threshold for flooding. The higher the ratio of membrane speed to applicator roll speed, the easier it is for flooding to occur.

As a secondary verification, the results in Figure 44 show the comparison of the mean polymer thickness from simulations with the polymer thickness estimated from mass loss measurements. In contrast to the SEM images, which show the thickness in a small cross -sectional area on arbitrary sample spots of the membrane, the measured mass loss yields an integral measure for the total amount of liquid (and thus polymer) that is transferred to the membrane. As the mass loss rate is a linear regression fit over several minutes of coating, it can be considered as an average value. However, these measurements have a relatively high uncertainty, as the evaporation was fluctuating in experiments and cannot be measured independently during the coating procedure. The fluctuation of the evaporation rate may be caused by changes of air convection, temperature, or humidity during the fabrication process. More probable though, most of the fluctuation might be explained by inaccuracies of the measurement method, for example due to air bubbles in the tubing that connect the overflow back to the reservoir and hinder the outflow. This might cause larger volumes of the liquid to stay in

the overflow basin before going back into the reservoir, causing fluctuations in the outflow rate and thus an uncertainty in the deduced regression slope.

Nevertheless, the estimated transferred mass and calculated remaining polymer are generally in good agreement with the SEM images and the CFD model. In Figure 44, the deduced thickness for the 3 w% solution is about 20% smaller than expected given the simulation and SEM results. One possible explanation could be, that within the chosen time interval, i.e. coating area, the average gap size might have been increased (for example due to variations in the underlying support structure thickness), which would have strong enough effect on the thickness (see Figure 46). Since SEM images only represent a very small area corresponding to a coating of 10^{-3} m, while mass loss measurements were averaged over several meters, this possibility cannot be ruled out and so these deviating observations are not necessarily contradicting.

In addition to the coating thickness of polymer on the final membrane, confocal laser displacement measurements confirmed that the predicted film thickness on the applicator roll is approximately in the expected range of 30-50 μm. The measured thickness was somewhat lower for the 2 wt% solution compared to simulations. This might have a multitude of reasons, some coming down to uncertainties of the applied measurement method in this context. For correct thickness computation, the measurement software requires refractive index correction, which was done based on the value of the solvent Isooctane that has a refractive index of 1.39 (Isooctane Data Sheet Carl ROTH). However, it has long been known that dissolved macromolecules can influence the refractive index of a solution depending on the wavelength of the incident light and the polymer concentration (Huglin, 1965; Sultanova et al., 2014), which could possibly mean a high correction term for this solution is needed, especially for higher weight percentages. Using the refractive index of pure Isooctane might in that case cause an underestimation of the actual thickness, even though the effect will not be large for the given concentration range. But this remains speculation as no literature data on this combination of solvent and polymer could be found. On the other hand, alignment of the measurement device is done manually therefore some degree of overestimation of the film-thickness due to an angle of deviation from the vertical is very likely.

As a second line of thought, it is equally possible that the measurement reflects a real experimental deviation, and the thickness is truly below the simulation value. One reason might be that the real filling height of the solution in the basin is below the height assumed in the basic CFD model. Later simulations for PolyActive™ used a modified version of the geometry, where the filling height is reduced which decreased the film thickness on the applicator roll by up to 10-20%, depending on the exact position. The exact filling height cannot be measured in the current setup and will also be slightly different for each experiment, as the overflow is adjusted manually be setting the volumetric inflow of the feed. While this had only a small effect of 5-10 % thickness decrease on the membrane coating in the PolyActive™ simulations, it might be enough to explain some of the deviation in confocal laser measurements of the film on the applicator roll. Furthermore, the measured thickness by the confocal laser shows strong fluctuation in the signal. Again, it is unclear whether this reflects an artifact somewhere in the measurement process or a true small variation of thickness on the rolls, for example due to vibrations in the coating device. Since the fluctuation do not appear to be random but show some periodicity, the latter explanation seems more likely.

Finally, the basic CFD model works under the assumption of an isothermal process, which was tested for via infrared temperature profiles. As shown in Figure 37, the temperature of the liquid stayed approximately at room temperature until the point where it was transferred to the membrane. Thus, it can be assumed, that the evaporative heat loss on the roll was compensated by an equal heat transfer from the solid applicator roll made of stainless steel. Even though the heat conductivity of

stainless steel is not as high compared to other metals, it is presumably high enough to prevent the formation of any temperature gradient in the liquid film. As soon as the liquid is transferred to the membrane, the membrane itself forms a thermal resistance, slowing down the analogous compensation process from the membrane roll. Moreover, when the membrane detaches from the roll, there is no compensating heat source anymore and the liquid cools down quickly. However, for the prediction of coating thickness only the force balance in the meniscus region is important. When the liquid leaves the meniscus, the amount of polymer on the membrane is fixed and temperature changes only affect the time until complete evaporation of the solvent. In other setups where the liquid films are thicker so that gravitational effects might play a role, this may not be the case. But here, the film thickness on the membrane is of the order of 5-10 μm and velocity gradients in the liquid film due to gravity can be neglected, Thus, the amount of polymer on the membrane is fixed as soon as the liquid film leaves the meniscus.

In summary, the initially implemented basic model delivers a good-enough prediction of the coated thickness to be used as a guide for the experimentalist when applying PDMS. As one interesting phenomenon, the model shows an increase of coated thickness when the gap size is reduced beyond a certain threshold. Notably, a decreased applicator roll speed can also increase the thickness slightly. From a fluid mechanical standpoint, this can be understood, as the decreased velocity changes the force balance in the gap region. When the applicator roll speed decreases, the relative membrane roll speed, which is dragging the liquid to the opposite direction, gets bigger. The phenomenon is illustrated in Figure 60. In consequence, a larger part of the liquid is transferred to the top, but the accuracy of the experiments conducted do not allow this effect to be validated. Still, both phenomena described above can also be seen in former studies on reverse roll flows, as presented by Gaskell *et al*. (Gaskell, Innes, et al., 1998).

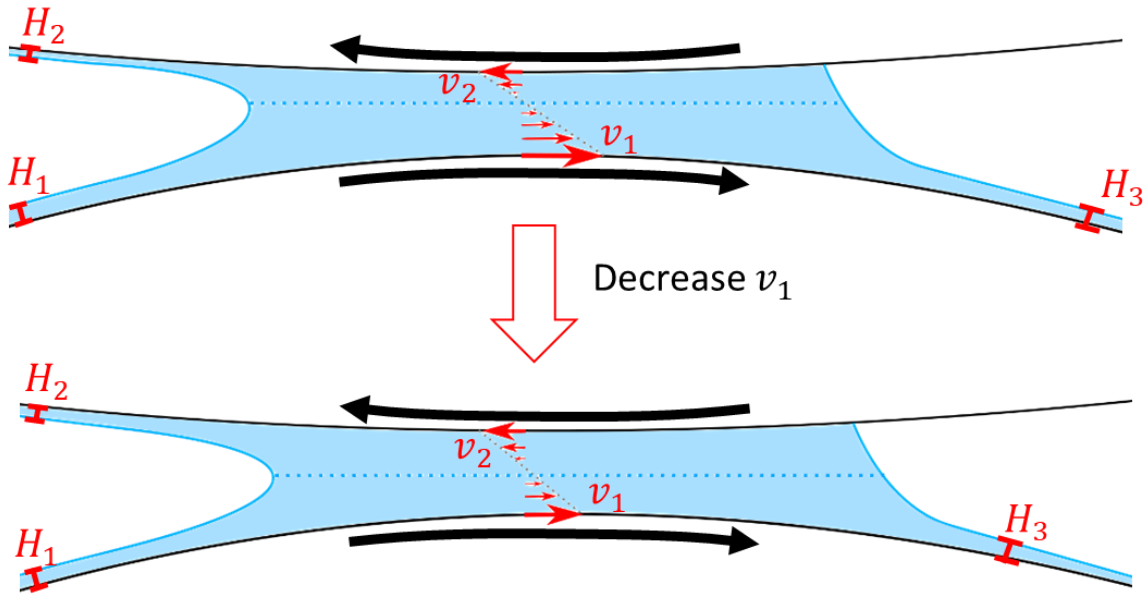

Figure 60 Schematic overview of the relative fluid forces in the middle of the meniscus region between applicator roll and membrane. A decrease of applicator roll speed v_1 increases the ratio between v_2 and v_1 and the force exerted by the membrane roll on the liquid is relatively stronger, hence pulling more of the liquid onto the membrane and increasing the film thickness H_2 on the coated membrane.

5.2 Application and extension of the CFD model for PolyActive™ coating

5.2.1 PolyActive™ in a solvent mixture

Performance of the standard model

Applying the thoroughly tested basic CFD model to the coating of PolyActive™ in a solvent mixture (see section 4.3) showed drastic and unexpected contradictions of the predicted thickness compared to the experimental values. Based on cross-sectional SEM images, the polymer thickness was increased by a factor 4-5, while the integral measurement via mass loss suggests a slightly lower but still significant thickening of factor 3-4. The somewhat different findings in these two experimental approaches might be explained to some extent by the variation of coating thickness along the axis of the applicator roll, as shown in Figure 50. Towards the edges of the roll, the coating thickness seems to increase slightly, which is probably caused at least in parts by the evaporation of solvent in the basin. Since the feed solution is fed in at the axial centre point in the basin, the polymer concentration is still very close to the feed concentration at this point. The solution then flows towards both overflows at the edges of the basin and solvent evaporation along the way causes an increase in polymer concentration, thereby increasing the viscosity and thus coating thickness. Furthermore, the inertial forces of the incoming feed flow at the centre might also locally affect the filling height and meniscus shape, influencing the thickness H_1 on applicator roll as well. This must be kept in mind when looking at cross-sectional SEM images, which are often taken somewhere between the centre and the edge of the coated membrane area. Nevertheless, taken together the experimental results point towards a thickening effect of approximately factor 4 for PolyActive™ coating when compared to the basic CFD model predictions. Hence, it must be concluded that one or more simplifying assumptions made in the basic model do not hold for the changed polymer and solvent.

Looking at the main forces that determine the coating thickness in the roll-to-roll process, pressure variations from the pumps and velocity gradients due to gravity can almost be neglected. The dominating forces are viscous forces, surface tension forces and inertial forces, which follow from the interaction of viscous forces and no-slip boundary conditions of the rotating system. Because of the successful PDMS benchmark, there is no apparent reason to doubt the basic validity of the chosen two-dimensional CFD model and the benchmark studies also suggest, that the chosen mesh is resolved finely enough to compute correct velocity gradients and thus inertial forces. It therefore seems likely, that either some form of non-Newtonian viscosity effect (see sections 2.3.2) or gradients of surface tension (see section 2.4.2) occur for this polymer/solvent system. Of course, any combination of both effects is also possible.

Before going into the viscoelastic and Marangoni extensions of the model, some additional analysis was done with the basic model and should be discussed briefly. Comparisons of both model geometries indicate that the filling height of polymer solution in the basin influences the film thicknesses on both applicator and membrane roll that perhaps should not be ignored. This effect is no surprise, as the reduced filling height in this system also means a reduced angle of inclination of the applicator roll wall with respect to the liquid. For the film thickness to stay the same in this situation, the meniscus curvature would have to increase, which is unfavourable in terms of surface energy. Thus, the surface tension provides an increasing counterforce for sharper coating angles (meaning the angle between roll surface and liquid surface in the lower meniscus region gets sharper), an effect that is well-known and exploited for plate dip-coating applications (Arfsten et al., 1997).

Albeit not being dramatic in the effect, the second geometry with reduced filling height is assumed to provide better predictions, especially for the liquid film thickness on the rolls, which is why these simulations were chosen for comparison with experimental film measurements. In addition, the reduced amount of liquid in the gap region that corresponds to the reduced film thickness is also assumed to be more accurate and simulations concerning dynamic contact angle sensitivity were also performed with this geometry. The results are briefly discussed in the paragraph on surface effects following later in this section.

Validity of the isothermal assumption

As described in the theoretical background, both viscosity and surface tension depend on temperature, which might change during the coating due to enthalpy of evaporation. However, mass loss measurements of the evaporation rate show an even smaller evaporation when compared to Isooctane in the PDMS benchmark. This probably comes down to the fact that SMC3 is the only component of the solvent system that is very volatile, but only constitutes 25 wt% of the solvent. Since the overall evaporation rate is lower than for Isooctane, while the enthalpy of evaporation of SMC 3 is comparable to that of Isooctane, it is thus unlikely that temperature variations play a significant role in the observed deviations. This is underpinned by the findings in infrared temperature profiles (see Figure 38), which essentially show the same stability of temperature for the liquid on the applicator roll as already discussed for the PDMS benchmark. Hence, the isothermal assumption can be assumed to be valid as well.

Surface energy effects at the phase-interface

A more plausible explanation may start by asserting that the main difference between the PDMS benchmark and PolyActive™ coating probably lies in the nature of the utilized polymer. While PDMS is a homogeneous chain of dimethylsiloxane monomers, PolyActive™ is a MBCP which consists of two alternating blocks, namely PEO and PBT. As the PEO block is more hydrophilic than the PBT block, the polymer is thus amphiphilic and might show surface activity, as found four similar MBCP's in the literature (see section 2.4.2). The following schematic depiction (Figure 60) should illustrate the inhomogeneous surfactant distribution that might arise from a surface velocity gradient, as it is present in the in the roll coating device (for instance at the lower meniscus region). The schematic depiction was motivated by literature findings for dip coating and the governing equations describing the phenomenon were then adapted to the roll-to-roll coating device employed in this thesis, as described in the methods section (3.8.3).

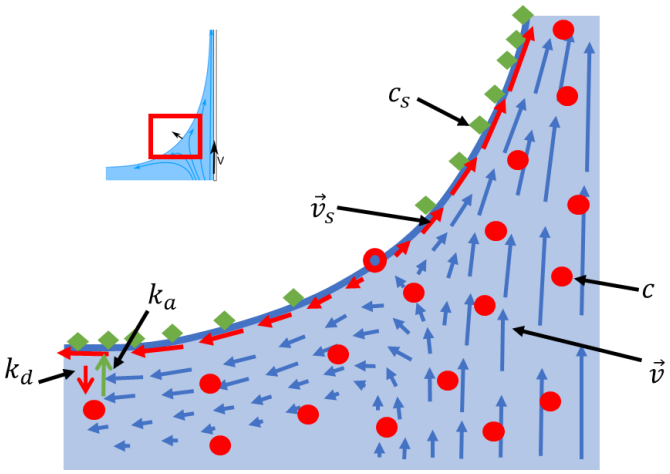

Figure 61 Graphical representation of the Marangoni extension to the CFD model. The model assumes a surfactant like behaviour of the polymer and distinguishes between the polymer in the liquid (c) and bound to the surface (c_s). A Langmuir adsorption/desorption kinetics (with constants k_a and k_d) describes the equilibrium between both. Due to differences in surface velocity v_s, surface areas with a high surface-velocity gradient get 'diluted' in surfactant concentration, leading to a minimum of surface concentration at the stagnation point of the meniscus, where the gradient of surface velocity is maximal.

Thus, to model the effect of a surface-active polymer on the surface tension in the coating process, a surfactant mass balance was implemented and coupled to the surface tension via a Volmer isotherm. Caused by the substantial surface velocity gradients along the phase interface of the coated liquid, the surfactant mass balance yielded strong gradients in surface concentration of the presumed surfactant polymer. Figure 54 shows the surface concentration profile along the interface of the lower and upper meniscus of the roller coating device.

The inhomogeneous distribution of surfactant can be explained by the surface velocity gradients that are schematically depicted in Figure 63. As described in section 2.2.1, a positive gradient in surface velocity corresponds to a stretching of the interface, which has a diluting effect on the surfactant concentration. Vice versa, a negative gradient corresponds to compression and increases the surfactant concentration. The stretching effect can be found at three stagnation points (that are points where surface velocity is zero) where a thin liquid film leaves both the lower meniscus (stagnation point I in Figure 63) and upper meniscus (stagnation point III and IV in Figure 63). Here, inertial and viscous forces are in balance with the counteracting surface tension forces, that try to minimize curvature and therefore constrict the liquid film formation. That part of the liquid with high enough momentum to overcome surface tension forces forms the liquid film on the applicator or membrane roll, respectively. The remaining liquid diverges, as it must change its flow direction away from the film, thus causing a surface velocity gradient. On the other hand, the upper meniscus also contains two stagnation points where the surface velocity gradient is negative, and the interface gets compressed (stagnation points II and V in Figure 63). Stagnation point II is found when the incoming liquid on the applicator roll enters the meniscus region and meets that part of the liquid that did not go on the membrane. The latter part of the liquid cannot continue its path and must move inwards, following the liquid on the applicator roll. The second stagnation point with a compressing effect can be found on the opposite site of the meniscus, at the dynamic contact line of the meniscus with the moving membrane surface (stagnation point V). Here, the surface flow of the liquid decelerates as the liquid cannot penetrate the membrane 'wall' and must have a wall-normal velocity of zero directly at the contact point, thus also causing an accumulation of surfactant at this point.

In effect, the inhomogeneity of surfactant concentration causes an inverse gradient of surface tension, with the minimum of surface tension being found at the point of highest surfactant concentration. As

described in section 2.4.2, the difference in surface tension - or surface pressure – induces a secondary flow which is called Marangoni effect. In the roll-to-roll system this has essentially two effects.

Firstly, for slow enough adsorption rates of the surfactant, the film thickness H_1 on the applicator roll increases to some degree. This can be understood as follows: the stretching at stagnation point I dilutes the surfactant and if the applicator roll velocity is much higher than adsorption rate of the surfactant, the surfactant concentration stays low on the roll. i.e. the right side of the stagnation point. On the left side, there is no high surface velocity, and the equilibrium concentration is restored more quickly. This creates a net surface pressure gradient from left to right with a secondary flow that goes on top of the applicator roll film. For an illustration of this effect, see Figure 62. This thickening effect is also described in the literature and well known for simple dip-coating applications on a vertical plate (Daripa & Paa, 2009; Delacotte et al., 2012; Rio & Boulogne, 2017). The described effect on the coating flow pattern is explained in detail and also experimentally visualized in the work by Mayer *et al.* (Mayer & Krechetnikov, 2012)

Secondly, the surfactant distribution along the interface of the upper meniscus also creates a secondary flow pattern that essentially forms a 'shortcut' which directly transfers some of the incoming liquid from the applicator roll to the membrane. Even though stemming from very different causes, the pattern of the secondary flow is reminiscent of the secondary transfer jet that can be found in the flooding regime of the upper meniscus region (see Figure 47). Like the thickening on the applicator roll, it can also be understood mechanistically from the surface tension gradients.

As discussed before, the surfactant accumulates at stagnation point II. Here the surfactant concentration is increased with respect to concentration on the interface of the incoming film on the applicator roll. Thus, the surface tension is higher on the left side of point II than on the right side. In principle, this would create a Marangoni-convection from right to left. However, the molecules on the applicator roll have a much higher momentum in the other direction (transferred from the applicator roll via viscous interaction) and the surface tension gradient is not big enough to overcome this.

Looking at point III, the situation changes. Here, the fluid dynamical conditions are very similar to that of point I. At point III, the surfactant gets diluted and on the left side of point III it will stay so for a time that is dictated by the ratio of membrane roll speed v_2 and adsorption rate k_a. On the right side of point III, along the curvature of the meniscus, the surfactant concentration soon rises again due to the surfactant adsorption flux and the compression of the interface towards point II. Like for the lower meniscus, this creates a net surface pressure difference along the meniscus which is the driving force of a Marangoni-convection going from point II onto the membrane. On the other side at the outlet of the meniscus, there is an analogous situation at point IV. However, quantitatively the effect is not as strong as the surfactant concentration gradient is less pronounced here. Taken together, the Marangoni effect firstly increases the amount of liquid on the applicator roll and subsequently forms a direct transfer jet from the incoming liquid, thereby increasing the ratio of H_2 versus H_3. The strength of this effect depends on the adsorption constant, as fast adsorption kinetics will annihilate concentration gradients quickly (see Figure 52). However, this only works until a certain maximum is reached, as further decrease in adsorption rate means a dilution of surfactant beginning at stagnation point I will carry on along the whole interface of the meniscus region, effectively depriving the upper interface of surfactant and thus diminishing its effect. A lower desorption rate, and therefore higher surface coverage constant K_c, means, that a higher enrichment of surface concentration can be sustained, thereby increasing the impact of the described Marangoni effect. The lowest adsorption and desorption rates computed in the Marangoni parameter study are still quite fast in comparison to literature data, where interfacial adsorption rates of polymers are on the order of 0.01 $m^3/(mol \cdot s)$ (Diéz-Pascual et al., 2007). Such low adsorption rates are numerically very challenging to compute as

they correspond to a much higher adsorption time compared to the characteristic flow time of the system, thereby making the differential equations stiff and leading to convergence problems. It is for this reason that the parameter range of adsorption constants was not extended in the simulations. On the one hand, this introduces some quantitative uncertainty in the model results, as it could mean, that the strongest thickening effect seen in these simulations may not be realistic. On the other hand, it should also be noted that the low adsorption rates of polymers at interfaces in the same literature are attributed to the low diffusion speed of polymers, which is thought to be the time-limiting part of the process, while the adsorption from the direct subsurface to the interface is thought to happen more quickly. It is unclear in how far this bottleneck applies in the roller-coating setup, as simulations show no strong effect of surface accumulation of PolyActive™ on the bulk concentration (see Figure A 25 in the Appendix), suggesting a quasi-static bulk concentration and therefore enhanced adsorption capacity. Because of this finding the coupling between bulk and surface concentration was omitted in most simulations to reduce the computational effort.

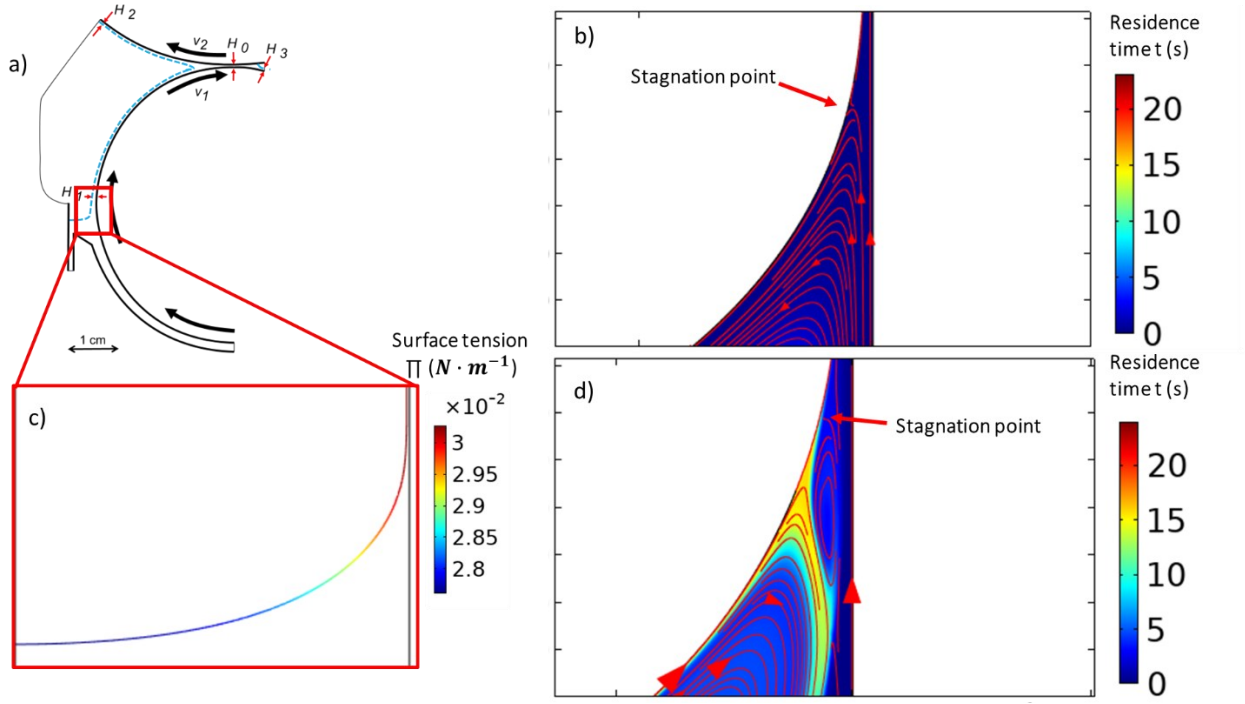

Figure 62 Overview and flow fields from CFD simulations with (c+d) and without (b) Marangoni effect at the lower meniscus of the applicator roll. Picture a) highlights the position in the overall geometry. Picture c) shows the gradient of surface tension along the meniscus interface, following from the surfactant concentration being higher at the left side of the meniscus than on the right side. Picture b) and d) show streamlines that show the flow field. Without Marangoni effect (b), there is a stagnation point on the interface where the fluid has not taken up enough momentum from the applicator roll and reverts its flow direction. When a surface tension gradient is present (d), there is a secondary flow pattern that transports liquid from the left-hand side of the meniscus to the right and onto the applicator roll.

Some experimental observations made in contact angle measurements might underpin the proposed surface activity of PolyActive™. On the more hydrophobic Teflon surface, the initial contact angle was higher, indicating a lower liquid/solid interaction. In contrast to the homogeneous droplet shrinking (meaning constant contact angle and shape during shrinking) for the pure solvent, the polymer mixture effectively showed a pinned contact line that causes a decrease in contact angle. In the literature, numerical simulations of droplet evaporation with insoluble surfactants explained this behaviour with the decrease in surface tension near the contact line due to the increase of surfactant concentration that could not equilibrate fast enough via diffusion (van Gaalen et al., 2020). Moreover, experimentally the dynamic contact angle could be shown to decrease with increasing surfactant concentration in aqueous solution (Semenov et al., 2013). However, in the case of a PDMS base gutter layer surface,

this was not observable and the apparent difference in contact angle after 50 s is probably not big enough to be considered significant, given the fluctuation of the contact angle during the measurement.

The prolonged time that a droplet of polymer solution was visible on the Teflon surface could in theory be attributable to a decrease of solvent evaporation due to a blocking effect of surfactants at the interface. However, the explanatory power of this theoretical phenomenon is often challenged or not confirmed in the literature (Akanno et al., 2021; Lunkenheimer & Zembala, 1997). An alternative explanation could be, that the diffusion of solvent into the substrate, which was visible in all experiments, is slowed down in this case as the polymer concentration will also rise at the solid/liquid boundary and increase the viscosity, which would hinder solvent diffusion. By the same rationale, the contact line pinning could also be caused or at least supported by this accumulation effect of polymer. If the hydrophobic segments of the polymer adsorb to the surface, while the hydrophilic parts reach inwards to the liquid, this could increase the average surface interaction with the solvent, thus promoting stronger wetting.

In this context, a few further remarks to the CFD model should be made regarding the dynamic contact line at stagnation point V. As explained in section 2.4.1, the hydrodynamic situation here is very complicated, as this point marks a dynamic wetting line. Based on the contact angle measurements (see section 4.2.5), the static contact angle of the PolyActive™ polymer solution on PDMS can be estimated to be approximately 35°, which is much lower than the default contact angle of 90° assumed at the dynamic contact line in COMSOL. However, the relative movement of the membrane effectively makes this an advancing wetting line, where the advancing contact angle must be considered. Advancing contact angles are generally much higher than static ones, the exact deviation depends primarily on the capillary number *Ca*. Experimental studies for a range of *Ca* numbers showed an increase of contact angle from 65°(static) to 85° (advancing), even for $Ca < 10^{-2}$ (Shikmurzaev & Blake, 2002). Nevertheless, in this case the advancing contact angle could still lie beneath the assumed value of 90°. Therefore, simulations with an advancing contact angle value of 75° and 60° were carried out but yielded no substantial effect on the final film thickness (see Figure A 18 in the Appendix). As a primary observation, the right side of the meniscus is shifted away from the centre of the gap, while the left meniscus does not change. This appears logical, since a lower contact angle corresponds to a higher surface energy of liquid/solid, thus a higher amount of liquid can be contained in the gap region. But, at least in the conducted simulations, this had no substantial effect on the force balance in the meniscus and consequently film thicknesses. Looking at the experiments, this might not come as a surprise, since the assumed deviation of contact angle should be most pronounced for smaller viscosities (and thus smaller *Ca*), but the observed thickening effect does not appear to depend on viscosity. Furthermore, the coating of PDMS in isooctane operates at very similar *Ca* numbers and here the default value of 90° was apparently a good enough to predict correct coating thicknesses over the whole viscosity range tested.

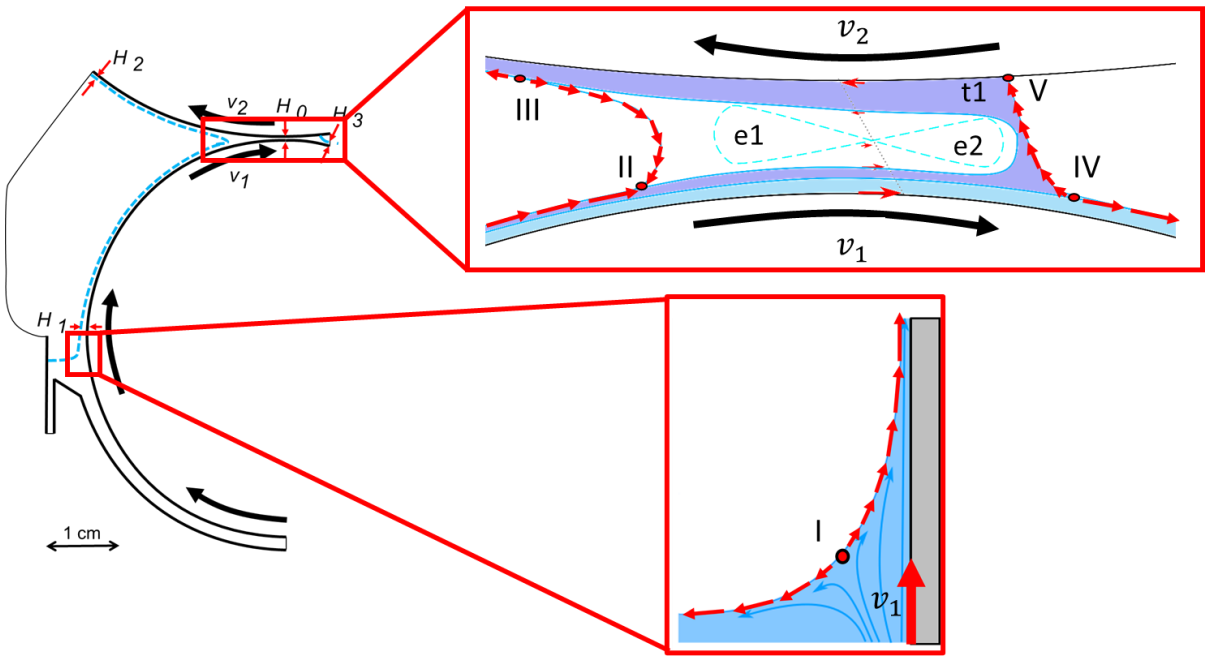

Figure 63 Schematic representation of the roll-to-roll coating device on the left, highlighting the surface velocities in the lower and upper meniscus region on the right side. Red arrows on the interface indicate the surface velocity vector, while red dots with black contour indicate stagnation points where the surface velocity is zero.

Another factor influencing the surface tension is the composition of the solvent. As explained before, the evaporation during the coating procedure is primarily driven by the volatility of SMC 3. Since SMC 3 has the lowest surface tension among the three solvent components, a decrease of SMC 3 content could be expected to increase the surface tension of the mixture. Analysing the residence time distribution of the liquid in the meniscus region, the only point where a significant gradient in residence time - and thus presumed SMC 3 content – occurs is at stagnation point II. Here the incoming liquid meets that part that already travelled through the complete gap region. The resulting gradient in surface tension would then enhance the Marangoni effect of surfactants that was described above.

However, the difference in residence time at this is only a few seconds. Given the evaporation rate of 0.57 g/m²s, this translates to 0.008 mol/m²s for SMC 3. For a residence time difference of 5 s this yields an absolute loss of SMC 3 of 0.04 mol/m². Considering that the initial concentration of SMC 3 for 25 w% is approximately 4000 mol/m³, it seems very unlikely that changes of solvent composition due to the residence time gradient have a significant impact on the surface tension.

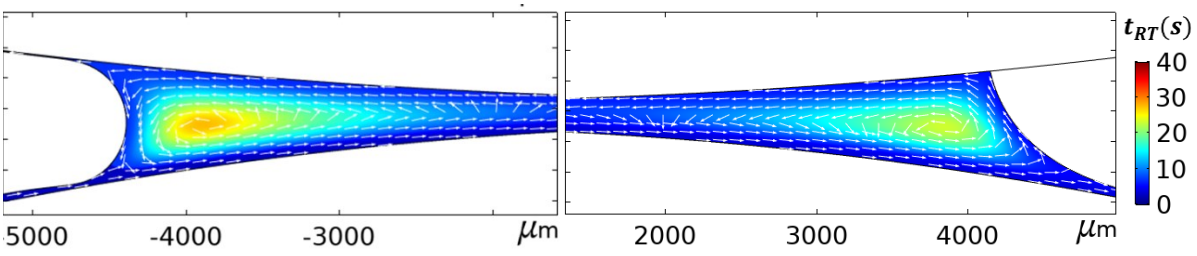

Figure 64 Residence time (t_{RT}) distribution in the upper meniscus region as computed by the standard CFD model for a 1 wt% PolyActive™ solution and applicator roll speed of 0.045 m/s.

Viscous interactions to explain the thickening effect

Looking at simulation results in Figure 56, a second explanation of the thickening effect could be found if the polymer shows viscoelasticity. This hypothesis derives its reasoning from the mechanics of viscoelastic polymer solutions in high shear regions, as presented in section 2.3.2. The following schematic depiction (Figure 65) should illustrate, why the incorporation of viscoelastic phenomena might be worth the investigation.

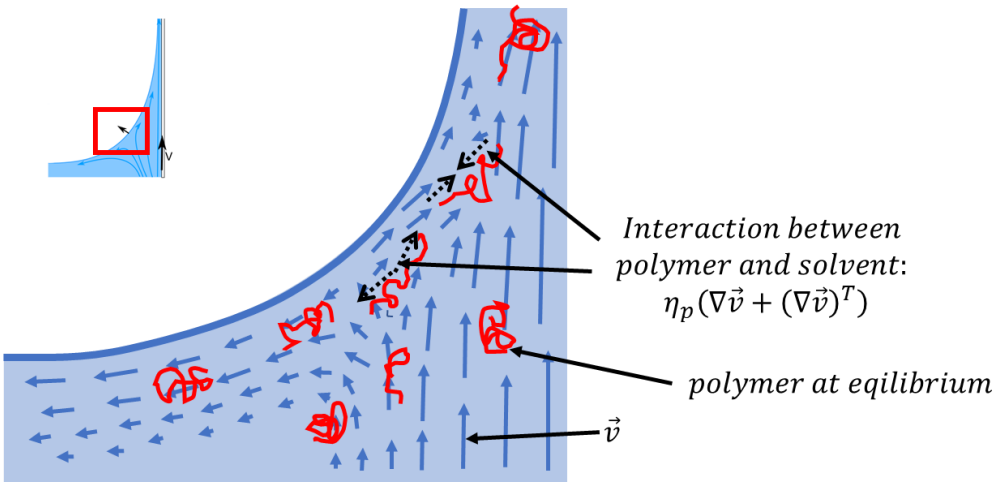

Figure 65 Graphical representation of the proposed viscoelastic effects added to the CFD model. Assuming elastic effects of the polymer, the polymer-solvent interactions are complicated by the fact, that the polymer is first stretched by drastic changes in shear or strain, as present near the stagnation point of the meniscus. The polymer thus stores some of the mechanical energy and will then start to give it off to the surrounding solvent, as the external stress vanishes further upstream. The increase in polymer-solvent interaction might cause a thickening of the film, similar to the swelling effect as it is known to be observed for viscoelastic liquids flowing out of a nozzle.

Consequently, a viscoelastic FENE-P model was implemented as described in section 3.8.3 and simulated for the coating of 1 wt% PolyActive™ solution. For low enough relaxation time, the system shows a thickening on both the applicator roll and the membrane, which increases with the viscous interaction parameter. The resulting effect can probably be compared to the thickening phenomenon in extrusion flows (see Figure 14). Directly at the point where the liquid film leaves the meniscus, for example above stagnation point I, the shear and strain rates in the liquid flow rise drastically (see Figure A 26 and Figure A 27 in the appendix). This is explained by the fluid mechanical situation near the stagnation point of a meniscus. Directly at the stagnation point the pressure due to surface tension equals the viscous stress that drags the liquid molecules along with the roll. Here, the liquid just below the stagnation point has not enough momentum to overcome surface tension and is accelerated downstream from the stagnation point, while the liquid that is closer to the roll has enough momentum and is accelerated upwards above the stagnation point. The acceleration along the streamline (directly at the surface and also in the sublayers just beneath) corresponds to a strain rate, while the thereby created velocity gradient perpendicular to the roller-wall (where the velocity is fixed due to the no-slip condition) corresponds to a shear rate.

In this region, the polymers get stretched due to the strain and, if the relaxation time is very small, start to contract almost immediately. Only if that process happens fast enough, can the viscous interaction of the contracting polymer molecules exert a force on the surrounding liquid and drag an increased part of the liquid onto the film, which would have been stopped and redirected by the surface tension otherwise. Of course, this effect is more pronounced if the viscous interaction parameter is bigger.

To see the biggest possible effect, the simulation parameters were based on the zero-shear (Figure 34) and viscoelastic measurements of 1.5 wt% PolyActive™ solution (Figure 36). The zero-shear measurements pointed to a viscous interaction parameter around 2 mPa·s (difference to pure solvent viscosity). The viscoelastic measurements can in principle allow for an estimation of the relaxation time (Sunthar, 2010) as $\lambda = G` \cdot G``^{-1} \cdot \omega^{-1}$ and thus on the order of 0.1 ms, which fits to the values found in the literature (Zilz et al., 2014). Hence, the chosen parameters of the viscoelastic simulation model should be in a realistic range. However, these experimental results must be regarded with caution. The viscoelastic measurement results are only evaluable in the linear region above an oscillation frequency of 200 s^{-1} and no set of parameters could be found that fitted both the elastic and viscous modulus curve well. For lower shear rates, both the viscous and elastic modulus fluctuate as the results are below the resolution limit of the device. For higher shear rates above 10^{-2} s^{-1}, values for both moduli could be obtained but show no strict linear behaviour. Moreover, linear regression to determine the relaxation time (which would be more precise) was not delivering a good fit for both moduli curves at the same time. Due to the relatively low viscosity of the solution, artifacts in the measurement due to inertial effects of might be a possible source of error (Laun et al., 2014). Furthermore, the low intrinsic viscosity and experimental observation of precipitation above 1.5 wt% solutions indicate suboptimal or even bad solvent quality. Under these conditions, a high shear field can possibly induce phase separation of polymer solutions that can also influence viscosity (Yanase et al., 1991). Albeit being reported for more viscous polymer solutions, which also show shear thinning before this effect sets in.

Nevertheless, the given parameter range still appears reasonable. As elaborated in the mathematical analysis of the FENE-P model in the work of Wagner *et al.* (Wagner et al., 2015), the viscous interaction parameter can be estimated by the Huggins equation fitting the zero-shear viscosity of a polymer solution over a range of concentrations. The viscous interaction of the polymer η_p should be the difference between the total zero-shear viscosity η_0 and the solvent viscosity η_s. As the solvent viscosity is approximately 1 mPa·s and the zero-shear viscosity for 1.5 wt% PolyActive™ solution is approximately 2.4 mPa·s (see Figure A 3), the viscous contribution of the polymer can be estimated to be around 1.4 mPa·s, thereby being in the same range as the average fitting result from viscoelastic measurements. For the relaxation time, literature data provides similar results around 0.1 ms for PEO homopolymer solutions with Mw=10^6 Da and solvent viscosities around 1-2 mPa·s (Sur & Rothstein, 2018; Zilz et al., 2014). Higher relaxation times of 1 ms are only found for much bigger polymers (10^7 Da) or higher solvent viscosity, both indicative of stronger molecular interaction that prevent a fast relaxation (Sur & Rothstein, 2018). This, however, also implies that any elastic component of the stress in PolyActive™ solution should be even smaller for decreasing concentration of the polymer, rendering a viscoelastic thickening effect for the 0.5-1 wt% solution unlikely.

Furthermore, from Figure 57 it is also clear that the viscoelastic thickening effect is primarily found on the applicator roll. The film on the membrane subsequently also thickens, but not as much. Most of the thickening effect does not impact the final membrane coating. This likely comes down to the fact that the fluid dynamical situation in terms of shear and strain rates at both exit points of the upper meniscus (i.e. after stagnation points III and IV) is very similar and thus there is no mechanism that would increase the ratio of film H_2 with respect to H_3. A thickening of H_2 must therefore be mostly driven by a thickening of H_1, that is an increase of the incoming liquid in the meniscus. For this effect to be significant, it should be observable in the confocal laser measurements of H_1 and H_3. However, these measurements show no drastic deviation from the prediction of the basic model (compare results in section 4.3.3). The thickness on the applicator roll is relatively close to the value expected for a Newtonian liquid and also close to the value found for PDMS solutions, which has very similar viscosity (section 4.2.3). Of course, the same reservations concerning the confocal laser measurement accuracy must be made as discussed for PDMS. The polymer solution will affect the refractive index in

some way, which is further complicated due to the more complex character of a solvent mixture. Again, the alignment of the measurement device is done manually, leaving the possibility of an overestimation of film-thickness due to an angle of deviation from the vertical.

Further experiments can certainly be done to investigate the rheology of PolyActive™ solution but, all in all, viscoelasticity does not seem to hold up as an explanation for the found thickening effect. In the literature, even though investigated in aqueous solution, PEO homopolymers of similar size were considered non-elastic, while elasticity was important for longer polymer chains (M_w>10^6 Da)(Kim & Rothstein, 2015) , thereby also supporting this hypothesis.

Similar arguments can be made for shear rate dependent viscosity. Experimentally, shear rate dependence of the PolyActive™ solutions could not be identified clearly. There is an apparent rise in viscosity for high shear rates (4.1.4), but is much more likely to come from Taylor vortices (Schrimpf et al., 2021) (as explained in the theoretical part 2.3.2) since it also happens for the pure solvent and the onset of viscosity rise is delayed towards higher shear rates for a higher polymer content. If the effect was no artifact of the measurement and an actual property coming from the polymer in the liquid, this should not be the case. And even if it was true and the polymer solution was truly shear-thickening, by the same reasoning as given before, this should give a substantial increase of film thickness on the applicator roll, as shear rates go up drastically near the exit point of the liquid film from the meniscus.

For very low shear rates, the viscosity decreased in all measurements. This is likely due to the resolution limit of the rheometer, as the combination of a low-viscosity liquid and low shear-rates produces a very small torque to be measured and the results in that region (shear rates of 2-3 s^{-1} and below) are thus likely not reliable (Laun et al., 2014). However, this should not be of great concern, as the shear-rates in the roll-to-roll setup, especially in the critical meniscus region, are expected to be well above that (see Figure A 26).

Conclusion on the most likely explanation of the observed thickening

Considering all of the above points, Marangoni effects seem to explain the observed deviations from the standard model best. If anything, the confocal laser measurements of film thickness H_1 suggest only a small thickening that can also be explained by the Marangoni effect (see section 4.3.4). More importantly, in contrast to any viscosity related effects, the Marangoni effect can explain the relative increase in film H_2 with respect to H_3, thus explaining how the membrane coating increases significantly even though the film on the roll seems to be roughly as expected. Even more, for a suitable choice of model parameters the Marangoni model was able to yield thickening factors almost big enough to explain the empirically found deviations. For the viscoelastic model this was not possible in the presumed parameter range. Nevertheless, further research should be dedicated to this hypothesis, e.g. by highly accurate surface tension measurements of the solvent mixture and polymer solution with other devices as were available in this thesis. Earlier studies from the same research group at Hereon already used atomic force microscopy on coated PolyActive™ films and concluded, that the polymer rearranged its hydrophobic hard PBT segments to interact with the hydrophobic PDMS layer (Yave et al., 2011), while the more hydrophilic parts point outwards. While this should be reproduced with the current setup and solvent mixture, it is still intriguing. On the one hand, this would mean that the polymer molecules, which are supposedly arranged with their hydrophobic parts pointing outwards of the (mostly) hydrophilic liquid, would undergo a 180° rotation to align their hydrophobic parts with the PDMS layer, when the solvent further evaporates, and solvent-polymer interactions become less important than surface-polymer interactions. On the other hand, these findings also point

towards the amphiphilic character of the polymer. Measurements of surface roughness could also be done and juxtaposed with homogenous polymers like PDMS, which do not seem to show a Marangoni effect (Brennecke et al., 2021), but the hydrophobic interaction of polymer and surface complicates the issue and any differences in surface roughness, which might be indicative of a distinctive structure and conformation of the coated polymer, could thus only reinforce the notion of amphiphilicity, but do not necessarily prove the proposed surfactant-like properties.

Finally, there is another possible violation of the basic model assumptions remaining, which concerns the hydrodynamics at the coated membrane surface in the gap region. In all simulations, the membrane surface is treated as an impermeable wall and a no-slip condition is applied. Both implementations could be problematic to some degree. It is expected and clear from experimental observations that SMC 2 and 3 can permeate easily into the membrane substrate, thereby increasing the polymer concentration at the membrane surface, which would increase the viscosity. Given the residence time distribution in the gap (see Figure 64), this is unlikely to play a substantial role as the contact time of the solution with the membrane until it leaves the meniscus is less than one second. Nevertheless, some part of the thickening effect could be attributed to this rise in local polymer concentration. Moreover, the solvent-diffusion induced increase of local concentration together with some degree of surface adsorption of the polymer due to hydrophobic interaction with the gutter layer might create a boundary layer of polymers with concentrations high enough to be considered semi-dilute. For such a hydrodynamic situation, the no-slip condition might not apply any more, as elaborated in recent literature (Guyard et al., 2021). But again, given the timescale of the process the adsorption of polymer would have to happen within one second of contact with the membrane surface to be relevant for the effective film thickness. The short contact of liquid and membrane inside the meniscus region is most probably not enough to explain a thickening factor of 3-4, especially given that the observed thickening effect does not depend on the initial feed concentration. If the above stated effects were substantial, the effect should be more pronounced for higher feed concentrations that are already close to the semi-dilute regime.

5.2.2 PolyActive™ in pure SMC 3

The initial idea in using pure SMC 3 as a solvent was to eliminate the possibility of surface tension gradients due to inhomogeneous solvent mixture along the phase interface on the coating rolls. It was therefore expected that the thickening factor for PolyActive™ coating would either stay the same - if the solvent mixture had no significant effect on surface tension gradients - or decrease if the surface tension gradient was at least partially driven by changes in solvent composition. Surprisingly, neither was the case, as the thickening again increased substantially in both mass loss measurements and SEM images. One possible explanation lies in the fact that by changing the solvent to SMC 3, its high volatility also meant a great increase in evaporation rate (compare evaporation loss measurements in 4.3.1 and 4.4.1) and therefore heat loss. The evaporation for pure SMC 3 was more than three times higher compared to the solvent mixture. This is not surprising, as SMC 3 is the only component in the solvent mixture with high volatility. Assuming only SMC 3 evaporates in the mixture and aerodynamic conditions in the air domain of the coating apparatus were very similar in both solvent systems, the difference in evaporation is primarily determined by the difference in saturated vapour pressure found directly at the gas/liquid interface. For an ideal mixture, the Raoult law gives the partial vapour pressure of one component in a mixture as the product of its molar fraction with the saturated vapour pressure of the pure component. In real mixtures, the vapour pressure in the mixture is usually somewhat higher. As the molar fraction of SMC 3 is approximately 0.33 in the solvent mixture, an

increase in evaporation rate of a bit more than factor three for pure SMC 3 is therefore very much expected.

Apparently, the increased evaporative heat loss also affected the temperature profiles in the liquid domain of the coating device. In all the investigated cases, the infrared images of the liquid films showed a cooling of about 5 Kelvin compared to room temperature (see section 4.1.3). Temperature dependent simulations of this system conclusively suggest that this can only be explained by a temperature gradient inside the metallic applicator roll. This might seem surprising, since the heat delivered from the metal of the applicator roll should compensate the evaporative heat loss relatively fast, given that the heat conductivity of stainless steel is a factor 100 higher than the heat conductivity of SMC 3. However, looking at the film on the applicator roll, a thickness of around 30-40 μm is simply not big enough to yield any significant temperature gradient between the metal and the phase interface based on the heat conductivity of pure SMC 3. From that perspective, the simulation results are therefore plausible and a temperature gradient inside the solid roll seems to be the only viable explanation.

However, a temperature drop of 5 Kelvin (or even more) is likely not that important if it is homogeneous across all of the liquid domain. Corresponding changes of viscosity and surface tension due to temperature are not very big and the force balance in the upper meniscus would stay almost the same. Much more important though are gradients of temperature, since these produce gradients in surface tension that induce Marangoni flows, as already discussed for polymeric surfactants (section 5.2.1). So far, simulations only yielded relatively small temperature gradients that are found directly at the exit point of the coated membrane. If the heat conductivity of the coated membrane is low enough, the compensation of heat loss is hindered, and a cooling effect of the liquid will take place over time along the length of the membrane. The lower temperature then translates to a higher surface tension (see section 2.3.1) driving a Marangoni flow coming from the meniscus and going onto the membrane. The induced surface tension gradient is relatively small but can still produces a Marangoni convection big enough to be visible in the simulations. Nonetheless, the effective thickening effect on the coating film is not remotely high enough to explain the experimental findings of the coating thickness. A convincing explanation for the drastic increase of polymer thickness is not provided by these simulations.

But several comments can be made to this. The non-isothermal model, even though being a more realistic representation of reality, still uses several simplifications that could potentially affect the outcome. Both heat capacity and heat conductivity were assumed to be constant and equal to that of pure SMC 3, thus ignoring the influence of the dissolved PolyActive™ polymer. Realistically, both values depend on the polymer and differences in polymer concentration could therefore also induce differences in temperature distribution. Moreover, considering the assumed surface activity of PolyActive™ and respective simulation results hinting at an inhomogeneous surface concentration, the difference in thermal properties should be most pronounced at the phase interface. In addition, the problem gets even more complicated as the evaporation rate is presumably not constant along the interface, as assumed in the CFD model, but also changes due to the difference in polymer concentration along the interface. A very high coverage of the interface with polymer molecules should prevent the local evaporation at least to some extent. Lastly, the evaporation also depends on the aerodynamics in the air domain. The coating apparatus contains an extraction of air at the front side of the applicator roll, which probably means the evaporation is higher on that side compared to the back side, which might increase the effect of heat loss at the frontal meniscus even further.

All these considerations could not be tackled in simulations in the scope of this thesis, and it is not clear, whether the stated effects can be realistically incorporated into the two-dimensional model. The

fast evaporation rate in this case also leads to a quick decrease in liquid film thickness H_2 (around 2 μm for the 3 wt% solution), which gets numerically very difficult to handle. At such small films, the continuum approach starts to become problematic. The polymer distribution is computed with a convection-diffusion equation and therefore not modelled discretely but rather as continuous entity. If the size of the liquid domain is much bigger then the polymers, this might be a valid approach but when the film is only two orders of magnitude bigger than the polymers itself, this will become problematic. Among others, some effects of the high evaporation might also be that the precipitating polymers do not assume their equilibrium density in the solid state and perhaps obtain a higher FFV. This could possibly also explain the difference between the observed thicknesses in SEM images and the derived values form mass loss measurements, which were lower than the SEM results. If the density of the polymer on the membrane is lower than the equilibrium density in its dry form, this would mean that the final thickness on the membrane is bigger than what would be expected from the mass loss measurements, which essentially compute the thickness by dividing the mass loss per membrane area through the assumed (equilibrium) density. To test this hypothesis, further gas permeability tests of the obtained membrane should be done in the future, as this effect should be visible in both permeance and selectivity. Further insight might also be generated by other modelling approaches based on molecular dynamics simulations that can predict polymer chain relaxation under the highly volatile solvent conditions.

5.3 Uncertainties and error sources

With the understanding that "All models are wrong, some are useful"[2], this thesis aimed at developing a numerical model for the understanding of the fluid dynamics that govern the coating during TFC membranes. Like all models of the real world, it needs to make some assumptions and simplifications to be computable with feasible resources. On the flipside, this means there are inherent uncertainties that must be mentioned here.

Firstly, the geometry of the coating device used for the CFD model had to be two-dimensional to be computable. This means, that all gradients along the roll axis are ignored in the simulations. Furthermore, the inflow of the polymer solution into the basin is located at the middle, i.e. the axial centre, of the basin, and the inflowing liquid likely causes local disturbances in form of waves on the surface of the contained liquid. This will have an impact on the coating behaviour and the film thickness on the applicator roll, perhaps leading to further fluctuations in the final coating thickness on the membrane. Moreover, the effects that the local, three-dimensional flow patterns have on the surfactant concentration or visco-elastic stresses cannot be studied.

Secondly, the pump that delivers the liquid into the basin pumps a higher mass flow into the basin as what is coated onto the membrane (or evaporates). To reach a continuous steady-state process, the basin thus features an overflow at the sides that lets excess liquid flow out of the basin. This excess liquid is discarded in the case of PDMS but kept and fed back into the reservoir for the more expensive PolyActive™. This means, that (due to the evaporation of solvent) there will be a slight increase of polymer concentration over time, an effect that the steady-state simulations do not address. For the measurements in this thesis the solution was prepared freshly and membrane thickness was measured shortly after the coating procedure began to avoid confounding effects due to this. Nevertheless, this should be kept in mind for future use of the model. In addition, the mass flow induced by the peristaltic (roller) pump is also not exactly the same between experiments, as it will depend on the curvature and

[2] A famous quote attributed to the British statistician George Box.

length of the connected tubing and the air bubbles trapped in the tubes because of this. This is also why this thesis presented two geometries of the coating device, one with overflow of liquid (and unrealistically high filling height of the liquid) and one without overflow (and realistic filling height of the liquid). As discussed, the choice of overflow rate in simulations had no significant impact on the simulation results regarding the final coated film thickness but the choice of filling height had some influence. Future simulations should perhaps ignore the overflow and focus on a more accurate filling hight in the model geometry, as this seems to be more important for the overall result.

Thirdly, further irregularities in the coating process might be due to inhomogeneous polymer concentration, dust grains or small air bubbles in the gap region or increasing cross-linking effects of the polymer over time in the case of PDMS (PolyActive™ is not cross-linked). It should be noted that the liquid film on the membrane roll, after leaving the roll gap, soon enters the drying oven, where the remaining solvent evaporates quickly and the PDMS undergoes cross-linking. Factors like oven temperature might also influence the final polymer density and therefore also thickness to some degree, but this question was not addressed in this thesis.

Concerning the strong deviation between experimental findings of PolyActive™ coating and corresponding simulations, Marangoni flows and visco-elastic effects were considered as a possible explanation. The measured viscoelasticity of the polymer in solution suggests no strong viscoelastic effects in the relevant stress or strain range and the simulation results suggest the same. Furthermore, the simulation results suggest, that visco-elastic thickening should, if present at all, be visible as soon as the liquid is taken up by the applicator roll, which is not seen in confocal laser measurements. This is not the case for surface tension effects. The pattern of surfactant concentration on the phase interface in the upper meniscus region causes a surface tension gradient that is able to cause a secondary flow pattern (Marangoni flow) that transfer more of the incoming liquid onto the membrane. In the tested parameter range, this can cause substantial thickening of the coated film on the membrane without the need for a substantially increased film thickness H_1 on the applicator roll.

As mechanistically clear they appear to be, some limiting remarks on the numerical studies of both the Marangoni effect and viscoelasticity have to be made. In contrast to the PDMS benchmark, a mesh independence study for both extensions of the model could not be conducted. The original mesh resolution as determined in section 4.1.6 was not sufficient to yield numerical convergence in any of the model extensions. In all cases, the resolution had to be extended dramatically (see Figure 32 and Figure 33 for a visual representation of the typical mesh sizes). The substantially increased mesh resolution was the minimum for which a converged solution could be obtained, yet also marked the maximum resolution for which a computation was still feasible. For the given mesh resolutions, computations of the Marangoni and viscoelastic model would already take between one and several days for a single simulation, depending on the parameter combination and quality of the initial guess. To obtain a single successful simulation, a lot of experimentation of the solver and mesh settings was necessary (as simulations often crashed after re-meshing) and when it was finally possible to obtain convergent simulations for the more complex model extensions, the time horizon of this thesis was already approaching its end, thus the focus was put on testing different parameters on their effect instead of trying to produce an even finer mesh for a mesh independence study. Moreover, the large mesh sizes also meant a high load on the working memory of the computer and it was not clear whether further increases in mesh size were computationally possible, as some initial tries in that direction failed. Hence, substantially higher mesh resolutions could not be investigated so far, and a rigorous mesh study was not possible. The numerical findings should therefore be taken with caution and rather be regarded as qualitative results, as the absolute numbers are not reliable enough. Nevertheless, as elaborated, the obtained numerical results also make sense from a mechanistic point of view and fit to the experimental findings.

In addition, it might be hypothesized that the simulation results for the visco-elastic and Marangoni extension would not change qualitatively, even if a higher resolution was chosen. This is, of course, just a speculation, but nevertheless can be justified to some degree. For the visco-elastic simulations, one major result was that visco-elastic forces would already cause a thickening of the liquid on the applicator roll, which was experimentally not observed. This is clear from a mechanistic point of view. The shear and strain rates at the lower meniscus, where the applicator roll leaves the basin, are as high or even higher compared to the other menisci in the upper region between the rolls, where the liquid leaves either on the membrane or the applicator roll. This is understandable, as the applicator roll always has a much higher speed than the membrane roll. This finding was consistent across all mesh resolutions and geometries and it is unlikely, that a higher mesh resolution than the used one would revert that. On the contrary, a higher resolution might be able to resolve the local force gradients more finely and produce an even higher maximum shear or strain rate that compared to what is visible in the available simulations.

For the Marangoni model, the results show an accumulation of surfactant near the stagnation points of the interfacial fluid flow. These give rise to surface tension gradients and thus Marangoni flows. Again, the mechanism behind the accumulation of surfactant follows from the general flow pattern in the meniscus. The overall flow pattern (as depicted in Figure 47) is the same across all simulations (also for the standard Newtonian CFD model on the much coarser mesh) and fits the flow pattern described in the literature. The stagnation points of the surface flow, and thus the points where surfactant molecules will accumulate, arise directly from that flow pattern. A change in mesh resolution is likely going to change the surface velocity gradients and thus the strength of the surfactant accumulation, but the overall picture will remain the same. There will be some degree of surfactant accumulation near the stagnation point II and hence a local decrease in surface tension. Thus, it can be argued that the thickening factors determined by the Marangoni simulations cannot be trusted in terms of absolute numbers, as the effect might be weaker or stronger, depending on the change that a finer mesh would have on the surface dynamics. But the finding that Marangoni flows in the meniscus region can explain a thickening of the film H_3 on the membrane (at least to some extent) without an equally strong thickening of the film H_1 on the applicator roll is likely to remain true nonetheless.

6 Conclusion and Outlook

The initial motivation for this thesis was so to set up a model that delivers a useful tool for the experimentalist when producing TFC membranes with novel polymers or solvents in the given roll-to-roll coating device. Therefore, the general applicability of the presented modelling approach to other polymers or coating devices must be discussed.

The coating process in the roll-to-roll device is a relatively complex interplay of several factors that need to be accounted for. Primary factors are the geometry and constructive details of the apparatus, the physical properties of the dissolved polymer and its solvent and the roller speeds, all of which interact and must be usually balanced out by the experimentalist. All experiments presented here were done with polymer solutions where the typical viscosity is in the range of one to a few mPa·s. Changing the solvent or polymer (or both) can drastically change the viscosity. To sustain a similar liquid film on the roll (which is necessary for a stable meniscus), a much lower viscosity would require higher applicator roll speeds and vice versa. While for high velocities one might encounter a shear-rate dependent effect on viscosity (depending on the polymer) or instabilities in the meniscus. In contrast, lower velocities increase the residence time of the liquid on the roll and in the meniscus gap, thereby increasing the impact of evaporation. The same caveat applies for highly volatile solvents, as discussed in section 5.2.2, and both process configurations could mean that the process can no longer be considered to be isothermal, as temperature gradients of a few degrees can also have an effect on the local viscosity and, perhaps more importantly, on surface tension.

Another factor to be aware of in this context is the possibility of a gel-like layer of polymer at the phase interphase during evaporation, which is usually referred to as skin-formation. Assuming homogeneous evaporation, the standard CFD model suggests a concentration increase of approximately 10% at the interphase in most tested scenarios, for which such skin formation is not anticipated to occur. However, if the initial polymer concentration or evaporation rate is higher, this might cause skin-formation to happen at some point, which will impact the fluid mechanics, especially in the meniscus region. Additionally, the mentioned effects also depend on the material and geometry of the rolls and the gap size because this will also affect heat conduction and residence time of the liquid.

Even if the polymer solution at hand is in a similar viscosity range and the same setup, geometry and roll-speeds are used, the standard CFD model, which was very successful for the PDMS benchmark, deviated strongly from experimental results when the characteristics of the polymer were changed. By changing the polymer to a MBCP and using a solvent mixture, heterogeneity was introduced to the system, which can easily produce physical gradients that have a strong effect on the process. In this case, PolyActive™ is amphiphilic and its presumed surface activity delivered a relatively convincing explanation for the strong thickening effect via Marangoni flows. However, for other polymers non-Newtonian or viscoelastic effects might interfere. Through the analysis of both viscoelastic and Marangoni extensions of the standard CFD model, as well as the experimental findings for PolyActive™ (especially in pure SMC 3), it became clear, that the system is very prone to perturbations due to local fluctuations of surface tension and viscous forces. Although not proven with absolute certainty, this is very likely not a unique feature of this particular polymer/solvent system. The desire to produce very thin films on top of the porous substrate automatically leads the experimentalist to low polymer contents in the solution, which almost inevitably also means low viscosity. But low viscous forces also mean less resistance to applied shear, making the system sensitive to any gradient of fluid forces. In addition, many polymers used for the selective layer in TFC membranes are heterogeneous, as they were fine-tuned in terms of their chemical composition to fulfil specific separation tasks. Therefore, amphiphilicity may be a common feature.

All of the above points also have to be kept in mind when applying this model to any other material or coating setup (like conventional dip coating), where some process parameters may deviate strongly.

Condensing the discussion from section 5 and the above conclusions, some ideas for future research can be proposed. Firstly, some thoughts on the numerical aspect of this study will be given.

All extensions made to the initially implemented basic CFD model suffer from numerical uncertainty due to the lack of a rigorous mesh independence study. To capture the assumed force gradients in the model robustly, it would be necessary to go down to the sub-micrometer level. This makes the CFD model intrinsically difficult to solve and computationally very demanding, since the geometry of the coating roll is in the dimension of centimetres, therefore asking one single model to cover 5-6 orders of magnitude in spatial dimension. This is usually considered to be the absolute maximum for which the modelling of any physical system can still reasonably be done. Moreover, for very thin films of 1-2 μm, where only a few polymer molecules are present per μm^2, the continuum approach is likely unfeasible, and a discrete modelling approach should take over. Hence, more realistic future models might want to look at the polymer conformation (and therefore covered surface area) at the phase interface, its rearrangement due to surface shear stresses and interaction effects between polymers. Other interesting aspects on the same scale involve the conformational changes during solvent evaporation on the membrane and the possible effects of a preferred orientation of the amphiphilic polymer as it adsorbs to the underlying membrane surface, which was already speculated in earlier research on the same subject (Car et al., 2008). To address questions like phase transition of polymeric liquids, the model needs to look at the nanometre scale as well, as it is done via multi-scale models in the literature (Xu et al., 2015). It must be weighed up, if these endeavours are worth the effort, but if ambitious goals are desired for the complete understanding of the coating process, multi-scale are presumably inevitable. This seems particularly true for the coating with highly volatile solvents like SMC 3, for which the observed thickening cannot be explained so far.

As far as the experimental side is concerned, many ideas and open questions remain to be tackled. Still unresolved lies the question of how strong the diffusion of solvent into the coated membrane influences the overall coating process. Possible experiments may estimate the diffusion by measuring the flux of solvent through a porous support plus gutter layer on top. Another approach would be to use the same - or at least a very similar - coating setup and test the coating of polymer solutions onto an impermeable substrate, e.g. a foil with similar thickness. From the viewpoint of process parameters, some experimental tests could be done to further investigate the proposed Marangoni effects. Especially, changes of membrane roll speed should change the surface velocity and thus surface tension gradients, which might have an effect on the coated film thickness. This could be addressed by a range of simulations, producing predictions that could then be tested experimentally. Even more drastic effects might be expected for a change of direction of the applicator roll velocity, i.e. changing the mode from reverse to forward roll coating. This implies a drastic change in the meniscus flow structure (Gaskell, Savage, et al., 1998) which might strongly affect surfactant distributions, while shear and strain rates could remain the same.

Furthermore, the mechanistic insights from the model might guide the design of adjusted roller-coating setups. Understanding that a low viscosity of the solution means high sensitivity to temperature and concentrations gradients, while highly viscous solutions might deliver more stable coating conditions but produce thicker films on the applicator roll and may cause a flooding of the gap region, one possible adjustment may be the use of a doctor blade that constricts the film thickness H_1 on the applicator roll. Increasing the viscosity should increase the controllability of the meniscus force balance via relative roll speeds and decrease the overall importance of surface tension. Viscoelastic effects might become more important for higher polymer content, but by restricting the film thickness

on the applicator roll the overall thickening (or possibly also shear thinning) effect should be manageable. At least if the applicator and membrane roll speed are similar and thus shear and strain rates at both exit points of the liquid films remain comparable, thereby keeping the relative force balance the same.

Anyhow, the CFD model and its extensions presented in this thesis can be regarded as a starting point that provides deeper mechanistic understanding of the coating process of polymer solutions. In many scenarios, it will deliver a reasonable initial guess, either for the experimental production or for more intricate modelling approaches. It also raises awareness to the likely complications that can arise and allows to pin down the source of errors that one may encounter. But as useful as the CFD method is, it is clear that it also has its limits and the process of polymer coating is intrinsically one that covers many spatial dimensions, hence calling for a multitude of numerical approaches.

7 Literature

Abetz, V., Brinkmann, T., Dijkstra, M., Ebert, K., Fritsch, D., ohlrogge, K., Paul, D., Peinemann, K.-V., Nunes, S. P., Scharnagl, N., & Schossig, M. (2006). Developments in membrane research: from material via process design to industrial application. *Advanced Engineering Materials*, *8*(5), 328–358. https://doi.org/10.1002/adem.200600032

Akanno, A., Perrin, L., Guzmán, E., Llamas, S., Starov, V. M., Ortega, F., Rubio, R. G., & Velarde, M. G. (2021). Evaporation of sessile droplets of polyelectrolyte/surfactant mixtures on silicon wafers. *Colloids and Interfaces*, *5*(1), 12. https://doi.org/10.3390/colloids5010012

Alexander Morozov, & Saverio E. Spagnolie. (2015). Introduction to complex fluids. In *Complex Fluids in Biological Systems*. Springer New York. https://doi.org/10.1007/978-1-4939-2065-5

Andersson, B., Andersson, R., Hakansson, L., Mortensen, M., Sudiyo, R., & van Wachem, B. (2011). *Computational fluid dynamics for engineers*. Cambridge University Press. https://doi.org/doi.org/10.1017/CBO9781139093590

Arfsten, N. J., Eberle, A., Otto, J., & Reich, A. (1997). Investigations on the angle-dependent dip coating technique (ADDC) for the production of optical filters. *Journal of Sol-Gel Science and Technology*, *8*(1/2/3), 1099–1104. https://doi.org/10.1023/A:1018327618329

Bard, S., Schönl, F., Demleitner, M., & Altstädt, V. (2019). Influence of fiber volume content on thermal conductivity in transverse and fiber direction of carbon fiber-reinforced epoxy laminates. *Materials*, *12*(7), 1084. https://doi.org/10.3390/ma12071084

Bell, D. J., Wiese, M., Schönberger, A. A., & Wessling, M. (2020). Catalytically active hollow fiber membranes with enzyme-embedded metal–organic framework coating. *Angewandte Chemie International Edition*, *59*(37), 16047–16053. https://doi.org/10.1002/anie.202003287

Bird, R. B., Stewart, W. E., & Lightfoot, E. N. (2007). *Transport phenomena* . John Wiley & Sons Inc. https://doi.org/DOI 10.1149/1.2428074

Brennecke, F., Clodt, J., Brinkmann, T., & Abetz, V. (2024). Numerical and experimental investigation of the unexpected thickening effect during PolyActive^{TM} coating of TFC membranes. *Journal of Advanced Manufacturing and Processing*, *6*(2). https://doi.org/10.1002/amp2.10175

Brennecke, F., Clodt, J., Pohlmann, J., Abetz, C., Brinkmann, T., & Abetz, V. (2021). Computational fluid dynamics simulation of the roll-to-roll coating process for the production of thin film composite membranes including validation. *Journal of Advanced Manufacturing and Processing*, *3*(2). https://doi.org/10.1002/amp2.10076

Brinkmann, T., Lillepärg, J., Notzke, H., Pohlmann, J., Shishatskiy, S., Wind, J., & Wolff, T. (2017). Development of CO2 selective Poly(Ethylene Oxide)-based membranes: From laboratory to pilot plant scale. *Engineering*, *3*, 485–493. https://doi.org/10.1016/J.ENG.2017.04.004

Brinkmann, T., Naderipour, C., Pohlmann, J., Wolff, J. W. T., Esche, E., Müller, D., Wozny, G., & Hoting, B. (2015). Pilot scale investigations of the removal of carbon dioxide from hydrocarbon gas streams using poly (ethylene oxide)-poly (butylene terephtalate) PolyActiveTM) thin film composite membranes. *Journal of Membrane Science*, *489*, 237–247. https://doi.org/10.1016/j.memsci.2015.03.082

Car, A., Stropnik, C., Yave, W., & Peinemann, K.-V. (2008). Tailor-made polymeric membranes based on segmented block copolymers for CO $_2$ separation. *Advanced Functional Materials*, *18*(18), 2815–2823. https://doi.org/10.1002/adfm.200800436

Chhabra, R. P. (2010). Non-Newtonian fluids: An introduction. In *Rheology of Complex Fluids* (pp. 3–34). Springer New York. https://doi.org/10.1007/978-1-4419-6494-6_1

Chien, C.-H., & Jang, J.-Y. (2007). Numerical and experimental studies of thn liquid film flow between two forward-rollers. *Journal of Mechanical Science and Technology*, *21*, 1892–1990. https://doi.org/10.1007/BF03177446

Christen, D. S. (2010). *Praxiswissen der chemischen Verfahrenstechnik*. Springer Berlin Heidelberg. https://doi.org/10.1007/978-3-540-88975-5

Comsol Multiphysics Reference Manual, Version 5.5 (accessed 25-06.2025). (n.d.). Retrieved 25 June 2025, from https://doc.comsol.com/5.5/doc/com.comsol.help.comsol/COMSOL_ReferenceManual.pdf

Coyle, D. J., Macosko, C. W., & Scriven, L. E. (1990). The fluid dynamics of reverse roll coating. *American Institute of Chemical Engineers Journal*, *36*(2), 161–174. https://doi.org/10.1002/aic.690360202

Daripa, P., & Paa, G. (2009). The thickening effect of interfacial surfactant in the drag-out coating problem. *Journal of Statistical Mechanics*, *L07002*. https://doi.org/DOI 10.1088/1742-5468/2009/07/L07002

Davis, S. J., Lewis, N. S., Shaner, M., Aggarwal, S., Arent, D., Azevedo, I. L., Benson, S. M., Bradley, T., Brouwer, J., Chiang, Y.-M., Clack, C. T. M., Cohen, A., Doing, S., Edmonds, J., Fennell, P., Field, C. B., Hannegan, B., Hodge, B.-M., Hoffert, M. I., … Caldeira, K. (2018). Net-zero emissions energy systems. *Science*, *360*(eaas9793). https://doi.org/10.1126/science.aas9793

Decré, M., Gailly, E., & Buchlin, J.-M. (1995). Meniscus shape experiments in forward roll coating. *Physics of Fluids*, *7*(3), 458–467. https://doi.org/10.1063/1.868644

Delacotte, J., Montel, L., Restagno, F., Scheid, B., Dollet, B., Stone, H. A., Langevin, D., & Rio, E. (2012). Plate coating: Influence of concentrated surfactants on the film thickness. *Langmuir*, *28*(8), 3821–3830. https://doi.org/10.1021/la204386b

Demtröder, W. M. (2017). *Mechanics and thermodynamics* (N. A. W. B. M. D. M. F. M. H.-J. M. I. H. K. H. Sherif, Ed.). Springer International Publishing. https://doi.org/DOI 10.1007/978-3-319-27877-3

Dey, R., Saini, A., & Hingorani, H. (2016). A modified Frenkel approach for viscometric prediction of binary and multicomponent liquid mixtures. *RSC Advances*, *6*(49), 43838–43843. https://doi.org/10.1039/C6RA08960G

Diéz-Pascual, A. M., Compostizo, A., Crespo-Colín, A., Rubio, R. G., & Miller, R. (2007). Adsorption of water-soluble polymers with surfactant character. Adsorption kinetics and equilibrium properties. *Journal of Colloid and Interface Science*, *307*(1), 398–404. https://doi.org/DOI: 10.1016/j.jcis.2006.11.056

Ding, Y. (2020). Perspective on Gas Separation Membrane Materials from Process Economics Point of View. *Industrial & Engineering Chemistry Research*, *59*(2), 556–568. https://doi.org/10.1021/acs.iecr.9b05975

Donea, J., Huerta, A., Ponthot, J.-Ph., & Rodríguez-Ferran, A. (2004). Arbitrary Lagrangian-Eulerian methods. In *Encyclopedia of Computational Mechanics*. John Wiley & Sons, Ltd. https://doi.org/10.1002/0470091355.ecm009

Dong, S., Wang, Z., Sheng, M., Qiao, Z., & Wang, J. (2020). Scaling up of defect-free flat membrane with ultra-high gas permeance used for intermediate layer of multi-layer composite membrane and oxygen enrichment. *Separation and Purification Technology*, *239*, 116580. https://doi.org/10.1016/j.seppur.2020.116580

Dong, X., Lu, D., Harris, T. A. L., & Escobar, I. C. (2021). Polymers and solvents used in membrane fabrication: A review focusing on sustainable membrane development. *Membranes*, *11*(5), 309. https://doi.org/10.3390/membranes11050309

Dortmund Data Bank Software & Separation Technology GmbH (accessed 25.06.2025). (n.d.). *Dortmund Data Bank*. http://www.ddbst.com/

Galizia, M., Chi, W. S., Smith, Z. P., Merkel, T. C., Baker, R. W., & Freeman, B. D. (2017). *50th Anniversary Perspective* : Polymers and mixed matrix membranes for gas and vapor separation: A review and prospective opportunities. *Macromolecules*, *50*(20), 7809–7843. https://doi.org/10.1021/acs.macromol.7b01718

Gaskell, P. H., Innes, G. E., & Savage, M. D. (1998). An experimental investigation of menisucs roll coating. *Journal of Fluid Mechanics*, *355*, 17–44. https://doi.org/10.1017/S0022112097007398

Gaskell, P. H., Savage, M. D., Summers, J. L., & Thompson, H. M. (1995). Modelling and analysis of meniscus roll coating. *Journal of Fluid Mechanics*, *298*, 113–137. https://doi.org/10.1017/S0022112095003247

Gaskell, P. H., Savage, M. D., & Thompson, H. M. (1998). Stagnation–saddle points and flow patterns in Stokes flow between contra-rotating cylinders. *Journal of Fluid Mechanics*, *370*, 221–247. https://doi.org/10.1017/S0022112098002031

Gerbeau, J.-F., & Lelièvre, T. (2009). Generalized Navier boundary condition and geometric conservation law for surface tension. *Computer Methods in Applied Mechanics and Engineering*, *198*, 644–656. https://doi.org/10.1016/j.cma.2008.09.011

Greener, J., & Middleman, S. (1981). Reverse roll coating of viscous and viscoelastic liquids. *Industrial and Engineering Chemistry Fundamentals*, *20*, 63–66. https://doi.org/10.1021/i100001a012

Greener, Y., & Middleman, S. (1975). A theory of roll coating of viscous and viscoelatic fluids. *Polymer Engineering and Science*, *15*(1). https://doi.org/10.1002/pen.760150102

Guyard, G., Vilquin, A., Sanson, N., Jouenne, S., Restagno, F., & McGraw, J. D. (2021). Near-surface rheology and hydrodynamic boundary condition of semi-dilute polymer solutions. *Soft Matter*, *17*(14), 3765–3774. https://doi.org/10.1039/D0SM02116D

Hamadneh, N. N., Khan, W. S., & Khan, W. A. (2019). Prediction of thermal conductivities of polyacrylonitrile electrospun nanocomposite fibers using artificial neural network and prey predator algorithm. *Journal of King Saud University - Science*, *31*(1), 618–627. https://doi.org/https://doi.org/10.1016/j.jksus.2018.03.013

Hao, Y., & Haber, S. (1999). Reverse roll coating flow. *International Journal for Numerical Methods in Fluids*, *30*, 635–652. https://doi.org/10.1002/(SICI)1097-0363(19990730)30

Houde, A. Y., Krishnakumar, B., Charati, S. G., & Stern, S. A. (1996). Permeability of dense (homogeneous) cellulose acetate membranes to methane, carbon dioxide, and their mixtures at elevated pressures. *Journal of Applied Polymer Science*, *62*(13), 2181–2192. https://doi.org/10.1002/(SICI)1097-4628(19961226)62

Huglin, M. B. (1965). Specific refractive index increments of polymer solutions. Part I. Literature values. *Journal of Applied Polymer Science*, *9*(1), 3963–4001. https://doi.org/https://doi.org/10.1002/app.1965.070091219

Isooctane data sheet Carl ROTH (accessed 25.06.2025). (n.d.). https://www.carlroth.com/com/en/solvents-for-tlc/isooctane/p/cp80.1

Jankowski, A., Grabiec, E., Nocoń-Szmajda, K., Marcinkowski, A., Janeczek, H., & Wolińska-Grabczyk, A. (2021). Polyimide-based membrane materials for CO2 separation: A comparison of segmented and aromatic (co)polyimides. *Membranes*, *11*(4), 274. https://doi.org/10.3390/membranes11040274

Jarvis, S. M., & Samsatli, S. (2018). Technologies and infrastructures underpinning future CO2 value chains: A comprehensive review and comparative analysis. *Renewable and Sustainable Energy Reviews*, *85*, 46–68. https://doi.org/10.1016/j.rser.2018.01.007

Kárászová, M., Zach, B., Petrusová, Z., Červenka, V., Bobák, M., Šyc, M., & Izák, P. (2020). Post-combustion carbon capture by membrane separation, Review. *Separation and Purification Technology*, *238*, 116448. https://doi.org/10.1016/j.seppur.2019.116448

Karbalaei, A., Kumar, R., & Cho, H. J. (2016). Thermocapillarity in Microfluidics—A Review. *Micromachines*, *7*(1), 13–54. https://doi.org/https://doi.org/10.3390/mi7010013

Keszei, E. (2012). *Chemical thermodynamics*. Springer Berlin Heidelberg. https://doi.org/10.1007/978-3-642-19864-9

Kim, J.-H., & Rothstein, J. P. (2015). Dynamic contact angle measurements of viscoelastic fluids. *Journal of Non-Newtonian Fluid Mechanics*, *225*, 54–61. https://doi.org/https://doi.org/10.1016/j.jnnfm.2015.09.007

Klostermann, R., & Mewes, D. (1996). Das Beschichten von Oberflächen. *Chemie Ingenieur Technik*, *68*(10), 1243–1253. https://doi.org/10.1002/cite.330681003

Klostermann, R., von Bose, S., & Mewes, D. (1994). Comparison of calculated with measured flow fields in the gap between two rotating rolls. *Advances in Polymer Technology*, *13*(3), 187–199. https://doi.org/10.1002/adv.1994.060130301

Kol, R., De Somer, T., D'hooge, D. R., Knappich, F., Ragaert, K., Achilias, D. S., & De Meester, S. (2021). State-of-the-art quantification of polymer solution viscosity for plastic waste recycling. *ChemSusChem*, *14*(19), 4071–4102. https://doi.org/https://doi.org/10.1002/cssc.202100876

Ladewig, B., & Al-Shaeli, M. N. Z. (2017). Fundamentals of membrane processes. In *Fundamentals of Membrane Bioreactors* (pp. 13–37). https://doi.org/10.1007/978-981-10-2014-8_2

Lalia, B. S., Kochkodan, V., Hashaikeh, R., & Hilal, N. (2013). A review on membrane fabrication: Structure , properties and performance relationship. *Desalination*, *326*, 77–95. https://doi.org/10.1016/j.desal.2013.06.016

Laun, M., Auhl, D., Brummer, R., Dijkstra, D., Gabriel, C., Mangnus, M., Rüllmann, M., Zoetelief, W., & Handge. Ulrich. (2014). Guidelines for checking performance and verifying accuracy of

rotational rheometers: viscosity measurements in steady and oscillatory shear (IUPAC Technical Report). *Pure and Applied Chemistry*, *86*(12), 1945–1968. https://doi.org/DOI 10.1515/pac-2013-0601

Lawson, J., & Zidek, F. D. J. J. F. M. T. J. (2015). *Design and analysis of experiments with R* (1st Edition). Chapman and Hall/CRC. https://doi.org/10.1201/b17883

Lenth, R. V. (2009). Response surface methods in R, using rsm. *Journal of Statistical Software*, *32*(7). https://doi.org/10.18637/jss.v032.i07

Li, Z., Yang, J., Hollingsworth, J. V., & Zhao, J. (2020). Lateral diffusion of single polymer molecules at interfaces between water and oil. *RSC Advances*, *10*(28), 16565–16569. https://doi.org/10.1039/D0RA02630A

Liang, C. Z., S-Chung, T., & Y-Lai, J. (2019). A review of polymeric membranes for gas separation and energy production. *Progress in Polymer Science*, *97*(101141). https://doi.org/10.1016/j.progpolymsci.2019.06.001

Lin, H., He, Z., Sun, Z., Vu, J., Ng, A., Mohammed, M., Kniep, J., Merkel, T. C., Wu, T., & Lambrecht, R. C. (2014). CO2-selective membranes for hydrogen production and CO2 capture – Part I: Membrane development. *Journal of Membrane Science*, *457*, 149–161. https://doi.org/10.1016/j.memsci.2014.01.020

Lunkenheimer, K., & Zembala, M. (1997). Attempts to study a water evaporation retardation by soluble surfactants. *Journal of Colloid and Interface Science*, *188*(2), 363–371. https://doi.org/10.1006/jcis.1997.4781

Madenci, E., & Guven, I. (2015). *The finite element method and applications in engineering using ANSYS®*. Springer US. https://doi.org/10.1007/978-1-4899-7550-8

Manikantan, H., & Squires, T. M. (2020). Surfactant dynamics: hidden variables controlling fluid flows. *Journal of Fluid Mechanics*, *892*.

Marchand, A., Weijs, J. H., Snoeijer, J. H., & Andreotti, B. (2011). Why is surface tension a force parallel to the interface? *American Journal of Physics*, *79*(10), 999. https://doi.org/10.1119/1.3619866

Mayer, H. C., & Krechetnikov, r. (2012). Landau-Levich flow visualization: Revealing the flow topology responsible for the film thickening phenomena. *Physics of Fluids*, *24*(052103). https://doi.org/10.1063/1.4703924

Metz, S. J., Mulder, M. H. v., & Wessling, M. (2004). Gas-permeation properties of poly(ethylene oxide) poly(butylene terephthalate) block copolymers. *Macromolecules*, *37*(12), 4590–4597. https://doi.org/10.1021/ma049847w

Microfluidics Module User's Guide, COMSOL Version 5.5 (accessed 25.06.2025). (n.d.). https://doc.comsol.com/5.5/doc/com.comsol.help.mfl/MicrofluidicsModuleUsersGuide.pdf

Milling, A. J., Richards, R. W., Hiorns, R. C., & Jones, R. G. (2000). Surface viscoelastic properties of spread films of a polysilylene−poly(ethylene oxide) multiblock copolymer at the air−water Interface. *Macromolecules*, *33*(7), 2651–2661. https://doi.org/10.1021/ma990654w

Monteux, C. (2014). Adsorption of soluble polymers at liquid interfaces and in foams. *Comptes Rendus Physique*, *15*, 775–785. https://doi.org/https://doi.org/10.1016/j.crhy.2014.10.002

Moukalled, F., Mangani, L., & Darwish, M. (2016). *The Finite Volume Method in Computational Fluid Dynamics* (Vol. 113). Springer International Publishing. https://doi.org/10.1007/978-3-319-16874-6

Nunes, S. P., Culfaz-Emecen, P. Z., Ramon, G. Z., Visser, T., Koops, G. H., Jin, W., & Ulbricht, M. (2020). Thinking the future of membranes: perspectives for advanced and new membrane materials and manufacturing processes. *Journal of Membrane Science*. https://doi.org/10.1016/j.memsci.2019.117761

Park, J., Shin, K., & Lee, C. (2016). Roll-to-Roll coating technology and its applications: A review. *International Journal of Precision Engineering and Manufacturing*, *17*(4), 537–550. https://doi.org/10.1007/s12541-016-0067-z

Pohjoranta, A., & Tenno, R. (2011). Implementing surfactant mass balance in 2D FEM-ALE models. *Engineering with Computers*, *27*, 165–175. https://doi.org/https://doi.org/10.1007/s00366-010-0186-6

Pohlmann, J., Bram, M., Wilkner, K., & Brinkmann, T. (2016). Pilot scale separation of CO2 from power plant flue gases by membrane technology. *International Journal of Greenhouse Gas Control*, *53*, 56–64. https://doi.org/10.1016/j.ijggc.2016.07.033

Raffa, P., Wever, D. A. Z., Picchioni, F., & Broekhuis, A. A. (2015). Polymeric surfactants: Synthesis, oroperties, and links to applications. *Chemical Reviews*, *115*(16), 8504–8563. https://doi.org/10.1021/cr500129h

Rafiq, S., Deng, L., & Hägg, M.-B. (2016). Role of facilitated transport membranes and composite membranes for efficient CO_2 capture - A review. *ChemBioEng Reviews*, *3*(2), 68–85. https://doi.org/10.1002/cben.201500013

Rieutord, M. (2015). *Fluid dynamics*. Springer International Publishing. https://doi.org/10.1007/978-3-319-09351-2

Rikiyama, K., Horiuchi, T., Koga, N., Sanada, Y., Watanabe, K., Aida, M., & Yukitero Katsumoto. (2018). Micellization of poly(ethylene oxide)-poly(propylene oxide) alternating multiblock copolymers in water. *Polymer*, *156*(7), 102–110. https://doi.org/https://doi.org/10.1016/j.polymer.2018.09.047

Rio, E., & Boulogne, F. (2017). Withdrawing a solid from a bath: How much liquid is coated? *Advances in Colloid and Interface Science*, *247*, 100–114. https://doi.org/10.1016/j.cis.2017.01.006

Sanders, D. F., Smith, Z. P., Guo, R., Robeson, L., McGrath, J. E., Paul, D. R., & Freeman, B. D. (2013). Energy-efficient polymeric gas separation membranes for a sustainable future: A review. *Polymer*, *54*(18), 4729–4761. https://doi.org/https://doi.org/10.1016/j.polymer.2013.05.075

Scharnagl, N., & Buschatz, H. (2001). Polyacrylonitrile (PAN) membranes for ultra- and microfiltration. *Desalination*, *139*, 191–198. https://doi.org/10.1016/S0011-9164(01)00310-1

Schrimpf, M., Esteban, J., Warmeling, H., Färber, T., Behr, A., & Vorholt, A. J. (2021). Taylor-Couette reactor: Principles, design, and applications. *AIChE Journal*, *67*(5). https://doi.org/10.1002/aic.17228

Semenov, S., Trybala, A., Agogo, H., Kovalchuk, N., Ortega, F., Rubio, R. G., Starov, V. M., & Velarde, M. G. (2013). Evaporation of droplets of surfactant solutions. *Langmuir*, *29*(32), 10028–10036. https://doi.org/10.1021/la401578v

Shikmurzaev, T. D., & Blake, Y. D. (2002). Dynamic wetting by liquids of different viscosity. *Journal of Colloid and Interface Science*, *253*(1), 196–202. https://doi.org/DOI: 10.1006/jcis.2002.8513

Siddiqui, M. O. R., Sun, D., & Butler, I. B. (2018). Geometrical modelling and thermal analysis of nonwoven fabrics. *Journal of Industrial Textiles*, *48*(2), 405–431. https://doi.org/10.1177/1528083717725913

Stone, H. A. (1990). A simple derivation of the time-dependent convective-diffusion equation for surfactant transport along a deforming interface. *Physics of Fluids A: Fluid Dynamics*, *2*(1), 111–112. https://doi.org/https://doi.org/10.1063/1.857686

Sultanova, N. G., Kasarova, S. N., & Nikolov, I. D. (2014). Laser measurements of the refractive index of polymer solutions, thin films and bulk materials. *Journal of Physics: Conference Series*, *514*. https://doi.org/DOI 10.1088/1742-6596/514/1/012026

Sunthar, P. (2010). Polymer rheology. In P. K. J. Krishnan; A. Deshpande (Ed.), *Rheology of Complex Fluids* (pp. 171–191). Springer. https://doi.org/DOI 10.1007/978-1-4419-6494-6

Sur, S., & Rothstein, J. (2018). Drop breakup dynamics of dilute polymer solutions: Effect of molecular weight, concentration, and viscosity. *Journal of Rheology*, *62*(5), 1245–1259. https://doi.org/10.1122/1.5038000

van der Heijden, T. W. G., Darhuber, A. A., & van der Schoot, P. (2018). Macroscopic model for sessile droplet evaporation on a flat surface. *Langmuir*, *34*(41), 12471–12481. https://doi.org/10.1021/acs.langmuir.8b02374

van Gaalen, R. T., Diddens, C., Wijshoff, H. M. A., & Kuerten, J. G. M. (2020). The evaporation of surfactant-laden droplets: A comparison between contact line models. *Journal of Colloid and Interface Science*, *579*, 888–897. https://doi.org/10.1016/j.jcis.2020.06.099

Wagner, C., Bourouiba, L., & McKinley, G. H. (2015). An analytic solution for capillary thinning and breakup of FENE-P fluids. *Journal of Non-Newtonian Fluid Mechanics*, *218*, 53–61. https://doi.org/10.1016/j.jnnfm.2015.01.011

Wakeham, W., Assael, M., Marmur, A., Coninck, J., Blake, T., Theron, S., & Zussman, E. (2007). Material properties: Measurement and data. In A. L. Y. C. T. J. F. Foss (Ed.), *Springer handbook of experimental fluid mechanics*. Springer, Berlin, Heidelberg. https://doi.org/DOIhttps://doi.org/10.1007/978-3-540-30299-5_3

Wang, Y., Zhao, L., Otto, A., Robinius, M., & Solten, D. (2017). A review of post-combustion CO2 capture technologies from coal-fired power plants. *Energy Procedia*, *114*, 650–665. https://doi.org/10.1016/j.egypro.2017.03.1209

White, F. M. (2011). *Fluid mechanics* (7th ed.). McGraw-Hill. ISBN: 978-0073398275

Willenbacher, N., & Georgieva, K. (2013). Rheology of disperse systems. In *Product Design and Engineering* (pp. 7–49). Wiley-VCH Verlag GmbH & Co. KGaA. https://doi.org/10.1002/9783527654741.ch1

Woo, S. S., Shalev, I., & Barker, R. L. (1994). Heat and moisture transfer through nonwoven fabrics. *Textile Research Journal*, *64*(3), 149–162. https://doi.org/10.1177/004051759406400305

Wu, M., Di, Y., Man, X., & Doi, M. (2019). Drying Droplets with Soluble Surfactants. *Langmuir*, *35*(45), 14734–14741. https://doi.org/10.1021/acs.langmuir.9b02229

Xu, X.-H., Guo, X.-W., Cao, Y., Ren, X.-G., Chen, J., & Yang, X.-J. (2015). Multi-scale simulation of non-equilibrium phase transitions under shear flow in dilute polymer solutions. *RSC Advances*, *5*(67), 54649–54657. https://doi.org/10.1039/C5RA06099K

Yanase, H., Moldenaers, P., Mewis, J., Abetz, V., van Egmond, J., & Fuller, G. G. (1991). Structure and dynamics of a polymer solution subject to flow-induced phase separation. *Rheologica Acta*, *30*(1), 89–97. https://doi.org/10.1007/BF00366798

Yave, W., Car, A., Wind, J., & Peinemann, K.-V. (2010). Nanometric thin film membranes manufactured on square meter scale: ultra-thin films for CO2 capture. *Nanotechnology*, *21*(395301). https://doi.org/10.1088/0957-4484/21/39/395301

Yave, W., Huth, H., Car, A., & Schick, C. (2011). Peculiarity of a CO2-philic block copolymer confined in thin films with constrained thickness: “a super membrane for CO2-capture”. *Energy & Environmental Science*, *4*(11), 4656. https://doi.org/10.1039/c1ee02139g

Zilz, J., Schäfer, C., Wagner, C., Poole, R. J., Alves, M. A., & Lindner, A. (2014). Serpentine channels: micro-rheometers for fluid relaxation times. *Lab on a CHip*, *14*, 351–358. https://doi.org/DOI: 10.1039/C3LC50809A

8 Appendix

8.1 Viscosity and density measurements for the standard model

8.1.1 PDMS in Isooctane

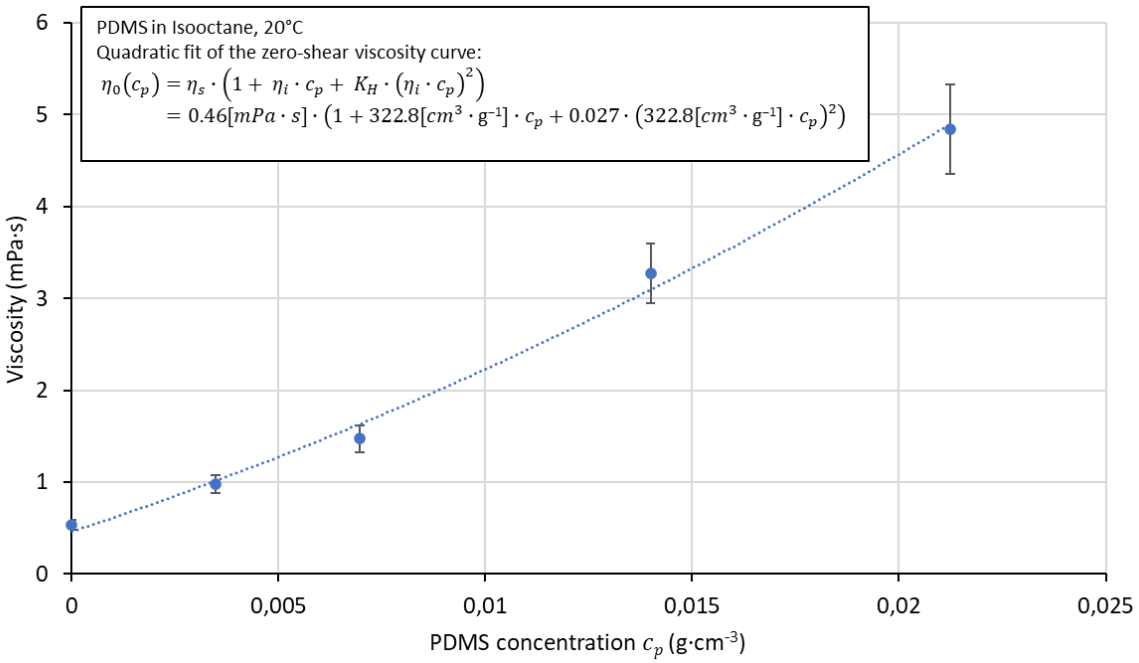

Figure A 1 Shear-zero viscosity of PDMS in Isooctane over a range of concentrations. A mass fraction of 1 wt % corresponds to a polymer concentration of approximately 0.007 g/cm³. The viscosity increases for increasing polymer concentration can be fitted with the quadratic Huggins equation.

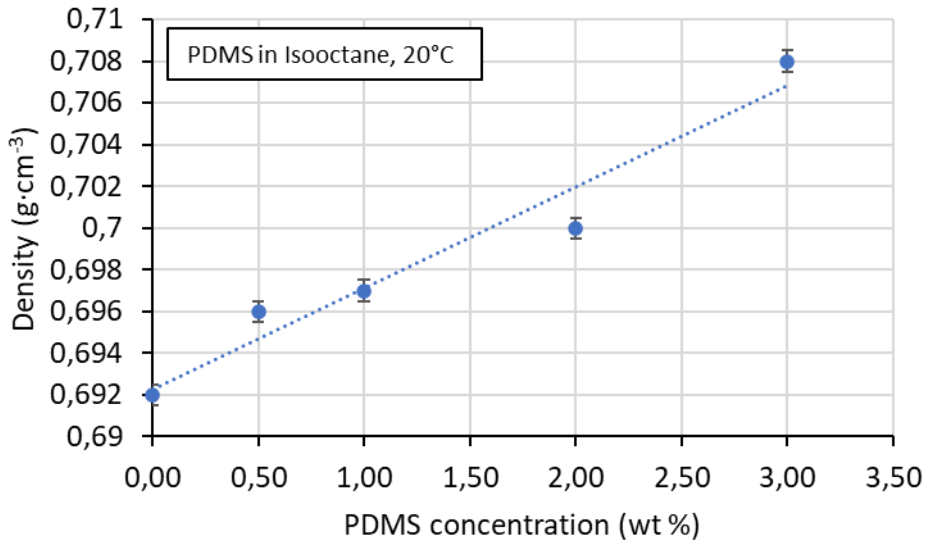

Figure A 2 Density measurements of PDMS in Isooctane over a range of concentrations. A mass fraction of 1 wt % corresponds to a concentration of approximately 0.007 g/cm³. The density increase for higher polymer concentration is not very strong and can be fitted with a linear equation.

8.1.2 PolyActive™ in solvent mixture

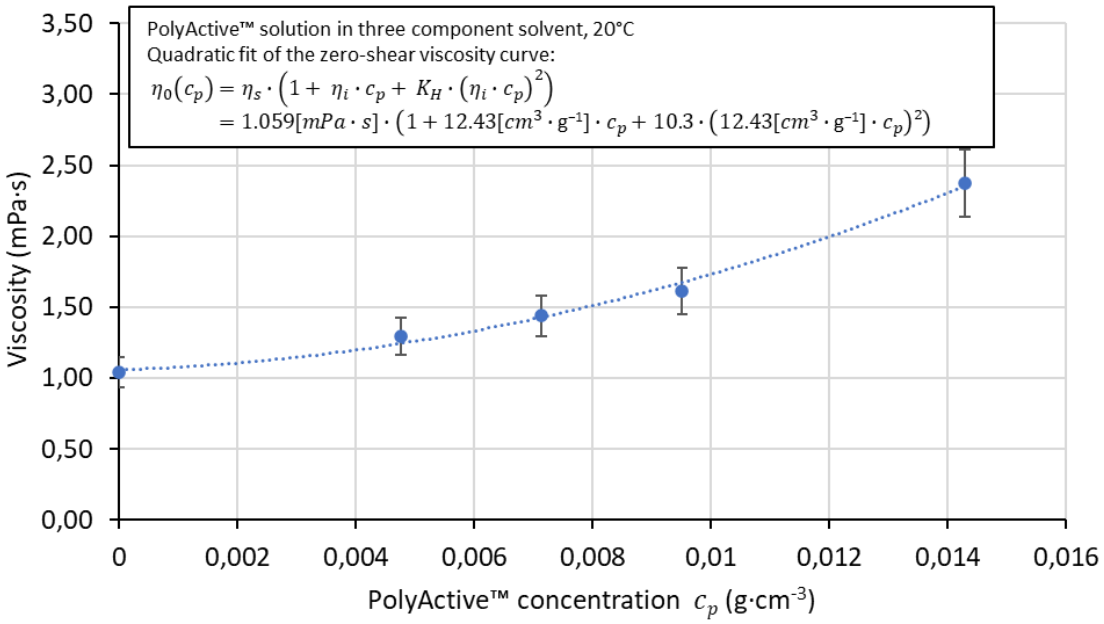

Figure A 3 Shear-zero viscosity of PolyActive™ in solvent mixture over the maximal range of dissolvable polymer concentrations. A mass fraction of 1.5 wt % corresponds to a polymer concentration of approximately 0.0143 g/cm³. The viscosity increase for higher polymer concentration can be fitted with the quadratic Huggins equation.

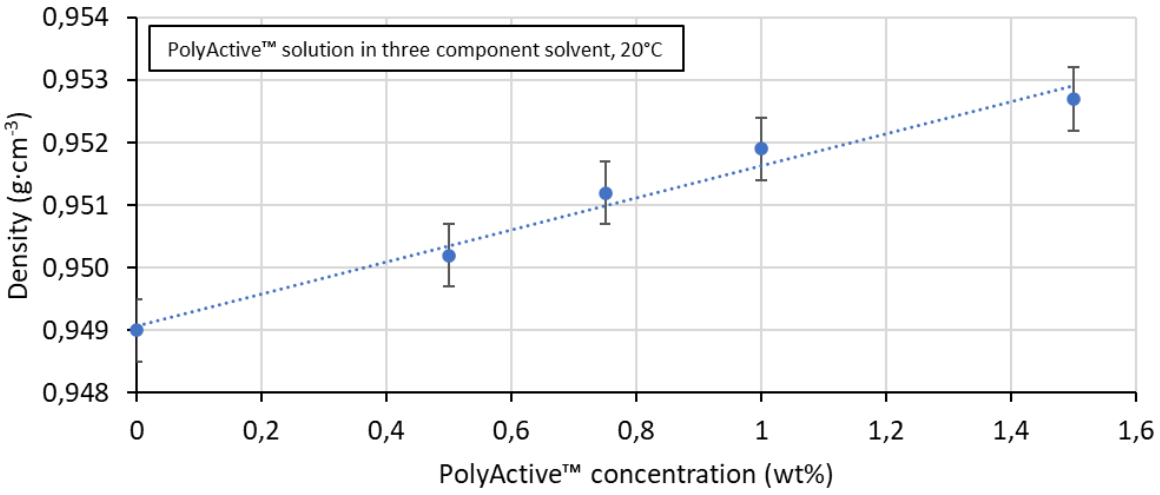

Figure A 4 Density measurements of PolyActive™ in solvent mixture over the maximal range of dissolvable polymer concentrations. A mass fraction of 1.5 wt % corresponds to a concentration of approximately 0.0143 g/cm³.

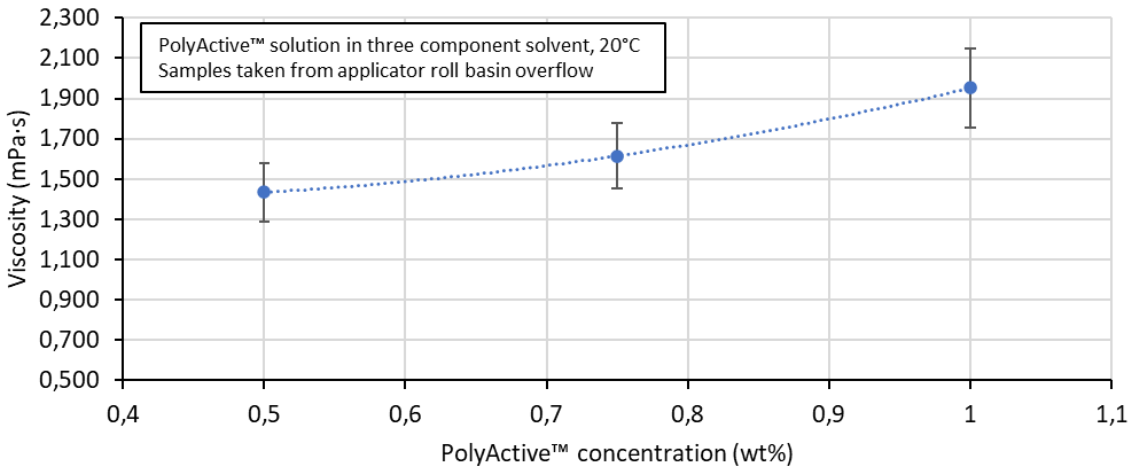

Figure A 5 Shear-zero viscosity of PolyActive™ in solvent mixture measured in the overflow of the applicator roll basin during coating. Concentrations refer to the original feed concentration.

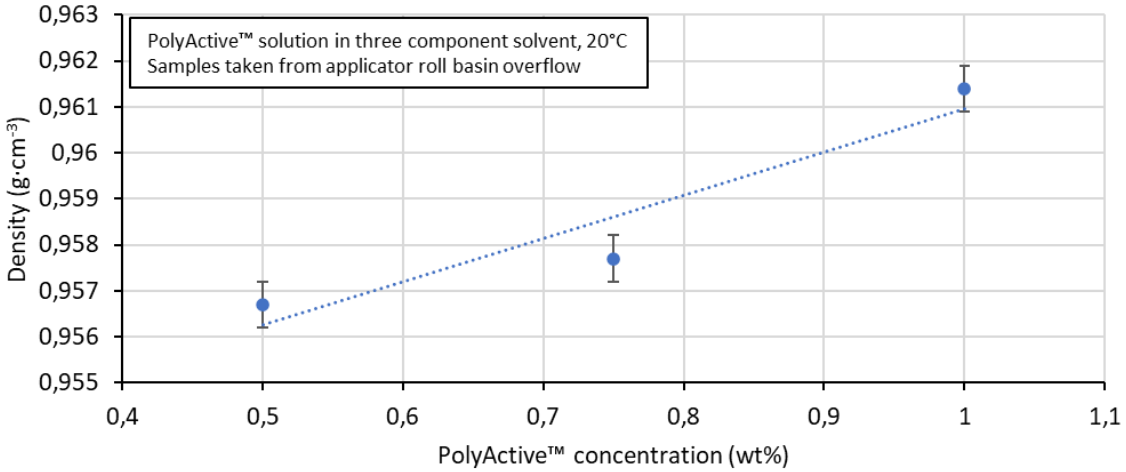

Figure A 6 Density of PolyActive™ in solvent mixture measured in the overflow of the applicator roll basin during coating. Concentrations refer to the original feed concentration.

8.1.3 PolyActive™ in pure SMC 3

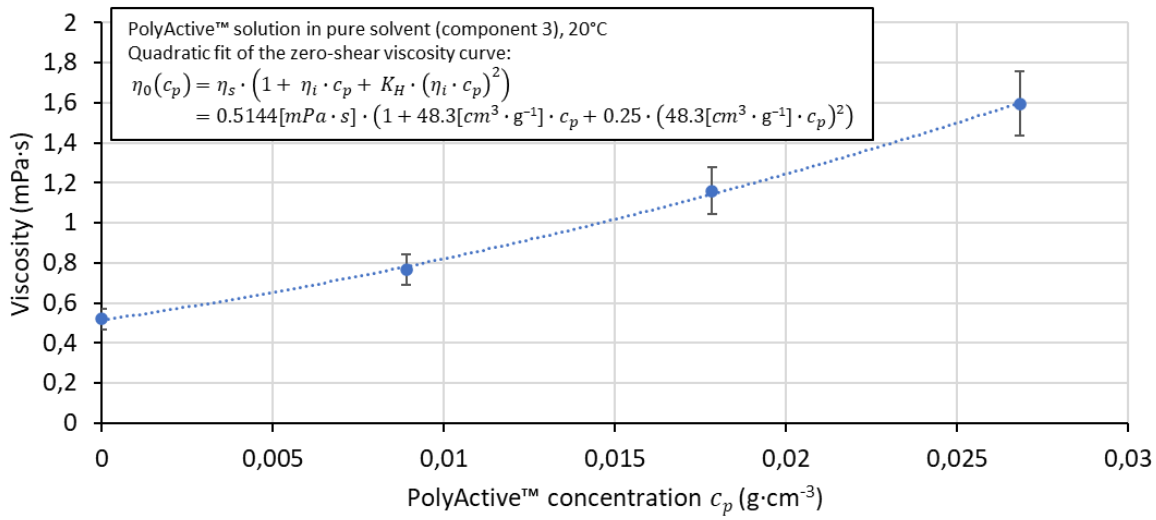

Figure A 7 Shear-zero viscosity of PolyActive™ in SMC 3 over a range of concentrations in the feed. A mass fraction of 1 wt % corresponds to a polymer concentration of approximately 0.009 g/cm³. The viscosity increase for higher polymer concentration can be fitted with the quadratic Huggins equation.

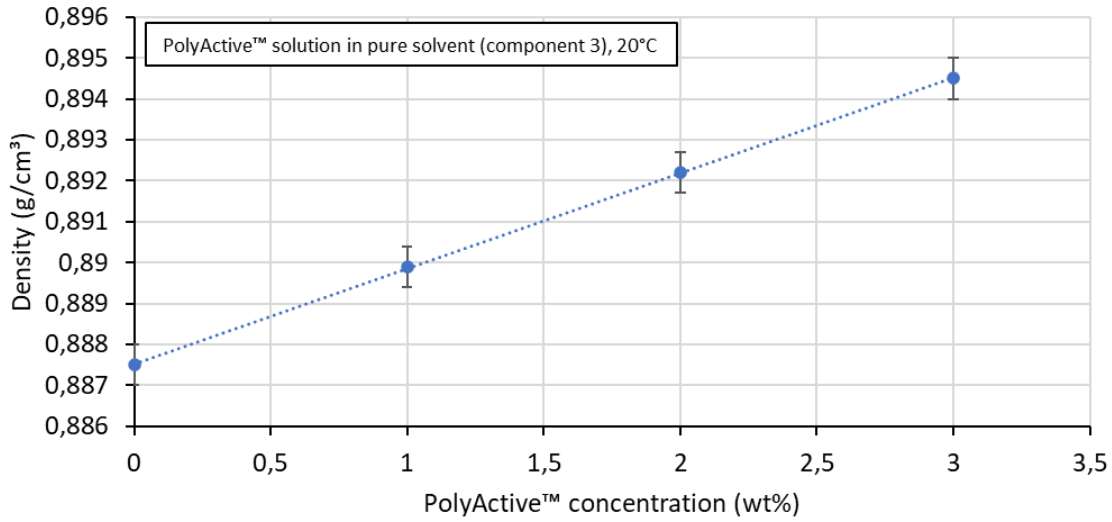

Figure A 8 Density of PolyActive™ in SMC 3 over a range of concentrations in the feed solution.

8.2 Cross-sectional Sem images

8.2.1 Coating thickness of PDMS

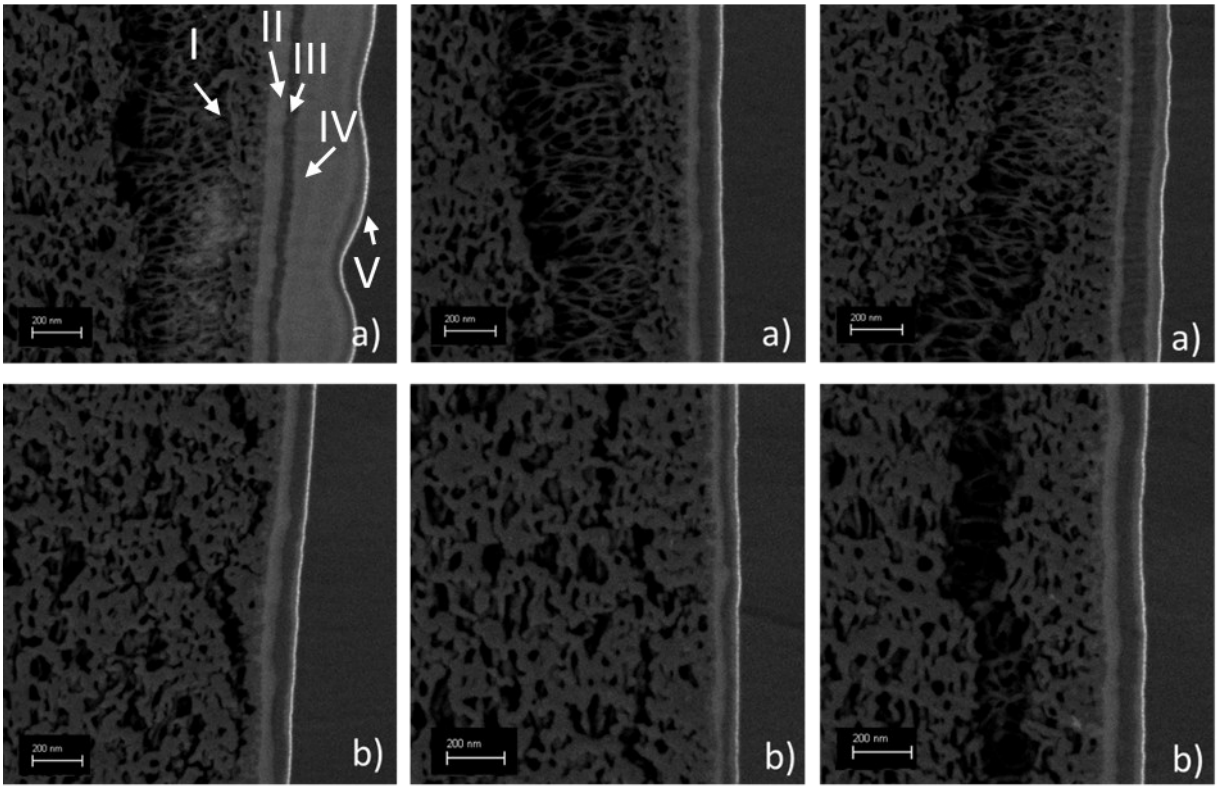

Figure A 9 Cross-sectional SEM images of TFC membranes consisting of PAN support (I), a PDMS based gutter layer (II), a selective PolyActive™ layer (III) and a PDMS based protective layer on top (IV). The brightest line in the image is caused by the platinum layer applied in the preparation (V). The following production parameters are shown for the protective layer: 1 wt% PDMS, v_1= 0.027 m/s (a); 1 wt% PDMS, v_1= 0.045 m/s (b).

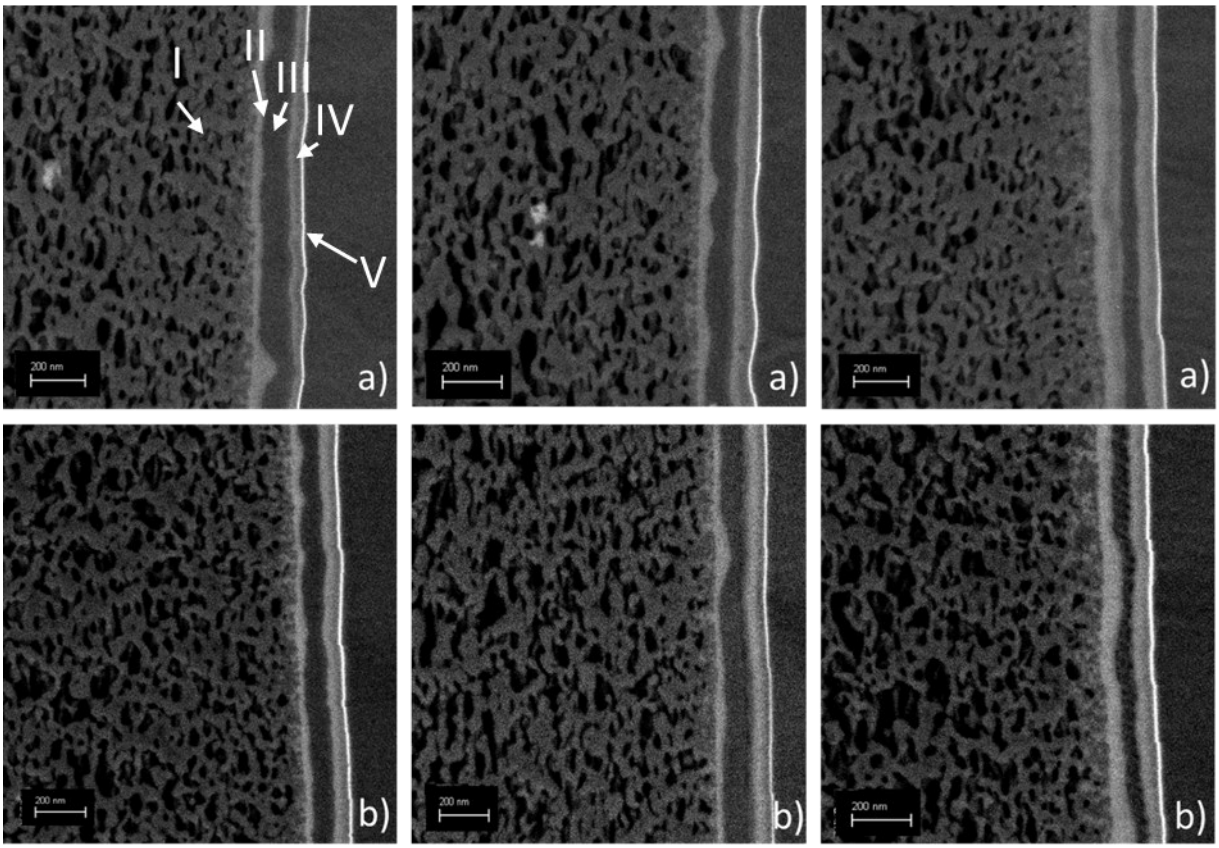

Figure A 10 Cross-sectional SEM images of TFC membranes consisting of PAN support (I), a PDMS based gutter layer (II), a selective PolyActive™ layer (III) and a PDMS based protective layer on top (IV). The brightest line in the image is caused by the platinum layer applied in the preparation (V). The following production parameters are shown for the protective layer: 2 wt% PDMS, v_1= 0.027 m/s (a); 1 wt% PDMS, v_1= 0.045 m/s (b).

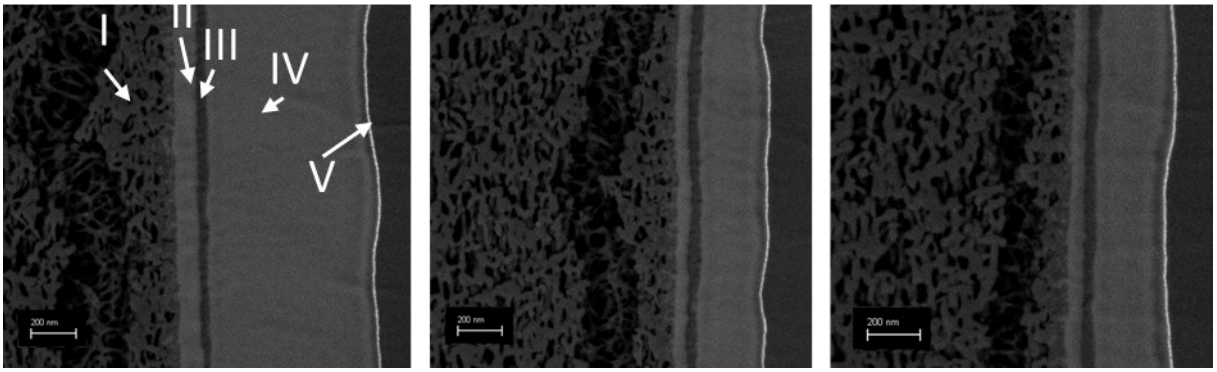

Figure A 11 Cross-sectional SEM images of TFC membranes consisting of PAN support (I), a PDMS based gutter layer (II), a selective PolyActive™ layer (III) and a PDMS based protective layer on top (IV). The brightest line in the image is caused by the platinum layer applied in the preparation (V). The shown images are all for 3 wt% PDMS concentration and applicator roll speed of 0.045 m/s.

8.2.2 Coating thickness of PolyActive™ in solvent mixture

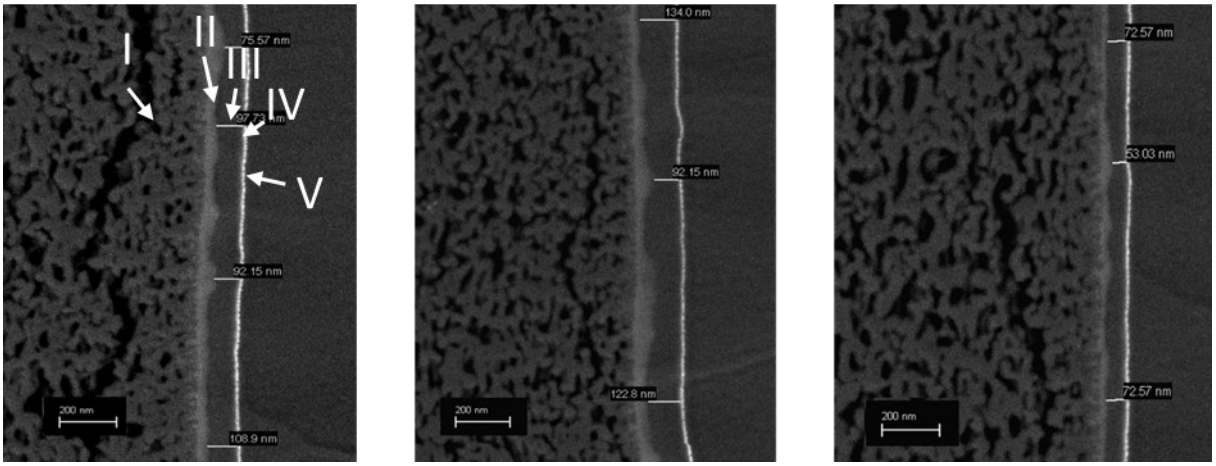

Figure A 12 Cross-sectional SEM images of TFC membranes consisting of PAN support (I), a PDMS based gutter layer (II), a selective PolyActive™ layer (III) and a PDMS based protective layer on top (IV). The brightest line in the image is caused by the platinum layer applied in the preparation (V). The process parameters for the PolyActive™ layer were 0.5 wt% and an applicator roll speed of 0.045 m/s.

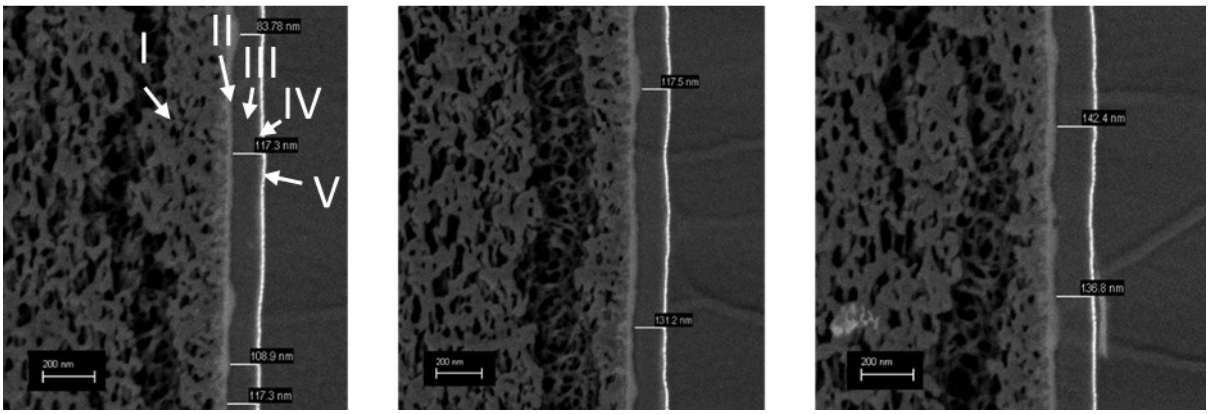

Figure A 13 Cross-sectional SEM images of TFC membranes consisting of PAN support (I), a PDMS based gutter layer (II), a selective PolyActive™ layer (III) and a PDMS based protective layer on top (IV). The brightest line in the image is caused by the platinum layer applied in the preparation (V). The process parameters for the PolyActive™ layer were 0.75 wt% and an applicator roll speed of 0.045 m/s.

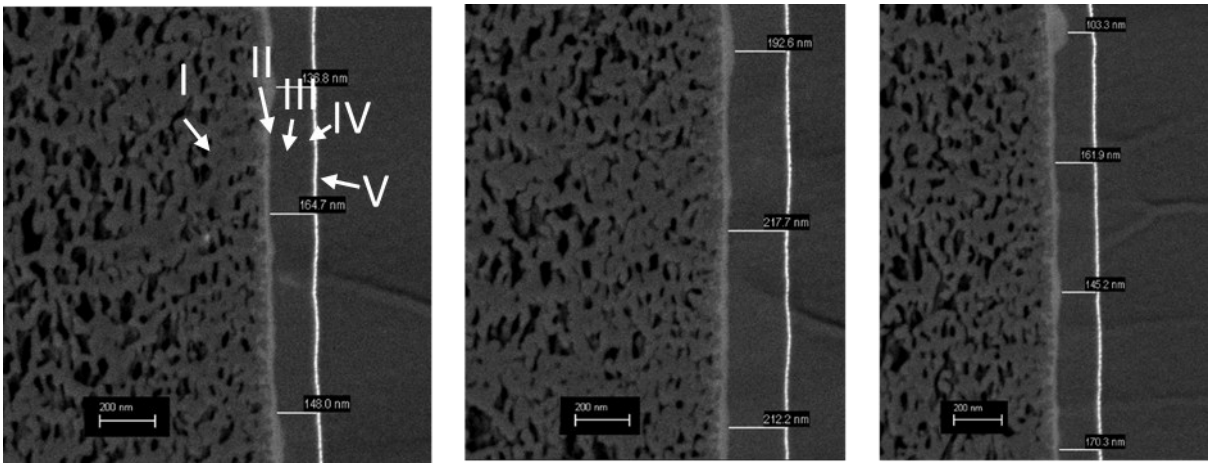

Figure A 14 Cross-sectional SEM images of TFC membranes consisting of PAN support (I), a PDMS based gutter layer (II), a selective PolyActive™ layer (III) and a PDMS based protective layer on top (IV). The brightest line in the image is caused by the platinum layer applied in the preparation (V). The process parameters for the PolyActive™ layer were 1 wt% and an applicator roll speed of 0.045 m/s.

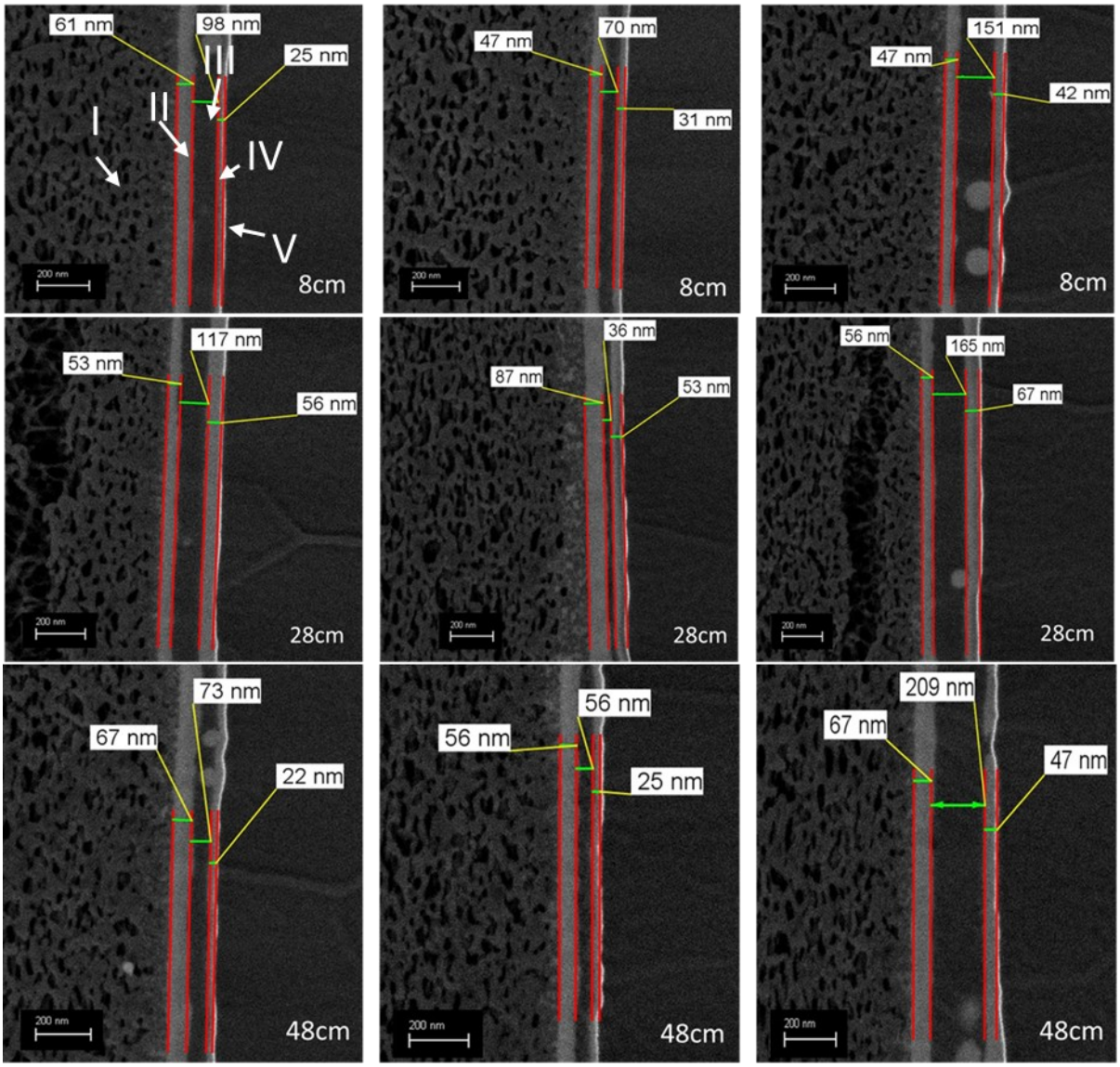

Figure A 15 Cross-sectional SEM images of TFC membranes consisting of PAN support (I), a PDMS based gutter layer (II), a selective PolyActive™ layer (III) and a PDMS based protective layer on top (IV). The brightest line in the image is caused by the platinum layer applied in the preparation (V). The images show the variation of selective layer thickness across the width of the membrane (in total 0.6m), as indicated in the respective right lower corner. Process parameters for the PolyActive™ layer were 1 wt% and an applicator roll speed of 0.045 m/s in all cases.

8.2.3 Coating thickness of PolyActive™ in pure SMC 3

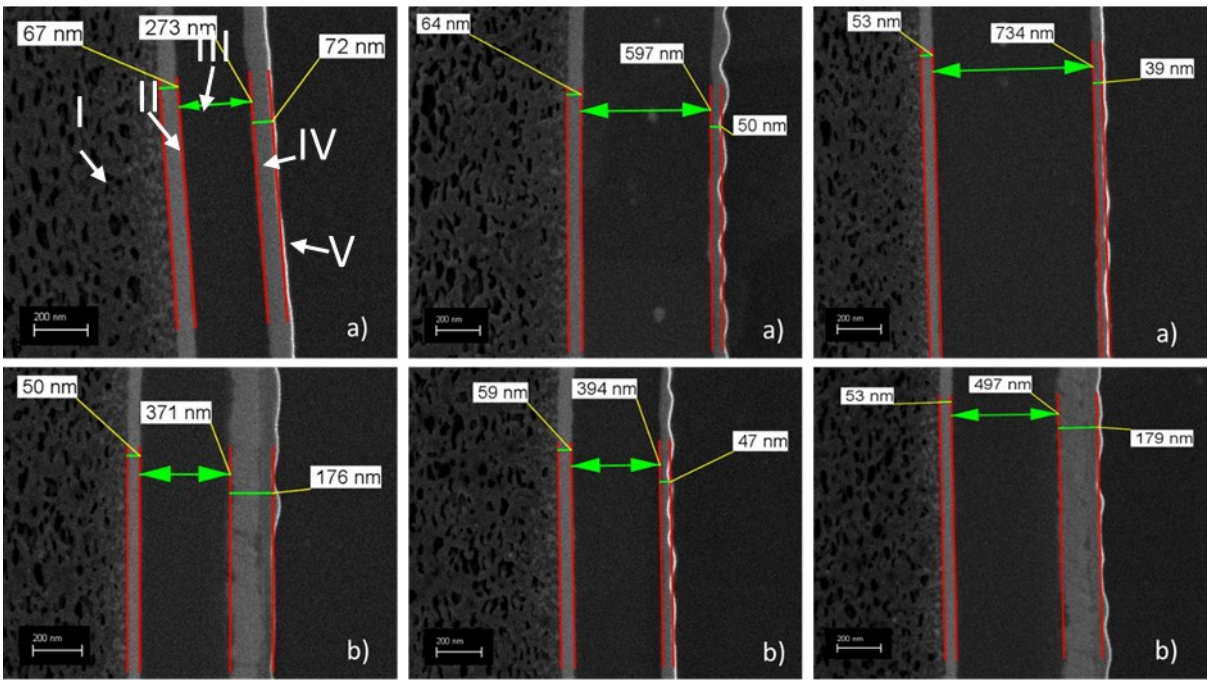

Figure A 16 Cross-sectional SEM images of TFC membranes consisting of PAN support (I), a PDMS based gutter layer (II), a selective PolyActive™ layer (III) and a PDMS based protective layer on top (IV). The brightest line in the image is caused by the platinum layer applied in the preparation (V). The images show the variation of selective layer thickness when pure SMC 3 was used as a solvent. The concentration of PolyActive™ was 1 wt% in all cases. The upper images show the results for an applicator roll speed of 0.034 m/s (a), the lower images for a roll speed of 0.056 m/s (b).

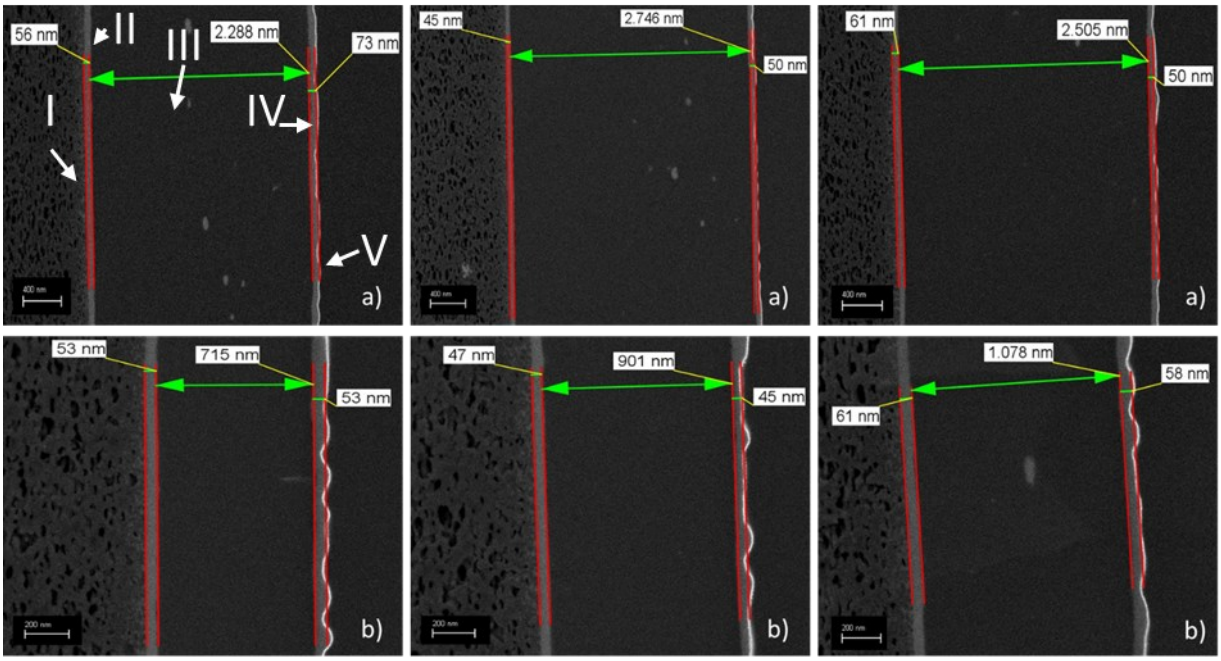

Figure A 17 Cross-sectional SEM images of TFC membranes consisting of PAN support (I), a PDMS based gutter layer (II), a selective PolyActive™ layer (III) and a PDMS based protective layer on top (IV). The brightest line in the image is caused by the platinum layer applied in the preparation (V). The images show the variation of selective layer thickness when pure SMC 3 was used as a solvent. The concentration of PolyActive™ was 3 wt% in all cases. The upper images show the results for an applicator roll speed of 0.034 m/s (a), the lower images for a roll speed of 0.056 m/s (b).

8.3 Analysed PDMS coating parameters

	Polymer concentration *c* (w%)			
Applicator roll speed v_1 (m/s)	0.5	1	2	3
0.045	*m*	*m; s; T; e*	*m*	*m; s; e*
0.036	*m*	*m; T; e*	*m*	*m; e*
0.027	*m*	*m; s; T; e*	*m*	*m; e*

Table A 1 Combination of process parameters used in PDMS coating experiments. The letters indicate the scope of measurements. Mass loss measurements during membrane coating were conducted in all cases and are denoted by "m". Moreover, "s" denotes SEM thickness measurements, "e" denotes evaporation mass loss measurements without membrane roll and "T" indicates infrared measurements.

Gap H_0 (µm)	Evaporation flux $\frac{\dot{m}_e}{A_{Surface}}$ (g/(m²·s))	Membrane roll speed v_2 (m/s)
146.6	0.597	0.558
146.6	0.903	0.558
183.4	0.597	0.558
183.4	0.903	0.558
146.6	0.597	0.742
146.6	0.903	0.742
183.4	0.597	0.742
183.4	0.903	0.742
165	0.75	0.65
165	0.5	0.65
165	1	0.65
135	0.75	0.65
195	0.75	0.65
165	0.75	0.5
165	0.75	0.8

Table A 2 Central Composite Design (CCD) plan for three fluctuating and/or uncertain process parameters influencing the coating thickness of the polymer solution. Simulations were done for all above parameter combinations, using an applicator roll speed of 0.045 m/s and polymer concentration of 1 and 2 w%.

8.4 Results from the standard CFD model

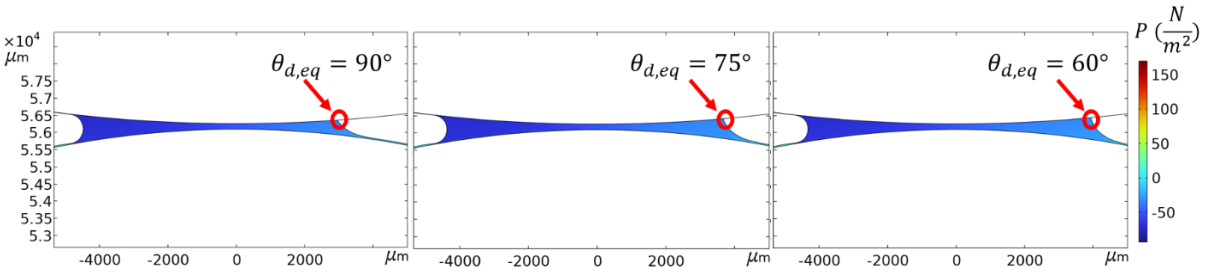

Figure A 18 Comparison of the meniscus shape in the gap region for different dynamic (advancing) contact angles $\theta_{d,eq}$ at the dynamic contact line (marked by the circle). A smaller advancing contact angle corresponds to a shift of contact line outwards of the gap region, while the left meniscus stays unchanged. There was no substantial change of film thickness on the applicator and membrane roll. The contour colours show the pressure distribution relative to atmospheric pressure, which is <0 due to the negative Laplace pressure.

8.5 Resulting contour plots of the DOE study

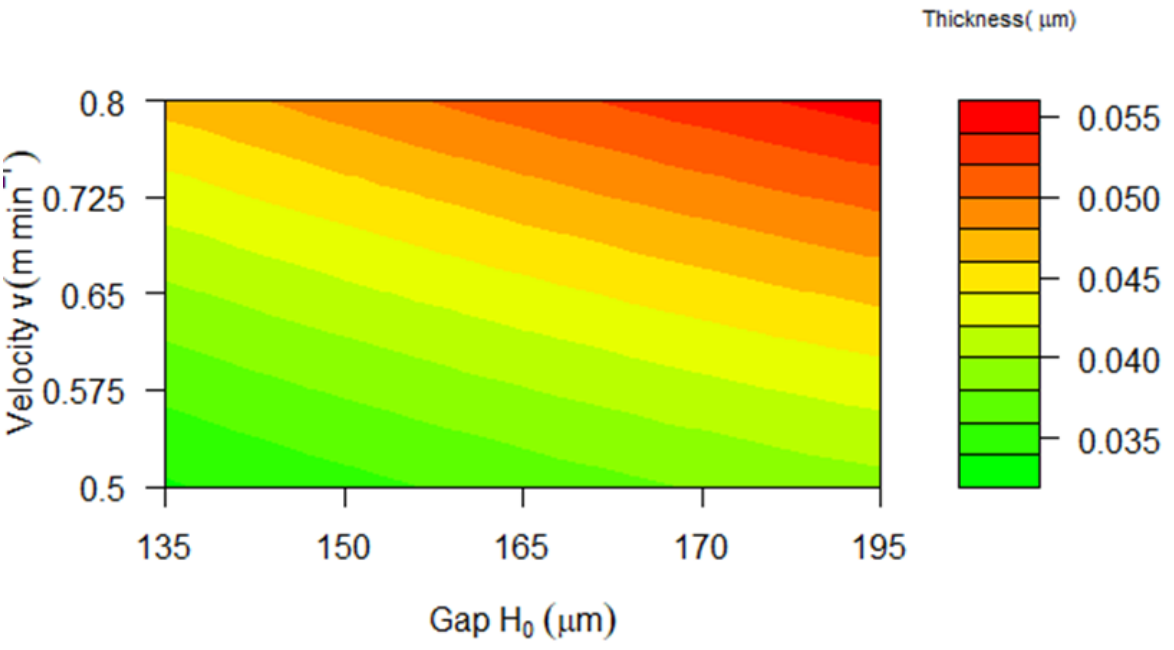

Figure A 19 Contour plot of the response surface showing a variation of polymer thickness δ between 0.035 µm and 0.055 µm depending on the membrane roll speed and gap size when a PDMS concentration of 1 w% is used.

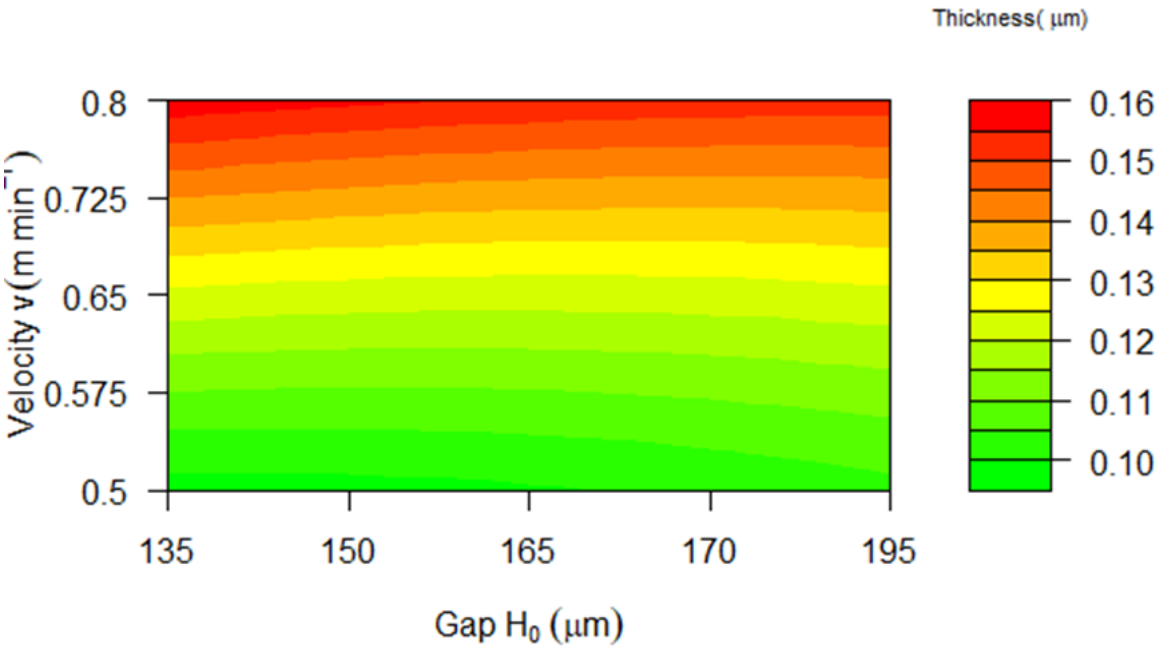

Figure A 20 Contour plot of the response surface showing a variation of polymer thickness δ between 0.1 µm and 0.16 µm depending on the membrane roll speed and gap size when a PDMS concentration of 2 w% is used.

8.6 Marangoni effect

8.6.1 Surface tension gradients

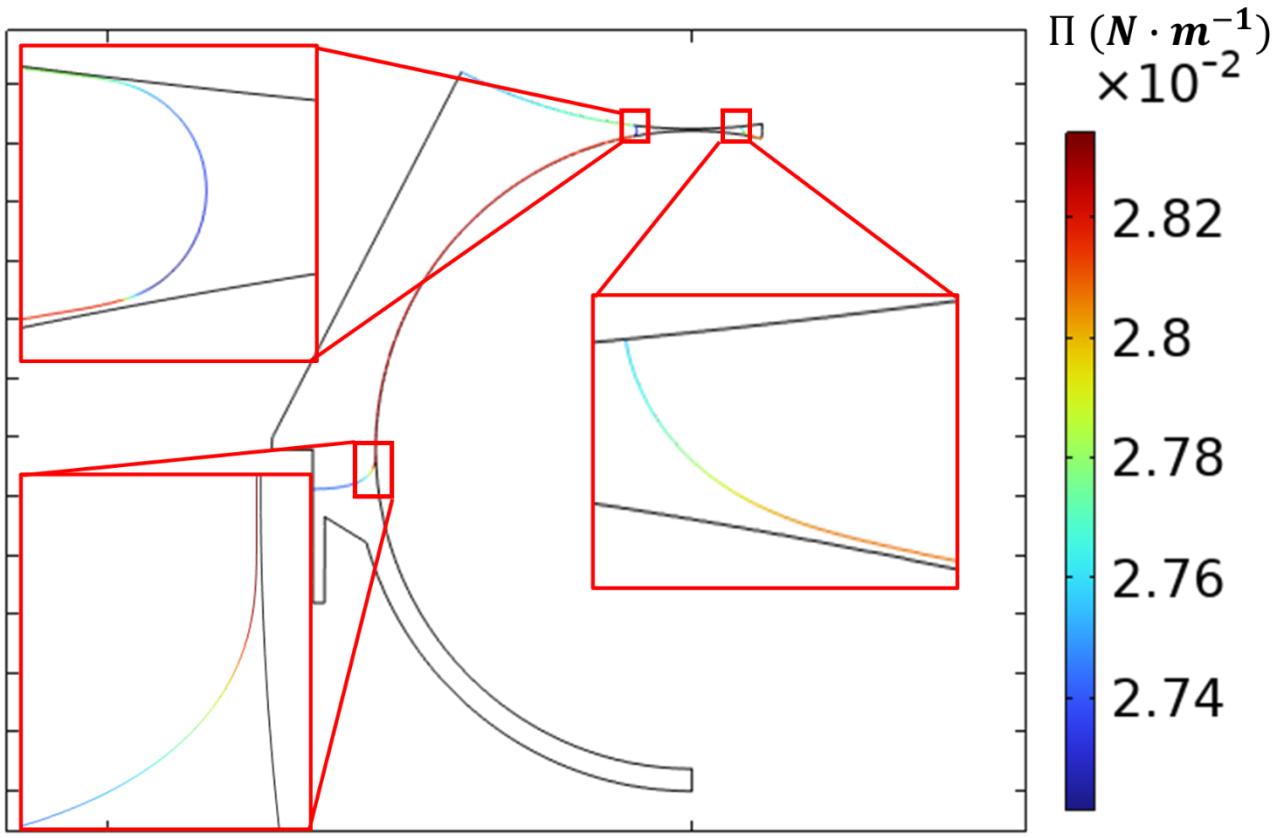

Figure A 21 CFD images showing the surface tension gradients along the lower and upper meniscus. The results are based on a Marangoni extension of the CFD model for 1 wt% PolyActive™ solution with an additional surfactant mass balance (parameters k_a =10 1/s and K_c =0.6).

8.6.2 Marangoni convection

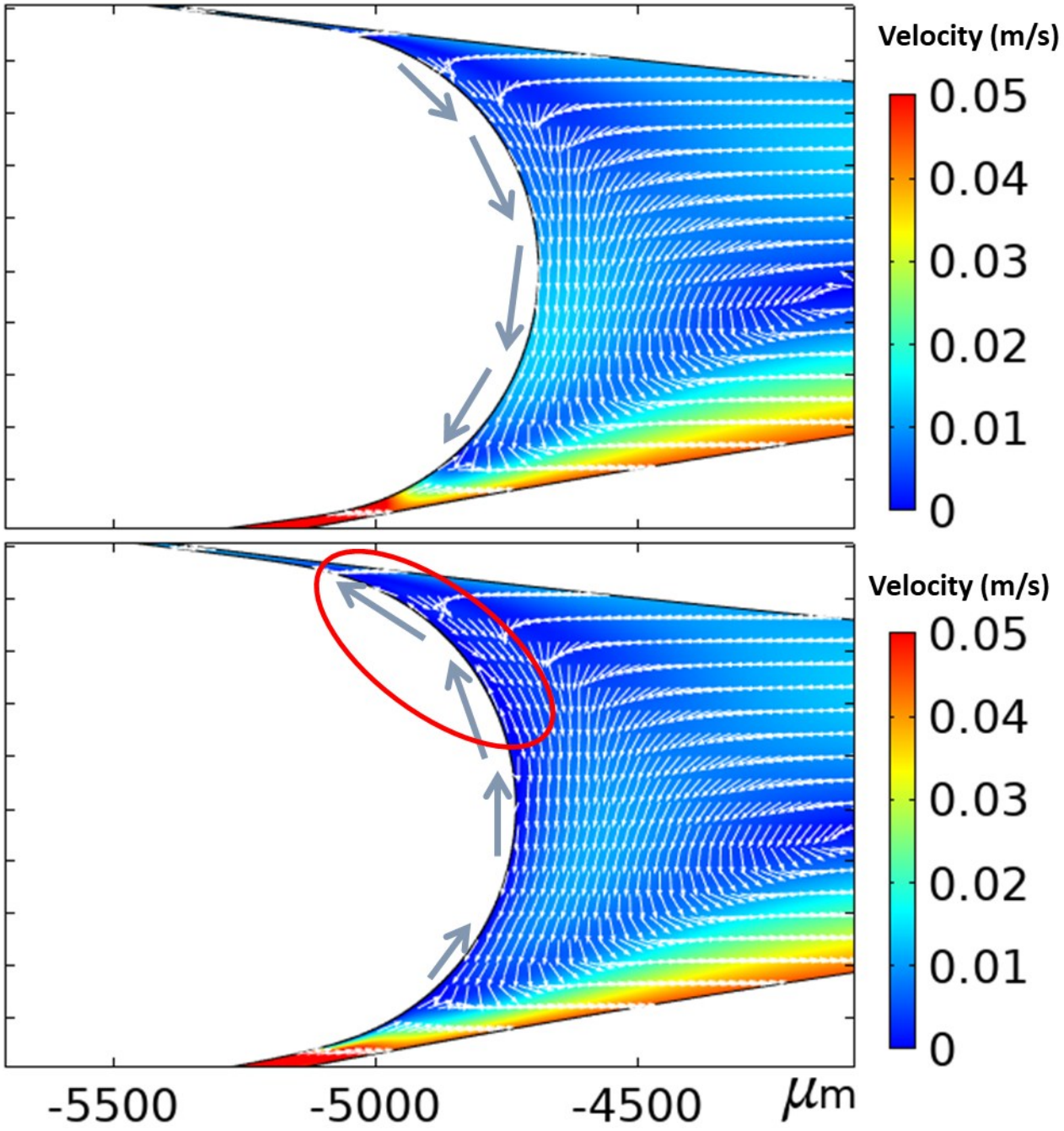

Figure A 22 Comparison of the flow field in the left meniscus of the gap region between applicator and membrane roll. The left image shows the flow field from standard CFD simulations without Marangoni effect (constant surface tension). The right image shows the flow field, when a surfactant equation is added that causes a gradient of surface tension and thus a Marangoni flow along the meniscus curvature in the upwards direction towards the membrane. The red circle highlights where the reversal in flow direction is visible in the velocity vector plot.

8.6.3 Surface tension isotherms

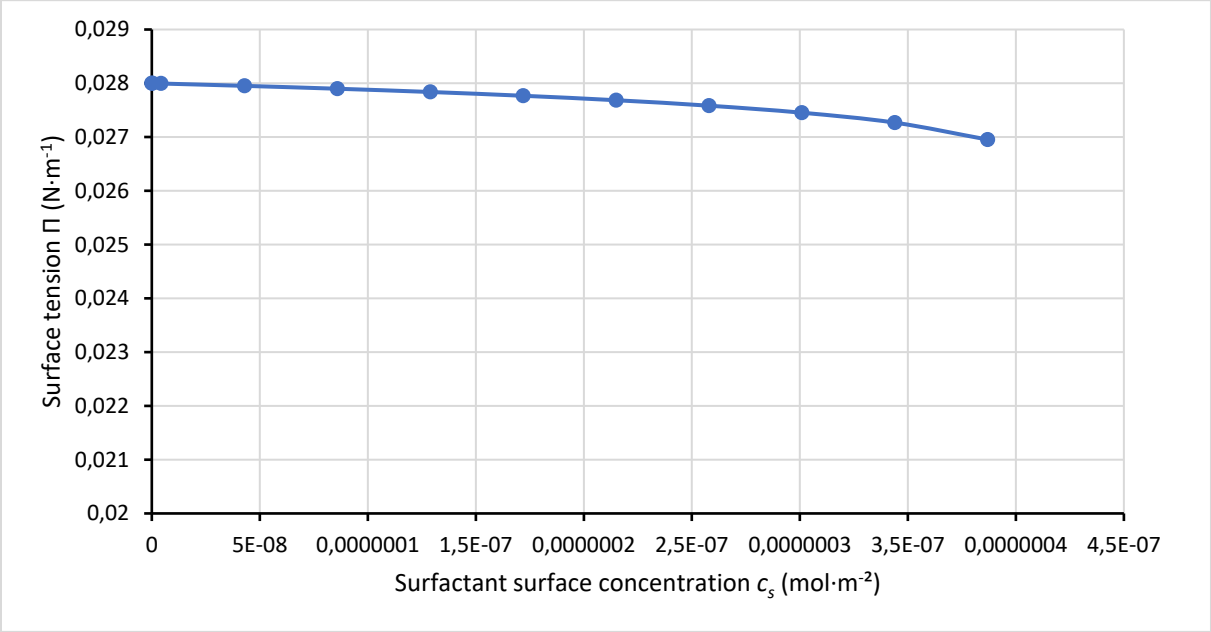

Figure A 23 Surface tension depending on the surface concentration of a surfactant as computed by the Frumkin model.

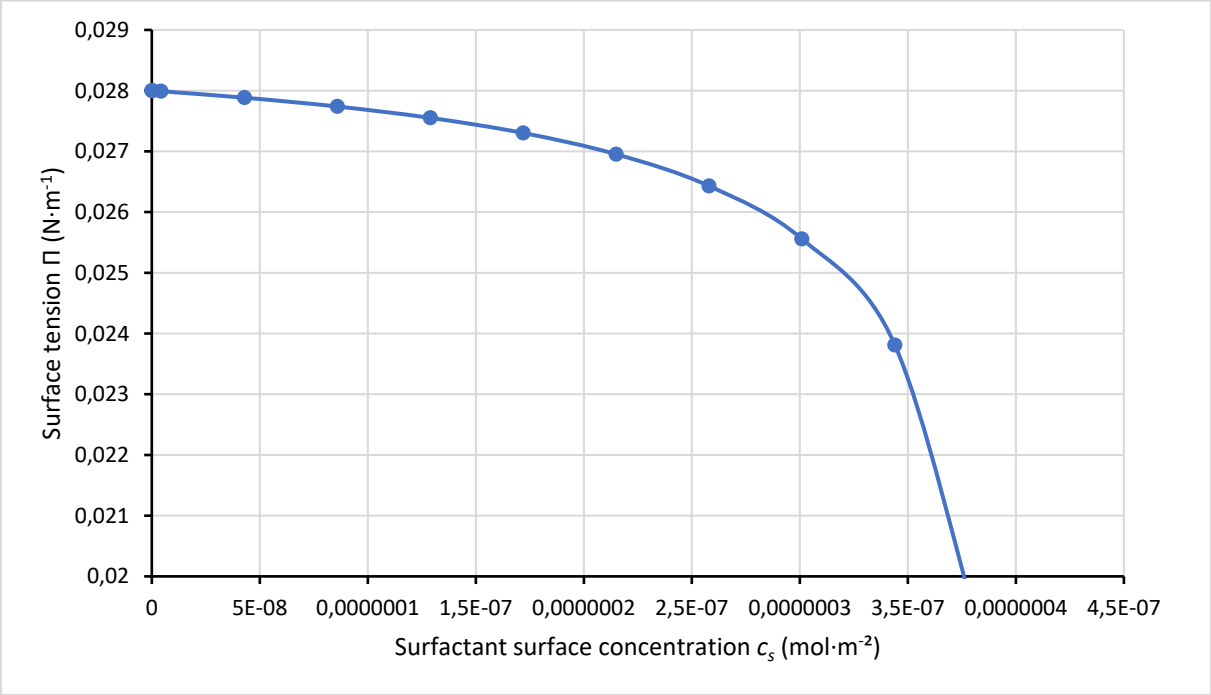

Figure A 24 Surface tension depending on the surface concentration of a surfactant as computed by the Volmer model.

8.6.4 Influence of surface activity on polymer concentration in the bulk

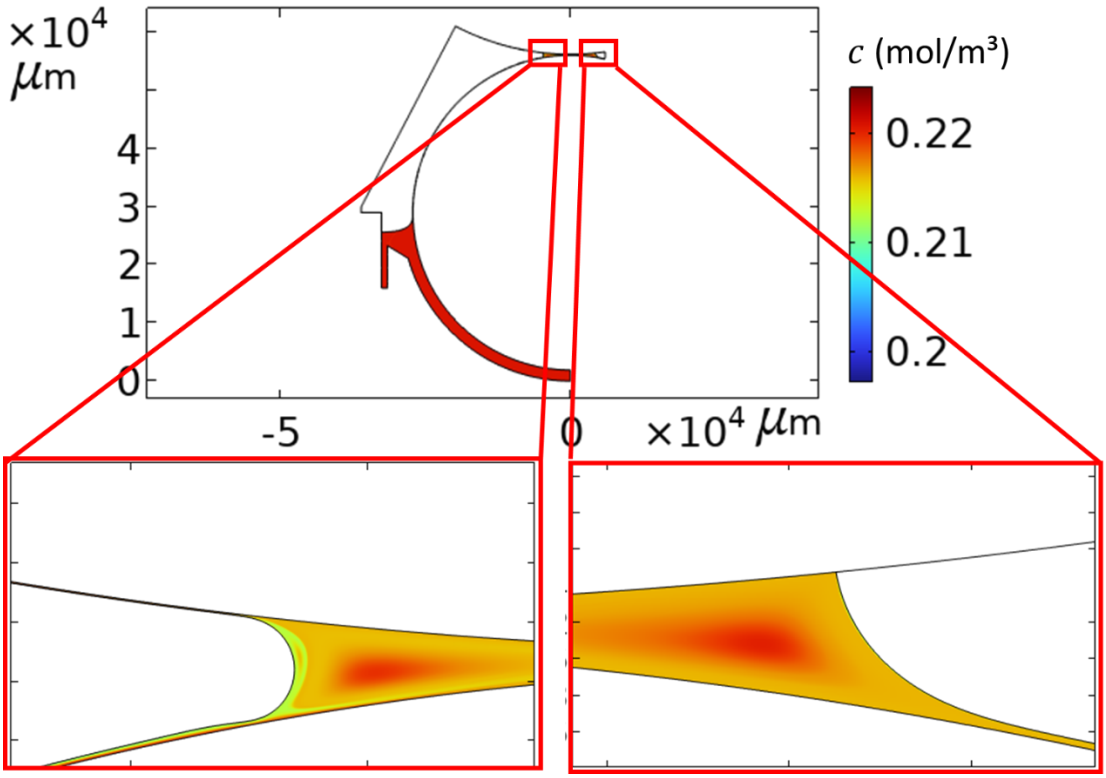

Figure A 25 Concentration profile of the polymer in the bulk when surface activity of the polymer and Langmuir adsorption to the interface is assumed. Due to the adsorption, there is a sink term of polymer concentration directly at the surface which reduces the concentration at the subsurface accordingly. Nevertheless, the effect is less than 5% compared to the initial concentration. Parameter: 1 wt% PolyActive™ solution, v_1=0.045m/s, k_a= 10 m³/(mol·s), K_c=0.6.

8.7 CFD computations of shear and strain rates in the meniscus regions

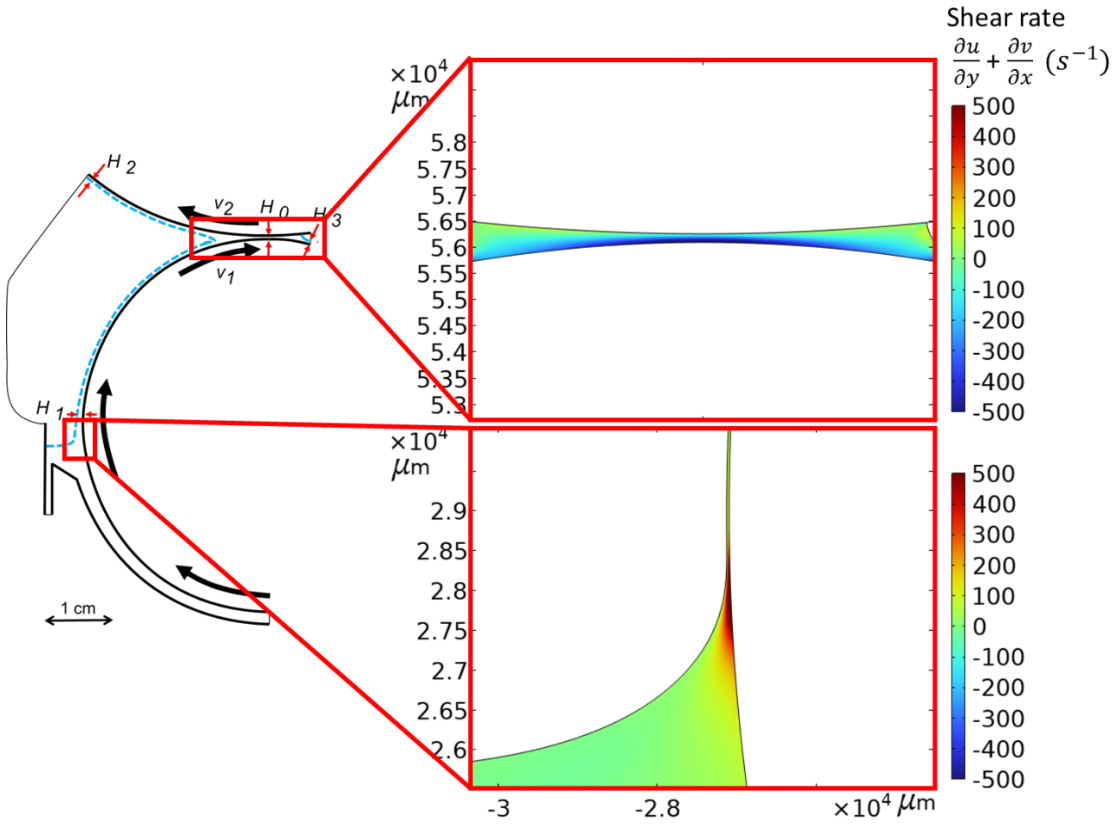

Figure A 26 CFD images showing shear rates in the lower and upper meniscus region (computed for the Newtonian standard model of 1 wt% PolyActive™ solution).

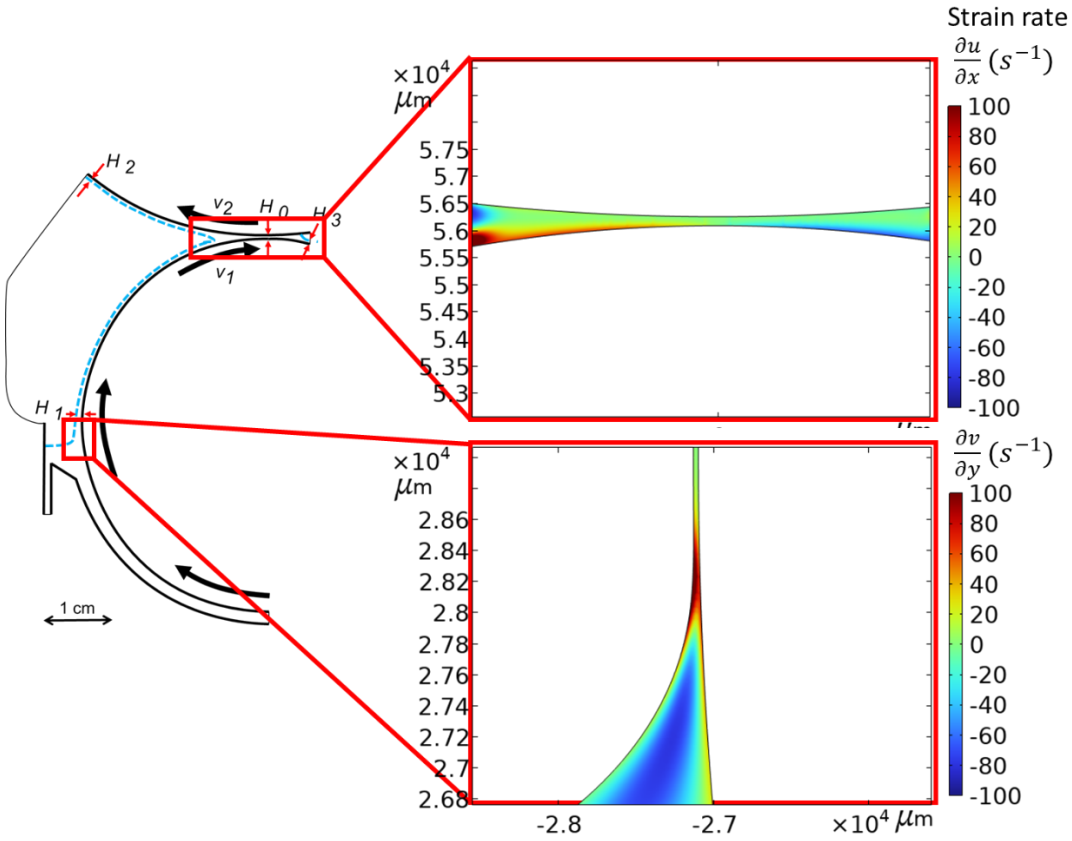

Figure A 27 CFD images showing the vertical and horizontal strain rate in the lower and upper meniscus region, respectively (computed for the Newtonian standard model of 1 wt% PolyActive™ solution).

8.8 CFD computations of viscoelastic stress in the meniscus regions

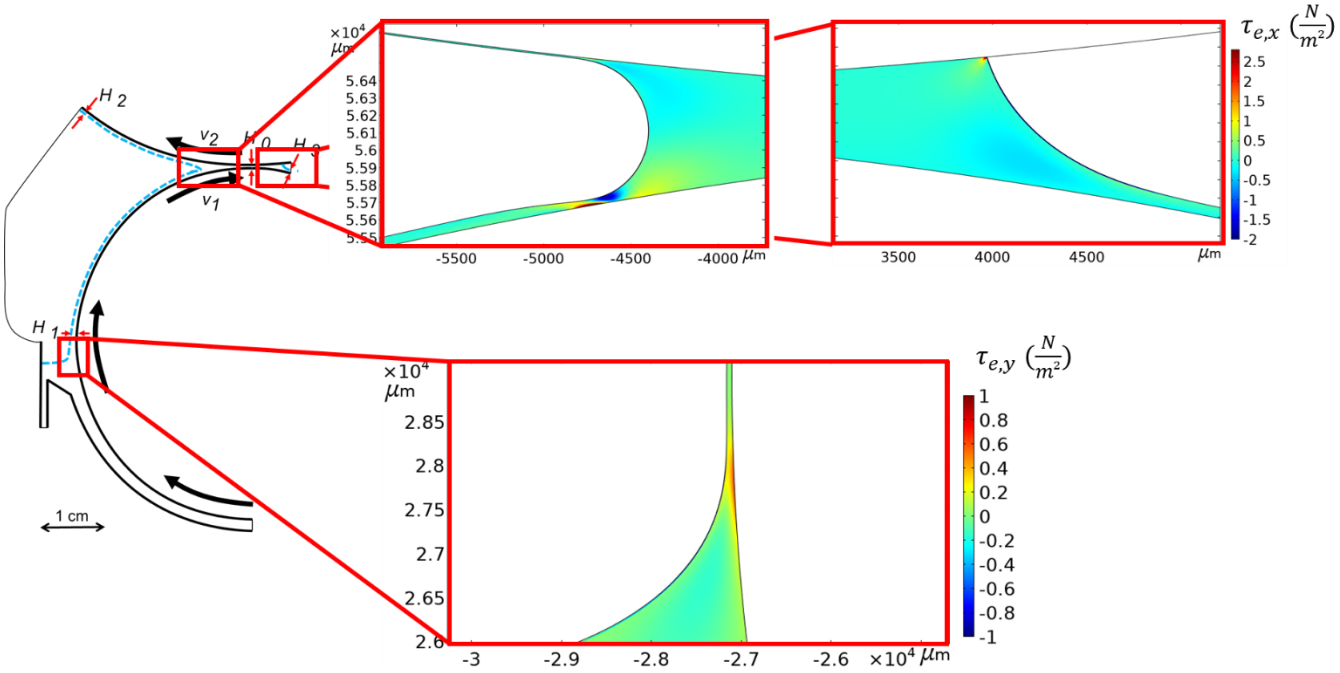

Figure A 28 CFD images of the viscoelastic stress distribution in the horizontal and vertical direction for the upper and lower meniscus region, respectively. Results are for 1 wt% PolyActive™ solution and an assumed viscous interaction parameter η_P=0.003 mP·s, a relaxation time λ = 0.0025 s an extensibility factor of 3.

8.9 CFD computations of temperature profiles

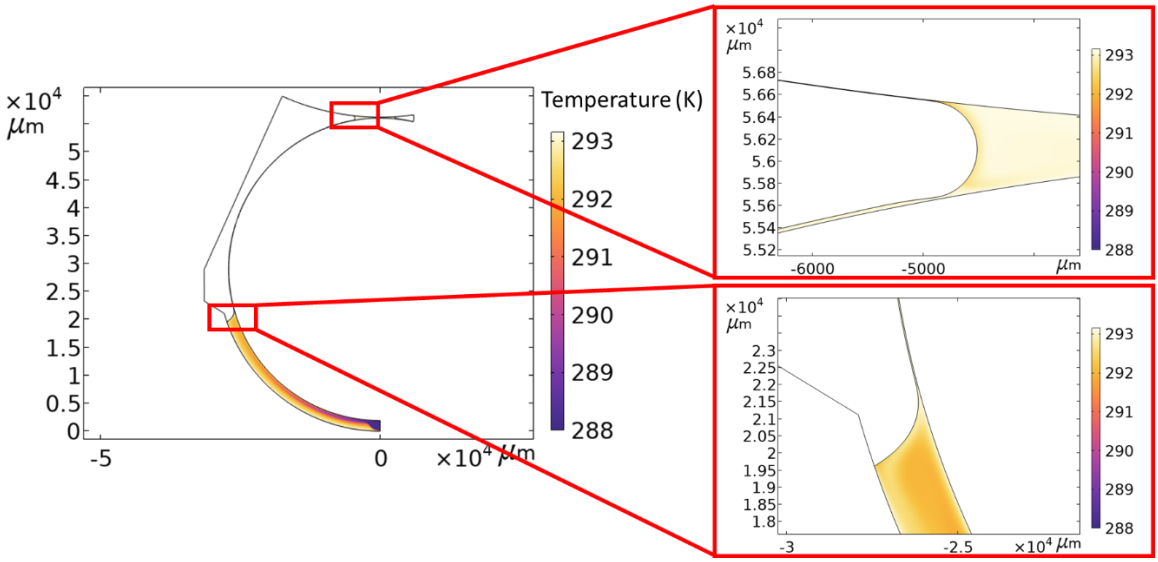

Figure A 29 Temperature profile along the roll-to-roll coating device as computed in CFD simulations based on 3 wt% PolyActive™ in pure SMC 3. The Inlet temperature of the feed was set to 288 K and the roll temperature at 293 K.

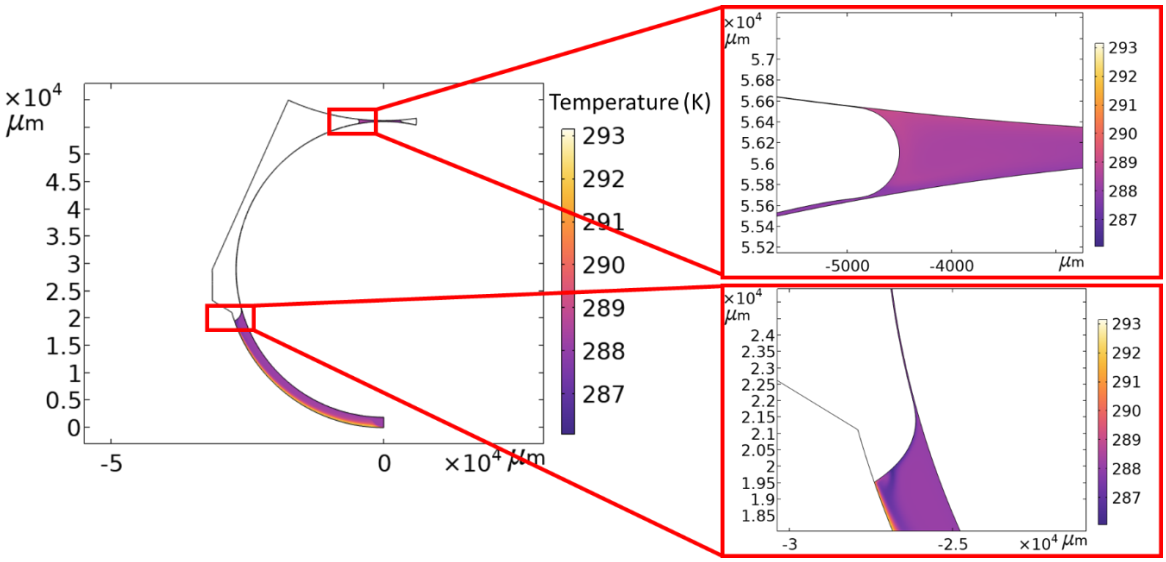

Figure A 30 Temperature profile along the roll-to-roll coating device as computed in CFD simulations based on 3 wt% PolyActive™ in pure SMC 3. Both, the Inlet temperature of the feed and the roll temperature were set to 288 K.